Applied AI/ML for Automatic Customisation of Medical Implants

by

Thomas Alexander Burge

Thesis submitted to Imperial College London

for the Degree of Doctor of Philosophy

April 2023

Dyson School of Design Engineering

Imperial College London

I hereby declare that this thesis and the work presented herein is my own work except where appropriated or acknowledged.

Thomas Alexander Burge

April 2023

Abstract

Most knee replacement surgeries are performed using ‘off-the-shelf’ implants, supplied with a set number of standardised sizes. X-rays are taken during pre-operative assessment and used by clinicians to estimate the best options for patients. Manual templating and implant size selection have, however, been shown to be inaccurate, and frequently the generically shaped products do not adequately fit patients’ unique anatomies. Furthermore, off-the-shelf implants are typically made from solid metal and do not exhibit mechanical properties like the native bone. Consequently, the combination of these factors often leads to poor outcomes for patients.

Various solutions have been outlined in the literature for customising the size, shape, and stiffness of implants for the specific needs of individuals. Such designs can be fabricated via additive manufacturing which enables bespoke and intricate geometries to be produced in biocompatible materials. Despite this, all customisation solutions identified required some level of manual input to segment image files, identify anatomical features, and/or drive design software. These tasks are time consuming, expensive, and require trained resource. Almost all currently available solutions also require CT imaging, which adds further expense, incurs high levels of potentially harmful radiation, and is not as commonly accessible as X-ray imaging.

This thesis explores how various levels of knee replacement customisation can be completed automatically by applying artificial intelligence, machine learning and statistical methods. The principal output is a software application, believed to be the first true ‘mass-customisation’ solution. The software is compatible with both 2D X-ray and 3D CT data and enables fully automatic and accurate implant size prediction, shape customisation and stiffness matching. It is therefore seen to address the key limitations associated with current implant customisation solutions and will hopefully enable the benefits of customisation to be more widely accessible.

Acknowledgements

My sincerest thanks go to my supervisor, Connor Myant. Thank you so much for your clear guidance, positivity, openness, and genuine passion for the work. Thank you for supporting me and for always making time, especially whilst on parental leave!

Thank you to my second supervisor, Jonathan Jeffers, for your detailed and constructive advice, help in finding various datasets, sharing your extensive list of contacts, and for your valuable industrial insights.

Thank you to Angelia Kedgley and Shuqiao Xie for sharing the KISTI dataset and SSM code. These helped enormously and allowed me to make rapid progress right from the start.

Thank you to Maxwell Munford and Stelios Kechagias for sharing data, your know-how of stochastic lattice design, and for helping me create prototype models.

Thank you to Gareth Jones and Christopher Jordan for your clinical insights and support in developing the implant size prediction tool.

Many thanks to the Korea Institute of Science and Technology Information, the Osteoarthritis Initiative, and Charing Cross Hospital for sharing your data which facilitated the research.

A huge thanks to my employer, GSK, for funding the project. Thank you also to my colleagues at GSK who helped me set the project up, reviewed my work, and provided support throughout.

Finally, thank you to my family, friends, and to my partner, Yaz. Without your love, support, and patience, I would not have been able to do this.

Table of Contents

List of Figures

List of Tables

List of Abbreviations

2D	Two-Dimensional
3D	Three-Dimensional
AI/ML	Artificial Intelligence and Machine Learning
AM	Additive Manufacture
AP	Anterior-Posterior
API	Application Programming Interface
CAD	Computer Aided Design
CNN	Convolutional Neural Network
CT	Computed Tomography
DRR	Digitally Reconstructed Radiograph
KISTI	Korea Institute of Science and Technology Information
K&L	Kellgren and Lawrence
GUI	Graphical User Interface
ICP	Iterative Closest Point
ML	Medial-Lateral
MRI	Magnetic Resonance Imaging
OAI	Osteoarthritis Initiative
OUH	Over or Under Hang
OTS	Off-the-Shelf
PDM	Point Depth Model
RMSE	Root Mean Squared Error
ROI	Region of Interest
SD	Standard Deviation
SSM	Statistical Shape Model
TKR	Total Knee Replacement

Chapter 1

Introduction

The following chapter presents a brief overview of the knee replacement procedure, as well as the key technologies enabling automated implant customisation. The objectives of the thesis and its structure are then outlined.

1.1. General Introduction

In a drive to achieve patient-specific implant products with higher degrees of functionality, more sophisticated design processes are required to overcome the challenges of cost viability and scalability. Current knee replacement customisation processes typically rely on extensive manual processing of patients' Computed Tomography (CT) scans and skilled Computer Aided Design (CAD) work to develop bespoke implant component geometries (Jun, 2011). The lack of automation inevitably means these solutions are more expensive with longer lead times compared to Off-the-Shelf (OTS) alternatives, which simply feature a set number of standardised sizes. Consequentially, the widely reported benefits of lower revision rates, shorter surgeries and reduced post-procedure pain associated with customised implants (Zeller et al., 2017) (Buller et al., 2018) (Ogura et al., 2019), have not been viable for the masses.

Recent advancements in Artificial Intelligence and Machine Learning (AI/ML), in particular computer vision techniques, are enabling previously time consuming and expensive manual processes, like the segmentation of CT scans, to be fully automated (Minnema et al., 2018). Moreover, numerous authors have shown how the use of statistical models, such as Statistical Shape Models (SSM), can be used to enable Three Dimensional (3D) anatomical models to be generated from Two Dimensional (2D) X-ray images. Thereby saving imaging costs and lowering the risks associated with high levels of radiation exposure (Zhu & Li, 2011) (Tsai et al., 2015) (Cerveri et al., 2017). Such technologies are opening a plethora of opportunities to eliminate the need for expensive and time consuming manual processes and enable cost effective solutions for customising medical products, including knee replacement implants.

1.2. Knee Replacement

To introduce the context of knee replacement, this section gives an overview of the knee anatomy, osteoarthritis, the surgical procedure, and both OTS and customised implant models.

1.2.1. Anatomy of the Knee

The knee is a complex ‘modified hinge’ joint which maintains stability and control during a variety of loading situations. The joint consists of two bony articulations; the articulation between the femur and tibia bones bears most of the body weight whist the articulation between the patella and femur creates a frictionless transfer over the knee of the forces generated by contraction of the quadriceps femoris muscle (Abulhasan & Grey, 2017). Figure 1 provides a schematic of the important bones, soft tissues, and features of the human knee.

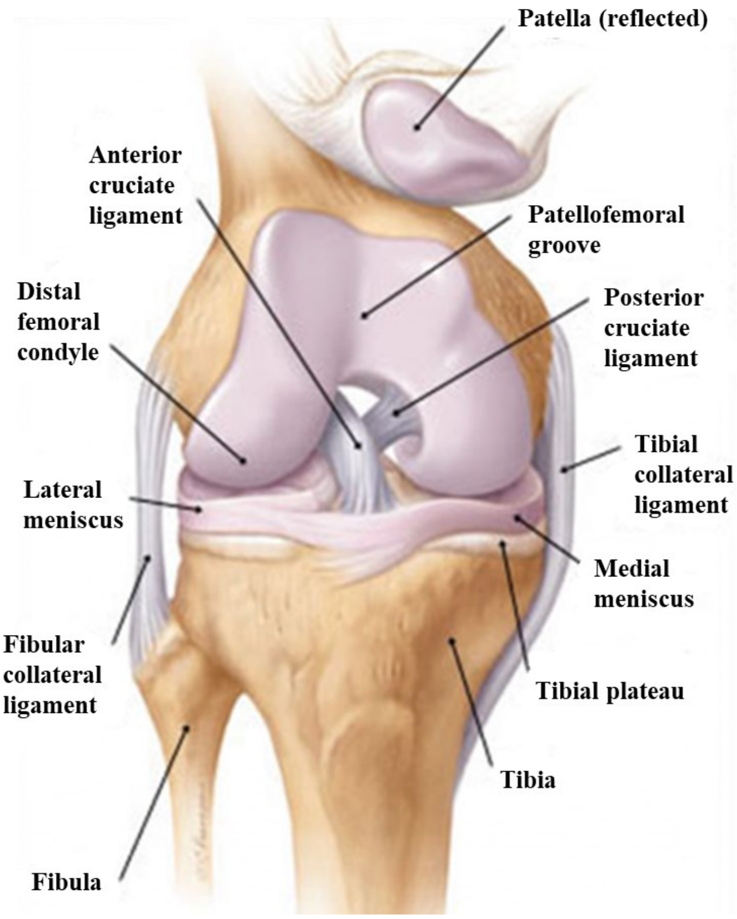

Figure 1: Anatomy of the human knee © Christy Krames (1999)

The knee has six degrees of motion in three different planes including the sagittal, coronal (frontal), and axial (transverse), as illustrated in Figure 2. It has the highest range of movement in flexion and extension about the sagittal plane. It also facilitates varus and valgus rotation about the coronal plane, in addition to medial rotation at the end of the knee flexion and lateral rotation at the terminal extension of the knee in the axial plane (Abulhasan & Grey, 2017).

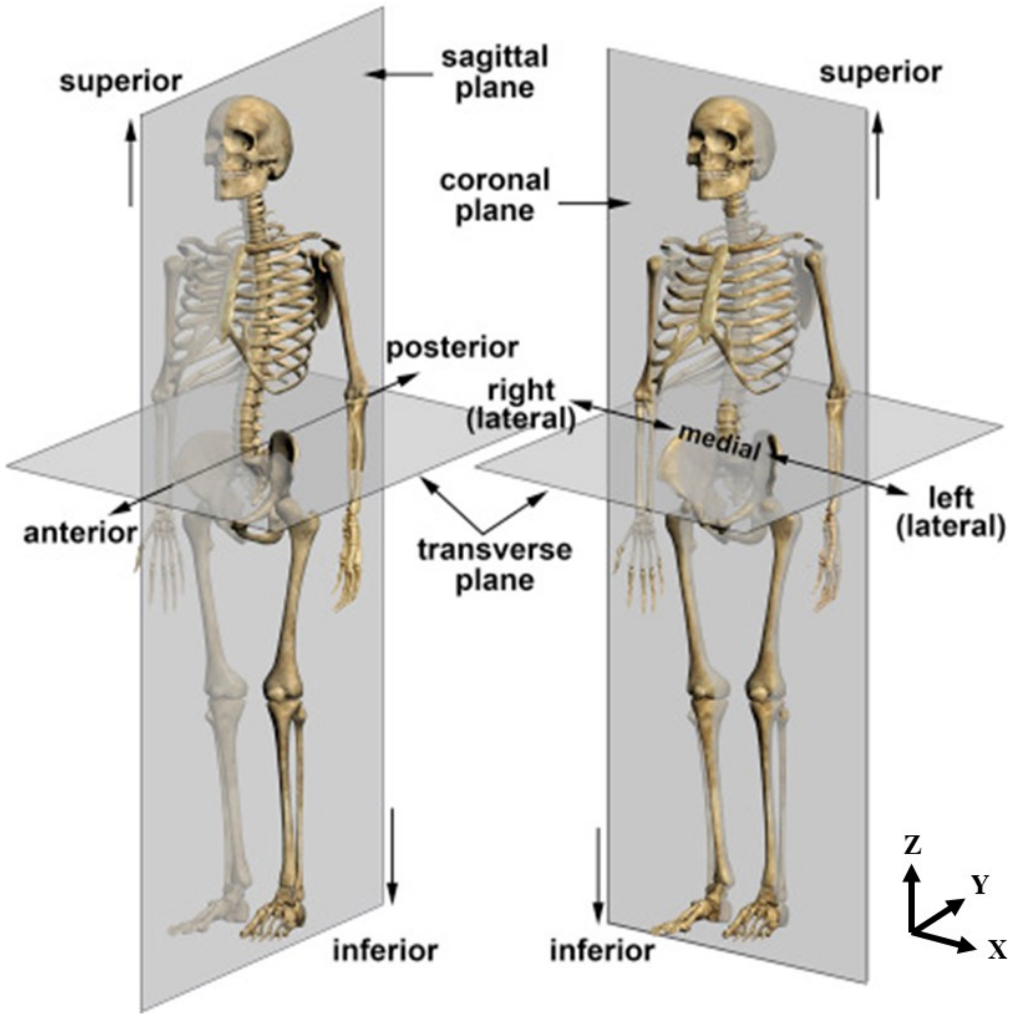

Figure 2: Overview of planes of reference and directional terms © (Nikita, 2017)

1.2.2. Osteoarthritis and the Surgical Procedure

Osteoarthritis is characterised by cartilage and other tissues within the knee (as well as other joints) breaking down and compromising the joint. Localised areas of cartilage loss increase focal stress across the joint, leading to further cartilage loss, misalignment and structural deterioration that ultimately can lead to joint failure. Local inflammation in the connective tissue and cartilage may contribute to significant levels of pain and lack of mobility for those who suffer with the condition (Scott & Kowalczyk, 2006).

Knee replacement, otherwise known as knee 'arthroplasty', is one of the most common surgical procedures with more than 100,000 performed annually in the United Kingdom and over 700,000 in the United States (Price et al., 2018). The quantity and prevalence of knee replacement continues to increase as populations age. The mean age of patients undergoing the procedure in the United Kingdom is 70 years with roughly 40% more females requiring knee replacement than males (Carr et al., 2012). The main clinical indication for the surgery is osteoarthritis which accounts for 94 – 97% of operations (Carr et al., 2012).

The key steps of the knee replacement procedure involve removing the damaged cartilage surfaces of the distal (inferior) femur and the proximal (superior) tibia (Figure 3A – B). This is achieved using cutting guides to resect (cut) the bone to the required shape and depth before replacement implants are fitted to rebuild the joint and restore biomechanical functionality (Sheth et al., 2017) (Figure 3C – E).

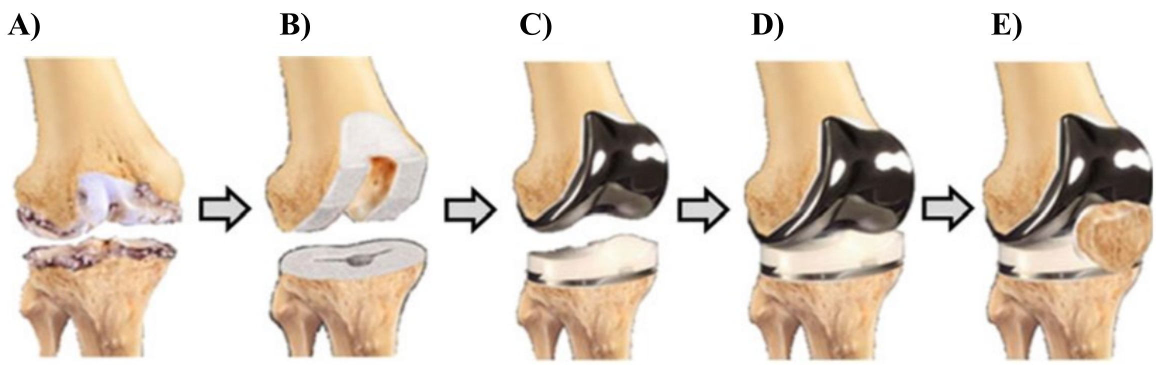

Figure 3: TKR surgical procedure – A) Anatomy before surgery with patella removed, B) Resected distal femur and proximal tibia, C) TKR components fitted, D) Bones realigned, E) Repaired joint with patella fitted © (Jun, 2011)

Knee replacement can be ‘total’ where the surfaces of both medial and lateral condyles are replaced (as illustrated in Figure 3), or ‘partial’ where only the most affected are replaced with ‘uni-condylar’ components. Partial replacement is popular for use with younger patients to minimise the amount of bone removed (Parratte et al., 2009). Nevertheless, Total Knee Replacement (TKR) is by far the most common form of knee replacement due to the substantially lower levels of revisions reported (Carr et al., 2012).

TKR is generally seen as safe with revision rates of approximately 5% after ten years reported (Postler et al., 2018). Despite the low revision rates, patient outcomes are often not optimal. Mahoney & Kinsey (2010) reported 40% of males and 49% of females experienced at least ‘occasional mild’ pain two years after surgery with 12% and 16% experiencing ‘moderate to severe’ levels respectively. This was supported by Beswick et al. (2012) who looked at long-term pain (five years post TKR surgery) and concluded an ‘unfavourable pain outcome’ was reported for 20% of patients. Pain is often the result of poorly fitting implant components which may be functionally acceptable, but can lead to inflammation and be highly uncomfortable for patients (Mahoney & Kinsey, 2010).

1.2.3. Preoperative Assessment and Size Selection

Before knee replacement surgery is performed, pre-operative assessment is necessary to confirm suitability, plan the procedure via templating, and estimate the required implant component sizes. Typically, this is done by capturing biplanar X-ray images of patients’ knee joints including ‘Anterior-Posterior’ (AP) or ‘front’ (Figure 4A), as well as ‘lateral’ or ‘side’ (Figure 4B) projections. The use of CT and/or Magnetic Resonance Imaging (MRI) 3D imaging is rarely used for standard OTS implant surgeries due to the high costs, additional radiation exposure, and limited accessibility associated with the imaging mediums (Tanzer & Makhdom, 2016).

A) B)

Figure 4: A) AP X-ray of knee joint, B) Lateral X-ray of knee joint

When selecting the best implant components to use the goal is to pick sizes that will provide the closest possible fit for individuals, thereby minimising the chance of complications, revisions, and pain post-surgery (Culler et al., 2017) (Buller et al., 2018) (Schroeder & Martin, 2019). Implant manufacturers typically supply models with between 5 – 8 standardised sizes (Hitt et al., 2003) (Wernecke et al., 2012). Sizing ranges however vary substantially, with some manufacturers providing 'gender-specific' solutions such as for the Zimmer Biomet 'NexGen' model. The size selection process is most commonly performed manually which has been shown to frequently result in poor accuracies (Hernandez-Vaquero et al., 2013). Due to the poor reliability of the manual process, surgeons can feel the need to re-evaluate the sizing during surgery and often opt to implant a different size (Sheth et al., 2017). This can lead to a higher chance of human error, as well as longer surgical procedures.

1.2.4. Implant Types and Designs

As shown in Figure 5, TKR implants consist of multiple components: A femur component is used to recreate the articulating surfaces of the distal femur condyles. It is grooved so the patella can move smoothly against the implant as the joint bends and straightens. The proximal end of the tibia is resected and replaced with a flat plate with a pin (keel) which protrudes into the centre of the bone for stability. Both the femur component and tibia plate (or 'tray') are typically made from titanium or cobalt-chromium metal alloys which provide the necessary strength, flexibility, resistance to wear, and biocompatibility. Some implants are also made of ceramics or ceramic/metal mixtures such as oxidised zirconium (Foran & Manner, 2021).

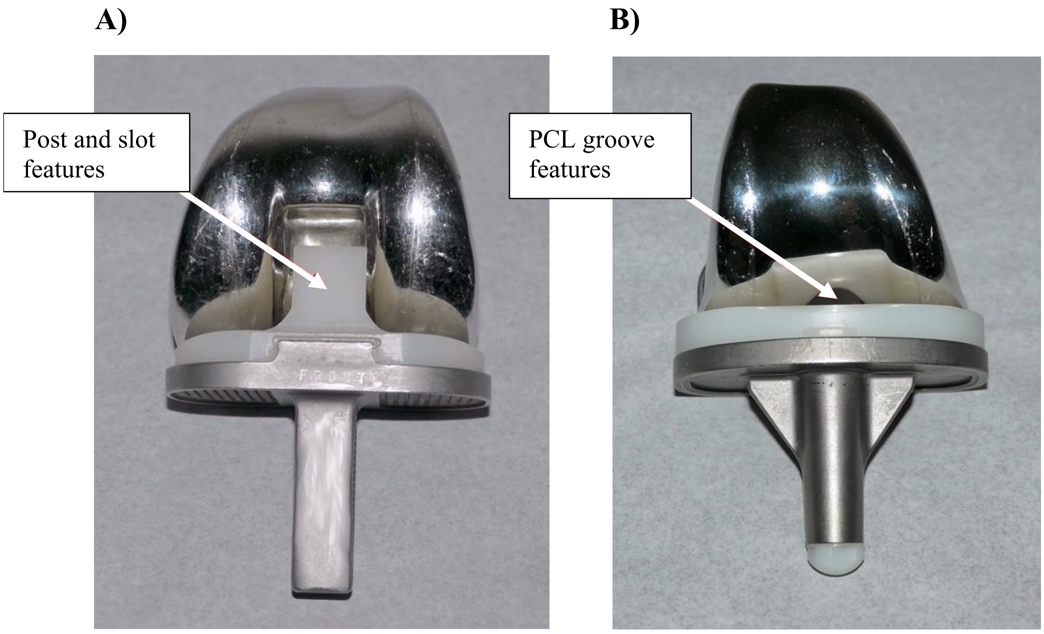

Figure 5: A) Posterior-stabilised and, B) Cruciate-retaining TKR implant designs © (Foran & Manner, 2021)

For most implants, a strong and durable polyethylene insert, or 'spacer' component is usually positioned in-between the femur component and tibia plate to add cushioning and achieve an effective bearing surface (imitating the meniscus in the natural joint – Figure 1). A small number of designs do not have separate metal plates and plastic spacers. In these cases, the polyethylene spacer component attaches directly to the bone. Lastly, in some cases, a patellar component is used. This is a dome shaped component, made of polyethylene, that duplicates the shape of the patella (kneecap). The patella does not always need to be resurfaced. In such cases, the bone can be left in place, like shown in Figure 3 (Foran & Manner, 2021).

Knee replacement implants come in a variety of models with over 150 different designs available on the market (Foran & Manner, 2021). TKR implants can be ‘posterior-stabilised’ (Figure 5A) or ‘cruciate-retaining’ (Figure 5B). In posterior-stabilised designs both the cruciate ligaments are removed during surgery (visible in Figure 1). To account for this, the tibia plate has an internal post that fits into a slot in the femur component to replicate the function of the posterior cruciate ligament (i.e., prevent the femur from sliding forward excessively on the tibia when the knee is bent). The posterior cruciate ligament is preserved in cruciate-retaining designs but the anterior cruciate ligament is still removed. Cruciate-retaining components do not have the post and slot features. Instead, they are designed with grooves to accommodate the posterior cruciate ligament. The implant type is usually selected for patients whose posterior cruciate ligaments are healthy enough to continue stabilising their joint. A small number of ‘bicruciate-retaining’ designs are also available where both the cruciate ligaments are preserved. These are however relatively new to the market and a limited amount of data exists on their performance (Foran & Manner, 2021).

Knee implants can be classified as ‘mobile-bearing’ or ‘fixed-bearing’. Mobile-bearing implants feature polyethylene spacers that are free to rotate short distances inside the tibia plate. The design feature allows patients the ability to rotate their knees slightly and more closely resembles a natural knee. In fixed-bearing implants the polyethylene spacer is fixed to the tibia plate to prevent any axial rotation (Foran & Manner, 2021). Mobile-bearing knee implants are designed for potentially longer performance with less wear but require more support from the cruciate ligaments to avoid dislocation. Mobile-bearings are therefore usually preferred for younger, more active patients (BoneSmart, 2022).

Lastly, implants can also be cemented in place or press-fitted onto the bone (referred to as ‘cementless’). Cementation is the most common approach and features a fast-curing bone cement (typically 'polymethylmethacrylate') to attach the femur component and tibia plate. Cementless fixation uses implants with textured or coated bone interfacing surfaces to enable new bone to grow into the implant and achieve the necessary fixation (Foran & Manner, 2021).

1.2.5. Customised Implants

To improve the outcomes of knee replacement, a small number of companies have developed shape customisation solutions where implants are designed to more accurately fit individuals' bones, facilitating greater bone preservation (Culler et al., 2017). This is especially useful when subjects are observed to have abnormal anatomies which lie outside the range of geometries that standardised OTS implants are designed for (Jun, 2011). The leader in the commercial customised knee implant space is ConforMIS (Billerica, Massachusetts, US) who offer various model options for TKR and uni-condylar implant types (ConforMIS, 2022). An illustration of custom designed and conventional femur components (with areas of poor fit highlighted on the latter as dashed red circles) is provided in Figure 6.

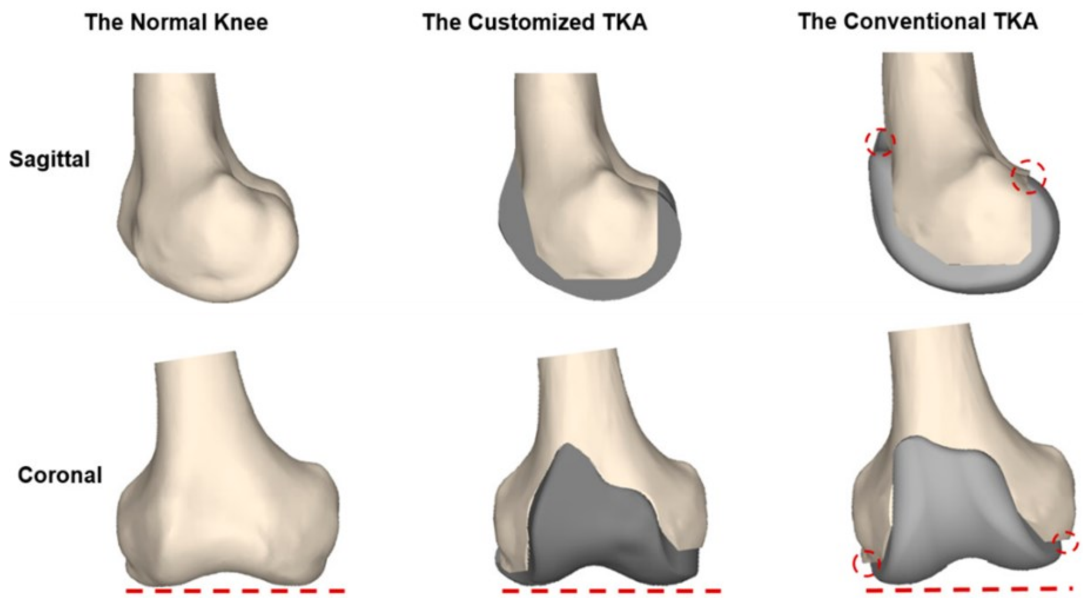

Figure 6: Custom design and conventional femur components © (Lee et al., 2020)

Numerous studies have demonstrated that customised knee replacement implants can afford better rotational alignment and fit without causing excessive Over or Under Hang (OUH)

(Ogura et al., 2019) (Arnholdt et al., 2020). OUH is the resulting gap (positive or negative) between the edges of the implanted components and bone after resection. Excessive OUH has been shown to lead to complications post-surgery, such as soft-tissue irritation, bleeding, osteolysis, laxity in flexion, subsidence, and instability with $\geq$ 3 mm generally regarded as clinically significant (Dai et al., 2014b), (Schroeder & Martin, 2019), (Shao et al., 2020). This value was therefore used as a threshold in this research to indicate poor implant fit.

As a result of their superior fit, custom implants have been shown to afford significantly lower transfusion and adverse event rates compared to standard OTS options and patients have experienced shorter hospital stays and better discharge disposition (Culler et al., 2017). This has translated into revision rates as low as 0.5% after four years compared to 2% for OTS products after the same duration (ConforMIS, 2018). Furthermore, authors have argued that by using customised implants, the overall cost of knee replacement can be reduced. Buller et al. (2018) compared possible cost reductions due to reduced surgery time, problems post-surgery, revision rates and implant storage against the typically higher component and imaging costs associated with custom solutions. The authors concluded that a net saving of $913.87 per patient, per episode of care, could be obtained. Nonetheless, the upfront costs of custom components and the additional imaging required can be 20 – 30% higher (Namin et al., 2019).

Despite the medical benefits, high patient satisfaction levels, and potentially lower costs of customised solutions, the technology currently makes up less than 1% of the knee replacement market (Evers, 2019). There are several reasons why customisation products are yet to revolutionise the industry, but the two principal reasons are believed to be that 1) none of the knee replacement customisation solutions identified were fully automated, and 2) that 3D medical imaging was always required (Seekingalpha.com, 2019). Consequently, laborious manual processing of imaging data and skilled implant design work is necessary which adds costs and lead time (Ortho Baltic Implants, 2020). Requiring 3D imaging (typically CT) is problematic as this is not commonly needed for OTS procedures and therefore adds additional costs and lead time. CT scans also expose patients to very high levels of radiation – for example, a chest CT scan typically delivers more than 100 times the radiation dose of a frontal and lateral chest X-ray (Smith-Bindman et al., 2009). Furthermore, they are expensive and are not widely available outside of large hospitals in developed countries. As a result, customisation solutions are currently used almost exclusively to treat clinical conditions that cannot be aptly addressed via OTS, sized implants (Ortho Baltic Implants, 2020).

1.3. Artificial Intelligence and Machine Learning

AI/ML is a widely trending topic with applications being deployed in most major business segments (Singh, 2018). ‘Artificial intelligence’ is an umbrella term that implies the use of computers to model intelligent behaviour with minimal human intervention. ‘Machine learning’ is represented by mathematical algorithms that improve learning through experience. The two main types of AI/ML algorithms are ‘unsupervised learning’ where an algorithm is able to find patterns in data without being provided with any labelled training data or prior examples, and ‘supervised learning’ where algorithms rely on previous examples to learn features of predefined classes (Hamet & Tremblay, 2017). ‘Deep learning’ is a subset of AI/ML that encompasses a variety of unsupervised and supervised feature learning algorithms that allow computational models of multiple processing layers to learn and represent data with numerous levels of abstraction (Voulodimos et al., 2018). ‘Computer vision’ is the field of AI/ML that focuses on using these algorithms to effectively identify and process objects in images and videos, primarily via the use of Convolutional Neural Networks (CNNs) (Mihajlovic, 2019).

CNNs form a class of deep machine learning algorithms that are highly effective at analysing patterns. They are designed to process data that come in the form of multiple arrays, such as colour images and videos. As such, they are often used in applications including facial recognition (Lecun et al., 2015). CNNs learn directly from inputted data which removes the need for manual feature extraction and means patterns/features that may not be identifiable by humans can be quickly recognised. The structure of CNNs was inspired by biological processes in that the connection between the neurons within CNN models resembles the organisation of a cat's visual cortex (El-Sayed & Sennari, 2014). An example of a CNN model architecture is shown in Figure 7.

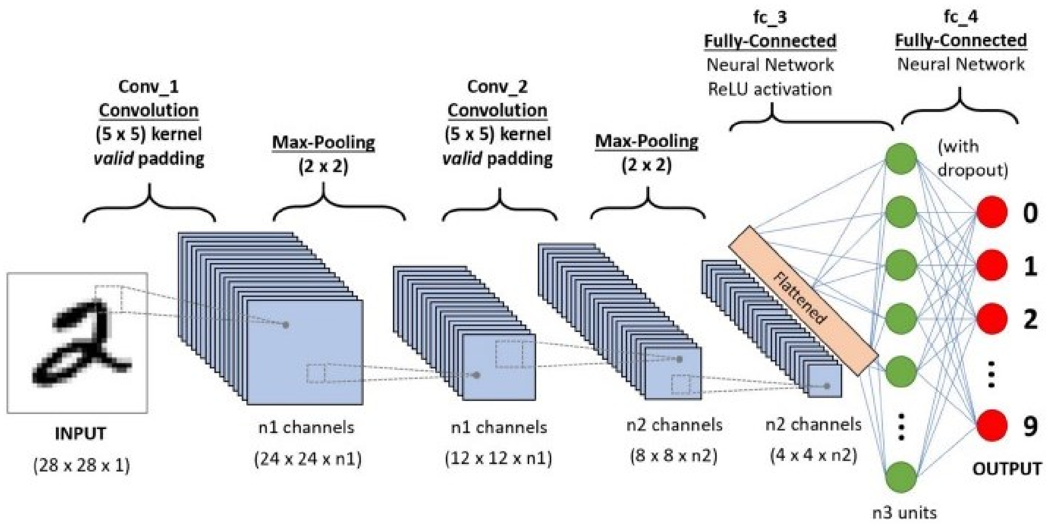

Figure 7: Example of the architecture of a CNN model © (Shah et al., 2020)

Each layer in the CNN architecture is called a 'feature map' where filtering, activation, and pooling operations are applied. Filters (convolutions) are applied at different resolutions within each feature map in the network with a proportion of the outputs used as inputs to the next. Filters start as simple elements, such as edges, and then increase in complexity to levels where specific objects can be defined. 'ReLU' (Rectified Linear Unit) activation functions are typically used after the filters to enable different features within the filtered images to be detected. 'Maximum pooling' is used to condense the image and enhance features. Usually, as the filter depth increases through the network, the output size (image height and width) decreases (Galvez et al., 2018). The feature map of the input layer of the architecture is usually a 3D matrix of pixel intensities for different colours where each pixel can be viewed as a separate feature. Depending on the tasks involved, the final layer with different activation functions is used to get specific conditional probabilities for each output neuron (Lecun et al., 2015). CNN networks can include hundreds of feature detecting layers which are typically alternated with a sub-sampling (pooling) layer to obtain properties leading to translation and deformation invariance (Matsugu et al., 2003).

Levels of importance (‘weights’) to features are learnt via CNN algorithms when trained with manually labelled image data. Weights can be seen as ‘knobs’ that are iteratively adjusted to best define the necessary input–output connections of the network in order to facilitate good predictions. Connections that are assigned high weightings will permit data to flow through to the subsequent filters and layers, consequently making more impact to output predictions than those with lower weightings (Lecun et al., 2015). In addition to weights, neural networks can feature ‘biases’. Biases add in additional units to the connections within a network to ensure, even if previous units have a value of zero, signals will be activated and data pushed forward in the network (Guha et al., 2005). The weights and biases of CNNs are learnt iteratively during model training by gradually tuning their values across the network, allowing their sensitivities to be learnt and model performance to be maximised.

There are numerous adjustments that can be made to improve how well a model performs, such as increasing the number of filter channels, operational steps, and/or the layers of a CNN architecture. Hyperparameters, such as the number of epochs (the number of training iterations or ‘passes through’ the training data), and batch size (the number of samples/images processed before the model is updated), can also be refined to optimise results for specified validation/test data (Koller et al., 2016).

CNN algorithms can be used to achieve various outputs. Three of the most common uses are image classification, object detection and image segmentation (Voulodimos et al., 2018). The difference between these is shown in Figure 8.

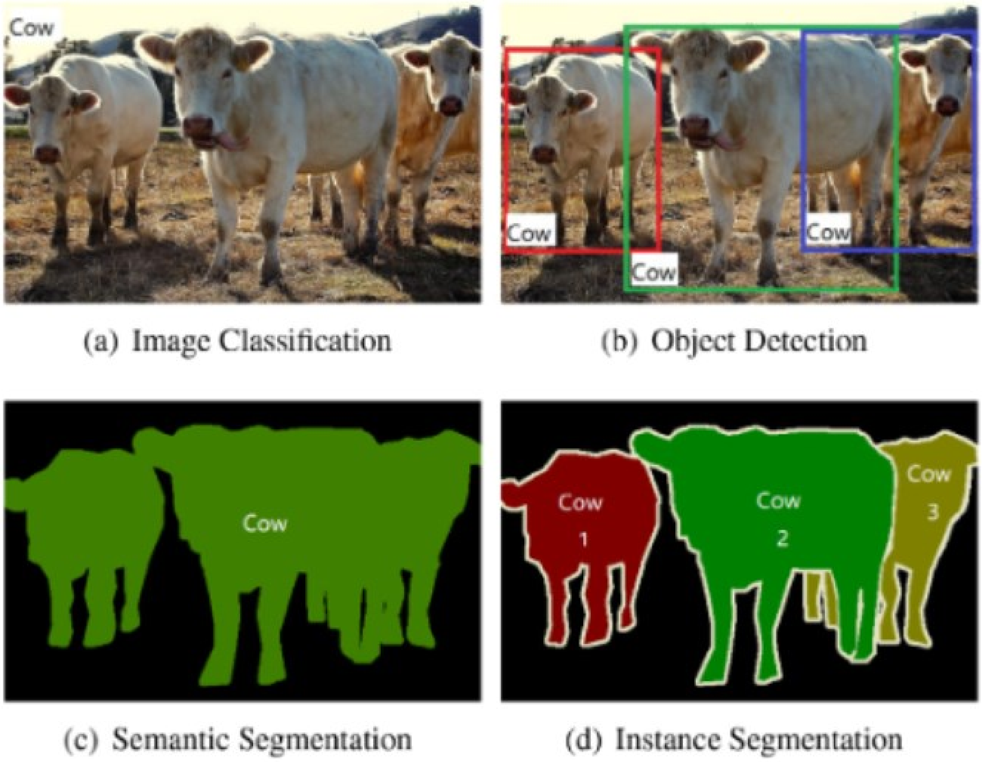

Figure 8: Difference between A) Image classification, B) Object detection, and C/D) Image segmentation © (Wu et al., 2020)

In image classification (Figure 8A), a CNN model is structured and trained to be able to recognise characterising features within an image to predict which of several user specified classes the image most likely belongs to. Classes can be binary (positive or negative) or multinomial for three or more. Examples of CNN based image classifiers include in the detection of tuberculosis (Liu et al., 2017), and for diagnosing COVID-19 (Narin et al., 2021).

Object detection involves classifying regions of images to find the location of specific objects within them and encasing the Region(s) of Interest (ROI) in rectangular bounding box(es). Algorithms can be trained to detect various or singular object types within images (Zhao et al., 2019), such as various instances of cows in (Figure 8B).

Image segmentation involves partitioning an image by labelling each pixel to isolate singular or multiple regions. The process allows for an image to be simplified into one that is more meaningful and/or easier to analyse (Shapiro & Stockman, 2001). 'Semantic' segmentation aims to predict pixel-wise classifiers to assign a specific category label to each pixel, resulting in binary images (Figure 8C). 'Instance' segmentation can identify different objects within an image and assign each of them a separate categorical pixel-level mask (Figure 8D). Segmentation models typically use a modified CNN architecture called a 'U-net', shown in Figure 9. U-nets enable segmentation models to work with fewer training images and yield fast and precise outcomes. In contrast to standard CNN architectures where the network purely contracts (downsamples), U-nets also include an expansive, upsampling path. Here the image size gradually increases back to the intended output image size as the depth of filters decrease. The expansive path typically mirrors the contracting side with pooling operations replaced by upsampling operators. The addition of the upsampling steps enable the model to assemble precise segmentation outputs in the form of new images (Ronneberger et al., 2015).

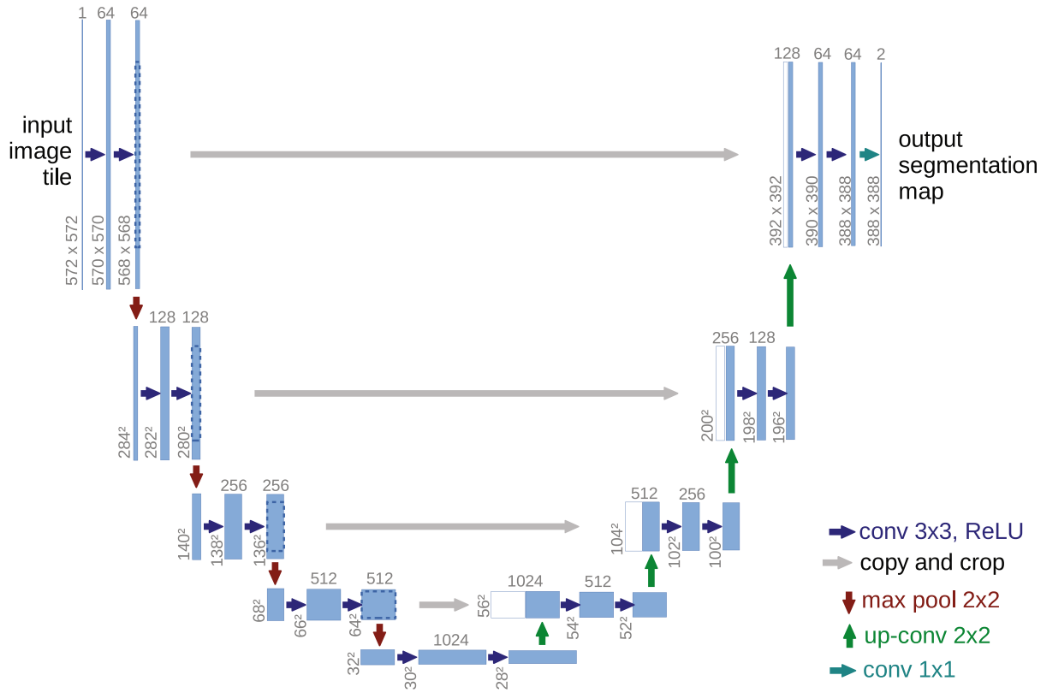

Figure 9: Example of an image segmentation CNN U-net model architecture © (Ronneberger et al., 2015)

1.4. Statistical Shape Models

Statistical models provide compact and efficient parameterisation of the variation in object classes (Davies et al., 2008). In SSMs, the relevant object class is shape, and the models allow for a population of semantically similar objects, such as various knee joint anatomies, to be described statistically. SSMs include an average 3D 'base' shape of a given population, in addition to describing the shape variation within it (Ambellan et al., 2019). 'Principal Component Analysis' (an unsupervised AI/ML method) is used to capture the geometrical variation of inputted training data and reduce its dimensionality down to a finite number of 'principal components' or 'modes of variation' along which the variation in the data is maximal (Seber, 2009) (Smoger et al., 2015). By using a few principal components often each sample can be well represented by just a few variables as opposed to potentially thousands (Ringnér, 2008). In the case of a knee joint, example principal components could include the epicondylar, femur, and tibia AP and ML widths, as illustrated in Figure 10.

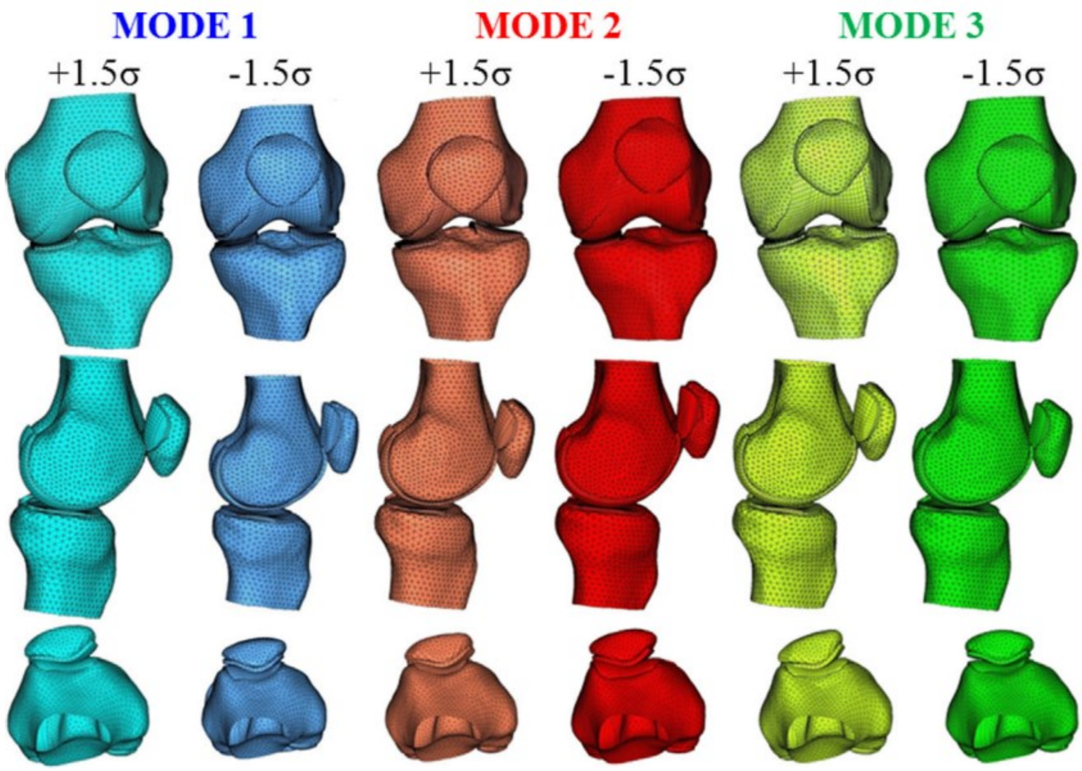

Figure 10: First three principal components/modes of a knee SSM © (Smoger et al., 2015)

The base shape of an SSMs is typically a parameterised mesh model which can be morphed, controlled by a specified number of the learnt principal components, to best fit the reference points (such as 2D profiles extracted from X-rays). The fitting process is completed iteratively using various optimisation algorithms to minimise the discrepancy between the SSM base shape and the reference points (Smoger et al., 2017). Once the solution has converged within an error tolerance, or the maximum number of morphing iterations is reached, a triangulated surface mesh 3D model reconstruction is generated and exported (Tsai et al., 2015).

1.5. Additive Manufacture

Additive Manufacture (AM) describes a set of manufacturing methods that function through material addition (adding layer upon layer) in contrast to traditional cutting, forming or casting methods (Deradjat & Minshall, 2017). There are numerous forms with 'Powder Bed Fusion' (Figure 11A) and 'Fused Deposition Modelling' (Figure 11B) being two of the most common.

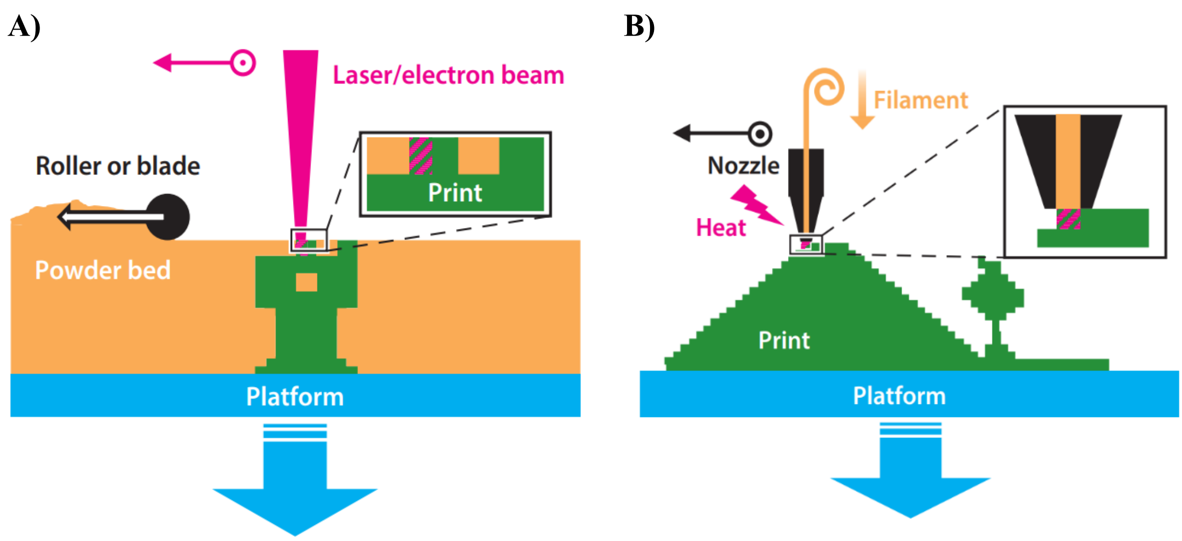

Figure 11: Schematics of A) Powder bed fusion, and B) Fused deposition modelling © (Velásquez-García & Kornbluth, 2021)

AM can be considered as a new type of ‘agile manufacturing’ that is capable of high product variety with minimal tooling required. Furthermore, once appropriate build parameters are defined (such as the build orientation, support structuring method, infill methods etc.), a significant degree of automation can be achieved, minimising the required labour. It is particularly appealing for producing bespoke products compared to standard manufacturing techniques as the systems can fabricate parts of almost any geometrical complexity. AM has historically been used extensively for prototyping, but is now being used more commonly to construct finished products as production speeds and accuracies improve (Tuck et al., 2008).

Various medical applications of AM have been shown possible including knee replacement implants (Namin et al., 2019), lower limb prosthetics (Chen et al., 2016), dental prostheses (Liaw & Guvendiren, 2017), wrist splints (Paterson et al., 2014), clavicle plates (Cronskär et al., 2015), and spine disks (Yu et al., 2019). The technology is also increasingly being used to enable the fabrication of customised medical implants (Giannatsis & Dedoussis, 2009). This has largely been because AM processes, such as metal ‘Selective Laser Sintering’ and ‘Selective Laser Melting’, have been shown to accelerate production, achieve better specifications, and reduce costs compared to traditional processes (Javaid & Haleem, 2018). Moreover, an increasing number of materials suitable for chronic implantation are compatible with AM processes. These include medical grade titanium (such as ‘Titanium 6Al-4V’) and medical grade stainless steel (including ‘304L’). The design freedoms of AM are also enabling porous structures, such as tissue scaffolds and compliant lattice structures, to be produced more efficiently (Munford et al., 2021).

Despite the many benefits of AM, there are important limitations to note. Some of the key points include that build speeds are limited compared to mass-manufacturing processes, like injection moulding, which can make scaling production at similar rates challenging (Beaman et al., 2020). The accuracy and resolution of certain AM techniques are often inferior compared to common processes like milling. Consequently, finishing processes are usually required to achieve smooth surfaces and producing parts requiring high levels of precision can be expensive (Wong & Hernandez, 2012). Postprocessing is normally required to remove support structures and/or binders. This is time intensive and often done manually. Lastly, only a limited number of materials can be used and, due to the layering process, the mechanical properties of the produced parts can be anisotropic and differ depending on factors such as build orientation (Beaman et al., 2020).

1.6. Software Pipelines

In software engineering, a 'pipeline' consists of a workflow constituting of a chain of processing elements (such as functions or algorithms), arranged so that the output of each element is the input of the next. For example, Ribeiro et al. (2009) outlined a pipeline for the 3D solid and finite element modelling of biomechanical structures. Their pipeline contained elements for loading images, image segmentation, mesh adjustments, solid model generation, and finite element modelling. Each element in the pipeline contained code which used data outputted from previous stages to feed algorithms (such as pretrained models) and transform inputs into outputted simulation results. This example was described as a 'semi-automatic' pipeline where a degree of user input, such as selecting nodes and boundary conditions in the simulation, was required. In this thesis, a 'fully' automatic pipeline is defined as one in which no further user feedback or input is necessitated after selecting the input data.

Software pipelines are typically formed of computer code and can be developed with or without user friendly front-end interfaces, often referred to as 'GUIs' (Graphical User Interfaces). The knee replacement customisation pipelines developed throughout this work (summarised in

Figure 12) were all developed using Python code (a high-level, general-purpose programming language) and executed through separate scripts. The standalone pipelines were then built into a single software application with a dedicated user GUI. This is described in Appendix 1.

1.7. Research Objectives

The research outlined in this thesis aimed to develop several automated 'pipelines' to demonstrate how customisation can be achieved more effectively for knee replacement, focusing predominantly on TKR as the most common type (Carr et al., 2012). Specifically, the research was conducted with the following objectives:

1) Develop both X-ray and CT based, fully automated mass-customisation pipelines for knee replacement surgery.
2) Demonstrate the accuracy of the pipelines across a broad patient population to validate their robustness.
3) Quantify the sensitivity of the pipelines to variations in input parameters and define necessary input imaging requirements.
4) Compare the performance of the X-ray and CT based pipelines with each other, as well as with currently available products.

1.8. Thesis Structure

Firstly, **Chapter 2** starts with a literature review of mass-customisation and the recent advancements in the various types of implant customisation and design methodologies.

Chapter 3 outlies the common materials and methods utilised to develop and test the several customisation pipelines developed through this work.

Chapter 4 details an assessment of OTS, standard sized TKR implants to establish the best possible performance of such products and verify the need for (shape) customisation solutions. The results of the analysis also serve as a useful comparison for the subsequent chapters.

Chapters 5 – 9 outline the various pipelines developed for automating the customisation of knee replacement surgery, illustrated in Figure 12. The first three chapters focus on biplanar X-rays as input and the last two focus on CT.

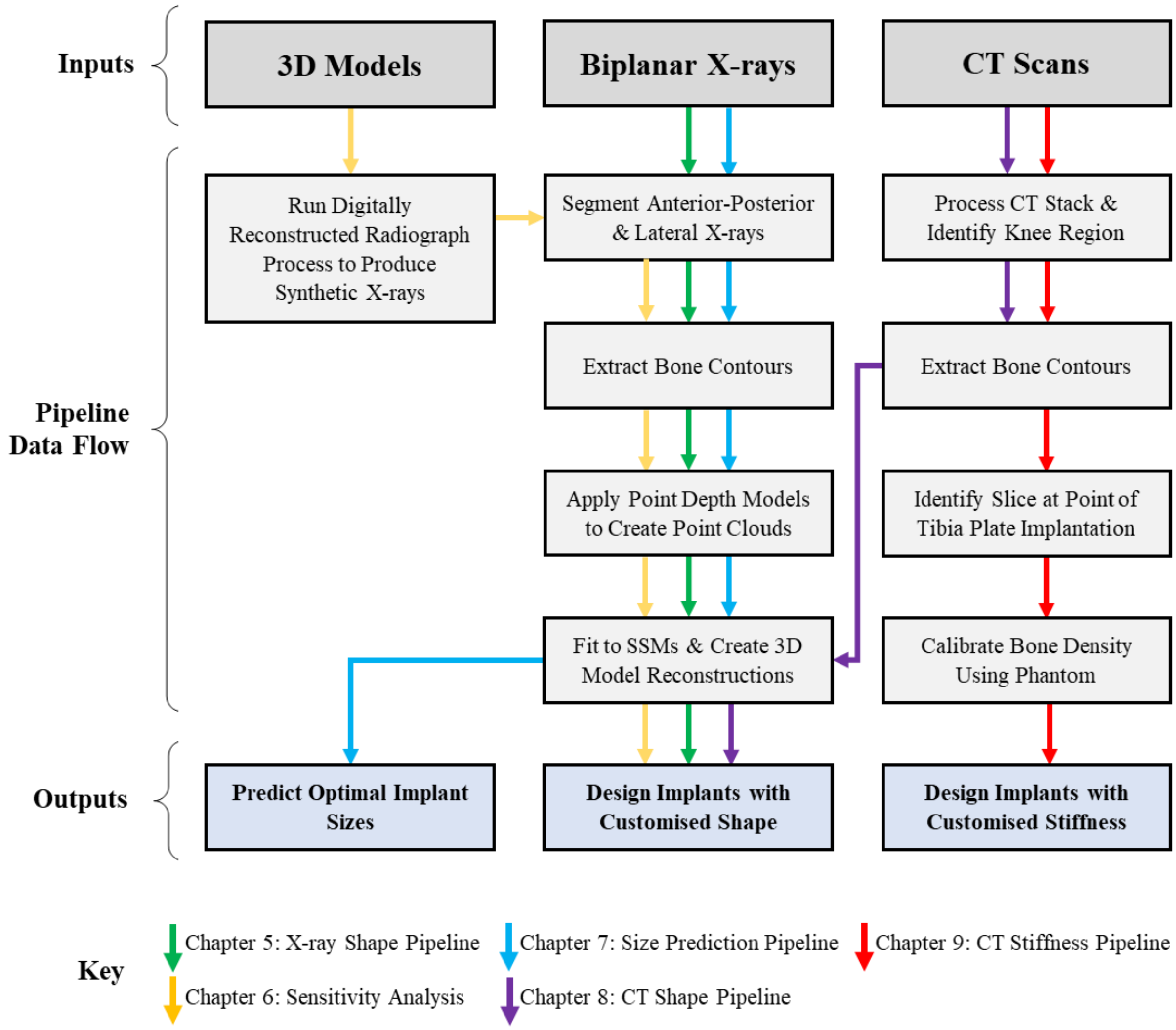

Figure 12: Flow chart illustrating the inputs, outputs and data flow of the knee replacement customisation pipelines developed in Chapters 5 – 9

Chapter 5 develops a pipeline to automatically design custom shape knee replacement implant components from biplanar X-rays and details initial results.

Chapter 6 utilises a Digitally Reconstructed Radiograph (DRR) approach to further evaluate the X-ray based pipeline's performance across a broader population and complete a sensitivity analysis of input parameters such as X-ray alignment and calibration accuracy.

Chapter 7 then utilises the 2D – 3D framework (developed in Chapter 5) to build a pipeline capable of automatically recommending the best OTS implant sizes for individuals, based on inputted X-rays. A performance analysis of the pipeline is provided.

Chapter 8 outlines a pipeline using 3D CT scan data to design custom fit knee replacement implants and details a results analysis.

Chapter 9 then studies whether CT scans can facilitate the additional level of implant stiffness customisation to optimise recovery and functional performance.

Finally, **Chapter 10** summarises and concludes the research before future work that should be completed is proposed.

Chapter 2

Literature Review

The following chapter reviews the relevant literature on mass-customisation, as well as recent advancements in medical implant customisation and associated design methodologies.

2.1. Mass-Customisation

‘Mass-customisation’ was defined as the ‘ability to provide individually designed products and services to every customer through high process agility, flexibility and integration’ by Davis (1989). Da Silveira et al. (2001) then further defined it as the ‘ability to provide customised products through flexible processes in high volumes and at reasonably low cost’. Additionally, Ferguson et al. (2014) argued that all aspects of a product’s life cycle should be considered from marketing through to distribution to facilitate the successful implementation of mass-customisation solutions.

Mass-customisation has gained increasing importance in the 21st century and is becoming more commonly adopted in economic sectors such as medical devices, automotive, and consumer electronics as demand for personalised products increases. Some of the key enablers for its increased adoption can be attributed to advancements in imaging technologies and ‘smart’ (AI/ML enabled) algorithms, as well as improvements in the scalability and accuracy of AM (Gandhi et al., 2013). For companies to successfully implement mass-customisation, Salvador et al. (2009) argued that three fundamental capabilities are always required. These include:

1) Solution Space Development – This involves developing software that enables large pools of customers/users to easily translate their preferences/data into unique product variants, and/or enable virtual prototyping of custom designs for evaluation.
2) Robust Process Design – This relates to automation that is not fixed or rigid and reuses or recombines existing organisational and value-chain resources to fulfil a stream of differentiated customer needs.
3) Choice Navigation – It is important that customers are supported in identifying their own solutions, whilst minimising complexity and the burden of choice.

'Customisation' can refer to various aspects of medical implant products and their related surgeries. The most obvious and common variant is to customise the shape and form of implant components for individuals' unique anatomies. Customisation could refer to the materials used to build an implant or incorporating lattice structures to tailor functional performance to match patients' bones. Customisation could simply refer to selecting the most appropriate OTS implant size, model, or type for an individual. Aspects other than the implant can also be customised, such as the cutting guides used during surgery (Cerveri et al., 2014), or whether 'open' or 'minimally invasive' surgery is performed (Fawzy et al., 2008).

Figure 13 illustrates various levels of customisation, or 'personalisation', that can be adopted for medical devices. This is categorised along the X axis with the level of automation involved with achieving said customisation along the Y axis. Paxton et al. (2022) argued that the 'holy grail' of medical device personalisation is the top right hand corner where custom-made products are enabled with fully automated design and manufacturing processes.

In knee replacement implants specifically, it was highlighted previously in Chapter 1.2.5 that current commercially available customisation solutions have so far failed to achieve large-scale success due to their high upfront component costs and long lead times (Ortho Baltic Implants, 2020). It is believed that this is principally because no solution has so far achieved the holy grail of fully automated customisation as defined by Paxton et al. (2022). Therefore, it is believed that a true mass-customisation solution is yet to be demonstrated. The following sections detail the methodologies identified in the literature that worked towards achieving differing levels of medical implant customisation with varying degrees of automation.

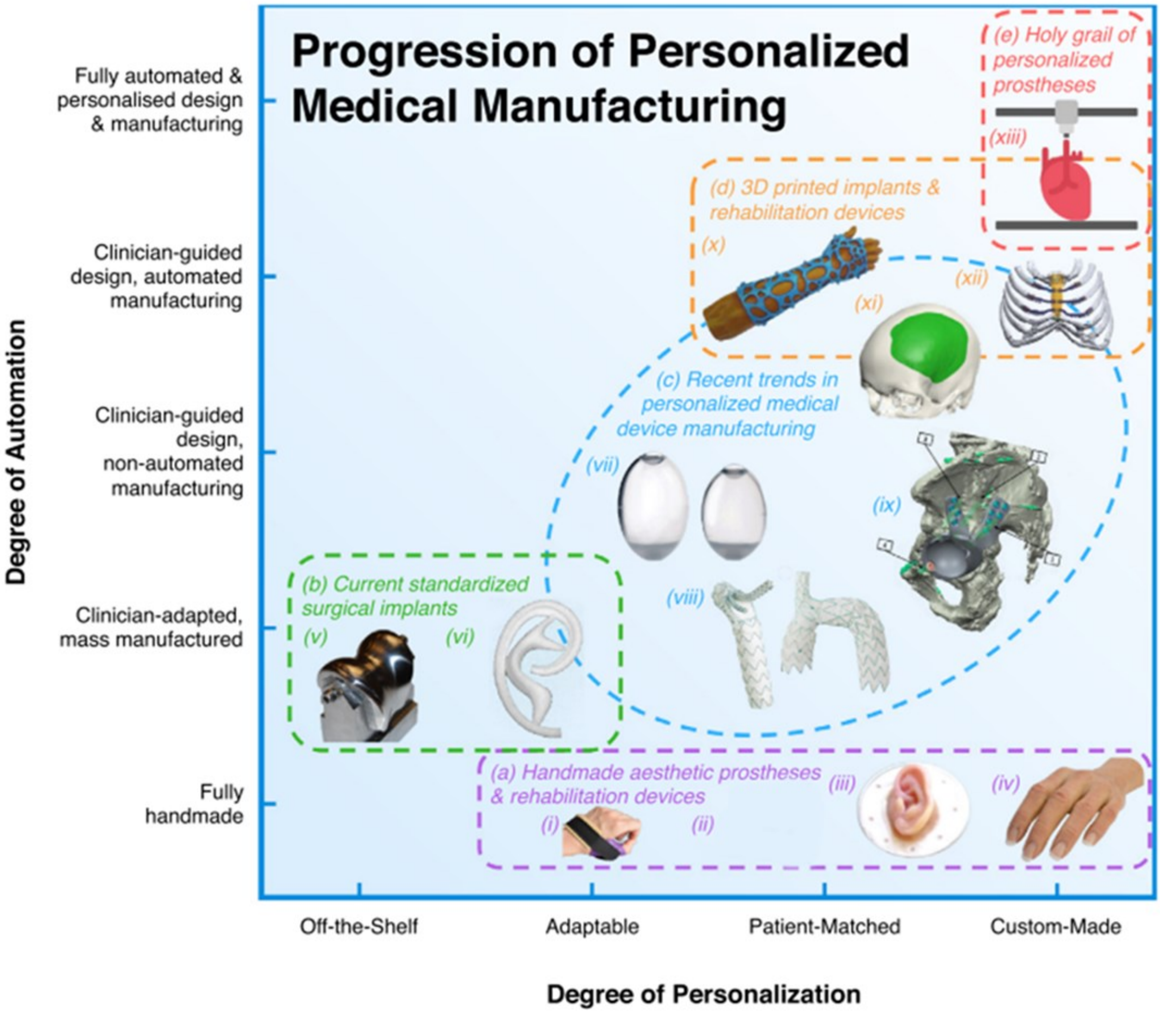

Figure 13: Medical product personalisation and automation matrix © (Paxton et al., 2022)

2.2. Patient-Matched Implant Size Prediction

Hernandez-Vaquero et al. (2013) summarised results from ten studies focusing on determining the accuracy of manual, X-ray based knee replacement implant size prediction. The authors reported mean pre-operative selection accuracies of 59.2% for femur components and 60.7% for tibia plates (when compared to the implanted size). With ±1 size permitted, mean scores of 97.4% and 96.4% were recorded respectively.

To improve the accuracy of conventional manual methods and to minimise the potential of complications post-surgery, authors have explored using computational approaches. Zheng et al. (2018) developed an X-ray based tool for pre-operative knee prosthesis planning named '3X'. The technology's workflow featured a knee joint immobilisation device and a calibration cage to help keep anatomical alignment consistent between patients and minimise X-ray magnification effects. Users of the tool then manually guided the identification of anatomical landmarks in captured biplanar X-ray images for bone contours to be extracted via a 'live-wire algorithm'. These were then used to guide SSM models to reconstruct 3D model predictions of subjects' anatomies (illustrated in Figure 14). The models were subsequently used by the algorithm to virtually fit potential implant sizes and form component size predictions for individuals.

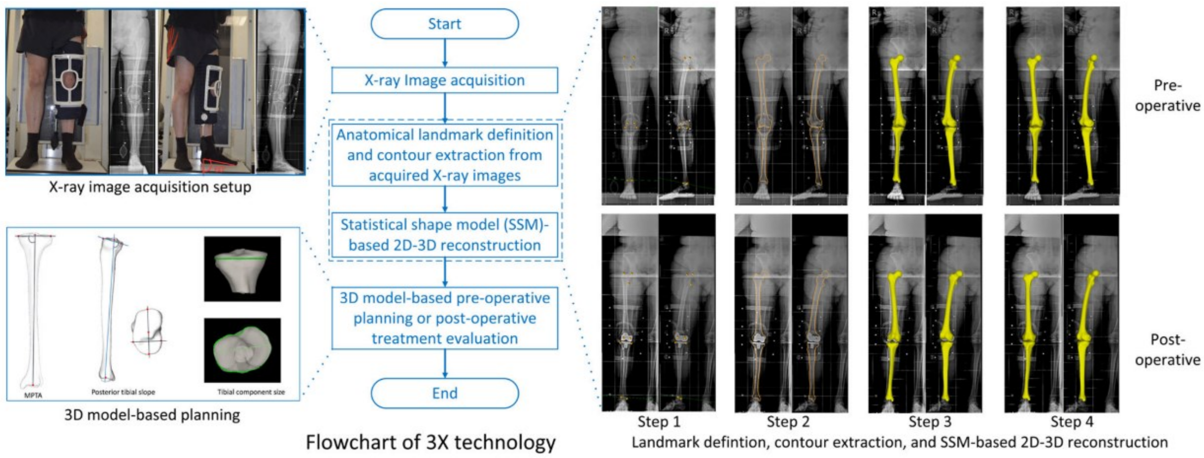

Figure 14: Schematic of the steps involved with the 3X technology to create 3D model reconstructions for implant size prediction © (Zheng et al., 2018)

The authors reported size prediction accuracies for the 3X technology of 78% (96% ± one size) for femur components and 70% (100% ± one size) for tibia plates, based on a study featuring 23 subjects and using sizes selected using 3D CT data as a ground truth comparison. The authors did not detail which specific implant model was used for the analysis, nor did they highlight how many sizing options were available for the femur or tibia plate components.

Massé & Ghate (2021) more recently developed a similar tool named 'X-Atlas'. The software was primarily aimed at creating patient-matched cutting guides from X-ray images, but also featured the additional ability to predict implant size. Like 3X, the X-Atlas workflow involved manually identifying key anatomical features to extract 2D bone contours which could then be used to drive SSM models and generate 3D reconstructions for size prediction. In the study, X-Atlas was tested using 45 subjects with the Zimmer Biomet 'Persona' knee implant. The number of available sizes was not reported in the paper, however, specifications for the product suggest there were 12 femur component and 9 tibia plate sizes available (Zimmer Biomet, 2023). Size prediction accuracies of 53.3% (95.6% ± one size) for femur components and 57.8% (100% ± one size) for tibia plates were reported using the sizes chosen and implanted by surgeons during the study as a ground truth comparison.

Both the processes detailed by Zheng et al. (2018) and Massé & Ghate (2021) featured 'semi-automatic' 2D-3D reconstruction workflows that needed users to perform manual tasks such as identifying anatomical landmarks. This would require users to be appropriately trained and mean the performance of the tools could be impacted by human error. Several other studies were identified that used SSMs to reconstruct 3D models of femur and tibia bones from X-ray images, including those by Laporte et al. (2003), Tang & Ellis (2005), Barratt et al. (2008), Zhu & Li (2011) and Tsai et al. (2015). All these works adopted similar processes where 2D contours, extracted from X-rays via edge detection techniques, were projected onto 2D outlines of SSM base shapes during fitting to drive the SSM morphing, as illustrated in Figure 15. Consistent 3D model reconstruction accuracies of approximately 1 mm Root Mean Squared Error (RMSE) were reported for both bones. Cerveri et al. (2017) further reported that accuracy could be improved to ~ 0.75 mm RMSE when three or more (synthetic) X-ray images were used to increase the level of anatomical detail captured. Only one study (Baka et al., 2014) was identified that detailed an approach that attempted to create 3D reconstructions automatically.

Yet, despite this claim, the authors only detailed how the bone contour extraction process could be automated; how automation was achieved for SSM fitting to then create 3D model reconstructions was not explored. Moreover, the proposed automated edge detection process failed for one out of just six test subjects due to 'too many spurious edges'.

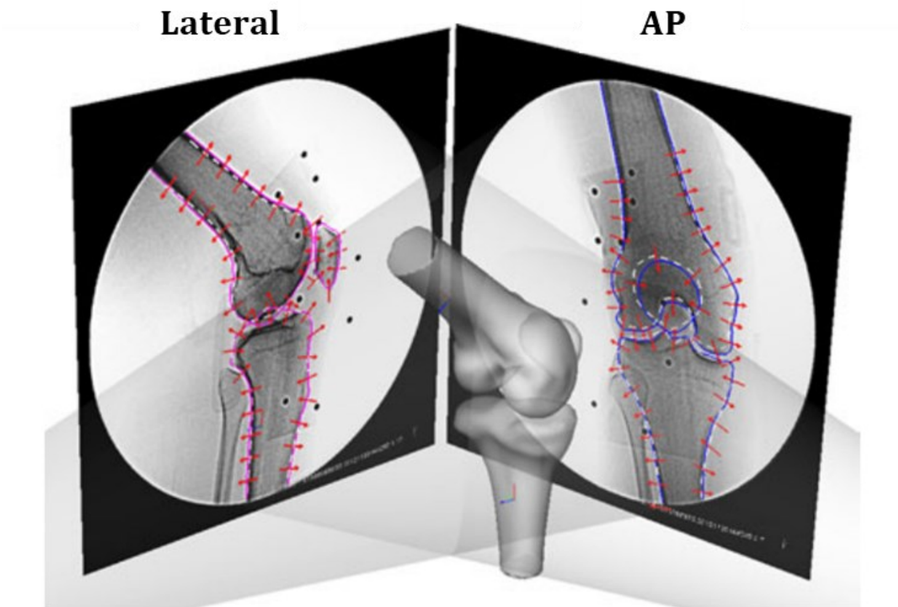

Figure 15: Knee SSM being fitted to contours from biplanar X-rays © (Tsai et al., 2015)

The only implant size prediction tool found that claimed to be fully automatic was the commercial computerised templating system, 'Traumacad', which has an 'Auto-Knee' function. Like the other examples highlighted, the programme detects anatomic regions in X-ray images and then positions resection lines to determine position and sizing on both AP and lateral images. How the programme completes this automatically was however not found to be thoroughly explained in the literature. Seaver et al. (2020) completed a study where 125 consecutive patients underwent primary TKA and compared the accuracy of using Traumacad for selecting the best femur and tibia plate components for individuals against a standard manual templating method. The authors highlighted low accuracies for the automated tool, reporting femur component accuracies of 19.2% (51.2% ± one size) and tibia plate accuracies of 26.4% (71.2% ± one size). Moreover, inaccuracies of up to ± 5 sizes were recorded for both implant types. By means of comparison, manual accuracies of 56% (97.6% ± one size) were reported for femur components, along with 61.6% (95.2% ± one size) for tibia plates in the study. Due to the significantly inferior size selection accuracies reported with the tool, the authors concluded by cautioning surgeons from exclusively using the automatic algorithm.

2.3. Implant Shape Customisation

A limited number of articles were identified that evaluated the performance of commercially available custom shape TKR implants. Ogura et al. (2019) completed a study featuring 55 patients fitted with ConforMIS 'bicompartmental' custom implants and concluded OUH ≥ 3 mm was not present in any case. Likewise, Arnholdt et al. (2020) reported no instances of OUH ≥ 3 mm in a study featuring 91 patients fitted with ConforMIS 'iTotal CR G2' implants. In contrast, OTS sized implant components have been shown to afford significantly poorer outcomes. Mahoney & Kinsey (2010) reported that overhang of ≥ 3 mm was present in 40% of 176 male and 68% of 261 female knees studied after surgery when OTS components were used. Similarly, Wernecke et al. (2012) reported 49% of 101 subjects would see 'posterolateral overhang enough to cause popliteal tendon impingement' in a study evaluating six different tibia plate designs superimposed on MRI images. Schroeder & Martin (2019) completed an intraoperative study comparing OTS and customised implants directly on the same 44 patients. The authors reported that cases of tibia plate overhang of ≥ 3 mm would be reduced from 18% for OTS implant designs to zero by using customised ConforMIS 'iTotal CR' implants, whilst underhang would be reduced from 37 to 18%.

Thorough detail of the workflows for commercially available custom TKR implant solutions, such as the market leader ConforMIS, was not possible to obtain. Nevertheless, Seekingalpha.com (2019) highlighted that, despite the marketing claims, such solutions are not yet fully automated. Consequentially, the authors of the article argued that manual CAD work is often outsourced to foreign countries to save costs from lower labour rates, thus incurring an increased risk in terms of quality, future costs, and lead times. In the literature, several 'semi-automatic' methods to customise the shape and fit of knee replacement implants have been proposed. Jun (2011) outlined a process using CT imaging to enable reconstructions of patients' knee anatomies to be generated and for important morphological parameters to guide the design process to be extracted (Figure 16). Tools such as finite element modelling and virtual surgery were then employed to optimise the design for individuals before manufacturing implant components using computer numerical controlled milling. In the paper, the authors argued that parameter extraction was not automated because it 'often lacks accuracy and stability for feature identification'.

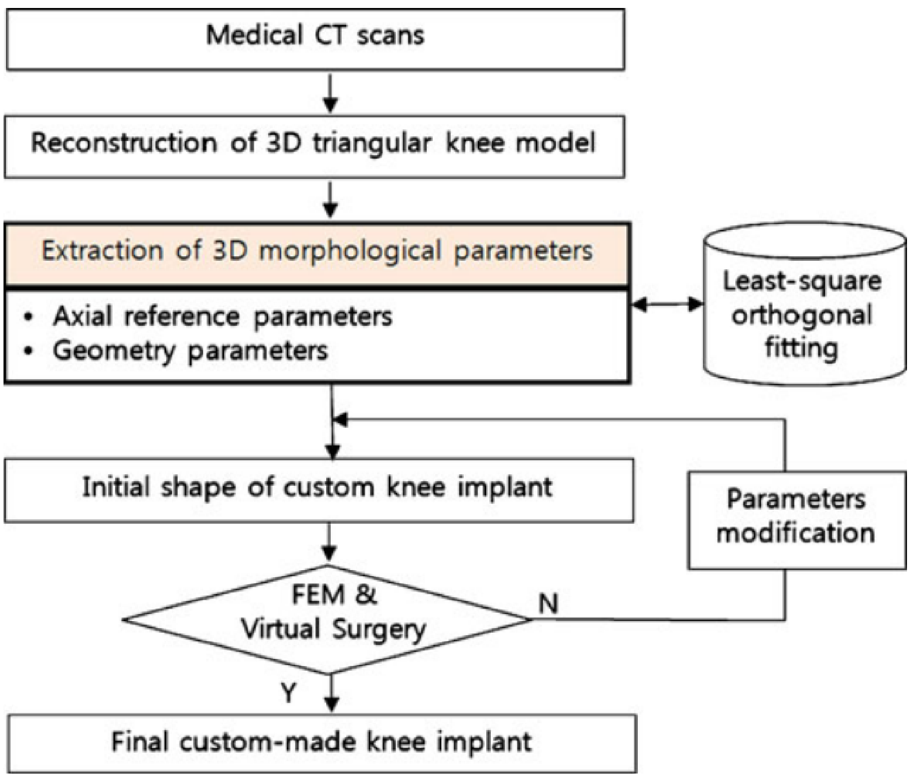

Figure 16: Workflow of custom-made implant design process proposed by © (Jun, 2011)

Li et al. (2017) and Balwan & Shinde (2020) also proposed similar CT based approaches. The former incorporated patient gait measurements and musculoskeletal modelling into the design process, described how patient-specific instrumentation could be produced using the reconstructed 3D models, and highlighted that AM could be used to fabricate the bespoke geometries. The latter detailed how '3D Slicer' – an open source software for visualisation, segmentation, registration and measurement of medical images (Fedorov et al., 2012), used in tandem with 'democratiz3D' – a suit of image processing tools available at www.embodi3d.com, could be used to help improve the efficiency of converting .dcm or 'DICOM' (Digital Imaging and Communications in Medicine – a standard for the communication and management of medical imaging information, developed to make image data standardised and easy to share between equipment from different manufacturers (Mustra et al., 2008)) CT files into 3D bone models for use in developing customised components. As with (Jun, 2011) however, both these solutions also required significant input from users to process scans and guide the 3D model reconstruction and implant design process.

Siemens published a white paper on a conceptual 'Image-to-implant solution for personalised medical devices' which claimed to be able to automate the entire 'engineer-to-order' process for planning, designing, and manufacture of patient-specific medical devices (Siemens, 2014). The paper suggested that by utilising the methodology, the TKR surgical procedure, implants, and/or instruments could be customised from inputted CT or MRI scans. Despite this, the workflow was found to rely heavily on input from clinicians via a 'web-based collaboration' interface for surgical planning and to generate implant designs. Furthermore, the white paper did not explicitly detail how 3D scans could be segmented automatically to produce the required 3D bone models, nor was any information possible to find on the concept's performance or where/how it had been implemented.

In terms of X-ray based workflows, the only article identified was by Chui et al. (2021) who demonstrated that SSMs could be used in parallel with X-ray images to reconstruct the femoral anatomy of ten test subjects, reporting a mean RMSE accuracy of (1.10 ± 0.18) mm. The authors used a single epicondyle width measurement taken manually from inputted AP X-ray images to morph an average femur shape model and create 3D reconstructions. Like the other studies referenced, these models were then used to develop customised femur component designs (created via manual CAD work), which were then prototyped via AM.

In other areas besides knee replacement, authors have demonstrated how advancements in computer vision techniques have shown promise for the progression towards automating traditionally laborious tasks involved with developing custom implants (Paxton et al., 2022). Examples include automating the segmentation of CT scans to expedite the generation of 3D models for structures such as the skull (Minnema et al., 2018) and the vertebrae (Lessmann et al., 2019). By utilising such technologies, the fully automatic design of customised products, including ocular prostheses and cranial implants, has been shown to be possible in a limited number of applications (Ye et al., 2018) (Venugopal et al., 2021).

2.4. Implant Stiffness Customisation

As mentioned earlier, commonly used knee replacement implant components are made of solid metal with stiffnesses significantly greater than the trabecular (spongy/porous) bone present in the distal femur and proximal tibia. The stiffness of bone correlates closely with density (Munford et al., 2020), which can vary substantially from person to person depending on factors including age, sex, weight and conditions like osteoporosis (Burger et al., 1994) (Khodadadyan-Klostermann et al., 2004) (Hamilton et al., 2013). Hence, the natural distribution of stresses and strains in the joint are inevitably disrupted which can hinder bone recovery and lead to extended resorption and increased probability of early revisions (Huiskes et al., 1992) (Deen et al., 2018). Nevertheless, positive bone remodelling and apposition can be stimulated by introducing localised strain gradients into implant components (Kumar & Narayan, 1984) (Elliott et al., 2016). Therefore, if implants are designed with stiffness matched structures that form a mechanical environment close to patients' native bones, it has been argued that it may be possible to further promote these effects (Elliott et al., 2016).

By using metal based AM techniques, porous (Figure 17A) and compliant (Figure 17B) lattice structures can be fabricated. Munford et al. (2022) demonstrated that, by integrating such structures into tibia plates, the load in the proximal tibia could be better distributed and the mechanical environment of the native bone restored. In contrast, for conventional solid implants, the authors reported > 70% of the resected bone area was found to be underloaded compared to native loading.

Figure 17: A) Porous acetabular hip replacement component © (Levine et al., 2006), B) Compliant stochastic lattice structure © (Kechagias et al., 2022)

Various companies such as 'nTopology' and 'Synopsys' offer generative design software tools that allow engineers to develop complex lattice structures with a broad variety of both repeating and stochastic (random) structures. These tools can be used to create and modify certain areas of lattice structures to reflect variations in inputs such as pressure values in the context of insoles, or to add strength to regions of medical implants that are known to experience higher loads (Veloso et al., 2022). Unlike shape customisation however, no commercially available solutions were identified that utilise such tools to enable implant stiffness customisation from medical images. A limited number of academic studies were found to outline conceptual methodologies, including Ghouse et al. (2019) who used micro-CT to characterise the stiffness of trabecular bone in the medial femoral condyle of an ovine model. The process, outlined in Figure 18, involved initially calibrating density in the CT scans via phantoms included in the images, mapping its distribution across the bone, converting to stiffness moduli via the use of a relationship built on experimental data, and adjusting the design of lattice structures to match. Porous titanium scaffolds with varying stiffnesses to replicate the variation observed were then fabricated via AM and implanted into the medial femoral condyles of six ewes. Promising levels of bone ingrowth compared to solid structures were reported across the test subjects.

Munford et al. (2020) outlined a similar method for characterising the stiffness of the proximal human tibia bone. The authors highlighted that stiffness moduli varied significantly between the ML, AP and IS (inferior – superior) axes. Principally, it was noted a significant difference in moduli was found between the medial and lateral condyles, as well as with subchondral depth (stiffness decreased rapidly distally from the condylar region). The authors proposed various power-law relationships for predicting stiffness moduli from density at different depths in the bone and for different axes. They then demonstrated an improved stiffness approximation could be obtained by using region and direction specific relationships compared to a global model. In subsequent work, Munford et al. (2022) applied the power-law relationships to calibrate stiffness variation in the tibia from CT scans and used this to develop implants with various types of stiffness matched lattice structures. These included lattices with uniform stiffnesses tailored to the mean axial modulus calculated in subjects' proximal tibia bones, lattices graded to replicate the difference in moduli observed between subjects' native condyles, as well as lattices graded with subchondral depth.

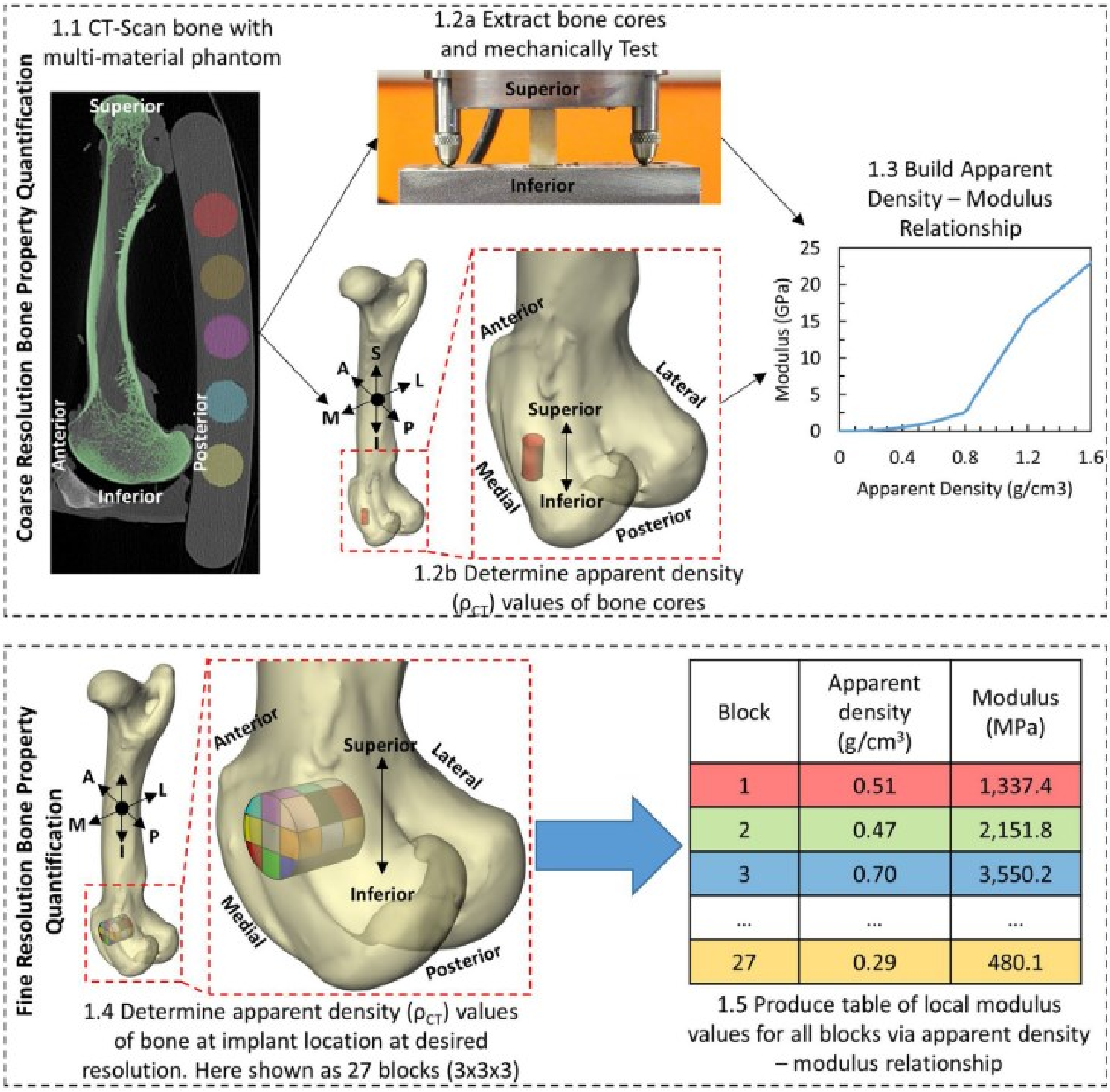

Figure 18: Process for predicting the 3D stiffness distribution of bone in an ovine model from calibrated CT images © (Ghouse et al., 2019)

Kechagias et al. (2022) provided a detailed process for how the design of stochastic lattice structures can be developed to match varying stiffness moduli. Their method, illustrated in Figure 19B, demonstrated that stiffness can be adjusted by varying three design parameters, namely 1) the connectivity of the lattice (the number of struts connected at each node), 2) the density of struts in the structure, and 3) the strut thickness. The design process for achieving the stochastic lattice designs by randomly distributing points in a volume, assigning zero thickness struts that comply with specified connectivity and density settings, and then assigning appropriate thicknesses, is also outlined in Figure 19A.

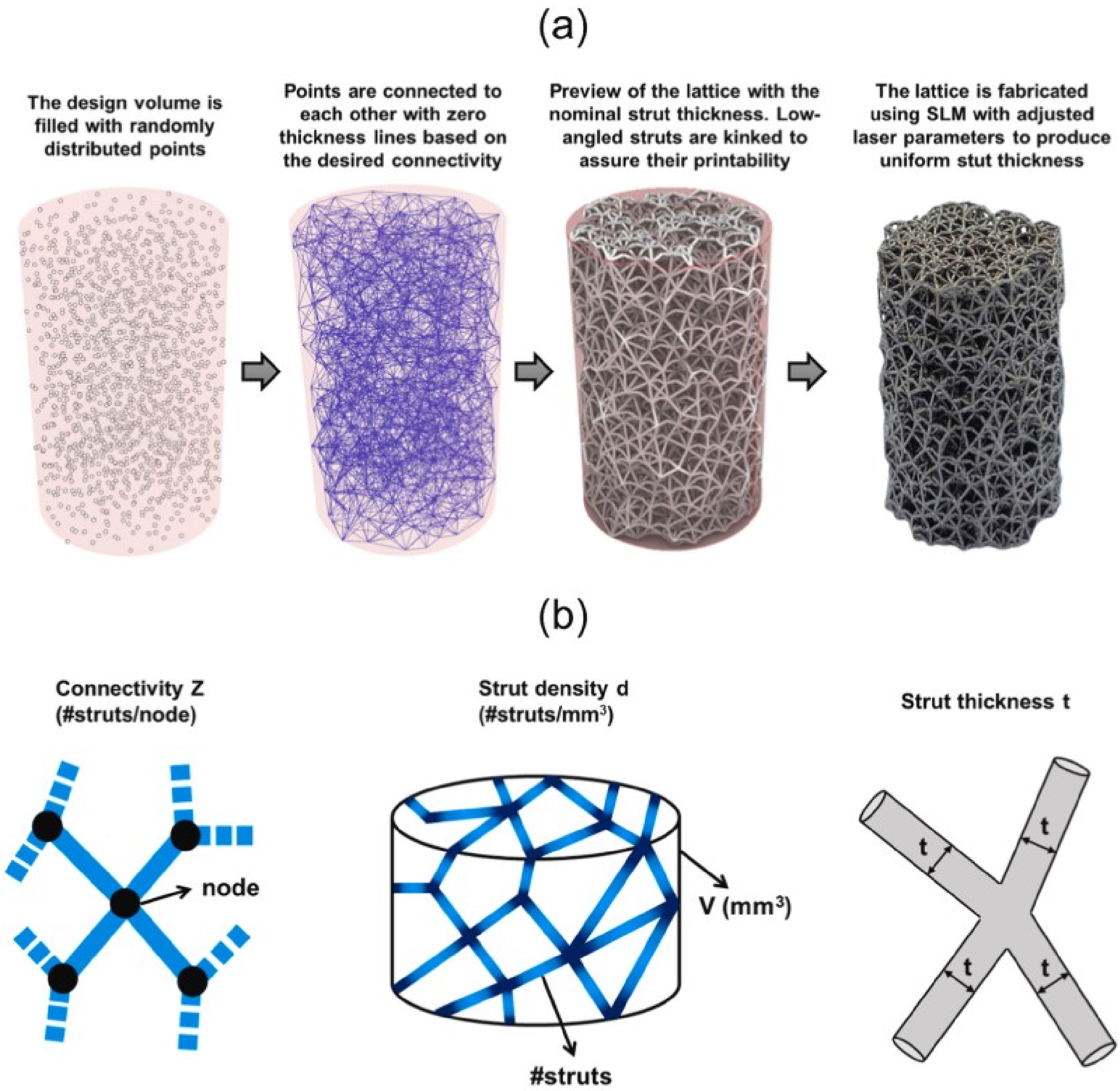

Figure 19: A) Design and manufacturing workflow of stochastic lattice structures, B) Lattice structure design parameters to influence stiffness © (Kechagias et al., 2022)

In the approaches detailed, to process and map bone density in CT scans, convert to stiffness values, and then use the information gathered to develop stiffness matched lattice structures, substantial input from users would be required. To help address this, Yu et al. (2019) proposed a process for automatically optimising the design and mechanical properties of personalised artificial spinal discs for individuals from CT data. An iterative finite element based optimisation approach was employed to calculate optimised material distribution which could then be fabricated using 'multi-material' AM to achieve 'physiological stiffness' under different loading cases. The authors however did not describe how the CT image segmentation process required to obtain subjects' bone stiffness information could be fully automated.

2.5. Summary

This chapter reviewed the relevant literature on mass-customisation and workflows for enabling various levels of medical implant customisation. A recurring theme identified was that a degree of manual input was almost always required to facilitate the processes. Therefore, user training would likely be necessary, human error could easily be introduced, and the solutions would probably have higher upfront costs and longer lead times compared to standard OTS alternatives (Ortho Baltic Implants, 2020). Consequentially, such solutions are not believed to be true examples of mass-customisation and will likely not become attractive options for widespread adoption until this key limitation is addressed (Namin et al., 2019).

To summarise the various knee replacement customisation tools identified (both commercial and research studies), Figure 20 is provided. The schematic is based on Figure 13 (Paxton et al., 2022) and shows the level of knee replacement customisation for each identified product/study on the X axis, with its corresponding automation level on the Y. Whether the tools are compatible with 2D X-ray images, 3D CT or MRI images, or both is also detailed. The figure highlights that the only 'fully automated' knee replacement customisation tool identified was the Traumacad Auto-Knee software used for predicting appropriate implant size. Contrary to this, in other areas of medical implants such as cranial implants (Venugopal et al., 2021), it was identified that authors have started to use recent advancements in AI/ML techniques to enable full automation of customisation processes.

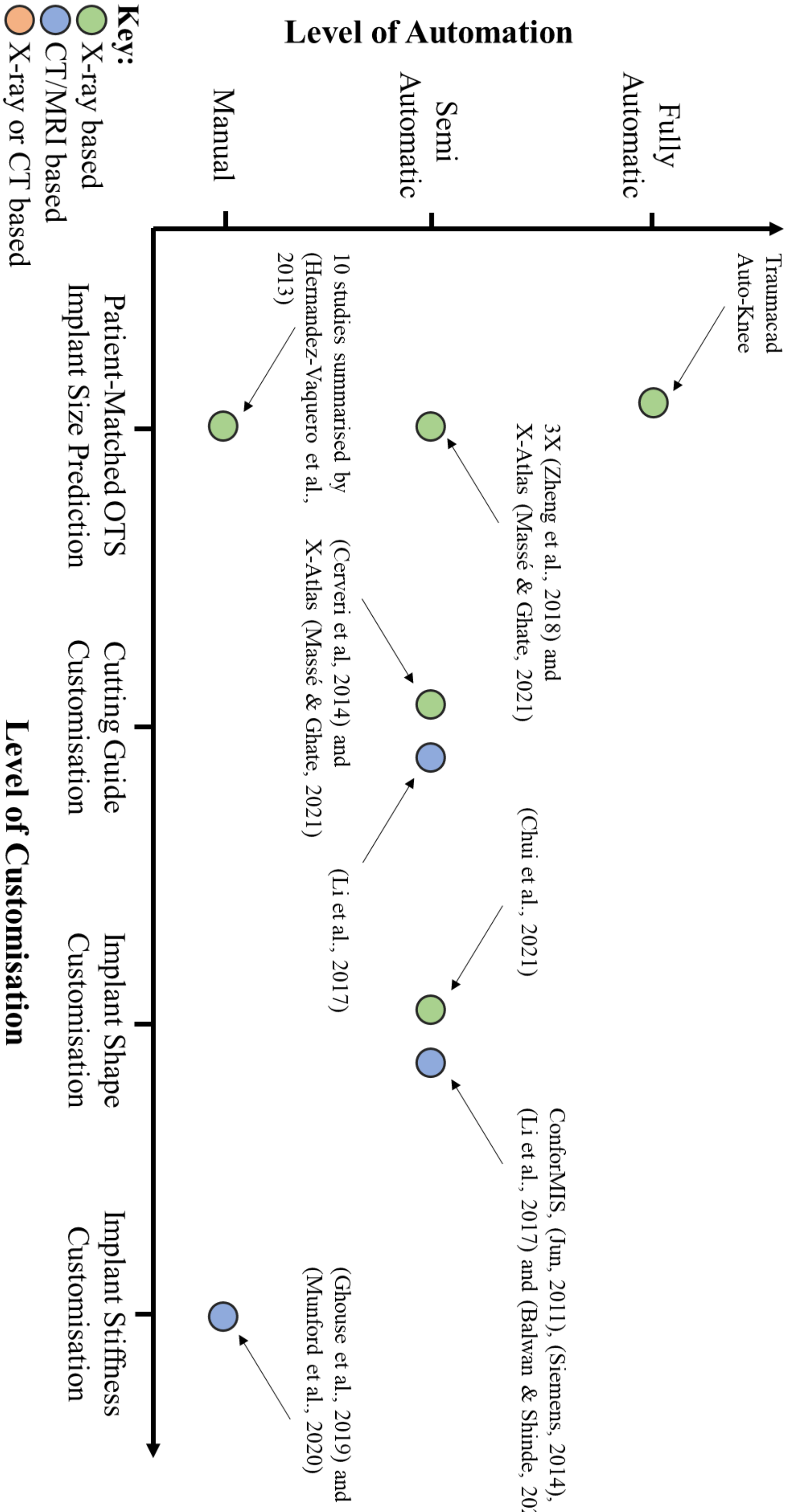

Figure 20: Commercial knee replace customisation products and research articles

Chapter 3

Materials and Methods

The following chapter outlines the common datasets, algorithms, methods, and performance metrics used to construct and evaluate the various knee replacement implant customisation pipelines developed.

Most of the contents of this chapter have been published in the following papers:

- Burge, T.A., Jeffers, J.R.T. & Myant, C.W. (2022) Development of an automated mass-customization pipeline for knee replacement surgery using biplanar x-rays. *Journal of Mechanical Design*. 144 (2), 1–11.
- Burge, T.A., Jeffers, J.R.T. & Myant, C.W. (2023) A computational design of experiments based method for evaluation of off-the-shelf total knee replacement implants. *Computer Methods in Biomechanics and Biomedical Engineering*. 26 (6), 629-638.

- Burge, T.A., Jeffers, J.R.T. & Myant, C.W. (2022) Performance and sensitivity analysis of an automated x-ray based total knee replacement mass-customization pipeline. *Journal of Medical Devices*. 16 (4), 1–12.
- Burge, T.A., Jones, G.G., Jordan, C.M., Jeffers, J.R.T. & Myant, C.W. (2022) A computational tool for automatic selection of total knee replacement implant size using X-ray images. *Frontiers in Bioengineering and Biotechnology*. 10, 1–11.
- Burge, T.A., Jeffers, J.R.T. & Myant, C.W. (2023) Applying machine learning methods to enable automatic customisation of knee replacement implants from CT data. *Scientific Reports*. 13, 1–9.
- Burge, T.A., Munford M.J., Kechagias S., Jeffers, J.R.T. & Myant, C.W. (2023) Automating the customization of stiffness-matched knee implants using machine learning techniques. *The International Journal of Advanced Manufacturing Technology.*

3.1. Introduction

In Chapter 2 it was observed that workflows or 'pipelines' for customising medical implants generally have similar stages. These involve 1) processing inputted images (usually X-ray or CT), 2) extracting the necessary geometrical and/or mechanical property data, 3) reconstructing patient specific 3D bone models, 4) using the extracted data and models produced to create customised components designs or virtually fit various OTS standard sizes, and 5) manufacture the implant designs or select the best size. Figure 12 previously provided a top-level overview of how this general framework was adapted in this thesis to enable various forms of knee replacement customisation to be fully automated. This chapter provides further detail on the materials and methodologies that were used to enable the automation of these pipelines. The individual pipelines are more thoroughly developed and evaluated through Chapters 5 – 9.

3.2. Datasets

Data was retrieved from multiple sources for use in the development and testing of the various pipelines outlined in this research. No original human tissue data was collected, instead secondary data collected from previous studies and controlled databases was utilised after ensuring appropriate ethics approval and informed consent were obtained. Where relevant this is further detailed in the following sub-sections.

3.2.1. Korea Institute of Science and Technology Information

Data from 98 cadaver subjects was sourced from the Korea Institute of Science and Technology Information (KISTI) 'Digital Korean' dataset (Lee & Lee, 2010). The dataset featured CT scans (in DICOM file format) with a resolution of 0.832 x 0.832 mm, 1 mm axial slice thickness, and an image size of 512 x 512 pixels. 3D models in the form of .stl mesh files (raw, unstructured triangulated surface models containing vertices and normal vectors) were supplied with the scans for subjects' left and right femur and tibia bones. Figure 21 illustrates a CT DICOM stack (A), a coronal slice through a full body CT scan (B), and a 3D .stl mesh model of the distal femur.

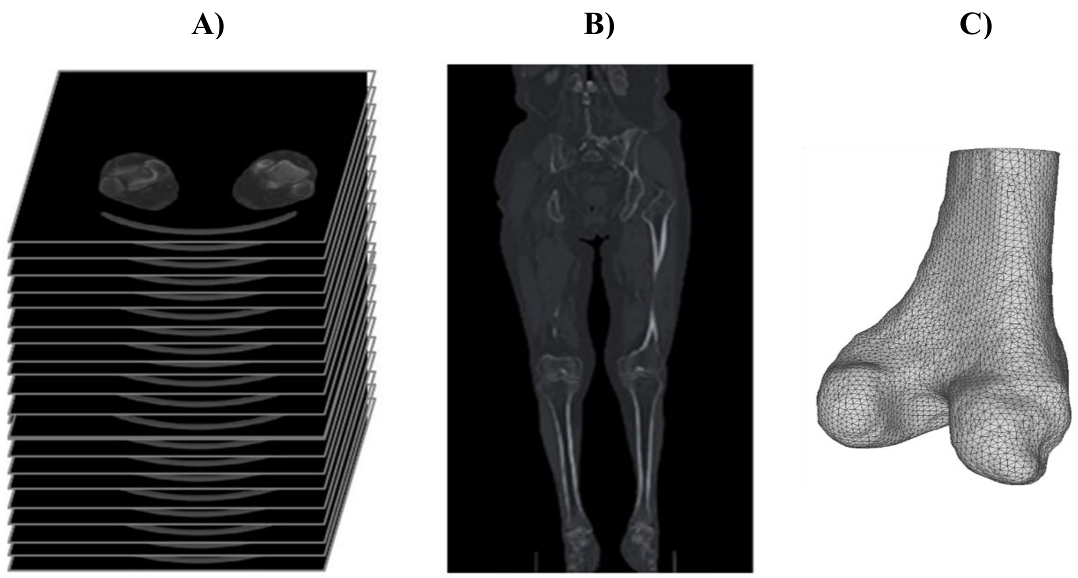

Figure 21: A) CT DICOM stack © (Chen et al., 2022), B) Coronal slice through a full body CT scan © (Chen et al., 2022), C) 3D .stl mesh model of the distal femur

The KISTI subjects comprised of Asian Koreans with roughly an even number of males and females. Age and height information was provided with subjects ranging from 21 – 60 years old and 146 – 176 cm in height. No information was supplied regarding subjects' health conditions, nor the level of joint damage/arthritis present.

Ethical approval and subject consent were obtained by KISTI who also ensured the data was appropriately anonymised before distribution. As the KISTI dataset was shared with Imperial College via a material transfer agreement, and thus is not 'publicly available', in line with Imperial College's relevant guidelines and regulations, the study protocols and associated ethics were reviewed and approved by the Research Governance and Integrity Team at Imperial College. Reference number 6423670.

3.2.2. Osteoarthritis Initiative

High resolution (0.365 x 0.365 mm) MRI scans of knee joints, with a sagittal slice thickness of 0.7 mm, an image size of 512 x 512 pixels, as well as AP and lateral X-ray images (like those shown in Figure 4), were retrieved from the Osteoarthritis Initiative (OAI) dataset (Nevitt et al., 2006). The dataset contained 4,796 subjects (alive at the time of the study), with image data captured at multiple time points over eight years. Both AP and lateral X-ray images with accompanying MRI data were only available for 122 of the total subjects.

The OAI subjects included both male and female Americans categorised into ethnicities of ‘White’, ‘Black’, or ‘Asian’. No further ethnicity detail, such as sub-ethnicity group or country of birth, was provided. Subjects ranged from 45 – 79 years old when first enrolled. Height information was not provided. All subjects in the dataset had some degree of osteoarthritis. Kellgren and Lawrence (K&L) grades for classifying the severity of arthritic joint damage (Kellgren & Lawrence, 1956) were supplied for all subjects.

The OAI database is publicly available for academic purposes and the data can be downloaded from https://nda.nih.gov/oai/. In line with Imperial College’s policy, further ethical approval was therefore not required to use this data.

3.2.3. Charing Cross Hospital

Four ‘fresh frozen’ lower limb CT scans, taken by Charing Cross Hospital, London, were retrieved from the Imperial College Healthcare Tissue Bank (ICHTB). The ICHTB is supported by the National Institute for Health Research Biomedical Research Centre, based at Imperial College Healthcare NHS Trust and Imperial College London. The four CT scans had a resolution of 0.738 x 0.738 mm, axial slice thickness of 0.6 mm, an image size of 512 x 512 pixels, and were taken with a voltage of 140 kVp. The scans each contained five-material calibration density phantoms (Model 3; Mindways Software Inc.), as shown in Figure 22. The subjects consisted of solely male subjects of ages 66 – 72. No additional demographic information (height, age, health conditions) was provided.

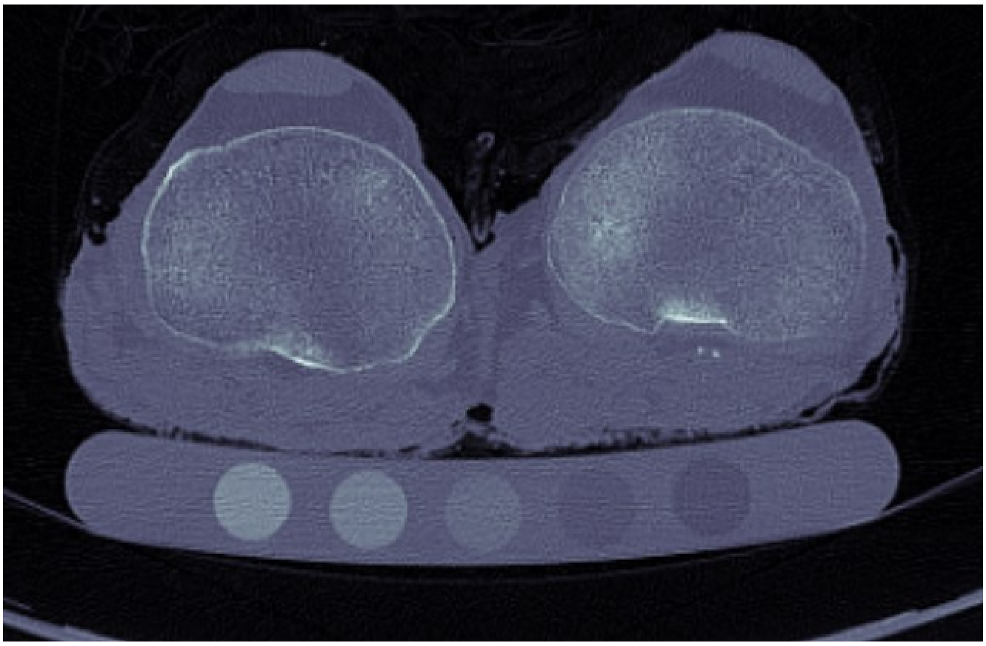

Figure 22: CT slice containing five-material density phantom

ICHTB is approved by Wales REC3 to release human material for research (17/WA/0161). Ethical permission to use the 'fresh frozen' lower limb CT scans was granted by ICHTB Review Committee under a UK Human Tissue Authority License 12 275.

3.3. Segmentation of 3D Image Files

To create 3D bone models from the MRI data provided from the OAI dataset, the 'Double Echo Steady State' imaging method with water excitation (no fat saturation) was selected to enable quantitation of cartilage volume and provide clear contrast to bone over the entire knee (Nevitt et al., 2006). Segmentation was completed using the software 3D Slicer as follows.

Manual segmentation of the bone volume was performed whilst visualising the ROI in the sagittal, coronal, axial, and 3D model views simultaneously (Figure 23). Multiple 'semi-automatic' tools available in 3D Slicer, such as 'thresholding' and 'island removal', were utilised. A consistent 'median' smoothing function with a kernel size (the width*height*depth size of the smoothing filter used) of 3 mm. This was equivalent to that used to create the 3D bone models supplied with the KISTI dataset for consistency. Using these tools, and following the MRI segmentation guidance outlined by Ahmed & Mstafa (2022), 3D bone geometries (like shown in the top right of Figure 23) were extracted.

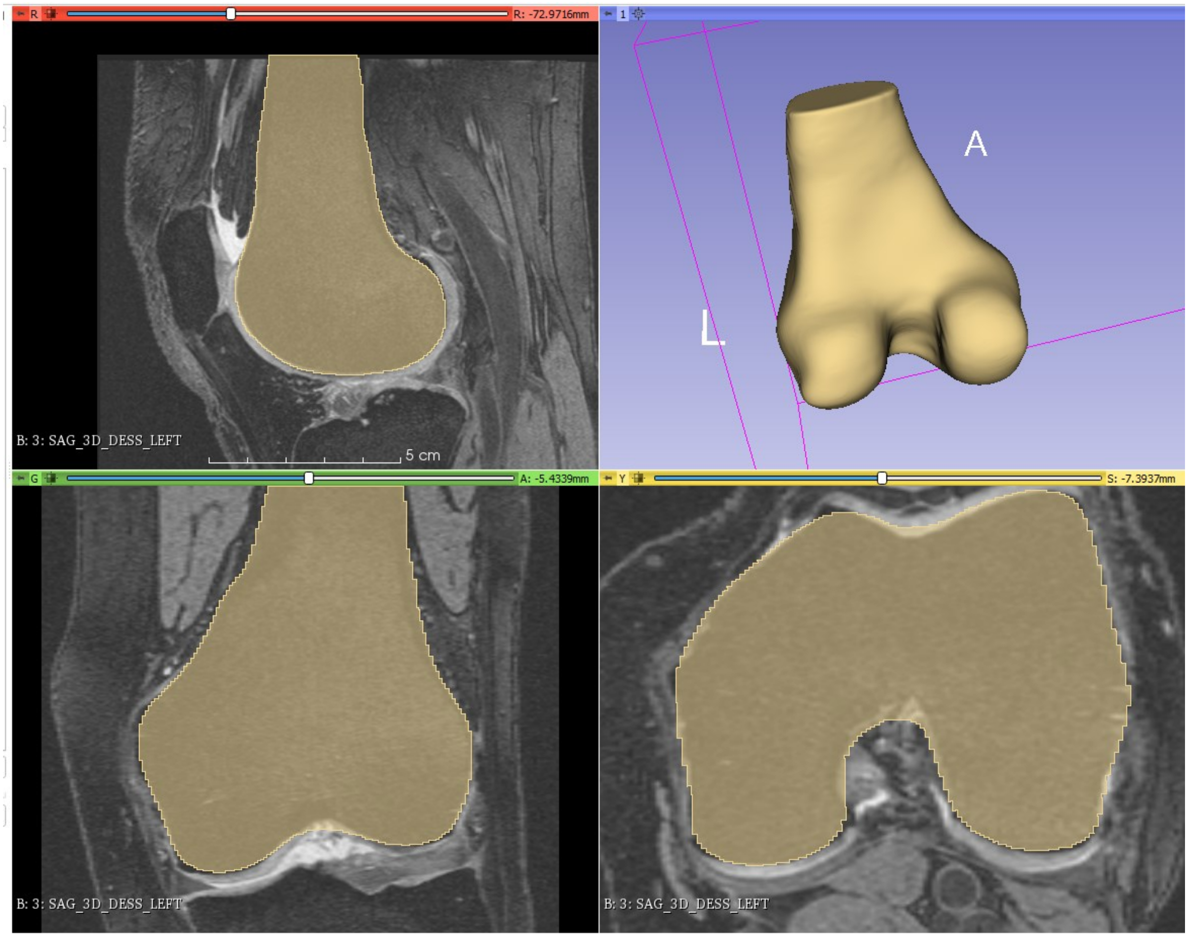

Figure 23: Segmentation of a distal femur bone (yellow shaded area) from an MRI scan in 3D Slicer. Top left – sagittal view, bottom left – coronal view, top right 3D model view, and bottom right – axial view

The .stl models outputted from 3D Slicer were then refined and remeshed using the software 'MeshLab' – an open source mesh processing tool (Cignoni et al., 2008). The refinement process involved using the 'Laplacian Smooth' tool within MeshLab to smooth out any course areas resulting from the segmentation process in 3D Slicer. For each vertex in a mesh model, the Laplacian smoothing algorithm worked by identifying a new position in 3D space based on the position of neighbouring vertexes, effectively averaging out (and smoothing) the surface (Herrmann, 1976). Equation 1 from (Hansen et al., 2005) describes the Laplacian smoothing operation used where $\bar{x}_i$ was the Cartesian (X, Y, Z) position of vertex *i*, $\bar{x}_j$ the position of the *j^th^* adjacent vertex, and *N* the number of adjacent vertices to *i*.

Equation 1: Laplacian smoothing operation

$$\bar{x}_i = \frac{1}{N}\sum_{j=1}^{N} \bar{x}_j$$

In MeshLab, Laplacian smoothing was implemented with *N* being limited to just the immediate (connected) neighbours of each vertex in the mesh (Sorkine, 2005). ‘Smoothing Steps’ related to how many times the smoothing operation was applied. ‘Isotropic Explicit Remeshing’ with a ‘Target Element Length’ of 0.5 mm was then applied. This involved operating directly on the original mesh surface and applying local ‘area-based’ modifications, instead of working on an ‘indirect’ representation of the surface. The number of vertices was adjusted to a density to achieve the target element length and their distribution was regularised to improve mesh homogeneity (Surazhsky & Gotsman, 2003).

The software ‘Blender’, an open-source 3D computer graphics software toolset used for various applications including 3D modelling, mesh processing and visualisation (Kent, 2014), was utilised to trim each mesh bone model to a consistent height of 100 mm. This limited the models to the condylar regions at the knee joint and discarded excess bone shaft. To allow the process to be completed automatically for multiple mesh models, custom Python scripts were written to run within the Blender interface, one for femur bones and another for tibia bones. For the femur, the script initially transformed the mesh so that its lowest point in the Z axes was set at

0 mm. An XY plane was then created 100 mm above this and the 'mesh.bisect' command was used to trim the mesh above this point. For the tibia, the script transformed the mesh so that the highest point in the Z axes was set at 0 mm before an XY plane was created 100 mm below this point and the shaft trimmed in the same manner. The option 'use_fill' was set to 'True' in both scripts so that trimmed meshes were closed after the bisection command had been used.

It was not possible to perform an analysis to evaluate the accuracy of the segmentation and bone mesh model generation method adopted since access to cadaver bones for physical measurement could not be obtained. Prior research has shown however that segmentation of CT and high resolution MRI files (like those supplied with the OAI dataset) can achieve 3D models with RMSE accuracies of approximately 0.5 mm (Van den Broeck et al., 2014). This provided confidence that models created via a similar approach could serve as suitable ground truth models in this research.

3.4. Machine Learning Models

Numerous image classification, object detection, and segmentation models (further introduced in Chapter 1.3) were utilised within the various customisation pipelines, all of which were built using 'TensorFlow' – a flexible machine learning model development platform (Abadi et al., 2016). The architecture of these CNN models (number of layers and filters, kernel size, convolution operators etc., like shown in Figure 7 and Figure 9) were adjusted for each specific model application and based off examples found in the literature.

When training CNN models, an optimiser was used to systematically adjust the attributes of the neural network (such as weights and biases). 'Adam', a stochastic gradient descent method, was used as it is the most commonly adopted optimiser for training CNN models (Kingma & Ba, 2015). The optimiser uses estimations of the first and second moments of the gradient to adapt the model learning rate (i.e. the step size or the 'pace' at which the values of parameters are adjusted in each training iteration (Murphy, 2012)). The goal of the optimiser in training models was to select the best possible network weights and biases to minimise the calculated 'loss' when the model was applied to a validation dataset. The loss function is a method of determining how well given data is modelled. Perfect predictions across a dataset would return a loss of 0. Whereas, if model predictions deviated too much from the known results, then high values would be returned. Loss functions can be split into 'regression losses' and 'classification losses' with the latter being relevant in the context of image processing (Parmar, 2018).

During model training a batch size of 10, and 100 epochs were specified unless stated otherwise. Model weights were saved after each training iteration with the configuration with the lowest calculated loss when tested on specified validation data selected to minimise overfitting and achieve optimal performance. Approximately 10% of training data was reserved for validation for all models. Trained models were then tested on new, independent data after being incorporated into the full pipelines.

3.4.1. Image Classification Models

To train classifier models, images were manually labelled as the relevant classes and sorted into 'train' and 'validation' folders before being imported into TensorFlow. Once models were trained, they could then be applied within the customisation pipelines to previously unseen images to predict which of the set classes the images belonged to, as illustrated in Figure 24.

3.4.2. Object Detection Models

To build object detection models, training and validation images needed to be manually labelled with the coordinates of where the corresponding bounding boxes should be placed. This was completed using the software 'ImageJ', an image processing programme developed at the 'National Institutes of Health and the Laboratory for Optical and Computational Instrumentation' (Schneider et al., 2012). To obtain bounding box coordinates for each training image, the files were loaded into the ImageJ software and a rectangle was manually drawn around the area of interest. An image can be seen as an array of square pixels (the smallest addressable element in a raster image) arranged in rows and columns (Basavaprasad & Ravi, 2014). When rectangles were drawn in ImageJ, the point locations of each corner within each image (in terms of the pixel row and column numbers) were identified as a series of XY coordinates. These were then stored within .csv files ('comma-separated values' files are text files that have a specific format which allows data to be saved in a table structured format).

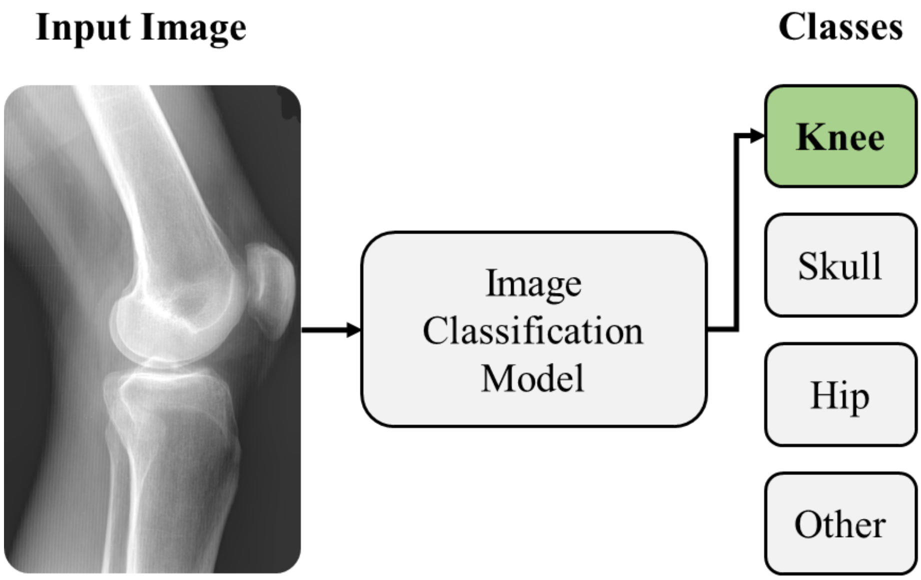

Figure 24: Image classification of an X-ray

To train the object detection models using the labelled data, TensorFlow used the learning capabilities of CNNs to iteratively define the distinct features within the labelled regions of training bounding boxes to be able to predict where boxes should be placed in new images. The application of an object detection model built via this approach is demonstrated in Figure 25 where the model has been trained to identify the region of CT slice images containing cross sections of the left tibia bone.

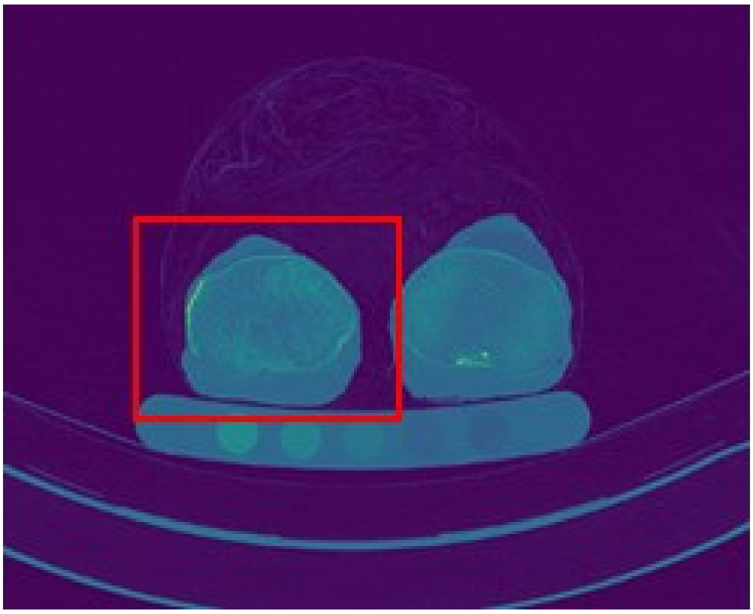

Figure 25: CT slice image containing density phantom with bounding box prediction around the left tibia bone © (Burge et al., 2023c)

3.4.3. Image Segmentation Models

For segmentation models, creating training data involved producing reference images with corresponding mask pairs. The ImageJ software was again used to create the necessary binary masks. To achieve this, training images (Figure 26A) were loaded into the software as 24-bit three channel colour images and manually labelled using ImageJ's 'Paintbrush' tool to mark the relevant areas in white (Figure 26B). The Paintbrush tool worked by adjusting the 'RGB' (Red, Green, Blue) channels of the pixels contained within the area highlighted by the Paintbrush tool to the maximum intensity level (255, 255, 255). The 'minimum' pixel value settings of the images were then adjusted so the bone (now marked in white) contrasted more clearly from the background by linearly mapping pixel intensity values within a range selected manually to values in the range 0 - 255. Lastly, the 'Convert to Mask' ImageJ command was used to create binary mask images (Figure 26C). The command initially converted images to 8-bit single-channel greyscale arrays where each pixel had an intensity value of between 0 – 255 with 0 being black and 255 white. Thresholding was then used where pixels with values <

128 were assigned as 0 and where ≥ 128 as 255. The resulting binary images were then saved as .PNG files (a file format widely used to display high-quality digital images).

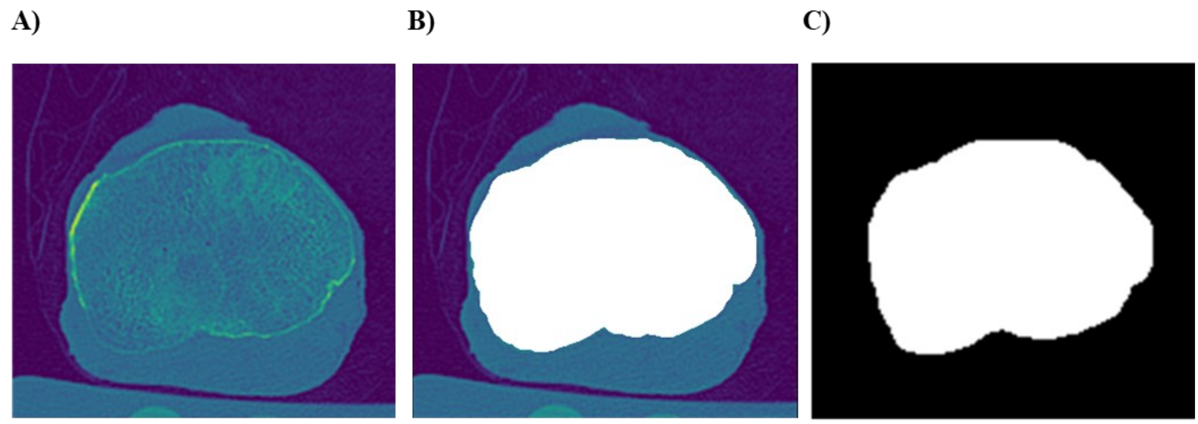

Figure 26: Creating training masks for image segmentation models – A) Training image, B) Labelled bone area in image, C) Resulting binary mask image © (Burge et al., 2023c)

As with bounding box object detection, TensorFlow used the CNN architecture to learn the features present in the regions contained within the corresponding masks to develop models able to make segmentation predictions for new image data. The output of the segmentation predictions was in the form of black and white binary images, like shown in Figure 26C.

3.5. Edge Detection and Contour Extraction

To process medical images and define the edges or 'profiles' of areas of interest (such as bones), edge detection algorithms are commonly employed in image analysis. Common algorithms include 'Canny' edge detection which utilises a thresholding approach to select which pixels within an image should be specified as edges. The approach consists of four key steps: 1) reducing noise in the image, usually via use the 'Gauss smoothing filter', 2) calculate the gradient amplitude and direction (typically 0, 45, 90, or 135 degrees), 3) apply 'non-maximum suppression which eliminates non edge pixels, and lastly 4) select the hysteresis thresholds which retain or exclude pixels to isolate edges (Xu et al., 2017).

Various edge detection methods were evaluated for extracting bone contours directly from medical images including 'Roberts', 'Sobel', 'Prewitt', 'Canny', and 'Laplace' (Shubhangi et al., 2012). However, due to the grainy nature of X-ray and CT images, these methods were often found to result in high levels of noise and required manual post-processing to reliably clean the contours. Cernazanu-Glavan & Holban (2013) demonstrated that to minimise noise and enable bone contours to be extracted from X-rays accurately without manual post-processing, segmentation CNNs (detailed in Section 3.4.3) could be used initially before applying an edge detection algorithm to the outputs. In this research, the combination of Canny edge detection (Canny, 1986), implemented via the Python module 'Open CV' as described in (Xu et al., 2017), with CNN segmentation models was therefore adopted. The effectiveness of this approach is illustrated in Figure 27A&B.

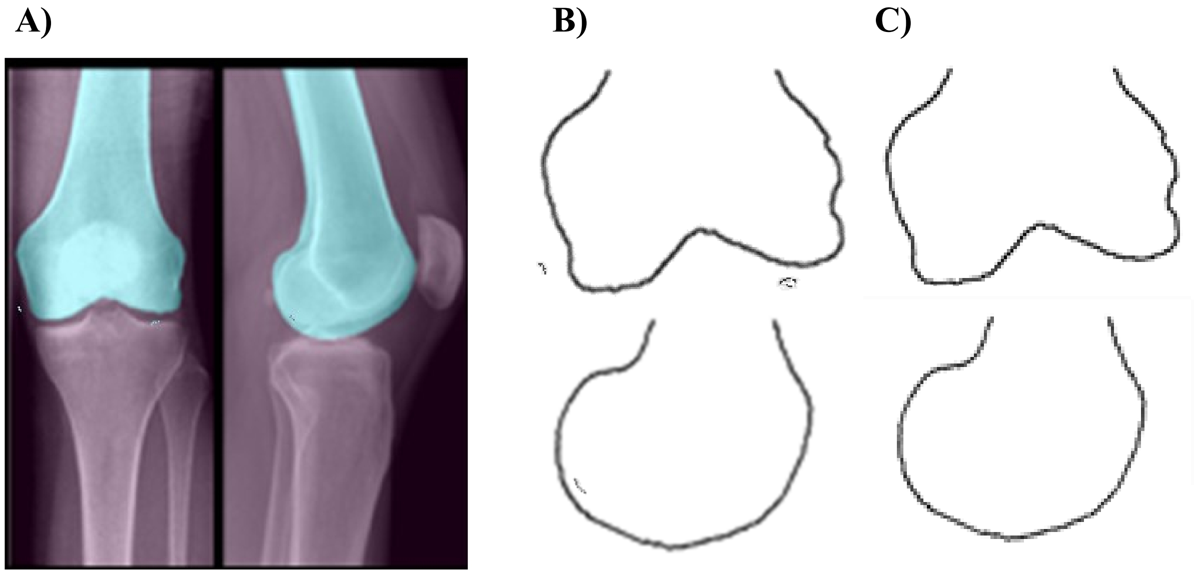

Figure 27: A) Femur bone segmentation from AP and lateral X-rays, B) Canny edge detection applied to segmentation outputs, C) Contours after cleaning algorithm applied

To further minimise noise artefacts, an automated cleaning algorithm was developed and used after the Canny edge detection step. The algorithm worked by disregarding any lines calculated to be below a specified minimum length, thus filtering out residual noise and ensuring just the bone contours remained (Figure 27C). The start/end points for the relevant contours were also identified, and whether a continuous line between the two was created was confirmed.

3.6. Digitally Reconstructed Radiographs

DRRs are typically used to create simulations of conventional 2D X-ray images ('synthetic X-rays') from 3D CT or MRI data (Moore et al., 2011). Authors have outlined multiple methods for creating synthetic X-ray images from CT data (Moore et al., 2011) (Moore et al., 2012) (Cerveri et al., 2017). In this research, 3D bone models were used to produce 2D profiles to mimic those in AP and lateral X-ray projections (as shown in Figure 28). To achieve this, firstly 3D models were positioned in a desired orientation in 3D space. The 3D points contained within models' .stl files (detailing the beginning/end of mesh elements) were then extracted and flattened to 2D. To form AP projections, Y coordinates were removed from each point. Similarly, X coordinates were removed to form lateral projections. Projections could then be outputted as series of 2D points or as binary images.

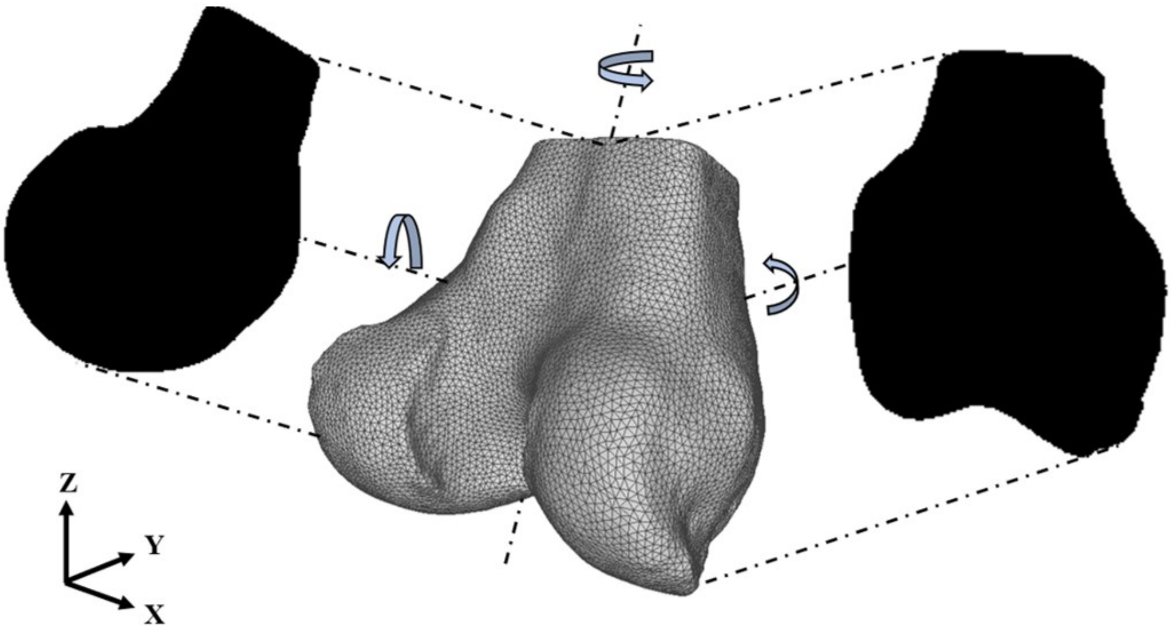

Figure 28: Illustration of DRR process using a femur bone model © (Burge et al., 2022b)

The DRR approach also afforded the ability to precisely control and vary the orientation of inputted 3D models before producing synthetic X-rays. The approach was also not affected by magnification errors (like in real X-rays), so dimensional scaling was not required.

3.7. Iterative Closest Point

Iterative Closest Point (ICP) is a rigid registration method to establish 3D alignment between a set of points on two surfaces. It is the most commonly used matching algorithm in 3D point cloud registration (Wang & Zhao, 2017). During the process, one surface was defined as the 'target' whilst the other was defined as the 'source'. Initially a 'Nearest Neighbours' search (Yianilos, 1993) was completed for each point on target surfaces to identify its nearest point on the source. This step also involved weighting and rejecting points if there were determined to be outliers. Once point to point pairs were defined, the target surface was fixed in space while the source was transformed via translation and rotation operations to fit it as closely as possible.

The fitting process was completed iteratively until a specified RMSE between the surfaces was achieved, or the number of iterations exceeded a specified level. Equation 2 (adapted from (Oomori et al., 2016)) details the equation that the process attempted to solve in each iteration for two sets of given points (A_i – source and B_i – target) where R was the rotation matrix and T the transformation matrix.

Equation 2: Relation of source and target points within an ICP transformation

$$B_i \approx RA_i + T$$

To estimate the rotation and transformation matrices required to minimise the Euclidean discrepancy between each point-point pairing in A_i and B_i, and best satisfy the equation, various objective minimisation techniques can be used with the 'singular value decomposition' method commonly adopted Wang & Zhao (2017). To execute ICP transformations in the pipelines the 'ICP' algorithm provided within the VTK Python module was used which employed the singular value decomposition objective minimisation approach.

ICP transformations are rigid which means the points within source points were only moved relative to the target and not themselves, i.e., the shapes of both surfaces were not distorted (as can be seen in Figure 29). ICP is particularly useful when there is no correspondence between surfaces as, unlike in other registration approaches such as the 'Kabsch' algorithm, this is not required as an input (Blatov et al., 2019). As such, ICP can be used for registration between surfaces that may be vastly different in point density and/or size. For an ICP transform to work effectively however, a limitation is that the two surfaces needed to be in 'reasonably good' initial alignment (Mitra et al., 2004).

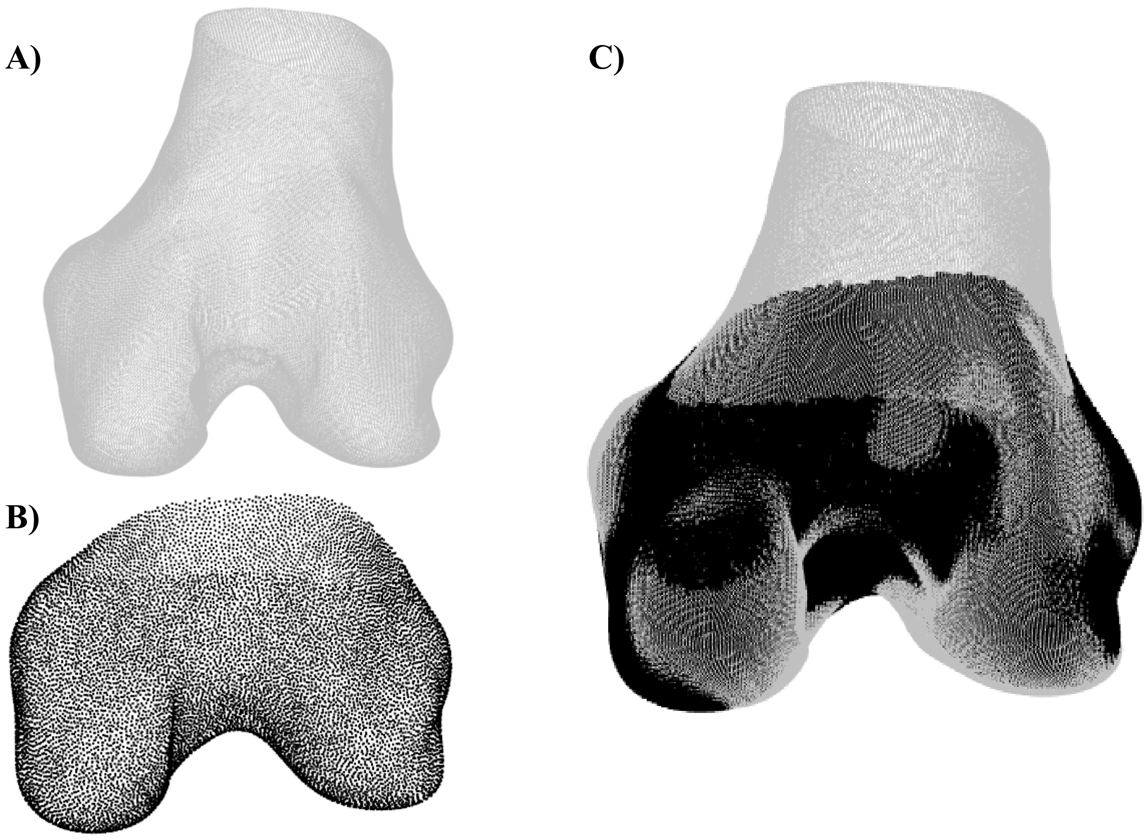

Figure 29: A) Mesh of distal femur bone including condyles and beginning of shaft, B) Mesh of femur condyles, C) Meshes aligned after ICP transform

3.8. Statistical Shape Models

SSMs were built using an algorithm originally developed by Nolte et al. (2020). To train SSMs, the algorithm first loaded specified 3D bone models (in the form of .stl files) as training data. The data was then normalised by, firstly, positioning and aligning the models consistently in 3D space relative to a selected 'base shape' reference model using the ICP method detailed in Section 3.7. The training models were then scaled to ensure consistent global sizing relative to the base shape. Lastly, for each training model, point correspondence was completed to establish point pairings relative to the base shape by leveraging a Nearest Neighbours search (Yianilos, 1993).

After normalisation, Principal Component Analysis was completed to reduce the dimensionality of inputted training data and establish the controllable modes of operation (principal components) of the SSM. To achieve this, the algorithm developed by Nolte et al. (2020) initially calculated the covariance matrix of all feature dimensions (points in the 3D models). Eigen decomposition of the covariance matrix was subsequently completed to output the corresponding eigen vectors and eigen values. In the context of SSM models, eigen vectors represent the directions of variance in the data (i.e., how the base shape could be morphed – as illustrated in Figure 10). From the outputs, the eigen vector with the largest corresponding eigen value gave the direction of maximum variance and thus the first principal component in the SSM. The eigen vector with the second largest associated eigen value represented the second principal component and so on (Dutt, 2021). The outputs from the SSM training algorithm consisted of a .vtk file (a binary file format comprising of polygonal geometrical 3D data, often used for visualisation) to represent the SSM base shape, along with a compressed archive file (.ssm), similar to a .zip file, containing detail on the established eigen vectors and values.

After SSM models had been created via the algorithm they could be loaded into pipelines and fitted to geometrical data extracted from inputted medical images (X-rays or CT scans) to form 3D model predictions. A Python based module, also written and provided by Nolte et al. (2020), facilitated this using an iterative optimisation algorithm to morph the base shape of a specified SSM in accordance with its principal components (as characterised by the eigen vectors and values learnt during training). The optimisation process utilised was based on the process published by Berghe et al. (2017). This approach involved iterating over all modes of variation in turn to find optimal values using a 1D line search with a 'bisection algorithm' incorporated to speed up convergence. Convergence was checked using the RMSE of the point to surface distances to allow reconstruction of incomplete shapes with a threshold set as 0.01 mm (as adopted by Berghe et al. (2017)). If the optimisation failed to converge before a specified number of iterations had passed, the process would terminate. The maximum number of optimisation iterations was typically set as 100 as it was found minimal improvements were achieved beyond this point and consequentially unnecessary compute time was incurred. In addition to specifying the error convergence threshold and maximum number of iterations, the number of principal components used to fit SSMs to specified data could also be adjusted. This facilitated control over the level of model compression used to fit data.

3.9. Point Depth Models

To estimate the depth in the third dimension of 2D contours extracted from X-ray images (Y for AP and X for lateral contours), and for 'sparse' 3D point clouds to be subsequently generated and used to inform the morphing of SSM models, 'Point Depth Models' (PDMs) were developed. PDMs for femur and tibia bones were defined by comparing the Euclidean distances (*d* – the length of a line segment created to connect two points directly) between 2D contour points (blue in Figure 30), created from reference 3D models via the DRR method (detailed in Section 3.6), against their nearest point (at the equivalent Z height) in the corresponding 3D models (red points in Figure 30).

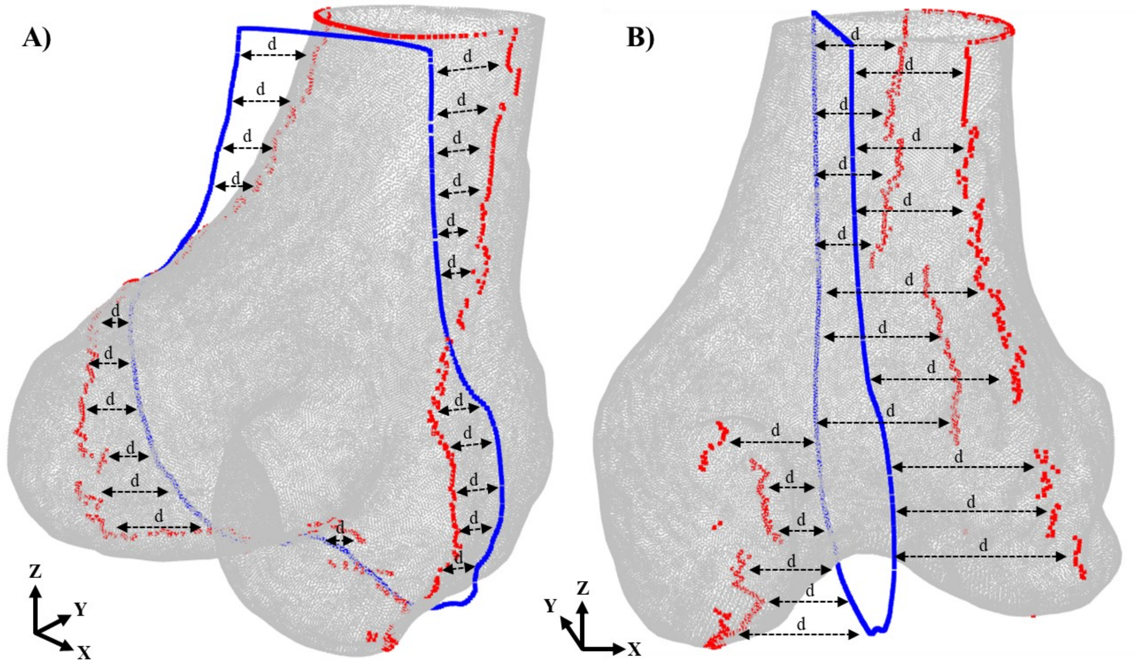

Figure 30: 2D DRR femur contour points (blue) compared against 3D model points (red) for AP (A) and lateral (B) projections

Before PDM analysis was performed, a consistent alignment was enforced for all reference models via a rigid ICP transform (detailed in Section 3.7) using manually orientated models as targets. The positioning of the reference models subsequently reflected the anatomical alignment in real X-ray projections before DRR contours were captured. The number of points considered in the analysis was downsampled to a specified number to be consistent across each reference model. The Euclidean distance for each point in each contour from each reference model was then converted to a depth coefficient (c) to normalise the measurements taken at each point index (n) by dividing the calculated depth (d) by a reference global measurement for each model (W_{ref}). For AP contours, the reference measurement was subjects' lateral condylar width (maximum Y width). For lateral contour coefficients, the AP width (maximum X width) was used. Depth coefficients ranged from -1 to 1 with negative/positive values representing depths either side of a calculated mid-point (blue lines in Figure 30). Equation 3 describes the relationship to calculate the depth coefficients for each index along the contours.

Equation 3: Calculation of PDM depth coefficients at specified contour point indexes

$$c_n = \frac{d_n}{W_{ref}}$$

After depth coefficients had been calculated for each 3D model in the training set, these were then plotted along the length of the contours as illustrated for the tibia AP contour as blue points in Figure 31. The mean of the depth coefficients (red points) at each point index were then calculated, as well as the adjusted means (green points). The adjusted mean accounted for outliers and inconsistencies in patient anatomy and alignment by omitting values that were outside a specified window from the mean at each index (± 20% for example). Using the adjusted mean helped to smooth and generalise the outputted PDM coefficients.

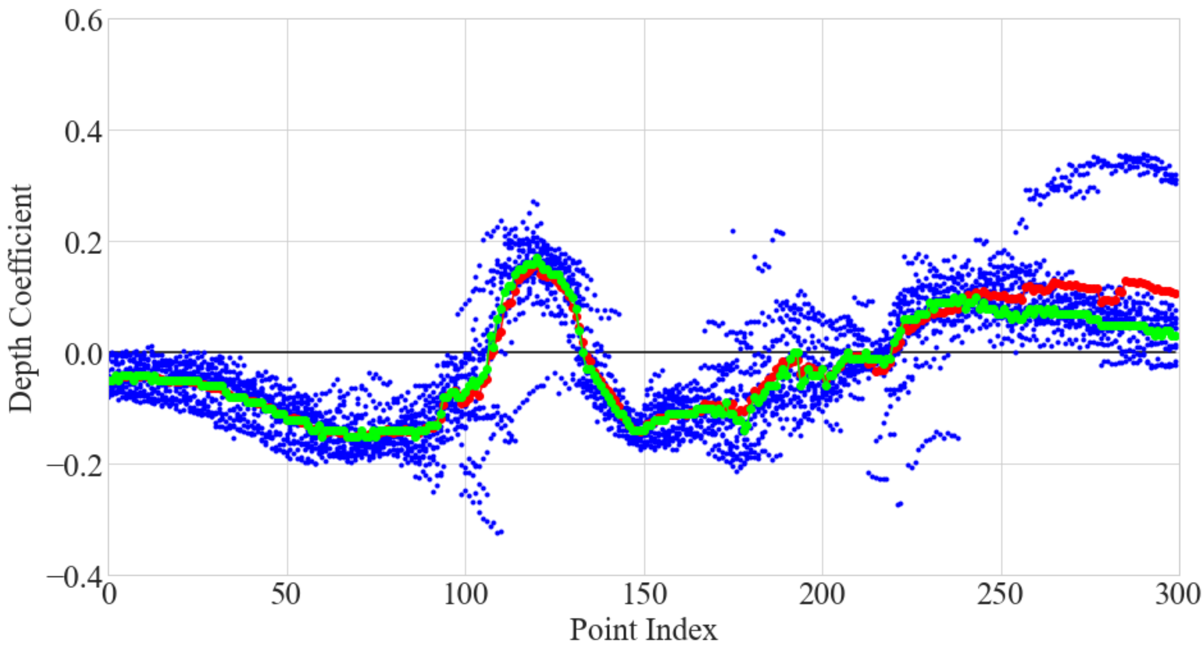

Figure 31: PDM analysis of AP tibia contour (blue points – calculated depth coefficients across training models, red – mean of depth coefficients, green – adjusted mean) © (Burge et al., 2022a)

Once adjusted means for the depth coefficients were calculated, these could then be utilised to estimate the depth along new contours (*d*). This was achieved by rearranging Equation 3 to Equation 4 for a particular point index (n). As before, C_n was the depth coefficient at index n and W_{ref} was the relevant reference measurement taken from each subject's X-rays.

Equation 4: Calculation of estimated depth at specified contour point indexes

$$d_n = C_n \times W_{ref}$$

3.10. Application Programming Interfaces

An 'Application Programming Interface' (API) is a way for two or more computer programmes to interface and communicate with each other (Reddy, 2011). In this research, this specifically related to Python scripts interfacing with CAD software to facilitate automated implant design processes. The free and open-source software 'FreeCAD' was utilised within the various pipelines as it offered 'headless' API functionality which allowed for it to be controlled externally by Python scripts (Machado et al., 2019). CAD operations could therefore be completed seamlessly without requiring users to manually switch between software packages to complete tasks such as loading meshes, extruding shapes, making cuts, adding chamfers/fillets, and exporting finished models. The scripted operations could also be adjusted to work for different individuals by employing parametric modelling methods.

3.11. Fit Metrics

To assess the performance of the pipelines developed in this research, reconstructed 3D bone models and implant components generated were evaluated in terms of RMSE and maximum OUH. RMSE was used as it provided an average of the global surface-surface fit performance in terms of both positive and negative discrepancies. This is unlike mean absolute error which can provide misleading results in cases where similar levels of both positive and negative errors exist. Maximum OUH was used in parallel to obtain a local, clinically relevant assessment where the maximum mismatch between implant and bone was recorded.

3.11.1. Root Mean Squared Error

RMSE is a method which calculates the average Euclidean distance between all points in one surface/mesh (source) and another (target) reference. Like for ICP, a Nearest Neighbour search (Yianilos, 1993) was used to find the closest point in the target reference mesh to each point in the source before each distance was calculated. Equation 5 was used to calculate the RMSE where N was the number of points and $x_i - \hat{x}_i$ was the Euclidian distance between corresponding points on the two surfaces.

Equation 5: Calculation of RMSE

$$RMSE = \sqrt{\frac{\sum_{i=1}^{N}(x_i - \hat{x}_i)^2}{N}}$$

Two forms of RMSE calculations were performed when assessing the fit performance of the various pipelines. The 'reconstruction' RMSE was calculated between the surfaces of 3D model reconstructions and corresponding ground truth bone models. The 'component' RMSE was calculated between the relevant surfaces of knee replacement implant components in relation to the same ground truth bone models. Prior to the calculations, both bone and component models were automatically trimmed to a consistent height of 50 mm for the femur and 25 mm for the tibia. This helped focus the RMSE calculation on the relevant condylar regions on each bone important for knee replacement components and not skew the results by considering unimportant regions, such as the bone shafts. Surface-surface fits are demonstrated via heat maps which illustrate the variation in Euclidean distance over the surfaces of reconstructed bone models and implant components in relation to ground truth models in Figure 32. For the tibia, the latter is shown with the tibia plate's 2D profile positioned at the intended implantation height on the bone.

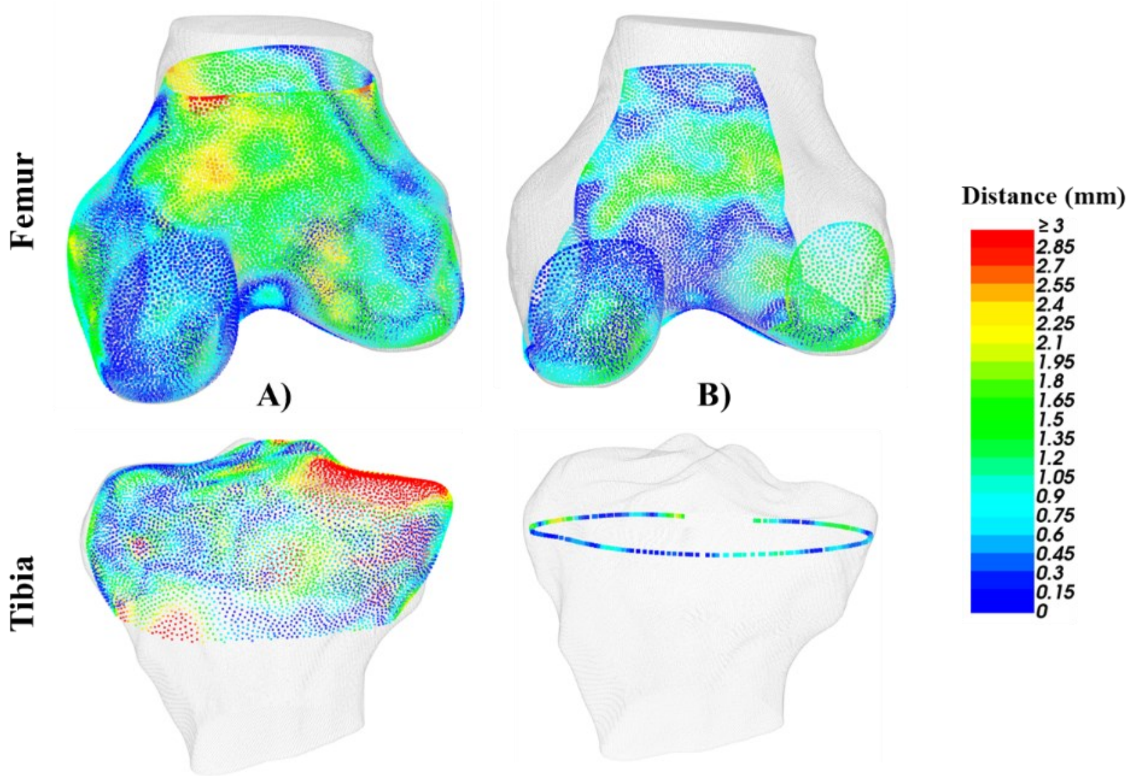

Figure 32: Distance heat maps for femur and tibia bones compared to ground truth models: A) 3D reconstructions and B) Implant components models © (Burge et al., 2023b)

3.11.2. Maximum Over or Under Hang

Various methods have been reported for calculating maximum OUH in knee replacement implants. Authors have utilised specific regions or measurements such as the widest mediolateral dimensions of bones compared to implants (Bonnin et al., 2013) (Dai et al., 2014b) (Sharma et al., 2017). Others reported fit discrepancies at any point along the edges of components (Wernecke et al., 2012) (Clary et al., 2014) (Shao et al., 2020). In this research, maximum OUH was calculated as the Hausdorff distance (h) (Aspert et al., 2002) anywhere between the edges of the component (C) and the edges of the resected bone (B). The distance

(d) between each point on the component (c) and bone (b) was calculated as the Euclidian distance. Equation 6 details the maximum OUH calculation.

Equation 6: Calculation of maximum OUH (Hausdorff distance)

$$h(C, B) = max_{\,c \in C} \{ min_{\,b \in B} \{ d(c, b) \} \}$$

The locations of calculated maximum OUH for both the edges of a femur component and a tibia plate (shown as a 2D profile), in relation to reference bone geometries, are illustrated in Figure 33A and Figure 33B respectively.

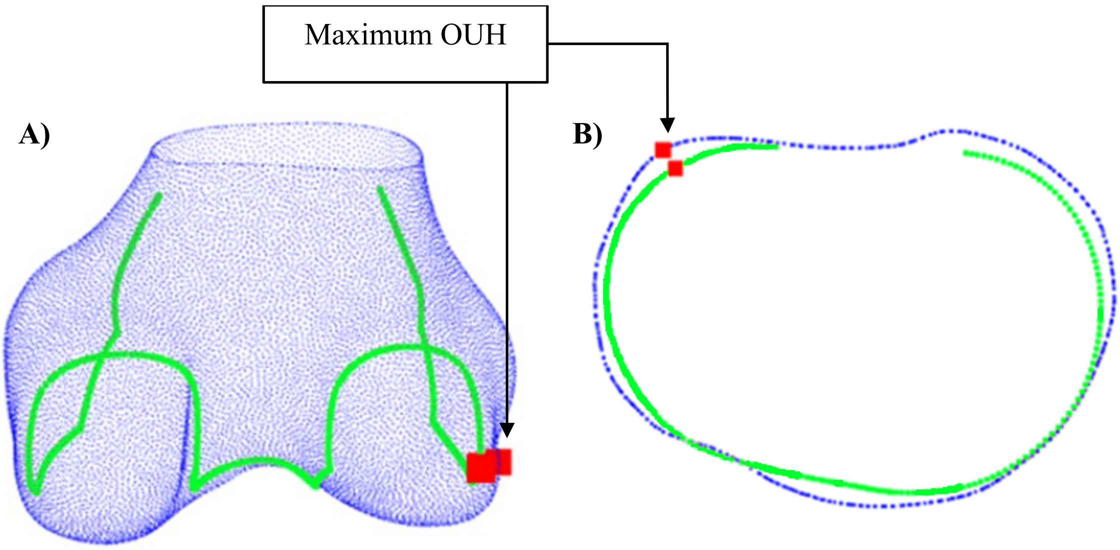

Figure 33: Identification of the point of maximum OUH for A) Femur component edges and B) Tibia plate edges, both compared to ground truth models © (Burge et al., 2023b)

3.12. Statistical Analysis

For statistical analysis of results, two-sample t-tests were utilised to evaluate differences in means between test subject attribute pairs, such as the performance of left vs. right knee sides. Before statistical tests were performed data was confirmed to be approximately normally distributed using quantile-quantile plots and results determined to be outliers were removed. p values ≤ 0.05 were considered statistically significant throughout the research.

To evaluate the correlation strength of continuous variables on performance, such as subject age and/or height, Spearman's correlation coefficients were calculated. Coefficients ≤ -0.5 or ≥ 0.5 were considered significant throughout.

3.13. Prototype Builds

To fabricate prototype designs via AM, a AM250 metal powder bed fusion system (Renishaw plc, UK) was utilised. Commercially pure 'titanium grade 2' powder was used, supplied by 'Carpenter Additive', with particle sizes ranging from 10 – 45 µm. The build chamber was vacuumed to −960 mbar and then back filled with 99.995% pure Argon to 10 mbar with an Oxygen content of ~0.1%. A consistent laser power of 50 W and point distance of 50 µm were used with exposure time adjusted to enable desired variation in strut thickness, as described by Ghouse et al. (2017). Prototypes were removed from the build plate after fabrication using electro discharge machining. Images of the build structures were then captured using scanning electron microscopy using 5 keV and 1nA (Mira Microscope, TESCAN, Czech Republic).

3.14. Summary

This chapter provided a general overview of the key materials, methods/algorithms and data utilised to build the various knee replacement implant customisation pipelines presented in this thesis. Unless otherwise stated, the algorithms and models were all written in Python 3 and were adapted for use in each of the pipelines. Specific details, such as how they were trained and tested, their designs and architectures, model settings, and how they were connected to form automated customisation pipelines, are more thoroughly explained in the method sections of the following chapters.

Chapter 4

Assessment of Off-the-Shelf, Sized Implants

The following chapter presents the method for, and results of, a virtual sizing study to explore the design space of OTS, sized TKR implant components and determine their theoretical best possible performance.

Most of the contents of this chapter have been published in the following paper:

- Burge, T.A., Jeffers, J.R.T. & Myant, C.W. (2023) A computational design of experiments based method for evaluation of off-the-shelf total knee replacement implants. *Computer Methods in Biomechanics and Biomedical Engineering*. 26 (6), 629-638.

4.1. Introduction

As highlighted previously, OTS implants with standardised shapes and sizes are currently far more commonly utilised for knee replacement compared to custom solutions (Evers, 2019). Implant manufacturers typically provide up to around eight sizes to cover all potential patient anatomies. Implant sizes are usually equally spaced (in terms of global dimensions) and follow linear ML-AP relationships (Hitt et al., 2003) (Lim et al., 2013) (Dai et al., 2014a). ML and AP sizes, as well as the ML/AP aspect ratios used, differ considerably among the many commercial models available and there is no consensus on the optimal (Hitt et al., 2003).

Numerous articles have investigated the fit of OTS TKR models via clinical approaches. Authors have measured the ML/AP sizes for distal femurs and proximal tibias and compared these to commercial models (Hitt et al., 2003) (Li et al., 2019) (Budhiparama et al., 2021). Others superimposed scans of tibia plates onto MRI images (Wernecke et al., 2012), and physically compared the fit of different implant types and sizes intraoperatively (Sharma et al., 2017). In terms of computational approaches, authors have utilised 'virtual surgery' where computer models of implants were fitted to digital subjects created from segmented CT scan data (Clary et al., 2014) (Dai et al., 2014b) (Shao et al., 2020). These studies however all focused on commercial designs with a set number of predefined sizes. Grothues et al. (2022) completed a study using 85,143 custom femur component dimensions obtained from ConforMIS, and virtually matched these to 1,049 bone models. The authors then used 'particle swarm optimisation' to find the best possible set size ranges for a various number of sizing quantities and assessed the resulting population coverage via a range of OUH fit criteria. No studies were however found that explored the full potential sizing window of both OTS femur components and tibia plates and definitively determined how successful implants with eight standardised sizes could theoretically be.

To serve as a useful comparison for the various customisation pipelines developed in Chapters 5 – 9, the analysis completed in this chapter sought to identify the best possible performance for OTS products by adopting a virtual, full factorial, design of experiments based method. Whether OTS implants with optimised sizes could ever meet the high performance shown achievable with custom products (Ogura et al., 2019) (Arnholdt et al., 2020) was then assessed.

4.2. Implant Sizing Study Method

In this section, the base designs of the generic OTS implant components used in the sizing study, as well as how the 3D models of said components were scaled and fitted to a test population, are outlined.

4.2.1. Base Implant Model Designs

Generic base TKR femur and tibia plate components, designed to mimic common manufacturer models, were created for use in the study. A single femur component (Figure 34) was created by using a femur bone model taken from the KISTI dataset and applying the Laplacian Smooth tool within MeshLab with Smoothing Steps set to '3' (in the same way as detailed in Chapter 3.3) to 'idealise' and normalise the geometry, creating a smooth bearing surface. It was then cut using operations in 'Autodesk Fusion 360' – a commercial CAD tool (Song et al., 2018), to resemble the shape of commercially available implants, using the Zimmer Biomet 'NexGen' as a reference in particular. No fixing pins or rounding/chamfers were included.

For the tibia plate analysis, both anatomic (asymmetric) and symmetric designs were utilised. The profile of the Smith and Nephew 'Legion' implant (Smith & Nephew, 2015) was used to inform the anatomic shape used (Figure 35A), whilst the standard '[E]8' shape used in (Shao et al., 2020) was traced to create the symmetrical (Figure 35B). Tibia plate fit was assessed in

2D, as opposed to in 3D like the femur component, as the component's function is to best match the profile of the resected bone on a singular face rather than replicate the 3D form of the bone. Similar 2D approaches were adopted by Clary et al. (2014) and Shao et al. (2020).

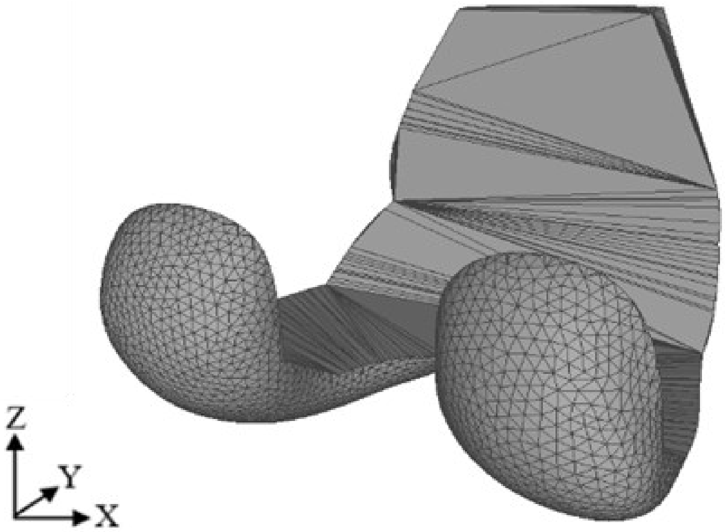

Figure 34: Generic femur component design

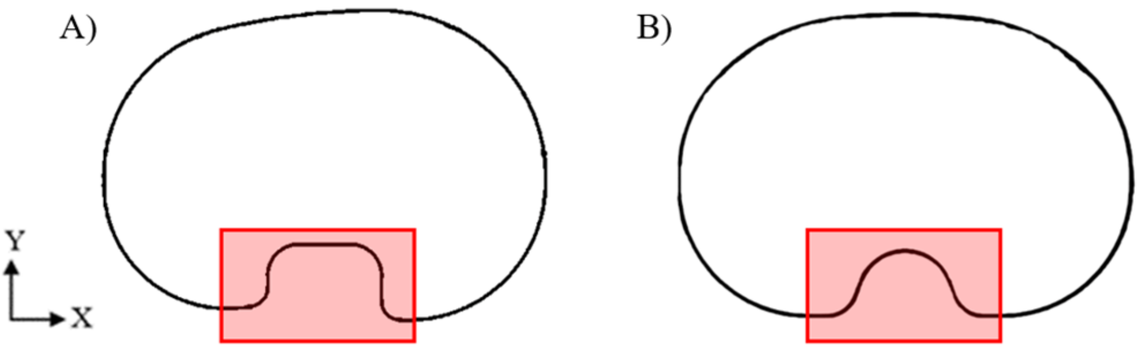

Figure 35: A) Anatomic and, B) Symmetric tibia plate designs © (Burge et al., 2023a)

4.2.2. Implant Model Scaling and Fitting

Before the components were fitted to test subject anatomy, the models were scaled in the X (ML) and Y (AP) dimensions by multiplying the respective coordinates of the models' vertex arrays by calculated scaling factors (*SF*). The X and Y scaling factors were established by dividing the target ML and AP dimensions respectively (d_{target}) by the dimensions of the generic base components (d_{base}), as expressed in Equation 7.

Equation 7: Calculation of scaling factors

$$SF = \frac{d_{target}}{d_{base}}$$

For femur components, scaling was also applied in the Z dimension by using the mean of the X and Y scaling factors to keep the height of the implant proportional. The effect of keeping the component height constant (without Z scaling), was also evaluated. To cover the measured variability in test subjects' bone dimensions, femur components were scaled in increments of 1 mm for all combinations of ML and AP dimensions of 40 – 110 mm. Likewise, tibia plates were scaled within ML and AP dimensions of 35 – 110 mm and 30 – 75 mm respectively.

After scaling, the components were virtually fitted to each test subject's bone models using a ridged ICP method (detailed in Chapter 3.7). For femur components, the fitting process was performed between the 3D patient anatomy and the implant surface. For tibia plates, the 2D profile of the scaled plate was fitted to a 2D cross-section of the bone captured via a bisection plane positioned 2 mm below the height of the widest point of the medial condyle, parallel with the surface of the tibia plateau (illustrated in Figure 36A). The Z height of this anatomical point was determined using Min/Max functions. A cross section (Figure 36B) was then obtained by calculating the location at which the plane intersected with elements in the 3D mesh models and outputting the established coordinates as a series of new points. The method was used for the tibia to achieve the largest possible surface area for stability while minimising bone loss and ensuring a continuous resection plane through the bone below the articular surfaces of the condyles (Schnurr et al., 2011). The cut section highlighted by the red dashed boxes in Figure 35 was excluded during the fitting process as this was an implant design feature and not intended to match the anatomy.

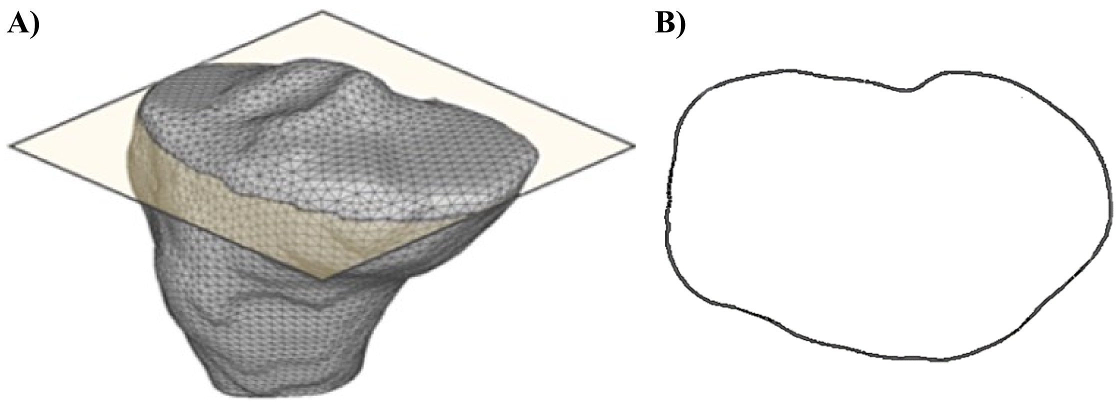

Figure 36: A) Cut plane created through tibia bone positioned at the intended resection height, B) 2D profile extracted from bone model © (Burge et al., 2023a)

4.2.3. Test Subjects

To serve as test subjects, 47 female and 30 male White American subject knee 3D bone models (77 in total) were generated from the OAI dataset by segmenting the supplied MRI data (as described in Chapter 3.3). A further 90 female and 77 male Asian Korean bone models (including both femurs and tibias) supplied with the KISTI dataset (167 in total) were also utilised. The test subjects selected ranged from 21 to 77 years old and all had K&L grades of ≤ 2, indicating up to mild levels of arthritis or unspecified (Kellgren & Lawrence, 1956).

4.3. Implant Sizing Study Results and Discussion

Component RMSE and maximum OUH results were calculated as described in Chapter 3.11 for all possible implant aspect ratios within the specified size ranges (detailed in Section 4.2.2) after being virtually fitted to the test subjects' ground truth models. This formed a full factorial design of experiments resulting in 1,024,800 component fittings in the femur analysis (for both with/without Z scaling), as well as 823,500 for each of the tibia plate design variants. From these, subsets of 'best fits' for each test subject, in terms of both RMSE and maximum OUH, were also outputted.

4.3.1. Comparison of Implant Design Types and Z Scaling

Figure 37 shows a box plot of the best fit data in terms of maximum OUH and RMSE for both proportional height and fixed height femur components (with and without Z scaling). The medians for both fit metrics can be seen to be higher when Z scaling was not applied with 9.43% of subjects seeing maximum OUH results ≥ 3 mm. Nonetheless, even when Z scaling was performed, 2.87% of subjects still had best possible outcomes above the clinically significant maximum OUH of ≥ 3 mm. The differences in maximum OUH and RMSE between the scaling types were found to be statistically significant (based on Chapter 3.12).

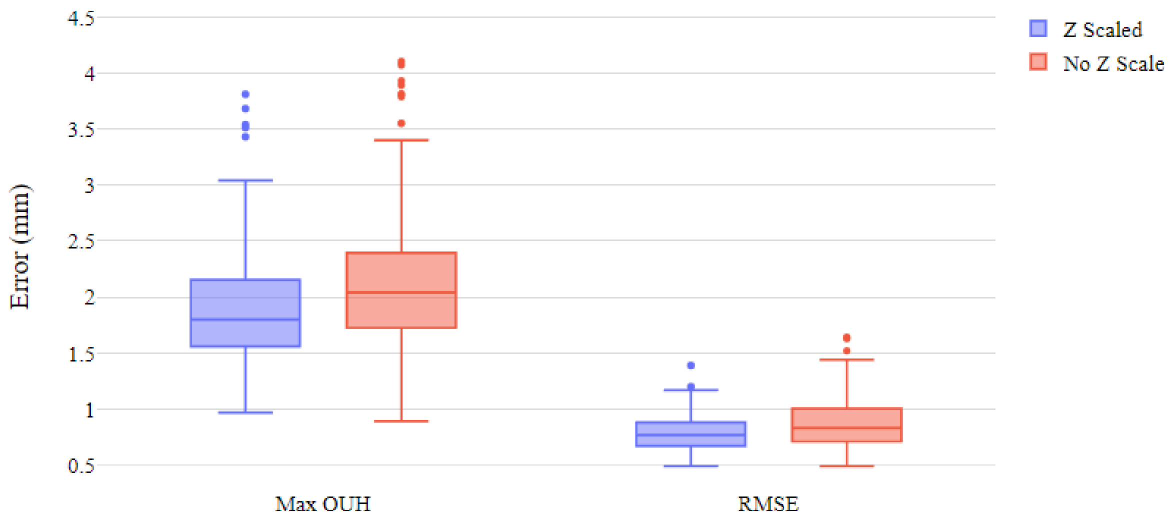

Figure 37: Box plot of test subjects' best fit femur component results with and without Z scaling © (Burge et al., 2023a)

Figure 38 shows the difference between the best fit data for the two tibia plate designs illustrated in Figure 35. The anatomic design was found to produce median values of maximum OUH slightly below the symmetric. However, for RMSE, the median of the symmetric design was marginally lower than the anatomic, but with more variability. The anatomic design resulted in no subjects with OUH ≥ 3 mm, compared to 4.10% for the symmetric. The difference in maximum OUH for the two designs was found to be statistically significant but the difference in RMSE was not (p value = 0.44).

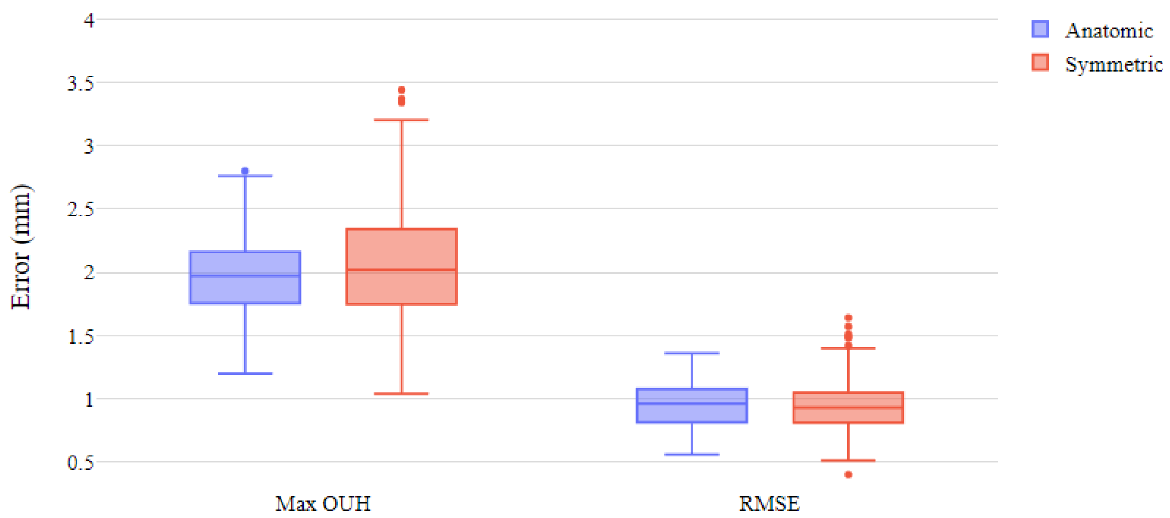

Figure 38: Box plot of anatomic and symmetric tibia plate best fit results © (Burge et al., 2023a)

4.3.2. Implant Sizing Requirements

Based on the results in the previous section, the remainder of the analysis was limited to femur components with Z scaling (proportional height designs) and the anatomic tibia plate design. Figure 39 shows an example plot of the implant AP and ML sizes that resulted in the lowest maximum component OUH across all test subjects. Figure 40 shows the same for ML/AP aspect ratios. Both plots are labelled with implant type, subject sex, and ethnicity.

The large range of implant sizes and aspect ratios required by the different subjects evaluated is clearly demonstrated via the high level of variability within the plots. A strong trend can be seen in Figure 39 that confirmed, as expected, males typically required larger implant components than females (in terms of both ML and AP dimensions). It was found that White subjects also required larger implant components compared to Asian subjects. The differences in required ML/AP aspect ratios between males and females, as well as between ethnicities, were however less pronounced (Figure 40). Nevertheless, large differences within the total population can still be seen for both implant types. Lastly, ML/AP aspect ratio was found to correlate negatively with AP size, which is supported by Hitt et al. (2003).

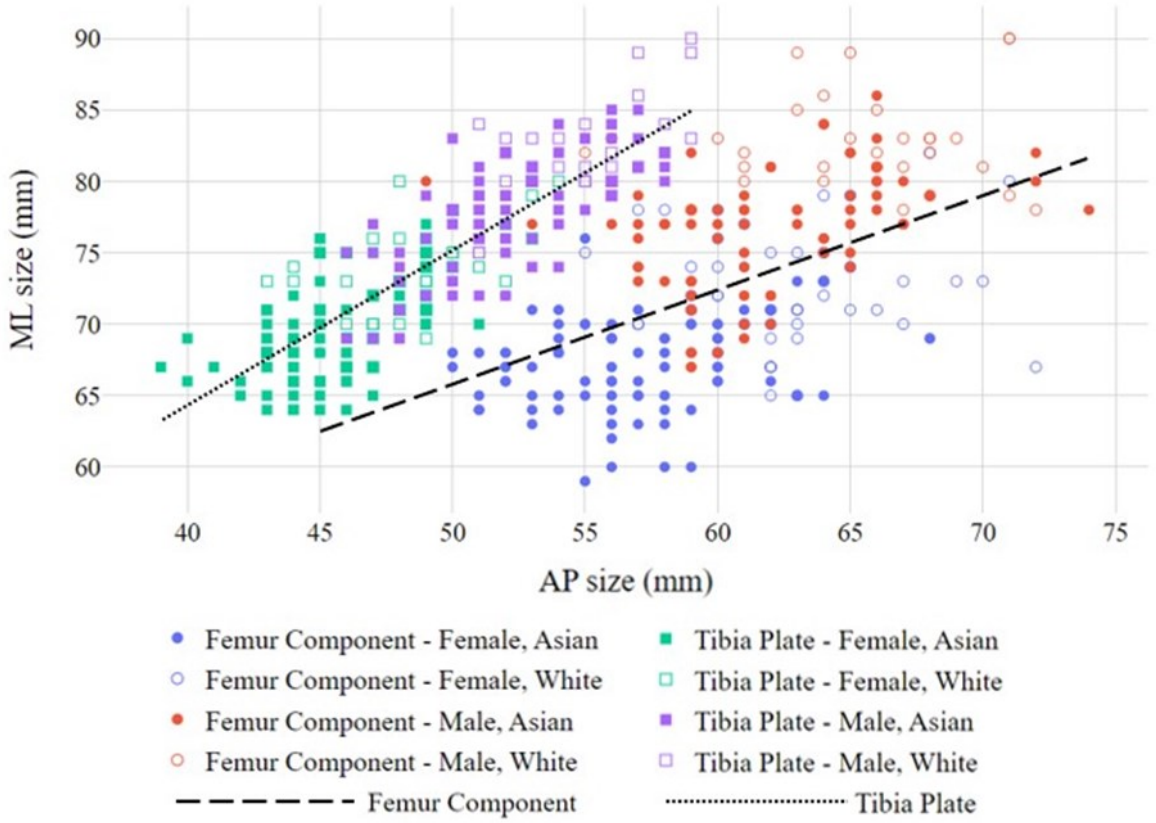

Figure 39: Best ML and AP sizes to minimise OUH across subjects © (Burge et al., 2023a)

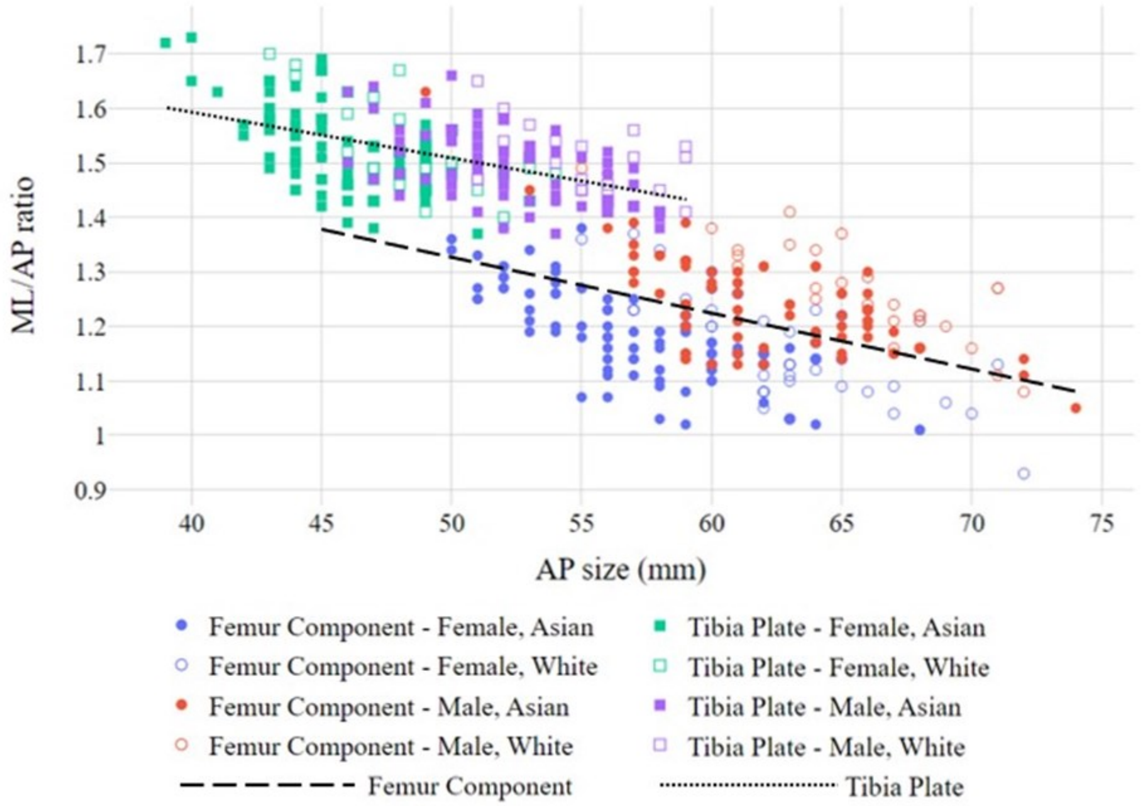

Figure 40: Best ML/AP ratios to minimise OUH across subjects © (Burge et al., 2023a)

4.3.3. Optimal OTS Sizes and Best Possible Performance

To determine the optimal fit performance that generic implants could achieve, the performance of all possible combinations of ML and AP dimensions that fell on the linear best fit curves shown in Figure 39 were calculated and ranked for up to eight sizing options. Figure 41 and Figure 42 show examples of the population covered by the four femur component sizes determined to afford the best possible coverage when a threshold of < 3 mm maximum OUH was specified. The former illustrates 'optimised' spacing where the dimensional difference between sizes was not required to be consistent. In this case, a 70.49% population coverage was achieved. The latter shows the population coverage when equal spacing between the sizes was enforced by omitting combinations with irregular spacing from the analysis. Here, a 68.44% population coverage was recorded. The colouring within the plots illustrates which test subjects were covered (dots) by each of the set implant sizes (diamonds).

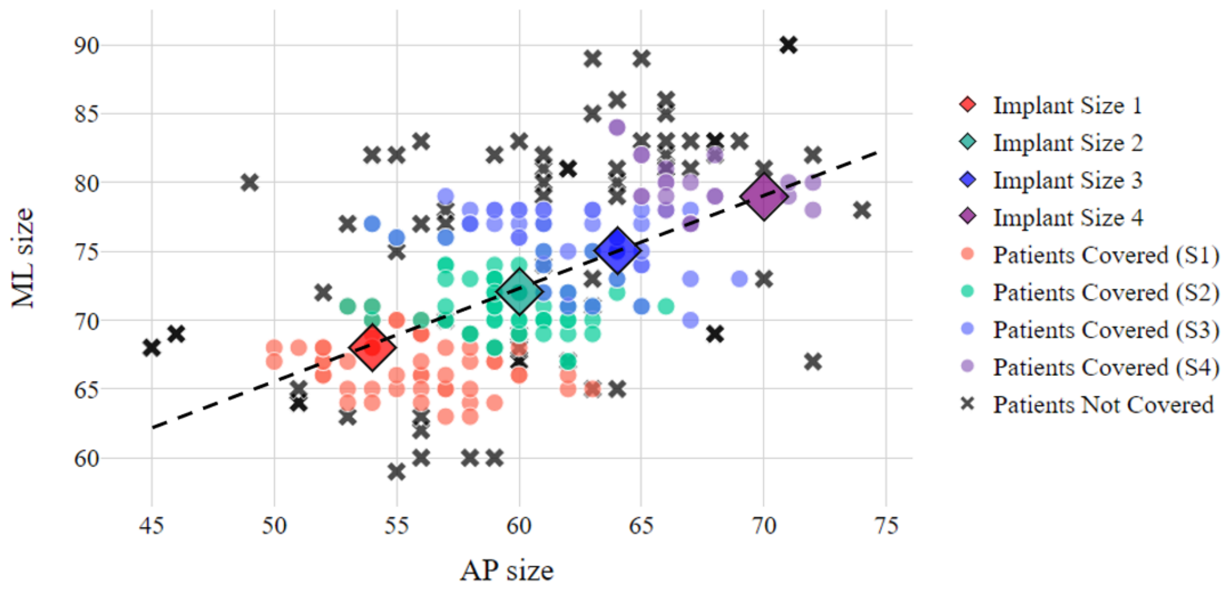

Figure 41: Population coverage (in terms of maximum OUH < 3 mm) for four femur component sizes with optimised spacing

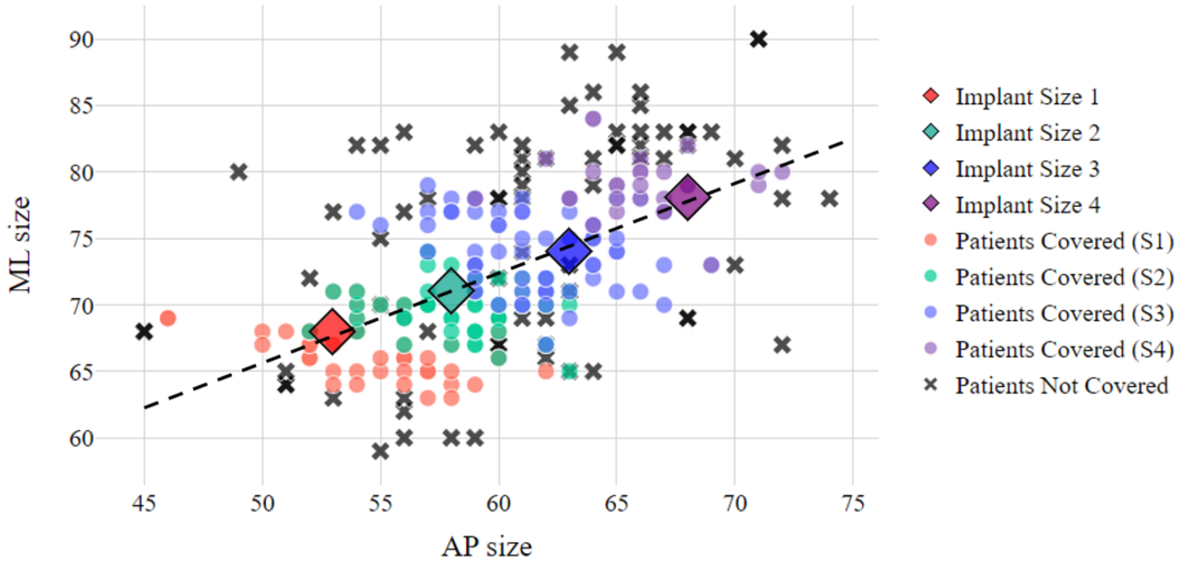

Figure 42: Population coverage (in terms of maximum OUH < 3 mm) for four femur component sizes with equal spacing

For the optimally spaced sizes in Figure 41, the first implant size (S1) covered subjects with ML dimensions ranging from 63 to 71 mm, the second (S2) 67 to 77 mm, the third (S3) 70 to 79 mm and the fourth (S4) 77 to 84 mm. In terms of AP sizes, the first option (S1) covered subjects ranging from 50 to 63 mm, the second (S2) 53 to 66 mm, the third (S3) 54 to 69, and the fourth (S4) 64 to 72 mm. For the equal spaced sizes in Figure 42, the first implant size (S1) covered subjects with ML sizes ranging from 63 to 71 mm, the second (S2) 65 to 74 mm, the third (S3) 67 to 79 mm and the fourth (S4) 73 to 84 mm. In terms of AP sizes, the first option (S1) covered subjects ranging from 46 to 62 mm, the second (S2) 52 to 63 mm, the third (S3) 54 to 69, and the fourth (S4) 59 to 72 mm.

It should be noted that, although some subjects were observed to be well within the anatomical sizing ranges generally covered by each implant size, their best possible results still exceeded the 3 mm OUH fit threshold. This is particularly clear in Figure 42 around the green implant size. This could have been due to the unique form of certain subjects' anatomies which may have been better served by other implant models. Figure 43 illustrates how three different tibia plate designs affected bone coverage for a particular subject in a study performed by Stulberg

& Goyal (2015). Contrary to this, it was found that in several other cases that test subjects could be adequately covered by more than one implant sizing option.

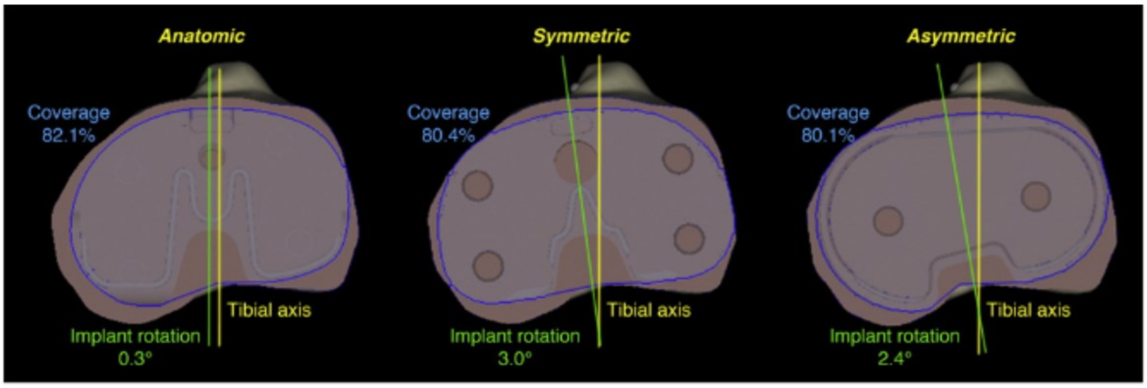

Figure 43: Comparison of bone coverage with 'anatomic', 'symmetric' and 'asymmetric' tibia plate shapes © (Stulberg & Goyal, 2015)

Figure 44 details the outcome of the full analysis for both component and spacing types when up to eight sizes were used. Population coverage thresholds of component RMSE < 1.5 mm and maximum OUH < 3 mm were used here to indicate both a reasonable global fit and provide a more clinically significant metric respectively. Optimised spacing resulted in approximately a 2% better population coverage on average compared to equal spacing when four or more sizes were used. In terms of component RMSE, > 95% of the test population were found to be adequately covered with just three femur component and five tibia plate sizes. Yet, when assessing maximum OUH, the best selection of eight optimised sizes covered 79.51% of the population for femur components and 88.52% for tibia plates. Therefore, although a reasonably low number of sizing options were found to afford a high coverage in terms of global sizing, regions of exposed bone and clinically significant OUH would likely still be present in a high portion of subjects. This was not surprising given the high level of variation in test subject requirements that can be seen in Figure 39 and Figure 40.

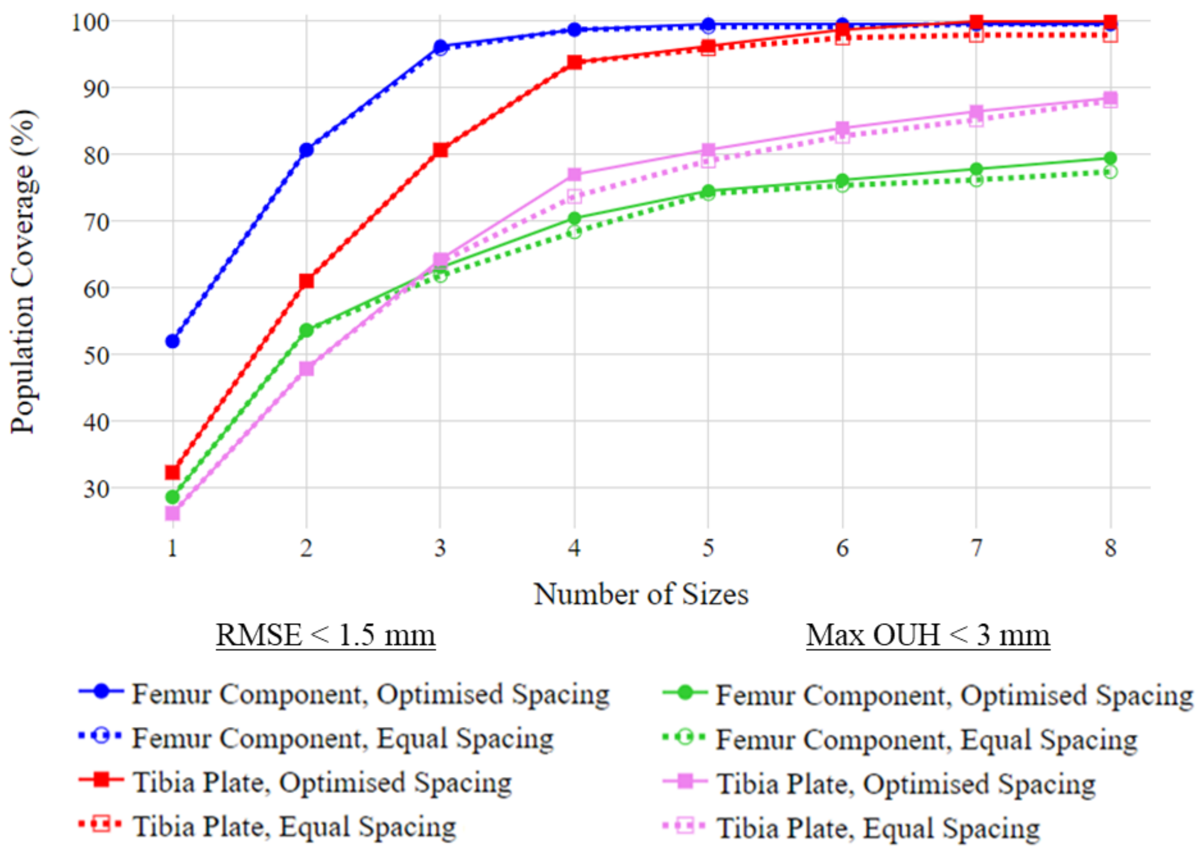

Figure 44: Population coverage vs. number of femur component and tibia plate sizes for equal and optimised spacing © (Burge et al., 2023a)

To see if introducing gender-specific sizings, like the Zimmer Biomet 'NexGen' model, would improve population coverage further, the analysis was repeated with two separate sets of optimally spaced sizes which used separate linear best fit curves created for males and females. Figure 45 demonstrates that, with two sets of eight gender-specific optimised sizes, 84.67% of females and 77.57% of males acheived maximum OUH values of < 3 mm for femur components, along with 92.70% of females and 94.39% of males for tibia plates. This improvement for both component types suggested that, although gender-specific sizes may not be needed for a reasonable global fit, they could however help lower areas of clinically significant OUH.

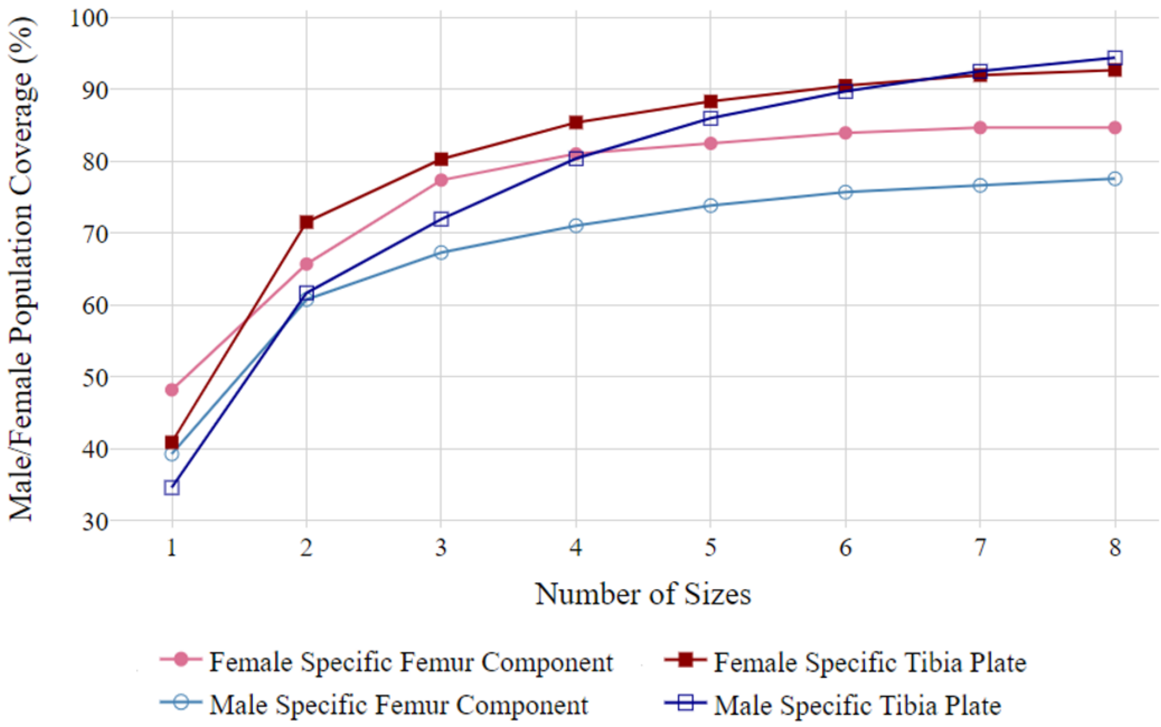

Figure 45: Male/female population coverage (in terms of maximum OUH < 3 mm) vs. number of implant sizes for gender-specific designs © (Burge et al., 2023a)

4.4. Summary

This chapter outlined a novel approach to identify the best possible set sizes of OTS TKR implant components in order to cover a broad population including a variety of sexes, ethnicities, and ages. It was shown that, even with optimally spaced gender-specific ranges, the standard eight OTS implant sizes (or 16 with gender-specific options) would likely never be able to achieve results comparable to those reported for customised solutions (Schroeder & Martin, 2019) (Arnholdt et al., 2020). The results obtained were consistent with those reported by Grothues et al. (2022) who found comparable patient coverage was achieved in their study when using eight optimised implant sizes. The authors also found that even with 30 standardised sizes some of the 1,049 subjects were still inadequately covered. Regardless, such a large number of implant sizing options would be impractical for clinicians to work with.

Despite demonstrating OTS implants would not be satisfactory for all patients, it was found that, if optimised, OTS solutions can afford adequate coverage for a large proportion of patients (approximately 80% for femur components and 90% for tibia plates). Therefore, if the previously highlighted limitations of customisation solutions (the need for 3D imaging, extra resource requirements, longer lead times and higher component costs) were to be mitigated, custom implants could potentially be used to compliment OTS options by servicing patients who lie outside of the standardised sizing architypes.

Chapter 5

X-ray Based Implant Shape Customisation Pipeline

The following chapter presents a method for, and results of, an automatic knee replacement implant shape customisation pipeline, using biplanar X-ray images as an input medium.

Most of the contents of this chapter have been published in the following papers:

- Burge, T.A., Jeffers, J.R.T. & Myant, C.W. (2022) Development of an automated mass-customization pipeline for knee replacement surgery using biplanar x-rays. *Journal of Mechanical Design*. 144 (2), 1–11.
- Burge, T.A., Jeffers, J.R.T. & Myant, C.W. (2022) Performance and sensitivity analysis of an automated x-ray based total knee replacement mass-customization pipeline. *Journal of Medical Devices*. 16 (4), 1–12.

5.1. Introduction

As previously detailed, customising the shape of knee replacement implant components can afford significantly improved outcomes for patients in terms of fit (Schroeder & Martin, 2019), revision rates (ConforMIS, 2018), and potentially save overall costs due to fewer complications post-surgery (Culler et al., 2017). Nevertheless, currently available shape customisation solutions are believed to only make up a very small proportion of the market because:

1) Extensive manual image processing and/or implant design work is required.
2) 3D imaging is necessitated which is not typically needed for OTS implants.

As a result of the points listed above, current customisation solutions incur higher component/ equipment costs, lead times, and increase radiation exposure risks compared to OTS alternatives. Moreover, access to the required CT or MRI equipment is often limited, especially in developing countries. Consequentially, health suppliers have continued to predominantly utilise OTS, sized implants, despite the benefits of customised alternatives being well reported.

As no previous work identified proposed a fully automated, biplanar X-ray based implant shape customisation solution, a proof-of-concept that could mitigate the highlighted limitations is proposed in this chapter. The approach adopted employed AI/ML and statistical methods to automate the workflow and negate the need for 3D medical images.

5.2. Pipeline Development and Test Method

In the following sub-sections, the various stages of the X-ray based implant shape customisation pipeline, as summarised in Figure 46, are outlined. Details of the subjects used to train and test the pipeline are also provided.

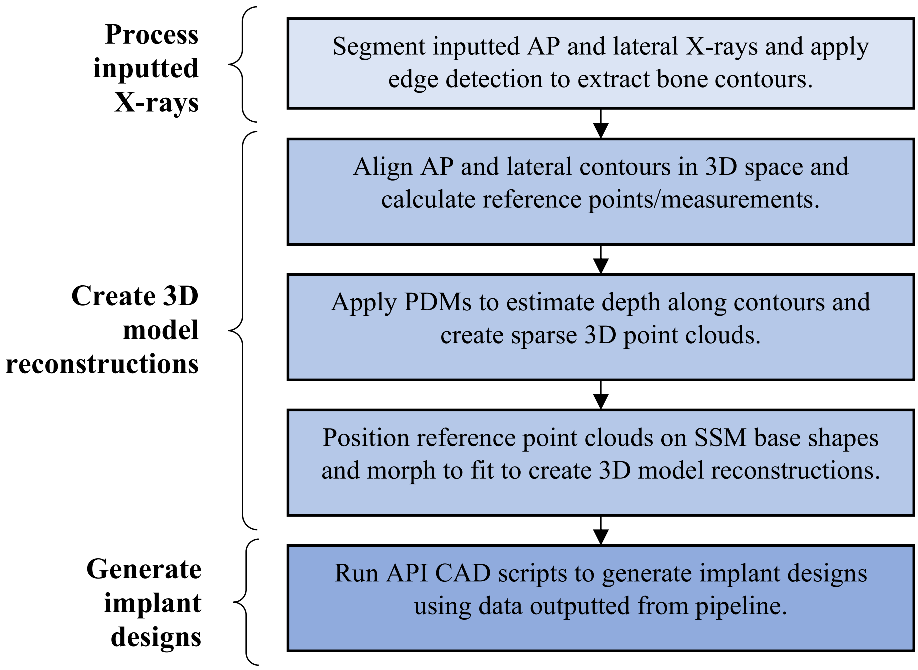

Figure 46: Key stages and workflow of the X-ray based implant shape customisation pipeline

5.2.1. Pipeline Training Data and Test Subjects

Data to train the various models used within the pipeline, including X-ray images and 3D bone models, was sourced from both the KISTI and OAI datasets. The OAI dataset was used exclusively to test the pipeline as it was the only dataset available which contained both AP and lateral knee X-rays, in addition to MRI data which could be used to create ground truth models via the process detailed in Chapter 3.3. For test subject inputs to be compatible with the pipeline, well-aligned and calibrated AP and lateral X-rays, with sufficient bone shaft lengths visible for both the femur and tibia, were required (detailed further in Section 5.2.2). The 122 subjects with the required X-rays from the OAI dataset (highlighted in Chapter 3.2.2) were therefore qualitatively assessed to determine whether they met the necessary requirements. Ultimately, 78 of the 122 subjects were deemed acceptable to be used for testing, comprising of 73 White, 4 Black and 1 Asian American subjects, all with K&L grades of ≤ 2 (none to mild levels of arthritis). No data used for training the pipeline was also used for testing.

5.2.2. Process Inputted X-ray Images

The first step in the pipeline was to extract geometrical information from inputted AP and lateral X-ray images. This was achieved using CNN based segmentation models, trained to isolate the femur and tibia bone shapes in inputted X-ray images. Four CNN based image segmentation models (one for each X-ray projection of each bone) were built for the pipeline using the process outlined in Chapter 3.4.3. These were developed solely for left sided geometry as the natural symmetry of femur and tibia bones in the human body could be exploited by horizontally flipping input images if the right knee was to be studied.

The architecture of the segmentation models developed for the pipeline was based on the U-net structure outlined by Ronneberger et al. (2015). The model is illustrated in Figure 47 using an equivalent style and key to Figure 9. Each box in Figure 47 corresponds to a feature map with grey boxes indicating where channels were copied from previous layers. The number of channels is denoted on top of each box with the image size provided at the lower left (for example, 256^2 = 256 x 256 pixels). The arrows denote different operations such as convolutions and pooling. To achieve accurate segmentations, the U-net CNN architecture proposed by Ronneberger et al. (2015) was adjusted to achieve the best results on specified validation data. Firstly, an additional filter resolution level (16 x 16 pixels) was incorporated as this was found to better capture the bone profiles occupying a large proportion of the X-ray images. The number of filter channels used in each layer were also adjusted to those described in Figure 47 to reach a compromise between model training time and segmentation accuracy. Further detail on the structure of CNN models and how they work is provided in Chapter 1.3.

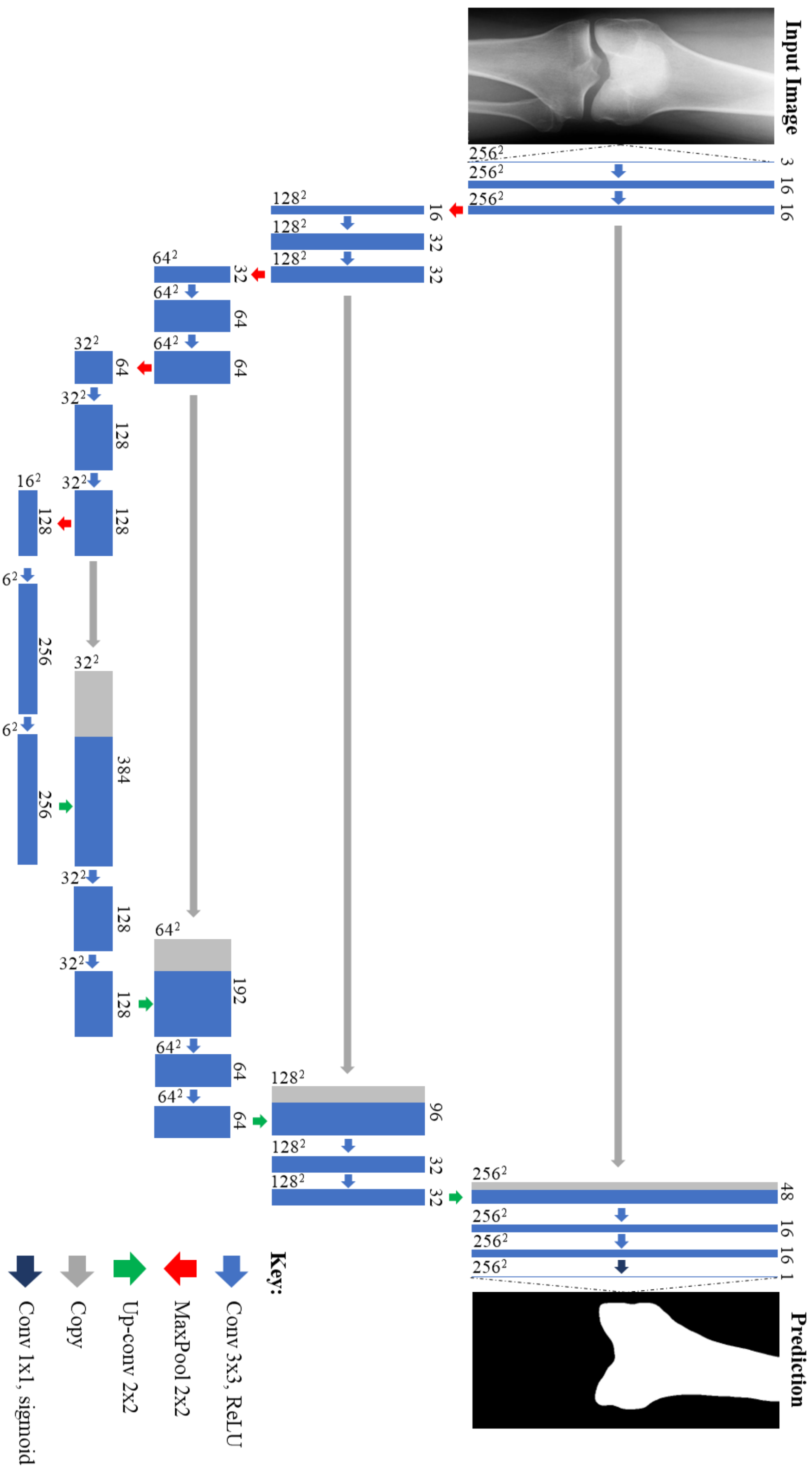

Figure 47: Architecture of U-net CNN image segmentation models used within the X-ray based implant shape customisation pipeline © (Burge et al., 2022c)

X-ray image/mask training pairs were developed from 176 images taken from the OAI dataset and used with the hyperparameters and optimiser detailed in Chapter 3.4 to train each model. 20 of the pairs (~10%) were reserved for validation which were separate to those used to test the full pipeline. It is noted that to build well generalised CNN models, capable of accurately segmenting specific bones in any inputted X-ray, potentially thousands of varied training images would be required (Liu et al., 2017). Due to the lack of suitable data in the OAI dataset to train segmentation models for the lateral X-ray projection, it was deemed acceptable in the proof-of-concept pipeline to mitigate this by adjusting the contrast and brightness settings of inputted X-ray images to improve compatibility with the models. Example results from the four segmentation models used within the pipeline are shown in Figure 48.

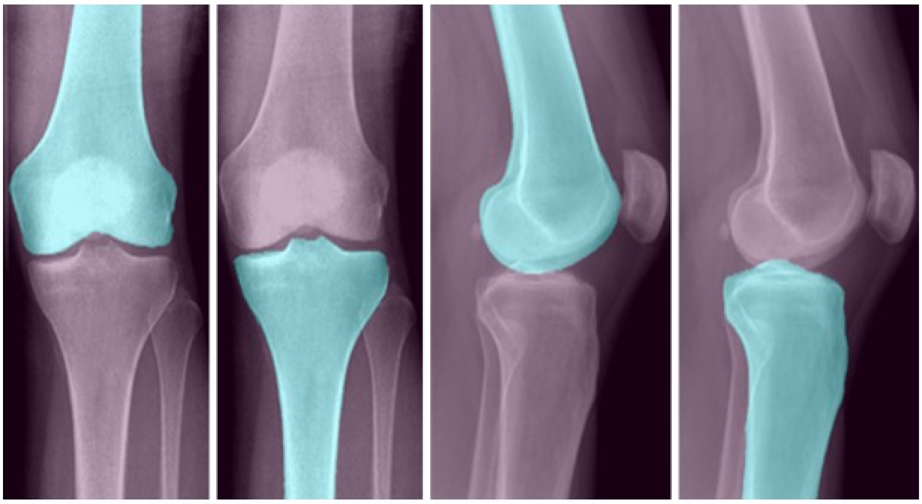

Figure 48: Bone segmentation (segmented areas shown in blue) © (Burge et al., 2022b)

For the segmentation models to capture accurate profiles of the femur and tibia bone geometries, and for the subsequent pipeline stages to run correctly, the inputted X-rays needed a consistent anatomical alignment. Specifically, the AP X-ray needed to be captured straight on with both the medial and lateral condyles pointing forward. In the lateral projection, the posterior surfaces of the femur condyles needed to be aligned flush. At least 10 cm of both femur and tibia shafts were required to be visible and the brightness and contrast needed to allow for clear outlines of the bones, as exemplified in Figure 48.

To minimise magnification errors and facilitate true reflections of patients' anatomical dimensions, inputted X-rays needed to be calibrated. Various methods have been proposed in the literature to scale X-ray images, such as including reference objects of known sizes within the X-ray frame (Wimsey et al., 2006) (Schumann et al., 2014). No calibration objects were included in the OAI X-rays. Therefore, to ensure consistency between imaging mediums, test subjects' X-rays images were scaled to match dimensions taken from their corresponding MRI scans as closely as possible. To facilitate this, a consistent set of measurements were taken of subjects' anatomies, including the maximum femur and tibia condyle widths in the AP view, the depth of the condyles in the lateral, and shaft widths in both views. To obtain the measurements, the 'Ruler' tool within 3D Slicer was used to manually select the relevant positions on both image mediums and output the linear distances as illustrated in Figure 49. Means of the scaling factors (calculated using Equation 7) were then used to resize each X-ray image (maintaining a consistent aspect ratio) to calibrate and align with the MRI data.

A) B)

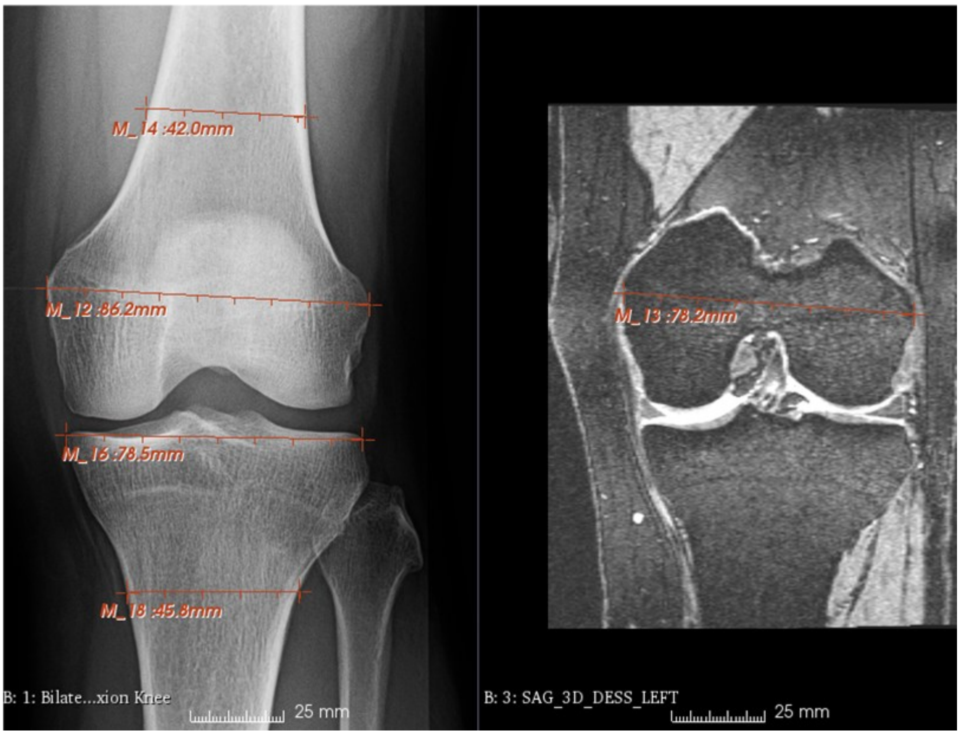

Figure 49: A) Various measurements taken from an AP X-ray, B) Maximum femur condyle width taken from an MRI scan

Within the pipeline, horizontal transforms were performed automatically for subjects' inputted X-rays if the right knee was specified to ensure compatibility with the workflow. The segmentation models described above were then applied to the relevant X-ray images to isolate the correct bone geometries (Figure 48). A Canny edge detector and cleaning algorithm (as detailed in Chapter 3.5) were then used to capture the contours of the femur and tibia bones in both projections. Lastly, the contours were separated, converted to Cartesian point coordinates, and arranged in sequential order as demonstrated in Figure 50.

Figure 50: Bone contours extracted from an AP X-ray post segmentation, edge detection and cleaning with red arrows showing direction of ordered points

5.2.3. Create 3D Model Reconstructions

To account for inconsistencies in X-ray orientation, the angle of the bone shafts with respect to the Z axis of the contours, were found using reference lines created down the centre of the bone shafts (using Min and Max functions) in both the AP and lateral views (Figure 51A). The contours were then rotated so that the shafts were aligned vertically (Figure 51B), and trimmed to a set height of 65 mm measured from the lowest Z value for the femur (Figure 51C) and highest for the tibia. Using a consistent height of 65 mm ensured the condylar regions were captured across all test subjects and helped when aligning the contours to SSM base shapes.

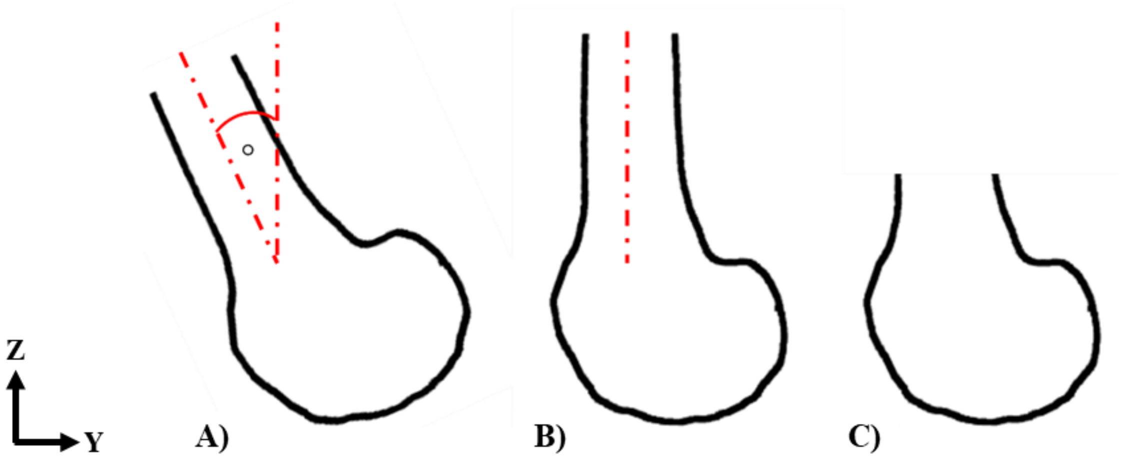

Figure 51: Adjusting the alignment of a femur contour – A) Original contour, B) Contour aligned so shaft is vertical, C) Trimmed and aligned contour © (Burge et al., 2022a)

Once aligned, reference points were found for both the AP and lateral contours. For the femur AP contour, these included the maximum and minimum X coordinates and the minimum Z point for each condyle. For the lateral femur contour, the maximum and minimum Y coordinates and the minimum Z point were located. The reference points identified for the femur are shown as crosses in Figure 52A. For the tibia, the maximum and minimum X and maximum Z coordinates were identified for the AP contour. For the lateral, the maximum and minimum Y and maximum Z points were found. The reference points identified for the tibia are also shown as crosses in Figure 52B.

Reference points were identified primarily using global Min and Max functions applied within each contour. The exceptions were to identify the lowest Z point on the medial condyle in the AP femur contour, and the front (maximum Y) point of the condyles in the lateral view. These are circled in red in Figure 52A. To identify the lowest Z point on the medial femur condyle the AP contour was initially split down the middle, using the maximum and minimum X points identified previously, allowing for the lateral side (with the lower hanging condyle) to be disregarded. The frontmost point of the femur condyles was found by ignoring the top 20 mm of the lateral contour to avoid the beginning of the shaft being unintentionally selected. Using the identified reference points, the lateral and AP contours for both bones could then be aligned perpendicularly in 3D space, as illustrated in Figure 52.

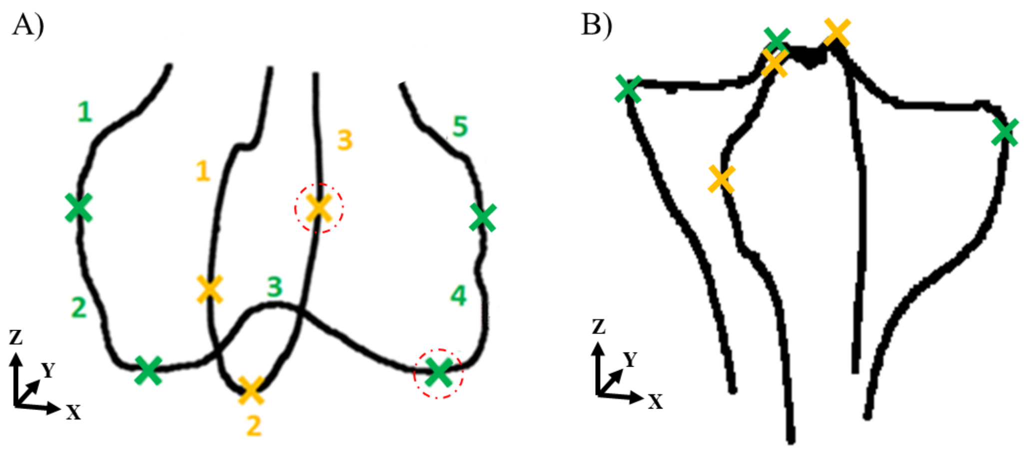

Figure 52: Aligned AP and lateral femur contours for (A) Femur and (B) Tibia. Green crosses show AP reference points, orange crosses show lateral reference points. Numbers relate to PDM contour sections on the femur © (Burge et al., 2022a)

PDMs were constructed and used in the pipeline to estimate the depth of the points in the aligned 2D contours (Figure 52). The models were built and trained as described in Chapter 3.9 using 20 reference femur and tibia bone models taken from the KISTI dataset. To be consistent with the image segmentation stage of the pipeline, a horizontal transformation was applied to right sided bones to ensure all reference models used for training had left sided geometrical forms.

For the femur, PDMs were established for separate sections of the two contours (as opposed to the full contour as shown in Figure 31), to better account for variations in anatomical form. Five separate sections were used for the AP and three for the lateral which were established by separating the contours using the previously detailed reference points. The resulting sections are labelled numerically in Figure 52A. It should be noted that for section 2 of the lateral contour, the region was defined as the curve between the maximum and minimum Y reference points and was not subdivided by the minimum Z reference point. This was because the location of the minimum Z reference point was found to vary largely between the training models and superior results were obtained by treating this region as a singular section.

For the AP sections, the lateral maximum femur condyle depth was used as the reference width measurement when calculating depth coefficients as described in Equation 3. 75 evenly spaced depth coefficients were calculated along sections 1 and 5, whilst 50 were calculated for the shorter sections 2, 3 and 4 to achieve ample coverage of the geometry. For the lateral sections, the AP maximum femur condyle width was used as the reference width measurement. Here, 75 depth coefficients were calculated along sections 1 and 2, whilst 50 were calculated for section 3. Figure 53 exemplifies the PDM analysis for section 1 of the lateral femur contour (following the process detailed in Chapter 3.9).

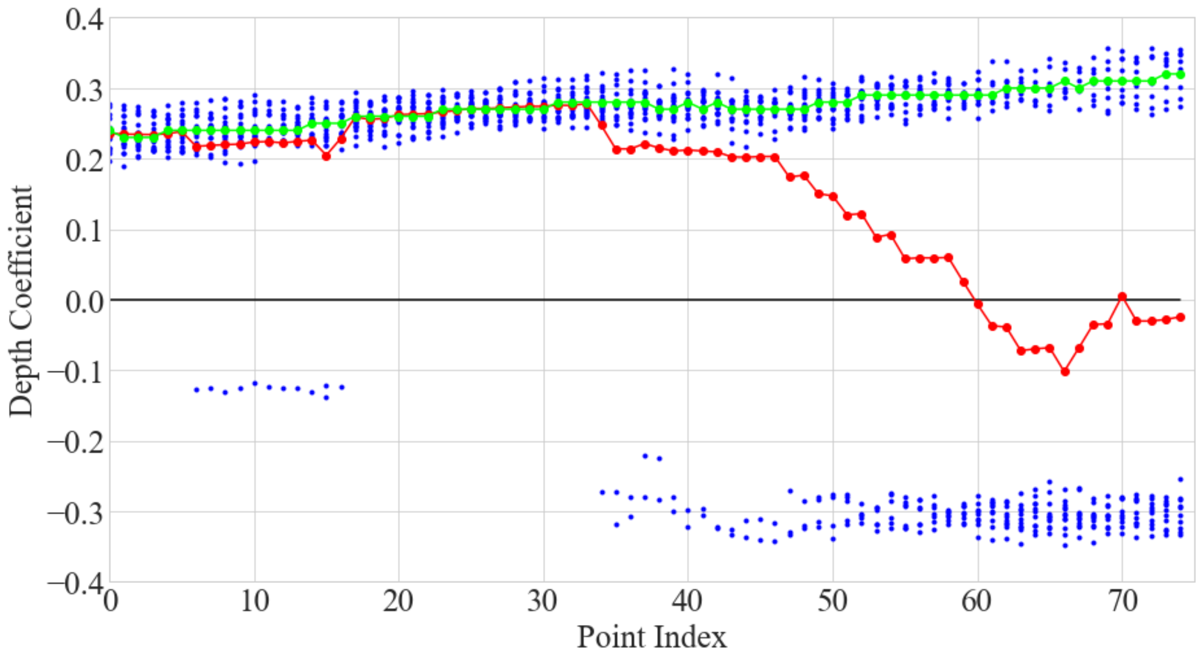

Figure 53: Example of lateral femur contour section 1 PDM analysis (blue points – depth coefficients, red – mean of coefficients, green – adjusted mean) © (Burge et al., 2022a)

The latter half of section 1 (shown in Figure 53 from approximately point index 35) is approaching the transition point where the outline of the femur in the lateral projection shifted abruptly between the medial and lateral condyles. This is demonstrated in Figure 54 and can be seen in the lateral X-rays in Figure 48 where the condyles are overlapping. The abrupt shift occurred at subtly different points across the reference models due to differences in alignment and anatomical form. This resulted in two clusters of depth coefficients calculated either side of the midpoint in Figure 53. Simply using the mean during this region would not have been useful so the values were manually refined to exclude coefficients below 0. This resulted in only the side of the transition point with the majority of points being included in the adjusted mean calculation. In the adjoining section (section 2), the points were refined to exclude coefficients above 0, resulting in a clean transition between the two condyles at the interface of the sections (shown by the blue arrow in Figure 54). A similar analysis was completed for the other AP and lateral sections to ensure the resulting PDM coefficients worked effectively.

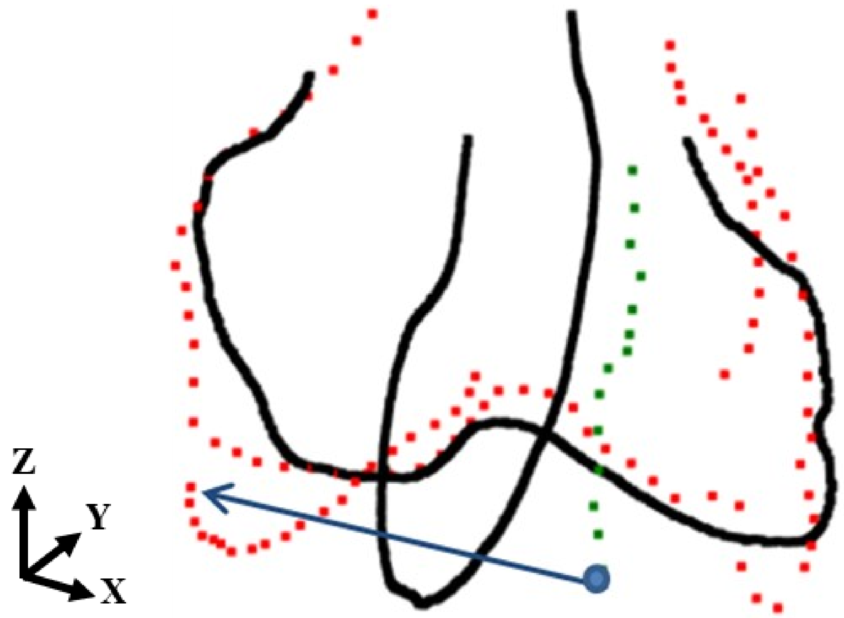

Figure 54: Points with depth (red) overlaid on 2D femur contours (black). Green points show the section analysed in Figure 53 © (Burge et al., 2022a)

For the tibia PDMs, the contours were not split into separate sections like in the femur process as identifying meaningful and consistent reference points to section the anatomy was not found to be feasible nor necessary. 300 depth coefficients were calculated for the AP and lateral tibia contours to ensure the geometry was sufficiently covered. An example of the PDM analysis performed to determine the AP tibia adjusted mean depth coefficients across the full length of the tibia AP contour can be seen in Figure 31.

Before the PDMs were applied to the aligned contour points extracted earlier in the pipeline, the contours were split into the relevant sections using the aforementioned reference points (for the femur), and downsampled evenly along their length to match the corresponding number of depth coefficients for each contour/section. Using the patient-specific reference width measurements, the depth values for each point along the respective contour sections were then calculated using Equation 4. This allowed the aligned 2D contours to be transformed into sparse 3D point clouds for the femur and tibia bones, as demonstrated by the red and green points in Figure 54. These could then be aligned to SSM base shapes using a ridged ICP method (detailed in Chapter 3.7).

100 femur and tibia 3D models (with left sided geometrical forms) were utilised from the KISTI dataset to build SSM models to be used within the pipeline (following the process described in Chapter 3.8). Like for the PDM reference models, both left and right sided bones were used for training after horizontal transformations had been applied to the latter. Two SSMs were built for the tibia – a nominal utilising unscaled models, and another using models scaled down by multiplying the vertex array of the models by 0.93 (resulting in a 7% reduction in global size). This was found to improve registration of the point clouds to the SSM base shapes across the full array of subject sizes after alignment issues were identified with smaller subjects when a single SSM base shape size was used. Multiple SSM sizes were not found to be necessary for the femur SSM. Selection of which tibia SSM to employ was achieved using a threshold value of 75 mm for the maximum width of the tibia condylar region (calculated using the femur AP reference points shown in Figure 52B). For condyle widths < 75 mm, the scaled/smaller SSM was selected. For widths ≥ 75 mm, the nominal SSM was selected. A threshold value of 75 mm

was chosen after an assessment of the condylar maximum width in the AP view for the 100 bone models used to train the SSMs determined the mean to be 74.8 mm (the range is illustrated as a box plot in Figure 55).

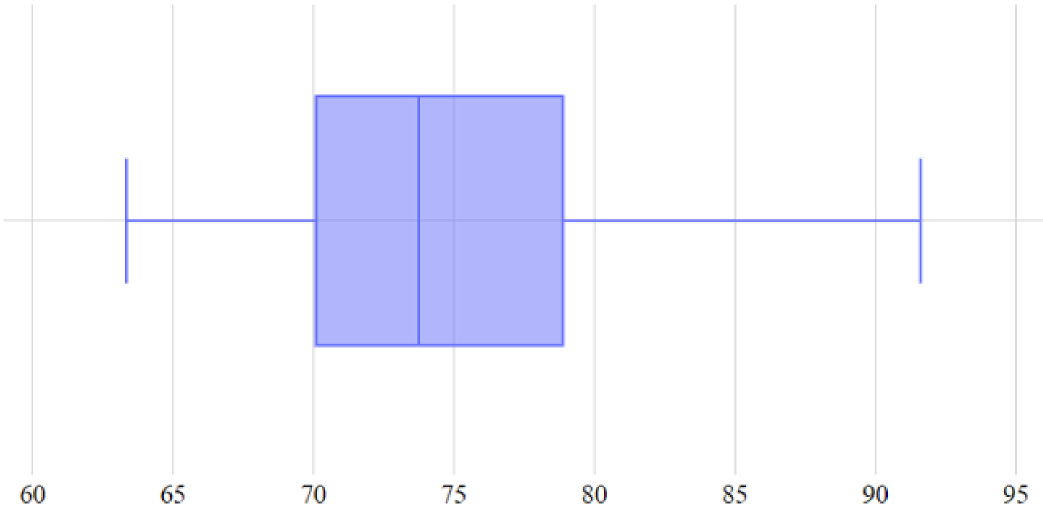

Figure 55: Range of tibia condyle max AP widths (mm) © (Burge et al., 2022b)

Once the appropriate SSM base shapes were selected, and the sparse point clouds (generated by the PDMs) were fitted via the rigid ICP method (Chapter 3.7), the SSMs were then morphed to best fit the reference point clouds following the process described in Chapter 3.8. The number of principal components used was limited to two for both bones and the shape of the SSM base models were smoothed and 'idealised'. This approach enabled the global size and shape of the anatomy to be captured, whilst imperfections such as holes and osteophytes were disregarded. This was important as replicating the damaged anatomy of an arthritic patient too closely would lead to implants with poor bearing surfaces and suboptimal biomechanical functionally. The effect of using more or fewer principal components, as well as training the PDMs and SSMs with differing numbers of reference models, was evaluated (detailed in Section 5.3.1). After the SSM fitting process was complete, 3D model reconstructions of subjects' femur and tibia bones (with left sided geometry) were outputted from the pipeline.

5.2.4. Generate Custom Implant Designs

After creating 3D model reconstructions, various additional information was exported from the pipeline to enable the automatic implant design process. Firstly, .csv files were outputted containing information such as subject ID, knee side, anatomical measurements, and the identified reference points. Secondly, further .csv files were created containing 2D coordinates constituting profiles of the femur condyles from the AP view, and describing an axial cross-section of the tibia at the point where the tibia plate was intended to interface with the bone after resection (explained further in the following sections). Then, using this information in addition to the 3D model reconstructions of the femur and tibia (in the form of .stl mesh files), various types and styles of knee replacement implants were produced using the FreeCAD API (detailed in Chapter 3.10).

5.2.4.1. Total Knee Replacement Implant Generation

The same generic TKR femur component design as used in Chapter 4 (shown in Figure 34) was adopted as a proof-of-concept. To customise the component for each subject, firstly, their (left sided) 3D surface model reconstructions were imported into FreeCAD and converted into solid bodies (Figure 56A). Predefined operations in both the AP and ML orientations were then applied to cut the condyles to the required implant shape, as illustrated in Figure 56B and C respectively. Finally, features such as fixation pins were extruded, and fillets/chamfers added to form the final component shape (Figure 56D).

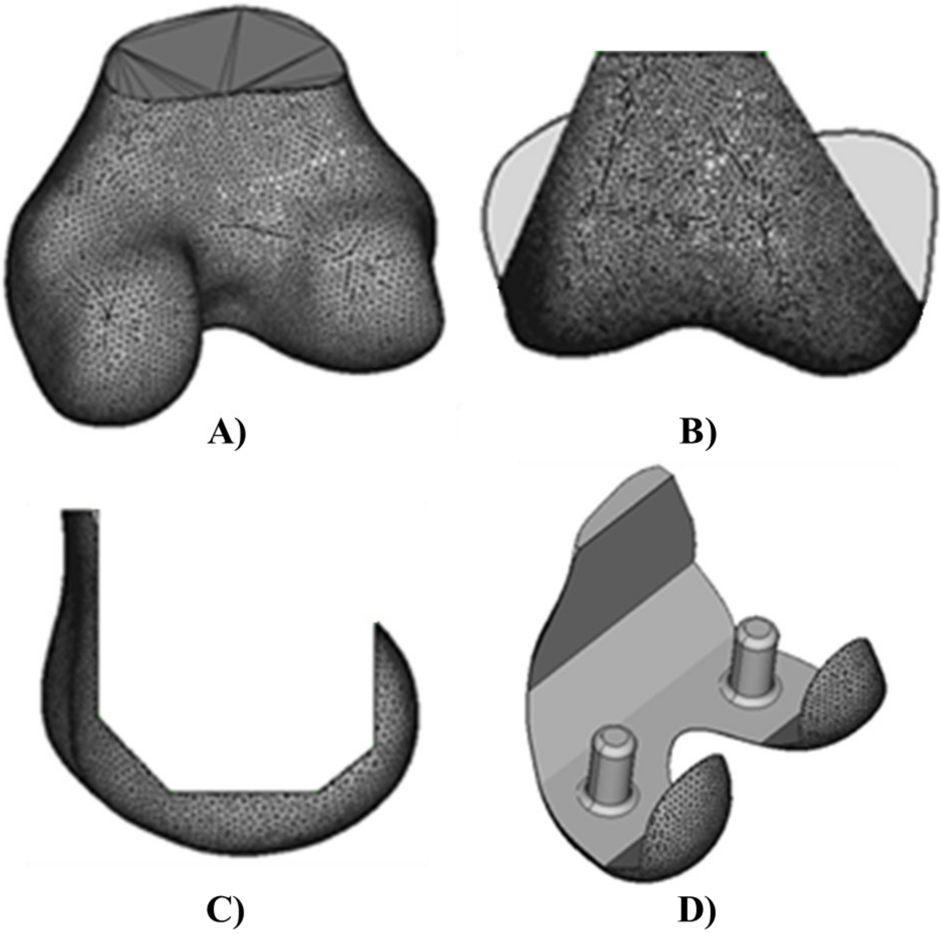

Figure 56: Automatic custom TKR femur component design process © (Burge et al., 2023b)

To design custom TKR tibia plates, using the same approach described previously in Chapter 4.2.2, a 2D cross-section was taken 2 mm below the widest point of the medial condyle on each subject's 3D model reconstructions from a plane created parallel with the surface of the tibia plateau (Figure 57A). The profile, imported into FreeCAD as a series of point coordinates saved in a .csv file, was converted to a spline sketch and extruded by a thickness of 5 mm to form the base shape of the tibia plate component (Figure 57B). Features were then cut for interfacing with a polyethylene insert and at the posterior of the plate (Figure 57C). Lastly, a fixation pin was extruded on the underside of the tray, and fillets/chamfers were added to form the final component shape (Figure 57D).

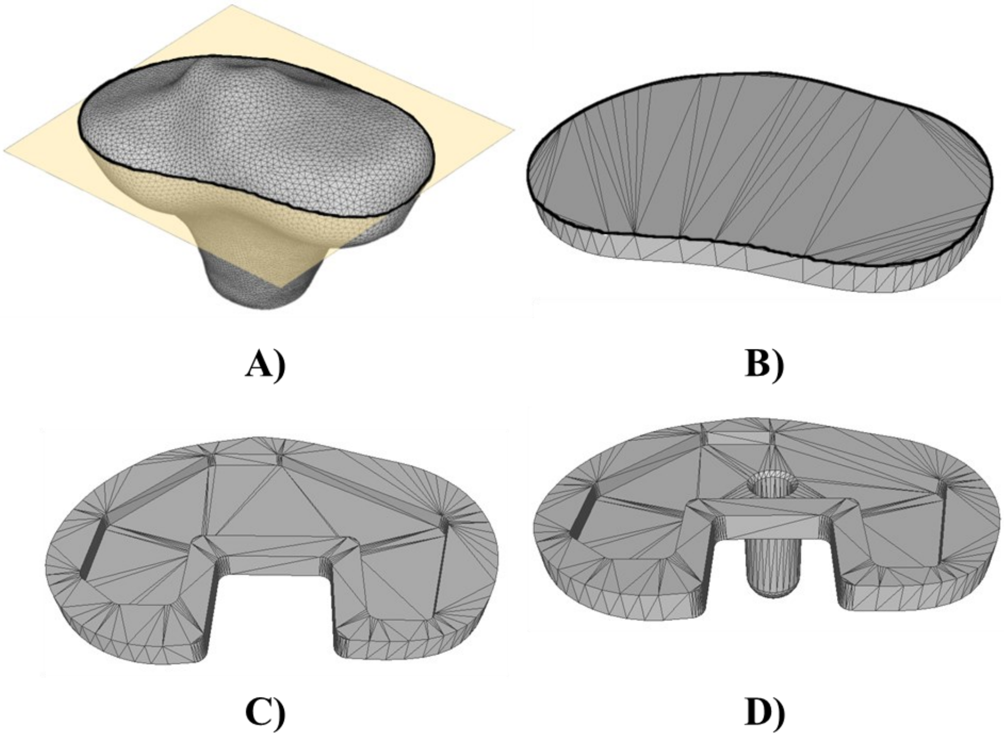

Figure 57: Automatic custom TKR tibia plate design process © (Burge et al., 2023b)

To design polyethylene insert components, firstly, the same 2D profile used for the subject's tibia plate was used to form the base of the insert by extruding the spline sketch by 30 mm (Figure 58A). A 2D profile of the condylar region of the reconstructed femur model in the AP projection (outputted by the pipeline) was obtained using the DRR approach (detailed in Chapter 3.6). This was then imported into FreeCAD as a series of point coordinates from a .csv file outputted by the pipeline and converted into a spline sketch (Figure 58B). The sketch was then used to cut through the full thickness of the extruded tibia profile to create the negative of the femur component and provide a matching bearing surface (Figure 58C). The positioning of the femur condyle sketch in the XZ plane (perpendicular to the extruded tibia profile) was determined using reference points extracted from the pipeline. This ensured correct spacing and alignment between subjects' femur and tibia bones was achieved. Finally, the positive of the connection feature included on the tibia plate (shown in Figure 57D), was then extruded from the bottom side of the insert (Figure 58D). This allowed for the two components to effectively interface when assembled.

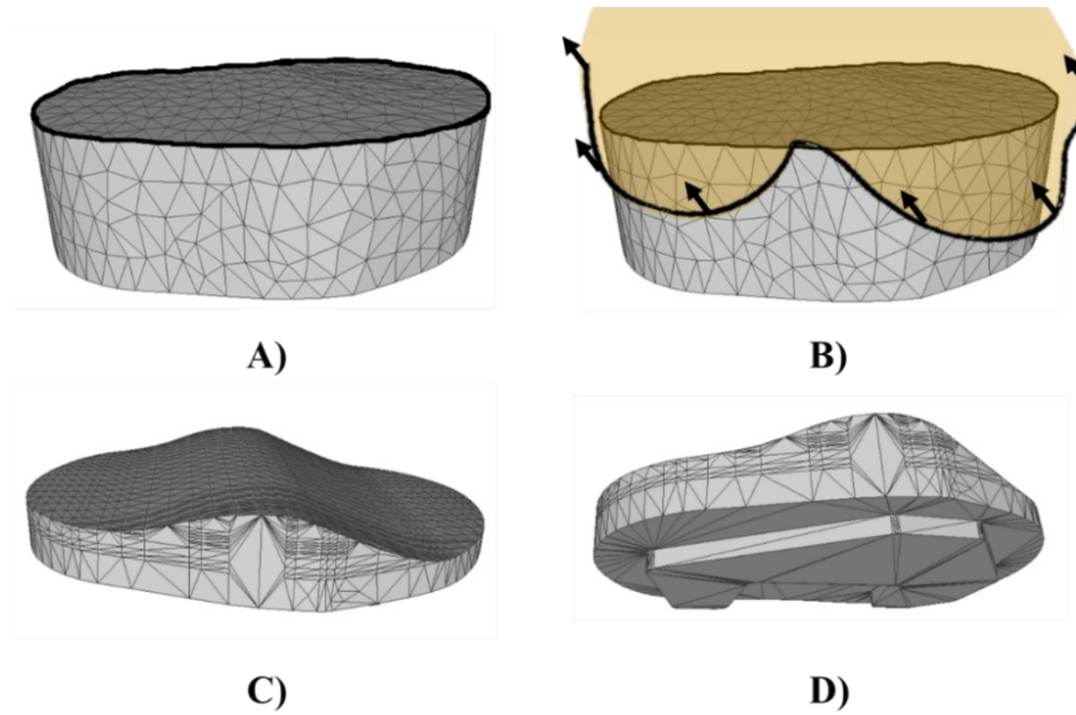

Figure 58: Automatic custom TKR polyethylene insert design process

For the automated component design processes to work for differing subject anatomical sizes and shapes, the dimensions used for the CAD operations were parametrically adjusted using information extracted by the pipeline. Scaling factors, calculated using Equation 7, were determined using subjects' maximum condylar AP and ML measurements, relative to nominal values taken when completing the process manually with a reference subject. These were then applied to the relevant dimensions of the CAD operations to tailor designs for individuals.

Component designs were created for left knee geometry to be consistent with the outputs from the pipeline. If the input X-ray images were specified to be of right sided knees, a horizontal transformation was performed within FreeCAD to invert the implant design about the sagittal plane. After the design process was complete, the component geometries were exported from FreeCAD as .stl meshes to be compatible with fabrication via AM (illustrated in Figure 59). For the fit of the resulting components to be assessed, femur components were also outputted without pins, nor fillets/chamfers as separate .stl files, along with the 2D profiles used to create the tibia plates in the form of point coordinates (saved as .csv files).

5.2.4.2. Generation of Other Implant Types and Design Variations

Pipeline outputs could also be used to facilitate variations on the generic TKR implant design by modifying the FreeCAD API scripts. Figure 59 illustrates two different TKR design variants: A) shows an implant with a polyethylene insert designed with flat edges on the medial and lateral sides whilst B) has curved edges which closely follow the condyles of the femur component. Figure 59C illustrates an example where scripts were written to use the pipeline outputs to produce uni-condylar implants. Numerous other design variations, such as posterior-stabilised or cruciate-retaining, mobile-bearing or fixed-bearing, as well as specific manufacturer designs, could also be incorporated into the FreeCAD API scripts.

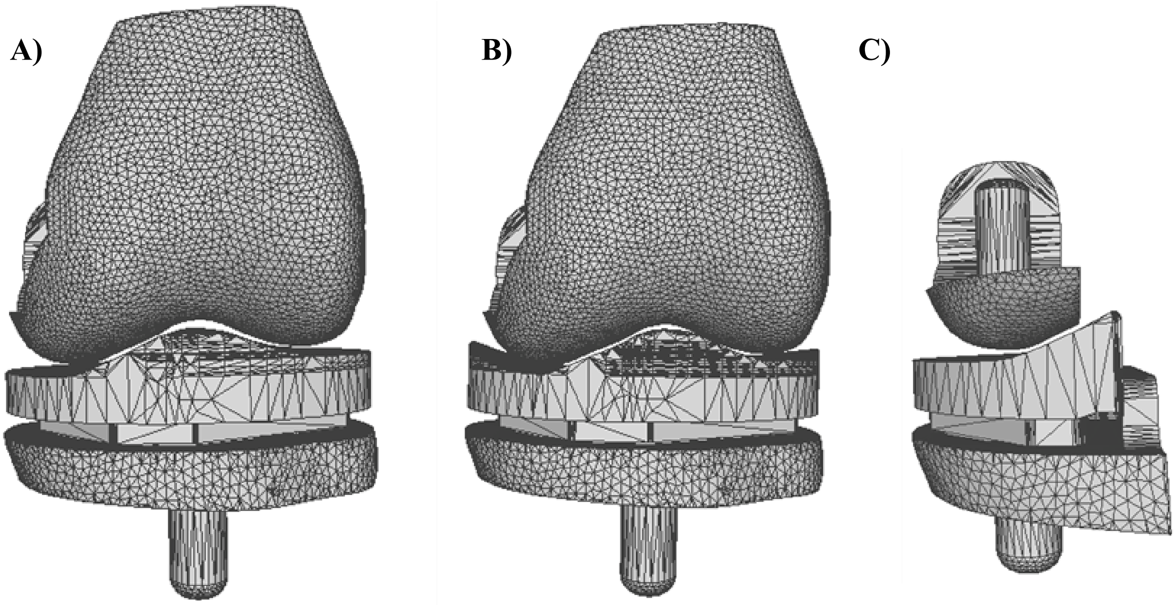

Figure 59: A) TKR implant design with flat edge insert, B) TKR implant design with curved edge insert, C) Uni-condylar implant design © (Burge et al., 2022a)

5.3. Pipeline Test Results and Discussion

In this section, how the parameters of the X-ray based implant shape customisation pipeline were optimised is described, an analysis of initial performance results obtained is outlined, and the necessary computational requirements to run the workflow are detailed.

5.3.1. Pipeline Parameter Optimisation

Before testing the pipeline on the 78 OAI subjects reserved for testing, a subset of 20 were sampled randomly and used to optimise various pipeline parameters. Parameters included the number of principal components used in the SSM models, as well as the number of reference models used to train the PDMs and SSMs. The effect of adjusting these settings was evaluated independently whilst the other highlighted parameters were kept constant. To assess performance, the mean reconstruction to ground truth RMSE (detailed in Chapter 3.11.1) across the 20 test subjects was utilised.

Figure 60 shows the mean femur and tibia results from the 20 test subjects when the pipeline was run with between one to five SSM principal components. For both the femur and tibia, the best results were recorded when using two. After this point errors started to increase rapidly. This was likely because the higher level modes of operation would require more geometrical information to drive more subtle geometrical adjustments than could be obtained from the sparse point clouds. Consequentially, over fitting was likely occurring above this number. Two principal components were therefore selected for both pipeline SSMs to maximise reconstruction accuracy and facilitate optimal implant bearing surfaces.

Figure 61 illustrates the mean femur and tibia results from the 20 test subjects when the pipeline was run with PDMs trained with between 2 to 20 3D reference models. The curves show that by increasing the number of training models, only marginal improvements were made, and by 20 test subjects, the curves had plateaued. PDMs trained with 20 reference models were therefore used in the pipeline.

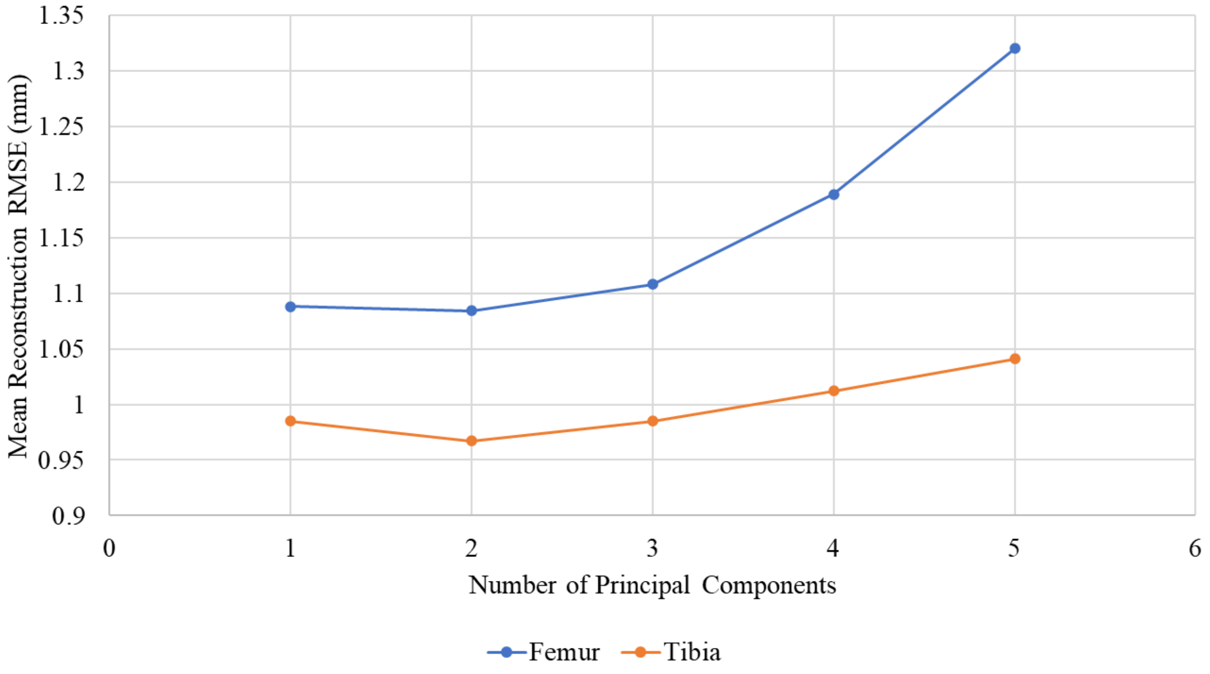

Figure 60: Impact of varying the number of X-ray based implant shape customisation pipeline SSM principal components

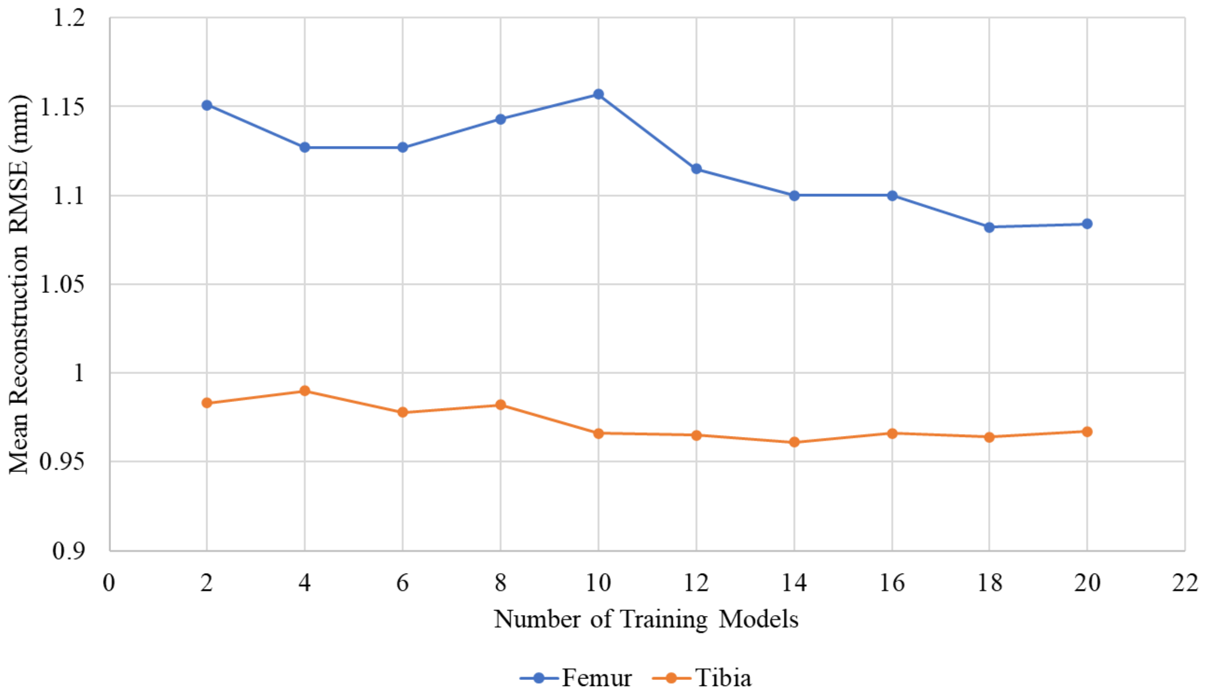

Figure 61: Impact of varying the number of 3D models used to train the X-ray based implant shape customisation pipeline PDMs

Lastly, Figure 62 shows the mean femur and tibia results from the 20 test subjects when the pipeline was run with SSMs trained with between 10 to 100 3D bone models. Here, the performance of the pipeline continued to improve as more training models were used, particularly for the femur SSM. Despite this, the number of training models used for the pipeline SSMs was capped at 100 to allow a sufficient number of independent KISTI 3D models to be used for training the PDMs and to be used as test subjects in subsequent analyses.

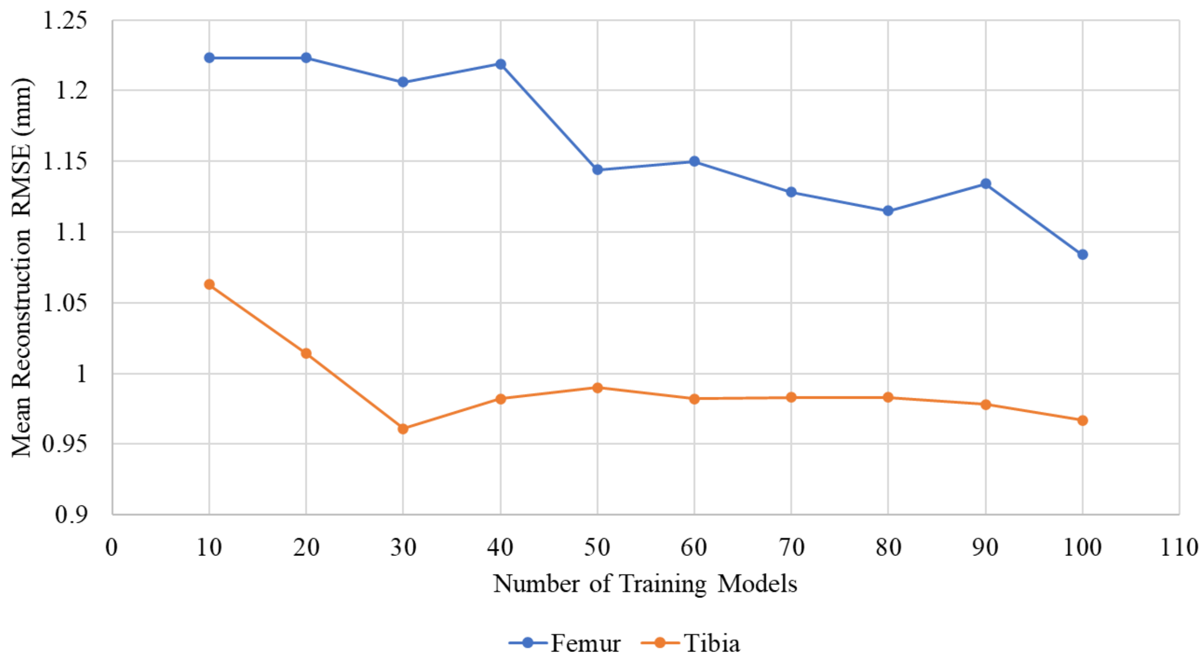

Figure 62: Impact of varying the number of 3D models used to train the X-ray based implant shape customisation pipeline SSMs

5.3.2. Pipeline Performance Results Analysis

After setting the pipeline parameters (detailed in the previous section), the full X-ray to custom shape implant pipeline was tested on the designated 78 OAI test subjects. Before the fit metrics were calculated in the femur analysis, the 3D reconstructed model and component surfaces (without fixation pins and chamfers/fillets) were fitted to the relevant subjects' ground truth 3D models utilising rigid ICP transforms (Chapter 3.7). For the tibia reconstructed model analysis, RMSE was calculated between the 3D surfaces of the reconstructed model and the subjects' ground truth in the same way as for the femur. The tibia plate fit however was evaluated in 2D using the same method as adapted in Chapter 4.2.2. Polyethylene insert components were not assessed in the fit analysis as they do not interface with the bone.

Table 1 and Table 2 provide an overview of the test subjects' demographics and pipeline performance across the model reconstruction and component fit metrics for the femur and tibia respectively. The results were not separated out based on ethnicity since all but five of the test subjects were classed as 'White'. In the following tables 'SD' refers to Standard Deviation.

Table 1: Summary of X-ray based implant shape customisation pipeline femur results

	Total, (%)	*Mean reconstruction RMSE (mm), (SD)*	*Mean component RMSE (mm), (SD)*	*Component maximum OUH ≥ 3 mm, (%)*
Overall	**78**	**1.09 (0.18)**	**1.01 (0.17)**	**14 (18.0)**
Sex				
Female	45 (57.7)	1.05 (0.13)	0.96 (0.14)	2 (4.4)
Male	33 (42.3)	1.14 (0.21)	1.08 (0.18)	12 (36.4)
Knee				
Left	40 (51.3)	1.10 (0.15)	1.02 (0.15)	6 (15.0)
Right	38 (48.7)	1.07 (0.20)	1.00 (0.18)	8 (21.1)

Table 2: Summary of X-ray based implant shape customisation pipeline tibia results

	Total, (%)	*Mean reconstruction RMSE (mm), (SD)*	*Mean component RMSE (mm), (SD)*	*Component maximum OUH ≥ 3 mm, (%)*
Overall	**78**	**0.98 (0.15)**	**0.96 (0.29)**	**7 (9.0)**
Sex				
Female	45 (57.7)	0.95 (0.14)	0.88 (0.26)	1 (2.2)
Male	33 (42.3)	1.02 (0.16)	1.07 (0.29)	6 (18.2)
Knee				
Left	40 (51.3)	0.97 (0.13)	1.00 (0.29)	4 (10.0)
Right	38 (48.7)	0.99 (0.17)	0.92 (0.28)	3 (7.9)

In terms of bone reconstruction, the pipeline was found to be able to create predictions of patient anatomy with a consistently high accuracy of approximately 1 mm RMSE. This was comparable with results previously reported in the literature for manual processes (Zhu & Li, 2011) (Tsai et al., 2015). In terms of generating custom implant components, significantly better results than generally reported for OTS, sized components (Mahoney & Kinsey, 2010) (Wernecke et al., 2012) (Schroeder & Martin, 2019) were demonstrated feasible. However, a substantial improvement was not obtained on that calculated theoretically possible in terms of the proportion of subjects with maximum OUH ≥ 3 mm if an optimised set of OTS sizes were used (based on the analysis completed in Chapter 4.3).

Lower errors across the three performance metrics were obtained for the tibia compared to the femur. These differences were calculated to be statistically significant for the reconstruction RMSE and component maximum OUH results. This observation was not surprising due to the disparity in bone and component morphological complexity, particularly around the insides of the femur condyles where the largest levels of OUH were generally identified. Females were found to perform better compared to males across all fit metrics with the differences calculated to be statistically significant for all except the tibia reconstruction RMSE which had a p value of 0.08. As expected, due to the anatomical symmetry, no statistically significant differences between the performance of left and right knees were found for any of the fit metrics.

Figure 63 shows a comparative box plot of the results and highlights numerous outliers where poor fits were recorded, especially for the femur. In these cases, it was found that the inputted X-rays were typically (visually) less well aligned compared to those that achieved the best reconstruction accuracies and implant fits. Consequently, it was determined that the alignment of the anatomy in the inputted X-rays was likely critical and, since it was only retrospectively controlled using a qualitative method (visually assessing anatomical alignment and image quality factors such as contrast), this likely influenced the results outlined in this analysis.

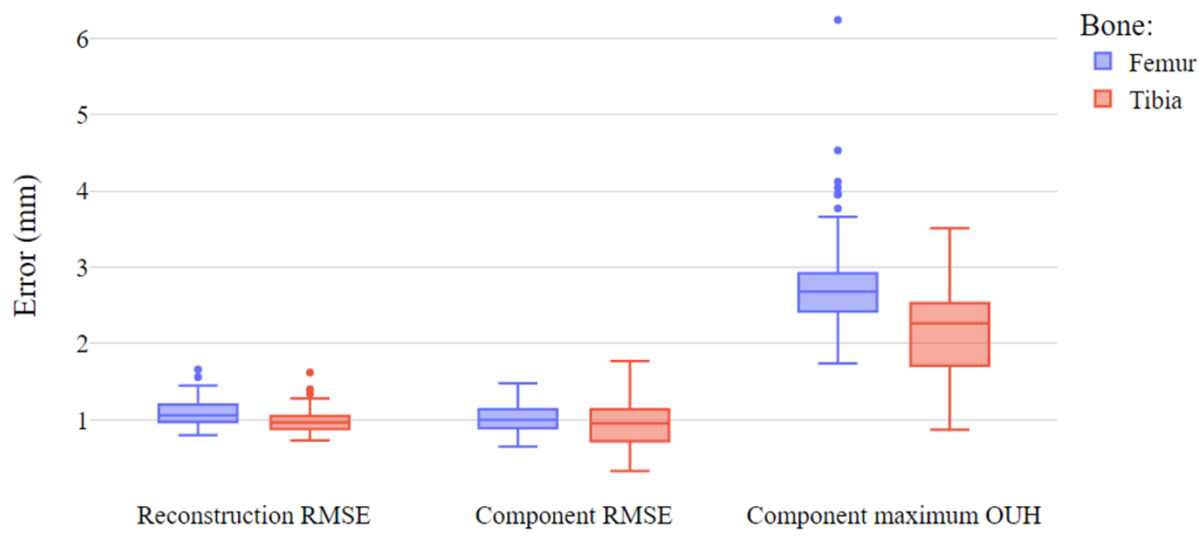

Figure 63: Box plot of X-ray based implant shape customisation pipeline results for the femur and tibia © (Burge et al., 2022b)

5.3.3. Pipeline Computational Requirements

In terms of computation time, the pipeline consistently took less than five minutes to generate custom TKR implant designs from inputted X-ray images when run on a personal laptop computer (2.38 GHz AMD Ryzen 5 4500U CPU with 6 cores/8 GB memory). This was considerably faster than a manual based approach which could easily take hours or days of an engineer's time. Therefore, a significant amount of the 6 – 8 week lead time required for current customisation solutions (as reported by Seekingalpha.com (2019)) could be saved.

5.4. Summary

In this chapter the feasibility of creating an automated, custom knee replacement implant shape design pipeline that used two calibrated biplanar X-ray images as input was demonstrated. The pipeline produced well-fitting component designs for the 78 OAI test subjects with 82% of femur components and 91% of tibia plates resulting in maximum OUH results < 3 mm. These results were significantly better than generally reported for OTS implants, but comparable to what could theoretically be achieved in an optimised scenario. Nevertheless, the proof-of-concept pipeline demonstrated the need for trained medical and/or engineering professionals to supervise or input into the custom design process could be removed and was shown capable of producing implant models, compatible with fabrication methods such as AM (after appropriate specification of build parameters such as orientation, materials, and support structures), in approximately five minutes. Therefore, it is believed that because of the performance shown possible by the fully automated pipeline, in combination with the fact only 2D medical imaging was required, the tool could offer significant cost savings over currently available customisations options and make the technology more commercially attractive.

In the analysis, it was observed qualitatively that the alignment of inputted X-ray images was likely highly important for achieving accurate reconstructions and component fits. The effect was however not possible to confirm quantitatively since test subjects' X-rays were used retrospectively and no information indicating anatomical alignment was provided with the OAI dataset. Additional error could have also been introduced because of factors such as inaccurate X-ray scaling and/or poor quality image segmentation (because no reference objects were included in the sans and the reasonably low number of training images used respectively). Furthermore, due to the data available, the analysis completed in this chapter was performed using test subjects with limited ethnic diversity and the influence of only a few demographical attributes was possible to assess.

Chapter 6

X-ray Based Pipeline Extended Results and Sensitivity Analysis

To enable a more thorough assessment of the X-ray to custom knee replacement implant shape pipeline, the following chapter outlines a methodology which involved replacing the real X-ray input with 'synthetic' alternatives generated using the DRR method. A sensitivity analysis is also detailed which enabled the impact of anatomical alignment and dimensional calibration of input X-rays to be quantified.

Most of the contents of this chapter have been published in the following paper:

- Burge, T.A., Jeffers, J.R.T. & Myant, C.W. (2022) Performance and sensitivity analysis of an automated x-ray based total knee replacement mass-customization pipeline. *Journal of Medical Devices*. 16 (4), 1–12.

6.1. Introduction

This chapter details a thorough evaluation of the X-ray based knee replacement implant shape customisation pipeline developed in Chapter 5 to further assess its robustness and characterise its limitations. To enable this, the DRR method (outlined in Chapter 3.6) was utilised to replace the inputted real X-ray images used previously with 'synthetic' alternatives. Employing the DRR approach allowed for the possible impact of dimensional calibration, anatomical alignment, and segmentation errors, highlighted as likely affecting the X-ray based pipeline, to be eliminated. This permitted a better understanding of the true potential of the pipeline to be obtained and evaluate the robustness of the approach.

Since only 3D models were required as input for the DRR method, the pipeline could be tested using considerably more subjects from multiple datasets compared to when real X-rays were used in the previous chapter. The robustness of the pipeline across various subject sexes, knee side, ethnicities, age, height, and severity of arthritis could therefore be examined more comprehensively. Furthermore, by utilising the DRR method, dimensional scaling and anatomical alignment could be treated as input parameters and controlled precisely. This enabled a sensitivity analysis to be performed that mimicked alignment and dimensional calibration in real X-ray images. Based on this, suitable input imaging specifications for the pipeline could then be determined.

6.2. Pipeline Development and Performance/Sensitivity Analysis Methods

In this section, the development of the DRR based implant shape customisation pipeline is detailed, as well as the method used for the pipeline sensitivity analysis. Details of the subjects used to test the DRR based pipeline and facilitate the sensitivity analysis are also provided.

6.2.1. DRR Based Pipeline Development

To facilitate the extended analysis, the same method as detailed in Chapter 5.2 was utilised, except that the DRR approach (detailed in Chapter 3.6) was used with subjects' 3D bone models as inputs (instead of real X-ray images). A flow chart of the full method is provided in Figure 64 with an orange border highlighting the difference to Figure 46.

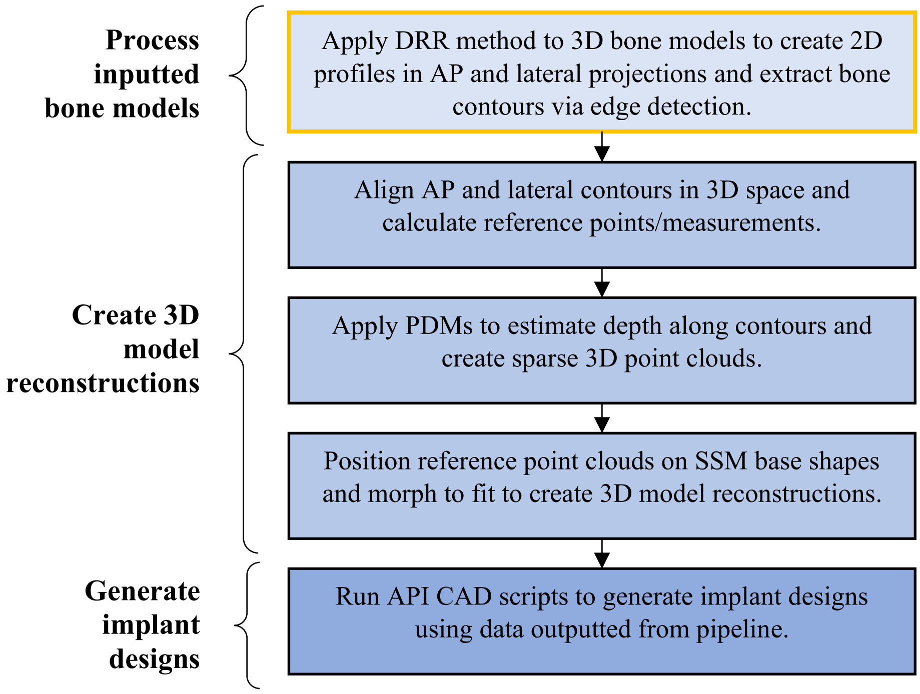

Figure 64: Key phases and workflow of the DRR based implant shape customisation pipeline

Before being inputted into the pipeline, test subject bone models were consistently aligned to reflect the necessary input X-ray requirements detailed in Chapter 5.2.2. All femur condyles and tibial plateaus were aligned parallel with the AP direction so that the bone shafts were vertical. After the pipeline had generated bone model reconstructions and custom implant designs for each test subject, these were then compared back to the respective subjects' ground truth models and the same fit metrics as detailed in Chapter 5.3.2 were calculated.

6.2.2. Pipeline Sensitivity Analysis Method

To perform the sensitivity analysis, the same workflow as detailed in Figure 64 was adopted, except that the alignment of the inputted 3D bone models and scaling of the resulting contours from the DRR process were systematically adjusted. The positioning of inputted bone models used to create the AP and lateral DRR profiles were manipulated individually to reflect the fact two separate X-rays are captured in practice and to allow the impact of variation in each projection to be evaluated independently. For the AP projection analysis, model position was rotated about the X and Z axes, whilst for the lateral projection, it was rotated about the Y and Z (according to Figure 28). Only two axial rotations were adjusted in each as the pipeline automatically accounted for rotation normal to the X-ray projection (as illustrated in Figure 51). For the AP projection, all combinations of rotations about the X and Z axes in increments of 1 degree from -30 to 30 were computed for both bones. The lateral projection was kept constant. The same was performed for the lateral about the Y and Z axes with the AP projection held constant. The rotation ranges were chosen to reflect the approximate variation in alignment observed within the OAI X-rays.

To study the impact of X-ray dimensional calibration accuracy, bone model alignment was held constant whilst the AP and lateral profiles outputted from the DRR method were gradually scaled. Scaling of width and height was completed equally to keep a consistent aspect ratio. All combinations of AP and lateral scaling factors, in increments of 0.01 from 0.85 to 1.15, were explored for both bones. The ranges for the scaling multiplication factors were selected as an exaggerated estimate for potential error in practice.

Reconstruction RMSE was used as the sole results metric in the alignment and calibration sensitivity analyses as generating custom implant components for every combination of alignments and scales (45,615 for both the femur and tibia) would have been highly computationally expensive (estimated to be approximately 4,000 hours of compute time).

6.2.3. Test Subjects

Subjects from both the OAI and KISTI datasets were utilised to test the DRR based pipeline. In some cases, the MRI data retrieved from the OAI dataset was found to include insufficient bone shaft lengths to facilitate models compatible with the pipeline, especially for the tibia. Such subjects were consequently excluded from the analysis. In total, 147 femur and 118 tibia bone models were created (using the process detailed in Chapter 3.3), and utilised as test subjects with demographical information summarised in Table 5 and Table 6. No subject data used for training was also used for testing.

The sensitivity analyses for the femur and tibia were each completed using three different subject bone models, selected to represent a broad demographic from across the OAI and KISTI datasets. The demographical information of the subjects used for the femur and tibia analyses is summarised in Table 3 and Table 4 respectively.

Table 3: Summary of femur sensitivity analysis test subject demographics

Subject	*Sex*	*Ethnicity*	*Knee side*
1	Male	Black	Left
2	Female	White	Right
3	Female	Asian	Right

Table 4: Summary of tibia sensitivity analysis test subject demographics

Subject	*Sex*	*Ethnicity*	*Knee side*
1	Male	White	Left
2	Female	Black	Left
3	Male	Asian	Right

6.3. Pipeline Performance and Sensitivity Analysis Results and Discussion

In this section the performance results obtained for the DRR based version of the implant shape customisation pipeline, as well as the sensitivity analysis, are outlined and discussed.

6.3.1. DRR Based Pipeline Performance Results

A detailed summary of the DRR pipeline results for the various datasets and test subject demographics is provided in Table 5 for the femur and Table 6 for the tibia. Figure 65 below shows a summary box plot of all the results.

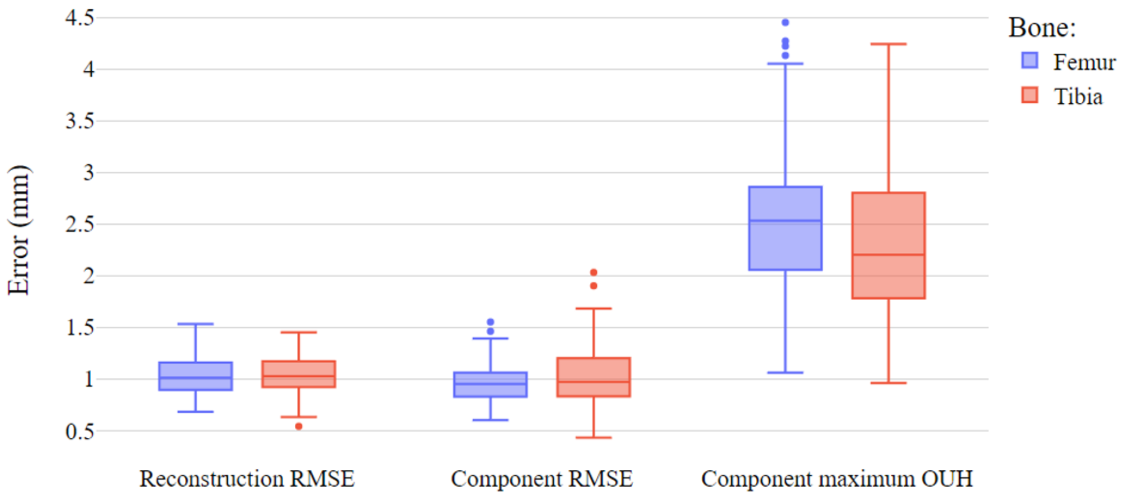

Figure 65: Box plot of DRR based implant shape customisation pipeline results for the femur and tibia © (Burge et al., 2022b)

In terms of the key clinical metric, maximum OUH, the results for both the femur and tibia improved on average compared to the previous analysis using real X-rays as input from 18% and 9% to 15% and 7.6% respectively. It is however noted that the overall mean reconstruction and component RMSE results worsened slightly for the tibia from 0.98 mm and 0.96 mm to 1.04 mm and 1.03 mm respectively. This was likely due to the larger pool of different test subjects utilised compared to in the X-ray based analysis.

Table 5: Summary of DRR based implant shape customisation pipeline femur results

	Total, (%)	*Mean reconstruction RMSE (mm), (SD)*	*Mean component RMSE (mm), (SD)*	*Component maximum OUH ≥ 3 mm, (%)*
Overall	**147**	**1.03 (0.19)**	**0.96 (0.18)**	**22 (15.0)**
Sex				
Female	82 (55.8)	1.06 (0.18)	0.96 (0.18)	10 (12.2)
Male	65 (44.2)	0.98 (0.19)	0.95 (0.18)	12 (18.5)
Knee				
Right	76 (51.7)	1.04 (0.18)	0.97 (0.17)	13 (17.1)
Left	71 (48.3)	1.02 (0.19)	0.94 (0.18)	9 (12.7)
Ethnicity				
White	74 (50.3)	1.01 (0.14)	0.96 (0.15)	12 (16.2)
Asian	53 (36.1)	1.00 (0.21)	0.92 (0.22)	5 (9.4)
Black	20 (13.6)	1.19 (0.20)	1.02 (0.14)	5 (25.0)
Dataset				
OAI	95 (64.6)	1.04 (0.17)	0.97 (0.15)	17 (17.9)
KISTI	52 (35.4)	1.00 (0.21)	0.93 (0.22)	5 (9.6)

Table 6: Summary of DRR based implant shape customisation pipeline tibia results

	Total, (%)	*Mean reconstruction RMSE (mm), (SD)*	*Mean component RMSE (mm), (SD)*	*Component maximum OUH ≥ 3 mm, (%)*
Overall	**118**	**1.04 (0.19)**	**1.03 (0.29)**	**9 (7.6)**
Sex				
Female	65 (55.1)	1.04 (0.17)	1.00 (0.27)	5 (7.7)
Male	53 (44.9)	1.04 (0.22)	1.08 (0.31)	4 (7.6)
Knee				
Right	64 (54.2)	1.05 (0.22)	1.04 (0.32)	4 (6.3)
Left	54 (45.8)	1.04 (0.17)	1.03 (0.26)	5 (9.3)
Ethnicity				
White	55 (46.6)	1.03 (0.15)	1.03 (0.25)	3 (5.5)
Asian	43 (36.4)	1.00 (0.23)	0.98 (0.29)	3 (7.0)
Black	20 (17.0)	1.15 (0.17)	1.17 (0.36)	3 (15.0)
Dataset				
OAI	76 (64.4)	1.06 (0.17)	1.07 (0.29)	6 (7.9)
KISTI	42 (35.6)	1.00 (0.23)	0.98 (0.29)	3 (7.1)

It was found that the difference between the femur and tibia performance was reduced when using the DRR method. Nevertheless, the differences in component RMSE and maximum OUH results between the two bones were still calculated to be statistically significant.

A less distinct difference between sexes was observed in the DRR results compared to those for the X-ray based pipeline. In contrast to consistently inferior male results across all metrics in the X-ray based analysis, when using the DRR approach males outperformed females in femur reconstruction and component RMSE, as well as marginally for tibia component maximum OUH. Only the difference in femur reconstruction RMSE was found to be statistically significant between the sexes. Therefore, it is likely that the observed difference linked to subject sex in the X-ray based analysis was not substantiated.

Inconsistencies in results were identified between the ethnicities evaluated. Asian subjects were found to produce the lowest errors for all metrics, except for tibia maximum OUH. White subjects followed closely with marginally worse results. Black subjects however showed distinctly poorer performance compared to White and Asian subjects across all metrics. All differences of Black subjects compared to White and Asian subjects, apart from in terms of tibia component RMSE, were found to be statistically significant. This phenomenon was likely a result of few Black subjects being used to train the pipeline. Similar observations were made by Mahfouz et al. (2012) who highlighted the importance of including a balanced and representative range of subjects when training SSMs.

The KISTI dataset produced on average lower errors across all metrics for both pipelines compared to the OAI. The differences could have been due to varying demographics between the datasets, the different imaging modalities used for the ground truth data (CT for KISTI and MRI for OAI), the fact segmentation of the two datasets was performed by different individuals, and/or because the KISTI dataset was used more heavily for training the pipeline.

The discrepancy between the datasets was however not found to be statistically significant, except for femur component maximum OUH.

To assess the influence of age and height on the results, Spearman's correlation coefficients were calculated using the method detailed in Chapter 3.12. These are detailed in Table 7 for the femur and Table 8 for the tibia. Both attributes were found to have minimal impact on the pipeline with all correlation coefficients close to 0, except for height in relation to femur reconstruction RMSE which had a coefficient of -0.5, indicating a moderate negative correlation. Despite this, the fact that the resulting femur component fits had very little correlation with height, and the same was not reflected for the tibia, suggested that the correlation was likely not representative or important.

Table 7: Spearman's coefficients for height and age relating to femur performance

	Reconstruction RMSE	*Component RMSE*	*Component max OUH*
Height	-0.50	-0.26	-0.08
Age	-0.02	-0.04	0.06

Table 8: Spearman's coefficients for height and age relating to tibia performance

	Reconstruction RMSE	*Component RMSE*	*Component max OUH*
Height	-0.09	0.16	0.31
Age	-0.14	-0.05	0

Like in the X-ray based pipeline results, no statistically significant differences between the performance of each knee side were found in the DRR analysis.

All subjects detailed in Table 5, Table 6 and Figure 65 had K&L grades of ≤ 2, indicating mild arthritis or unspecified (Kellgren & Lawrence, 1956). To assess the impact of increasing arthritis severity on performance, ten additional subjects with moderate (K&L grade 3) and ten with severe (K&L grade 4) arthritis were analysed and included in Figure 66 and Figure 67.

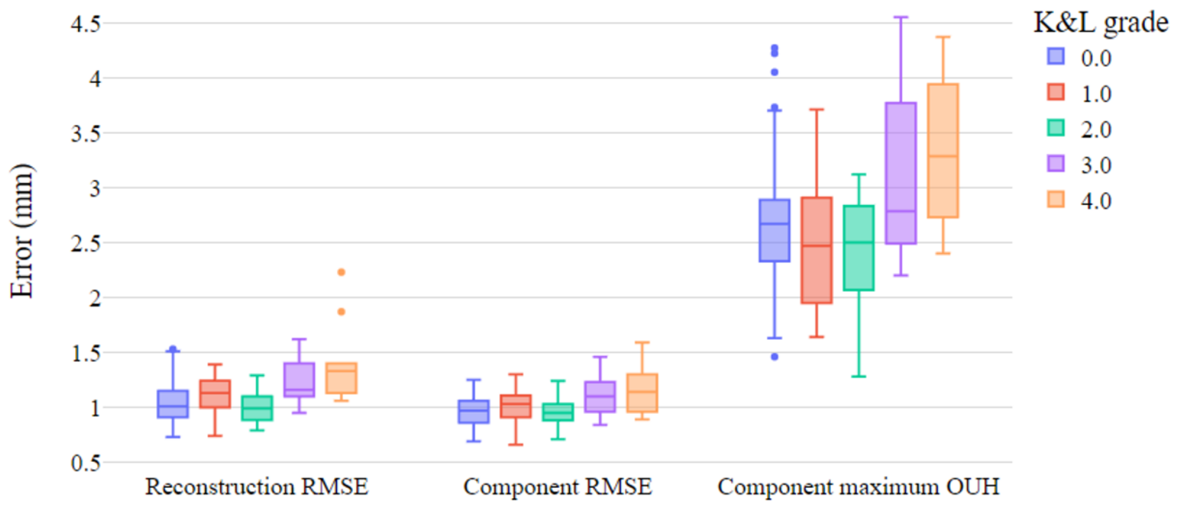

Figure 66: Box plot of femur results for different arthritis severities © (Burge et al., 2022b)

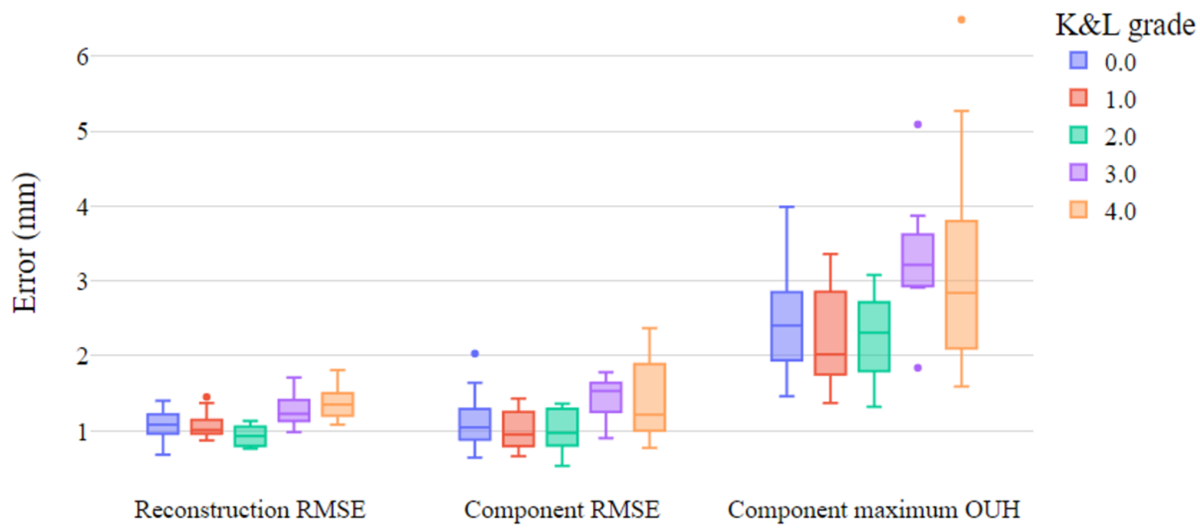

Figure 67: Box plot of tibia results for different arthritis severities © (Burge et al., 2022b)

The figures show that the pipeline worked effectively for most subjects with up to and including mild levels of arthritis (K&L grade 2). Yet, for moderate and severe arthritis (K&L grades 3 and 4), well-fitting implants were not achieved for a large proportion of subjects. For the femur results, the level of OUH ≥ 3 mm increased to 30% for grade 3 and then to 50% for grade 4. For the tibia, the proportion increased to 50% for both grades 3 and 4. It is noted that the results for grades 1 and 2 appear to perform slightly better for the tibia than those for grade 0. This is however not believed to be representative and was likely because the group sizes were unequal with grade 0 including 147/118 subjects for the femur/tibia respectively, whilst grades 1 and 2 only contained between 10 – 15 subjects each.

Due to the high level of deformity and irregular geometry observed at the moderate and severe levels of arthritis, and the dissimilarity compared to the training data, the decrease in pipeline performance with arthritis severity was expected. 3D imaging would likely be the only option to sufficiently capture such irregular bone shape. Nevertheless, as highlighted previously, perfectly replicating the morphology of damaged bones was not the objective of the pipeline and would in fact be detrimental for designing effective implant components. Therefore, the metrics utilised in this analysis, particularly component maximum OUH, are likely not reflective of true outcomes for bones with higher levels of arthritis severity. Moreover, according to Kellgren & Lawrence (1956), osteoarthritis can be determined to be present from K&L grade 2, and patients are usually deemed eligible for TKR surgery from this point onwards (Skou et al., 2018). It can therefore be concluded that the pipeline could be suitable for most arthritis sufferers who are diagnosed and undergo surgery at a sufficiently early stage.

Based on the results outlined above using the DRR approach, it is believed that, if X-ray alignment and calibration could be adequately controlled, the X-ray based pipeline would be capable of affording results superior to those determined to be theoretically possible for optimised, OTS components. Despite this, the pipeline still did not meet the exceedingly high levels of accuracy shown possible by 3D medical imaging based solutions (Ogura et al., 2019) (Arnholdt et al., 2020). To improve results further, increasing the number of X-rays used to capture more geometrical information (as demonstrated by Cerveri et al. (2017)), could be explored. However, this would incur additional imaging requirements compared to standard OTS pre-operative assessments and so was not investigated.

6.3.2. Pipeline Sensitivity Analysis Results

Figure 68 and Figure 69 outline the results of the pipeline sensitivity analysis, split into the AP alignment, lateral alignment, and X-ray scaling analyses for the femur and tibia respectively.

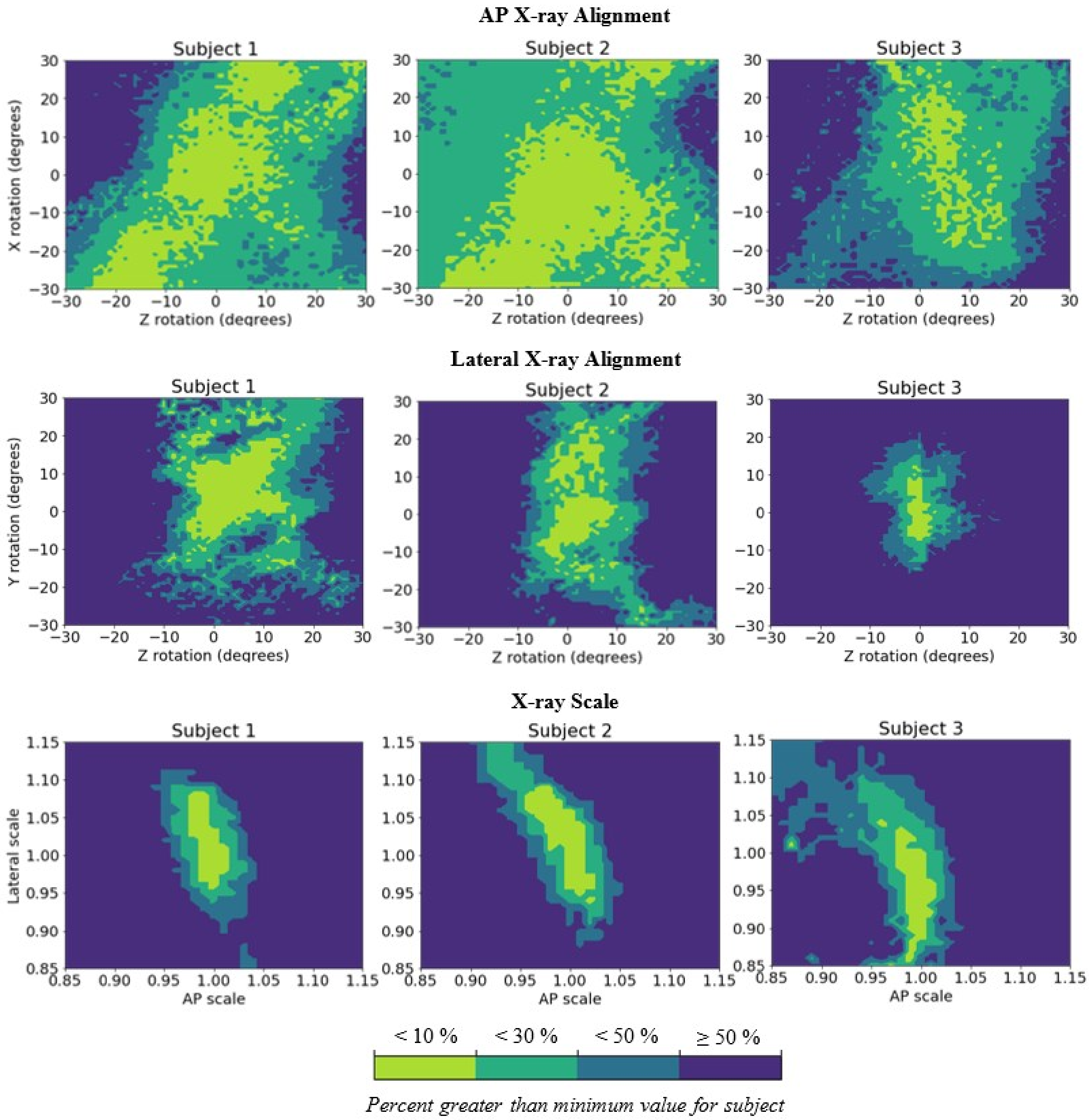

Figure 68: Femur sensitivity analysis heat maps © (Burge et al., 2022b)

The heat maps illustrate how the performance varied across the array of rotations and scaling factors investigated in terms of the percentage above each subject's lowest recorded reconstruction RMSE results. The results are shown bucketed into four levels for better clarity with < 10% indicating minimal error increase, < 30% indicating moderate error increase, < 50% indicating large error increase, and ≥ 50% indicating excessive error increase.

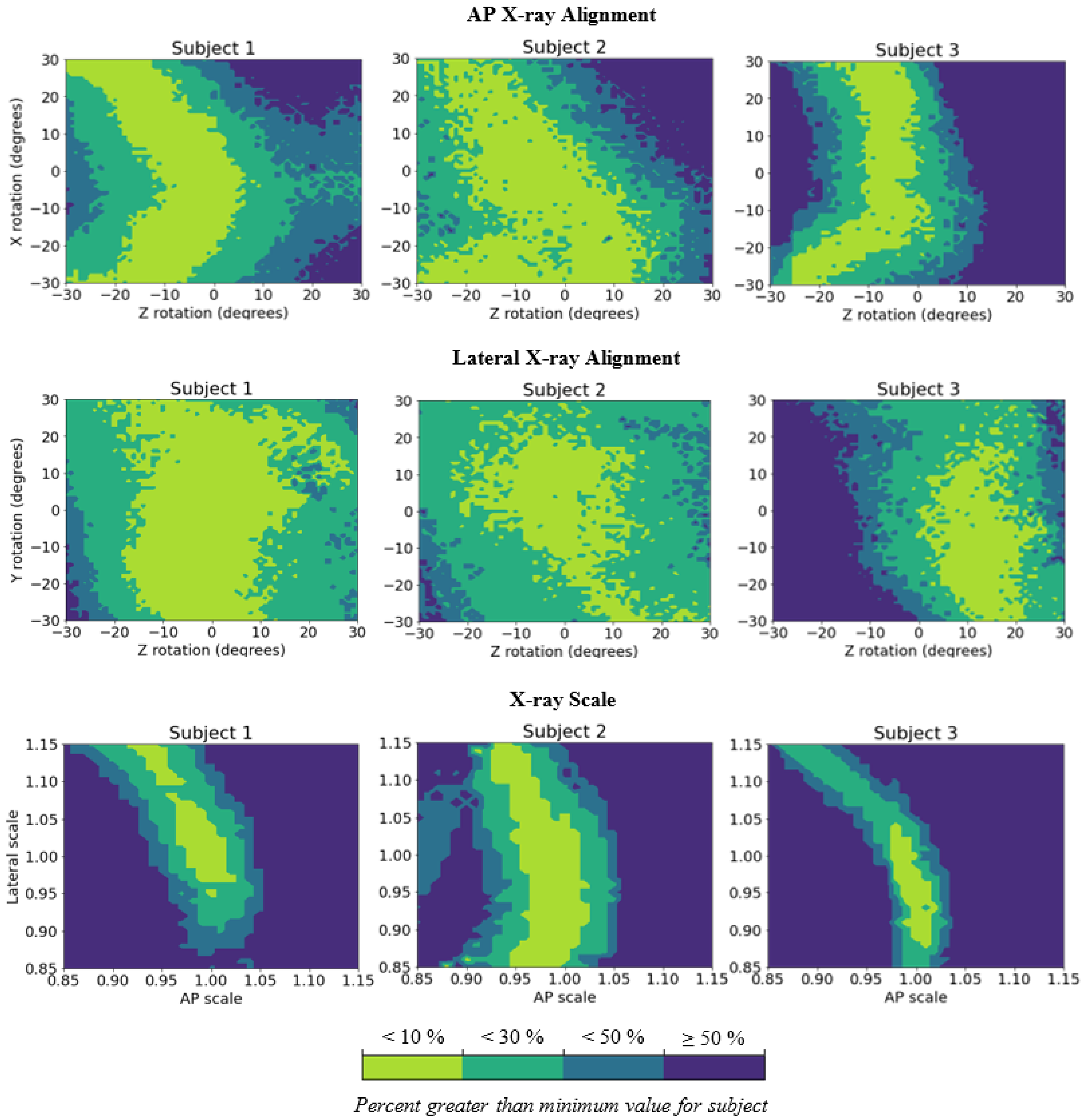

Figure 69: Tibia sensitivity analysis heat maps © (Burge et al., 2022b)

The heat maps demonstrate that the alignment of subject anatomy had a significant impact on pipeline performance. Generally, to achieve within 10% of the lowest recorded reconstruction RMSE for each subject, an alignment accuracy of approximately ± 5 – 10° was found to be required. The femur alignment, particularly in the lateral projection, was found to be considerably more sensitive than the tibia and afforded a very small window to achieve high quality results. The heightened sensitivity of the femur to rotation compared to the tibia was likely attributable to the difference in morphologies between the bones: Rotating the condyles of the distal femur bone in the lateral view was observed to cause large distortions in the resulting 2D profiles. Conversely, the proximal end of the tibia was found to be more axisymmetric and so varied less in shape and resulting pipeline performance with axial rotation.

The impact of positive and negative scaling, replicating inaccuracies in X-ray dimensional calibration, were found to be considerable for both bones. The bottom rows of Figure 68 and Figure 69 show that the level of error increased rapidly to over 10% above the minimum result for most cases with scale values of approximately ± 0.02 (2% error) in the AP projection. For the lateral projection however, a wider scaling accuracy ± 0.05 (5% error) was typically found to be needed to achieve similar outcomes.

6.4. Summary

In this chapter, a DRR method was adopted to eliminate errors stemming from poor X-ray quality and evaluate the knee replacement implant shape customisation pipeline (developed in Chapter 5) using a larger and more diverse test population. This facilitated a comprehensive understanding of the potential performance of the X-ray based pipeline, simulating a scenario where well controlled inputs were available. In terms of maximum OUH, results for both bones improved compared to the previous analysis using real X-rays and were shown to surpass those theoretically possible for optimised, OTS components. Nevertheless, it was established that the X-ray based pipeline would still not be able to match the performance previously highlighted possible if 3D imaging was utilised.

Based on the analysis, it was determined that the X-ray based pipeline would likely not be sensitive to differences in subject knee side, sex, height, or age. It was observed that subject ethnicity affected performance, with statistically significantly better results recorded for Asian and White test subjects compared to Black test subjects. This was however determined to probably be a result of low ethnic diversity in the training data and could be mitigated via the use of a larger dataset to train the pipeline more broadly. Moreover, the pipeline was found to produce lower quality results for subjects who had moderate to severe cases of arthritis. Nevertheless, the pipeline was demonstrated to be able to repeatably produce accurate, well-fitting designs for subjects with damage levels at the stage where knee replacement is usually recommended (K&L grade 2).

Through the pipeline sensitivity analysis, it was confirmed that anatomical alignment, as well as dimensional calibration, were highly impactful to 3D model reconstruction accuracy. It was found that to achieve high quality results for both bones, anatomical alignment in inputted AP and lateral X-rays would need to be accurate to approximately ± 5°, whilst dimensional calibration would need to be correct to ± 2%. To facilitate such specifications in practice, an alignment protocol similar to that outlined by Nguyen et al. (2022) could be established to guide the imaging process. The authors in this study demonstrated that, by ensuring patients fully extended their knees, placed their feet at a set distance and alignment relative to a standardised positioning template, and distributed their weight equally between each leg, that consistent X-ray alignments across multiple anatomical metrics (including the leg) of < 1° for 30 patients was achieved. Alternatively, an approach like that detailed in (Zheng et al., 2018) where a knee joint immobilisation device was utilised, could be explored. To assist with dimensional calibration, reference objects of known sizes could be included in the imaging frame as highlighted previously (Wimsey et al., 2006) (Schumann et al., 2014). Moreover, the use of a calibration cage like in (Zheng et al., 2018) could be considered. To minimise human related error during the X-ray capture process, and facilitate optimal segmentation results, additional AI/ML functionality could be incorporated to reject poorly aligned X-rays (Tack et al., 2021), and/or enable automatic dimensional calibration by detecting and segmenting included calibration objects (Konovalov et al., 2017).

Chapter 7

X-ray Based Implant Size Prediction Pipeline

The following chapter presents a method for, and results of, an automatic OTS knee replacement implant size prediction pipeline, using biplanar X-ray images as an input medium.

Most of the contents of this chapter have been published in the following paper:

- Burge, T.A., Jones, G.G., Jordan, C.M., Jeffers, J.R.T. & Myant, C.W. (2022) A computational tool for automatic selection of total knee replacement implant size using X-ray images. *Frontiers in Bioengineering and Biotechnology*. 10, 1–11.

7.1. Introduction

The focus of the last two chapters was on using the biplanar X-ray based 2D – 3D reconstruction pipeline to enable automatic customisation of the knee replacement implant shape. However, it was identified that it could also be used to enable other forms/levels of implant customisation as defined by Paxton et al. (2022), such as OTS implant size prediction.

In Chapter 2.2, it was highlighted that the accuracy of manual pre-operative X-ray size selection for knee replacement implants has been shown to be poor and linked with increased rates of complications post-surgery (Culler et al., 2017) (Buller et al., 2018) (Schroeder & Martin, 2019). Due to the lack of confidence in the accuracy of pre-operative implant sizing, surgeons often decide to implant different sizes than planned if deemed necessary mid-procedure (Sheth et al., 2017). This can lead to higher chances of human error, longer surgery times, and requires various implant sizes to be available in theatre.

Zheng et al. (2018) and Massé & Ghate (2021) developed tools capable of predicting TKR implant size from X-rays. These alternatives to the conventional manual based approach both featured ‘semi-automatic’ workflows which required feedback from users to facilitate the size prediction process. Consequently, such tools would incur the burdens of additional user training and resource to implement in practice. Moreover, both studies only featured a limited number of test subjects and evaluated the performance of the respective algorithms on single implant models without detailing the number of sizing options available.

This chapter explores how the X-ray based 2D – 3D pipeline developed in Chapters 5 and 6, could be applied to facilitate a ‘fully’ automatic OTS TKR implant size prediction pipeline. The hypothesis being that such a solution would be less impacted by inaccuracies in anatomical alignment and X-ray calibration (compared to custom implant generation), and may afford an attractive and viable tool which surgeons could rely on more so than currently available solutions, such as the highly inaccurate Traumacad Auto-Knee tool (Seaver et al., 2020).

7.2. Pipeline Development and Test Method

In the following sub-sections, the various stages of the X-ray based implant size prediction pipeline (summarised in Figure 70) are outlined. Details of the subjects used to test the pipeline and how its accuracy was evaluated are also provided.

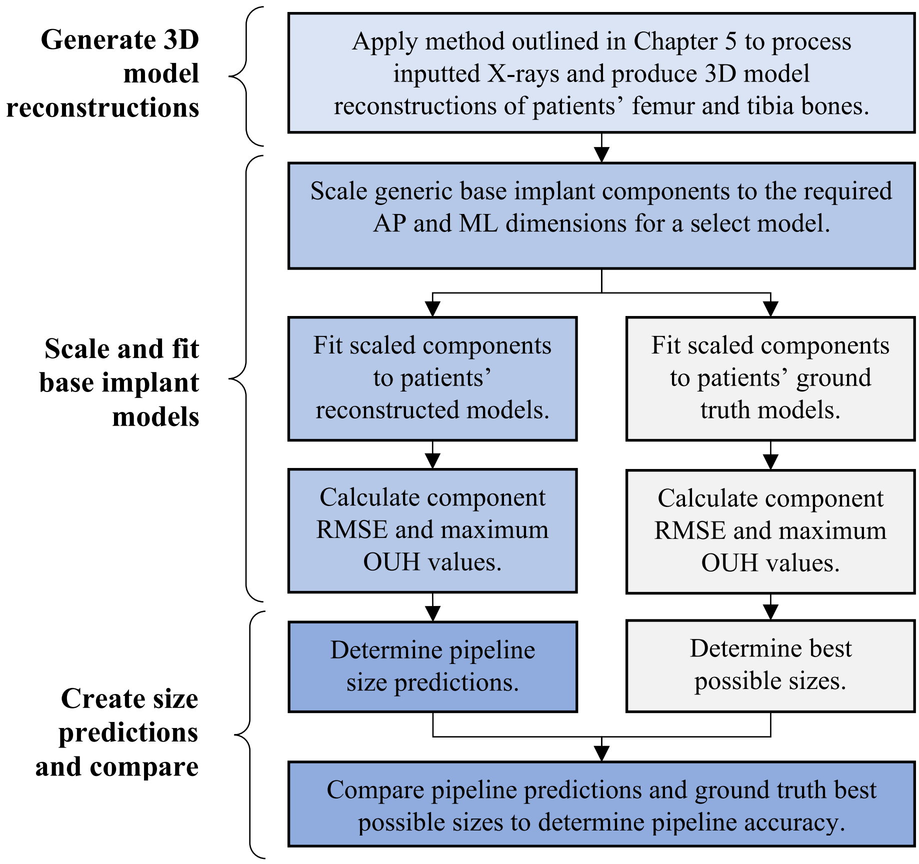

Figure 70: Key stages and workflow of the X-ray based OTS implant size prediction pipeline

7.2.1. Create 3D Model Reconstructions

Like in (Zheng et al., 2018) and (Massé & Ghate, 2021), the implant size prediction pipeline developed in this thesis initially used inputted AP and lateral X-rays to generate 3D estimations of patients' femur and tibia bones. These could then be used to fit different implant sizes to and form predictions. To achieve this automatically, the same method detailed in Chapter 5.2.2 was adopted to segment inputted X-rays and extract 2D contours. The process detailed in Chapter 5.2.3 was then applied to create the 3D model reconstructions using the same PDMs and SSMs.

7.2.2. Base Implant Model Designs and Sizes

Access to the official geometry of commercially available TKR implant models and sizes was not possible to obtain, nor was acquiring physical samples for reverse engineering. Therefore, the same generic base TKR models designs used throughout Chapters 4 – 6 (shown in Figure 34), were adjusted to reflect global sizes acquired for five commercially available products. A 3D base model was used for femur components, while a 2D profile was used for tibia plates. The width of the base femur component was subtly adjusted for each of the manufactures' models in the analysis to reflect differences in dimensioning approaches between the products. The design of the tibia plate was kept constant as no differences were found in dimensioning.

Sizes for the Zimmer Biomet 'NexGen', DePuy 'Sigma', Smith & Nephew 'Legion', Maxx Orthopedics 'Freedom' and Stryker 'Scorpio' products were used. These models were selected to provide a range of the number of implant sizes available, as well as the ML/AP ratios used. The AP and ML dimensions for the various sizes for each model were sourced from sizing charts contained within the respective manufacturers' surgical technique manuals. The dimensions are listed in Table 9 for femur components and Table 10 for tibia plates.

The same method used in Chapter 4.2.2 was utilised for scaling the generic base implant models to the listed AP and ML dimensions for each manufacturer model and size. The height of the 3D femur components was kept proportional by scaling the Z dimension in line with the AP and ML dimensions in the same manner as before.

Table 9: Femur component sizing chart (ML and AP dimensions in mm)

Zimmer Biomet (NexGen)			*DePuy (Sigma)*			*Smith & Nephew (Legion)*			*Maxx Orthopedics (Freedom)*			*Stryker (Scorpio)*		
Id	**ML**	**AP**	**Id**	**ML**	**AP**	**Id**	**ML**	**AP**	**Id**	**ML**	**AP**	**Id**	**ML**	**AP**
‘B’	58	50	‘1.5’	57	53	‘2’	58	50	‘A’	54	51	‘3’	57	51
‘C’	64	54.5	‘2’	60	56	‘3’	62	55	‘B’	58	54	‘4’	60	54
‘D’	68	58	‘2.5’	63	58	‘4’	66	59	‘C’	62	58	‘5’	62	56
‘E’	72	62	‘3’	66	61	‘5’	70	62	‘D’	64	60	‘6’	65	58
‘F’	76	66	‘4’	71	65	‘6’	73	66	‘E’	66	62	‘7’	67	61
			‘5’	73	69	‘7’	77	70	‘F’	70	66	‘8’	70	63
						‘8’	80	75	‘G’	74	70	‘9’	72	65
									‘H’	78	74	‘11’	77	70
												‘13’	82	75

Table 10: Tibia plate sizing chart (ML and AP dimensions in mm)

Zimmer Biomet (NexGen)			*DePuy (Sigma)*			*Smith & Nephew (Legion)*			*Maxx Orthopedics (Freedom)*			*Stryker (Scorpio)*		
Id	**ML**	**AP**	**Id**	**ML**	**AP**	**Id**	**ML**	**AP**	**Id**	**ML**	**AP**	**Id**	**ML**	**AP**
‘1’	56	41	‘1’	59.2	39	‘1’	60	42	‘1’	59	40	‘3’	61	40
‘2’	62	41	‘1.5’	61.8	40.7	‘2’	64	45	‘2’	62	40	‘4’	63	42
‘3’	67	46	‘2’	64.6	42.6	‘3’	68	48	‘3’	66	42	‘5’	66	44
‘4’	70	46	‘2.5’	67.1	44.2	‘4’	71	50	‘4’	66	46	‘6’	68	45
‘5’	74	50	‘3’	69.6	45.8	‘5’	74	52	‘5’	71	48	‘7’	71	47
‘6’	77	50	‘4’	74.9	49.3	‘6’	77	54	‘6’	72	50	‘9’	77	51
			‘5’	80.6	53.1	‘7’	81	56	‘7’	76	52	‘11’	82	54
			‘6’	86.8	57.2	‘8’	85	59	‘8’	78	54	‘13’	88	58

7.2.3. Create Implant Size Predictions

To predict which femur component and tibia plate sizes were the most suited for individuals, the pipeline systematically fitted each size of each implant model to the reconstructions generated for each subject's anatomy using the rigid ICP method detailed in Chapter 3.7. The analysis used the same 2D approach for the tibia plate fit as illustrated in Figure 36. This involved fitting the 2D tibia plate profiles to corresponding profiles extracted from reconstructed tibia bone models (positioned 2 mm below the height of the widest point of the medial condyle, parallel with the surface of the medial plateau). Femur component fit was assessed in 3D between the surfaces of the scaled components and subjects' ground truths.

After each size fitting, the component RMSE and maximum OUH were calculated as detailed in Chapter 3.11 and recorded. The size options for each manufacturer model that achieved the best fits (according to each of the two metrics) were then outputted as the pipeline's predictions for each test subject.

7.2.4. Test Subjects and Determination of Best Possible Sizes

To test the implant size prediction pipeline, the same 78 OAI subjects used in Chapter 5.3 were utilised since AP and lateral X-rays, as well as ground truth 3D models, were again required. After size predictions were made for all test subjects, all sizes for each implant model were positioned via an equivalent ICP method on ground truth models created for each subject using the manual MRI segmentation method detailed in Chapter 3.3. This produced the highest fidelity representations of the subjects' anatomies obtainable and was thus used as the method of determining the best possible sizes in lieu of physical assessment. Using this approach, the best possible sizes for each test subject (in terms of minimising RMSE and maximum OUH), for each implant component and model, were recorded. If the pipeline predicted the same size using the reconstructed bone model as deemed best via the use of the MRI ground truth model, the pipeline prediction was determined to have been correct.

7.3. Pipeline Test Results and Discussion

In this section, an analysis of performance results obtained for the X-ray based implant size prediction pipeline is outlined. The analysis is split into how accurately the pipeline was able to predict the best possible implant size for each model for each test subject, and how well the implant predictions subsequently fitted the individuals.

7.3.1. Implant Size Prediction Accuracy

The results for the pipeline's femur component and tibia plate size prediction accuracy, recorded for each manufacturer model, is reported in Table 11 and in Table 12 respectively. Accuracy is shown in terms of optimal size prediction, as well as ±1 size from the optimal.

Table 11: Femur component size prediction accuracies for each manufacturer model

Model (No. sizes)	*RMSE correct (%)*	*RMSE ±1 correct (%)*	*Max OUH correct (%)*	*Max OUH ±1 correct (%)*
Zimmer Biomet (5)	85.90	100.00	75.64	100.00
DePuy (6)	84.62	100.00	83.33	100.00
Smith & Nephew (7)	75.64	100.00	64.10	100.00
Maxx Orthopedics (8)	73.08	100.00	65.38	100.00
Stryker (9)	70.51	98.72	70.51	97.44
Mean	**77.95**	**99.74**	**71.79**	**99.49**

Table 12: Tibia plate size prediction accuracies for each manufacturer model

Model (No. sizes)	*RMSE correct (%)*	*RMSE ±1 correct (%)*	*Max OUH correct (%)*	*Max OUH ±1 correct (%)*
Zimmer Biomet (6)	87.18	100.00	74.36	98.72
DePuy (8)	85.90	100.00	82.05	100.00
Smith & Nephew (8)	65.38	100.00	62.82	98.72
Maxx Orthopedics (8)	83.33	98.72	69.23	97.44
Stryker (8)	80.77	100.00	75.64	100.00
Mean	**80.51**	**99.74**	**72.82**	**98.98**

For both component types, it was found the size prediction pipeline consistently more accurately predicted the best possible size in terms of component RMSE compared to maximum OUH. This was not unexpected due to the sensitivity of maximum OUH to any patient-specific local irregularities.

Of the five manufacturer models used to evaluate performance, it was found that the best implant size prediction accuracies (for both component types in terms of RMSE) were achieved for the model with the fewest sizes (the Zimmer Biomet ‘NexGen’ (5/6 sizes)). Whereas the femur component model with the most sizes (the Stryker ‘Scorpio’ (9 sizes)) achieved the lowest prediction accuracies. This observation was likely due to the larger discrepancy between sizes in the models with fewer sizing options, thus requiring a lower degree of model reconstruction accuracy for the pipeline to correctly predict the most appropriate size. Despite not being as accurate in terms of size selection accuracy for implant models with a higher number of sizes, the resulting fit outcomes using the pipeline predictions were often found to be superior to the best possible NexGen sizes. This observation is further detailed and explained in Section 7.3.2.

Minimal differences in prediction accuracies were observed across the five tibia plate models for males and females. For femur components however, males achieved 87.27% for both RMSE and maximum OUH, whereas accuracies of 71.11% and 60.44% respectively were recorded for females. The statistically significant difference in performance was likely due to the large White American male dimensions present in the test subject population – often requiring the upper limits of the femur component size ranges or beyond. Females on the other hand were found to require a broader range of smaller sizes which made predicting the correct option more challenging. Using a better balanced group of subjects, featuring ethnicities generally requiring smaller implant sizes, such as Asian Chinese (Li et al., 2019), would likely reduce this affect and result in similar prediction accuracies between sexes.

To investigate potential correlations between implant size prediction accuracy and subject age, Spearman's correlation coefficients were calculated as described in Chapter 3.12. As shown in Table 13, these indicated that no strong correlations for both component types and fit metrics were present.

Table 13: Spearman's coefficients for subject age relating to the pipeline's implant size prediction performance

	Femur components	*Tibia plates*
RMSE	-0.03	0.21
Maximum OUH	0.02	0.25

In summary, the results demonstrated that high levels of implant size prediction accuracy were obtained in terms of both RMSE and maximum OUH across the five implant model sizes. When compared to results reported in the literature for manual planning and templating, the size prediction accuracy of the pipeline was shown to be considerably better than the average across the ten studies summarised by Hernández-Vaquero et al. (2019), detailed in Chapter 2.2. In terms of other computational approaches, the pipeline achieved a better average tibia plate size prediction accuracy and matched the level reported for femur components (in terms of RMSE) when compared to the tool outlined by Zheng et al. (2018). Moreover, when compared to the results reported by Massé & Ghate (2021), the pipeline was on average > 20% more accurate for both component types. The large difference in accuracy compared to the latter was however likely (at least partially) due to a substantially larger number of sizing options being utilised in their study. Lastly, compared to the results published by Seaver et al. (2020) for

Traumacad's Auto-Knee tool, the pipeline was demonstrated to afford markedly improved performance whilst still maintaining a fully automated process.

7.3.2. Resulting Fit of Implant Size Predictions

For the sizes recommended by the size prediction pipeline for each test subject, implant model and fit metric, the resulting fits on the subjects' ground truth models (in terms of component RMSE and maximum OUH) were recorded. These results, alongside those for the best possible sizes determined using the ground truth models, are included in Table 14 and Table 15 for femur components and tibia plates respectively.

Table 14: Femur component mean RMSE and mean maximum OUH results for best possible sizes and pipeline predictions

Model (No. sizes)	*Mean prediction RMSE (mm), (SD)*	*Mean best possible RMSE (mm), (SD)*	*Mean prediction max OUH (mm), (SD)*	*Mean best possible max OUH (mm), (SD)*
Zimmer Biomet (5)	1.31 (0.35)	1.26 (0.36)	3.70 (1.23)	3.55 (1.24)
DePuy (6)	1.09 (0.23)	1.06 (0.23)	3.02 (0.77)	2.95 (0.77)
Smith & Nephew (7)	1.14 (0.47)	1.05 (0.22)	3.29 (1.75)	2.89 (0.63)
Maxx Orthopedics (8)	1.04 (0.18)	0.99 (0.19)	2.91 (0.61)	2.67 (0.53)
Stryker (9)	1.10 (0.47)	1.03 (0.31)	3.16 (1.71)	2.87 (0.79)
Mean	**1.13 (0.37)**	**1.08 (0.28)**	**3.22 (1.32)**	**2.99 (0.88)**

Models with more sizing options generally resulted in better fits in terms of resulting mean component RMSE and maximum OUH. Nonetheless, considerable differences in average component fits were still recorded between the various (tibia plate) models featuring the same number of sizing options. This was found to be true for both the pipeline predictions and the best possible outcomes. The importance of optimising sizing dimensions, and not just simply offering a larger number of sizes, is therefore emphasised.

Table 15: Tibia plate mean RMSE and mean maximum OUH results for best possible sizes and pipeline predictions

Model (No. sizes)	*Mean prediction RMSE (mm), (SD)*	*Mean best possible RMSE (mm), (SD)*	*Mean prediction max OUH (mm), (SD)*	*Mean best possible max OUH (mm), (SD)*
Zimmer Biomet (6)	1.77 (1.10)	1.73 (1.12)	3.63 (1.71)	3.48 (1.78)
DePuy (8)	1.19 (0.36)	1.11 (0.24)	2.70 (0.81)	2.52 (0.57)
Smith & Nephew (8)	1.25 (0.34)	1.11 (0.24)	2.85 (0.72)	2.53 (0.61)
Maxx Orthopedics (8)	1.38 (0.71)	1.31 (0.72)	3.20 (1.23)	2.91 (1.26)
Stryker (8)	1.21 (0.34)	1.10 (0.24)	2.71 (0.74)	2.48 (0.57)
Mean	**1.36 (0.68)**	**1.27 (0.67)**	**3.02 (1.16)**	**2.78 (1.14)**

It was often observed that when the pipeline failed to predict the best possible size, the optimal component dimensions would have been close to the centre of two adjacent sizes, particularly for models with many similar sizing options. As a result, it can be seen in Table 14 and Table 15 that the fits obtained using the pipeline predictions were on average only marginally inferior to the best possible outcomes for both component types. In the literature, it is noted that in such scenarios surgeons will usually downsize the component used (Dai et al., 2014b). Future iterations of the pipeline could therefore be configured to do the same to better align with the standard clinical approach.

Figure 71 and Figure 72 show the proportion of subjects who achieved maximum OUH < 3 mm for the various femur component and tibia plate model sizes. The figures demonstrate that the level of subjects obtaining below the threshold was approximately 10% less on average for femur components compared to tibia plates and that the levels varied significantly between the different manufacturer models. The proportion of subjects who saw maximum OUH of ≥ 3 mm when the pipeline's size predictions were used was on average 12% higher (across both implant components) than what was determined to be the best possible outcomes using the subjects' ground truth models. Moreover, the proportion of subjects who obtained clinically significant levels of OUH, even when the best possible sizes were used, was above 30% in most cases for the femur, as well as in several cases for the tibia. This aligns with the results reported by Mahoney & Kinsey (2010) and Wernecke et al. (2012) who documented similar high levels of OUH when OTS, sized implants were used.

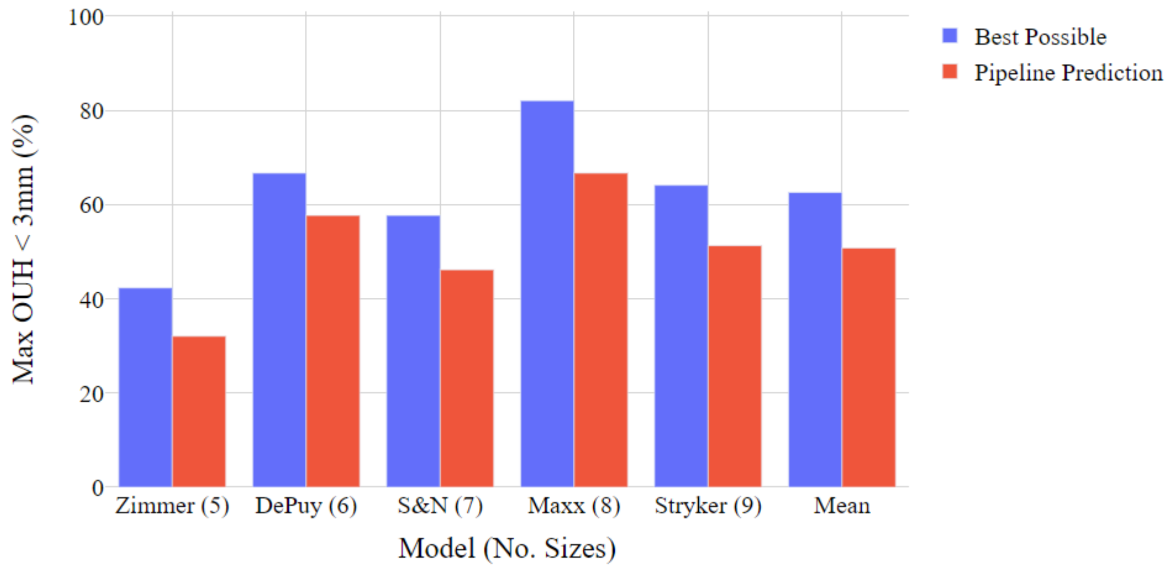

Figure 71: Proportion of test subjects achieving maximum femoral OUH < 3 mm © (Burge et al., 2022c)

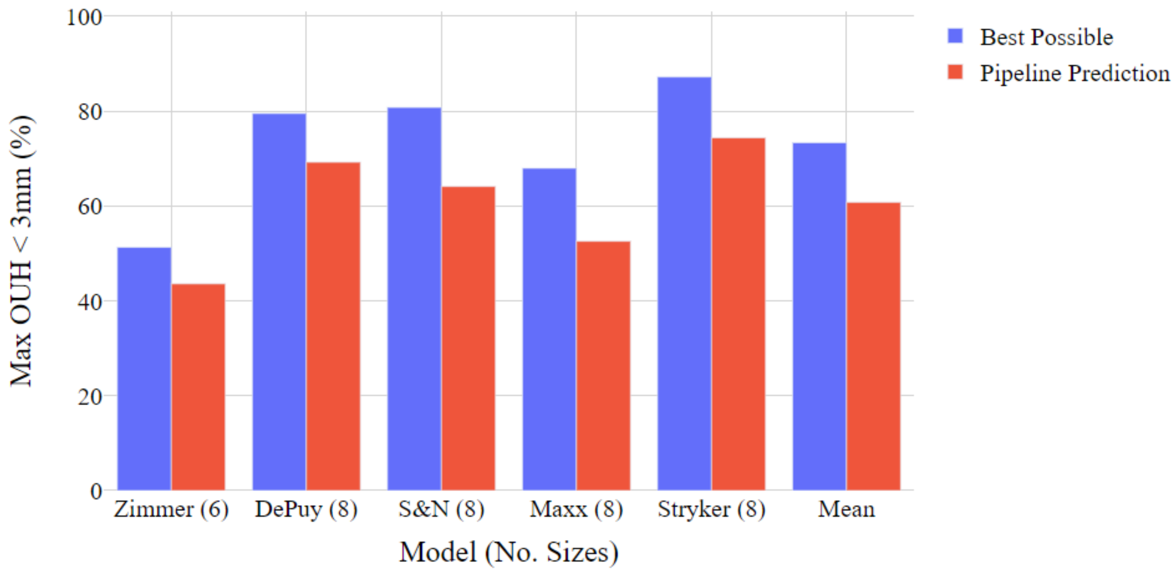

Figure 72: Proportion of test subjects achieving maximum tibial OUH < 3 mm © (Burge et al., 2022c)

7.3.3. Pipeline Computational Requirements

The pipeline used the same method and thus incurred the same approximate five minutes to create 3D model reconstructions of subjects' femur and tibia bones as the X-ray based implant shape customisation pipeline (detailed in Chapter 5.3.3). The computation time required to then fit each implant size for a selected manufacturer model and create best option predictions depended on the number of sizing options available. Said processing time varied from approximately one minute for five size options, to two minutes for up to nine options. This was consistent for both femur component and tibia plate predictions when tested on a personal laptop computer (2.38 GHz AMD Ryzen 5 4500U CPU with 6 cores/8 Gb memory). In total, to reconstruct the anatomy and obtain size predictions for both component types for any of the manufacturer models evaluated, no more than 10 minutes was required.

7.4. Summary

In this chapter, an automated OTS knee replacement implant size prediction pipeline that utilised the X-ray based 3D model reconstruction workflow developed in Chapters 5 was developed and assessed. Mean implant size prediction accuracies across the various femur component and tibia plate models evaluated between approximately 70 – 80%, and almost 100% for ± one size, were recorded. The pipeline's performance was therefore demonstrated to exceed that previously reported possible for manual templating, as well as when compared to other computational alternatives. Moreover, the algorithms developed by Zheng et al. (2018) and Massé & Ghate (2021) were tested on substantially fewer test subjects and the authors only used single implant models with one global fit metric in their evaluations. The superior results and more comprehensive assessment presented in this chapter, particularly when compared to that reported for Traumacad's Auto-Knee software (Seaver et al., 2020), therefore provide a better justification of the viability of such a tool. However, if a protocol like that detailed by Nguyen et al. (2022) was to be in place to control the alignment and calibration of inputted X-rays, it is likely performance could be improved even further.

It is hoped that the high accuracy and ease of use of the developed pipeline will increase surgeons' confidence in, and perceived value of, pre-operative size selection. As a result, this could minimise the possibility of size changes during surgery, reduce surgery time, lessen the level of component inventory required in theatre, lower surgeon accountability for determining the right size implants, and ultimately improve outcomes for patients.

Chapter 8

CT Based Implant Shape Customisation Pipeline

The following chapter presents a method for, and results of, an automatic knee replacement implant shape customisation pipeline, using CT scans as an input medium.

Most of the contents of this chapter have been published in the following paper:

- Burge, T.A., Jeffers, J.R.T. & Myant, C.W. (2023) Applying machine learning methods to enable automatic customisation of knee replacement implants from CT data. *Scientific Reports*. 13, 1–9.

8.1. Introduction

In Chapters 5 – 7 it was demonstrated that biplanar X-rays can be used as input to enable automatic reconstruction of patients' bones and subsequently customise the shape and size selection of knee replacement implants. Although using the 2D input medium would minimise radiation exposure, costs, and accessibility would not be compromised compared to current OTS procedures, precise anatomical alignment and image calibration specifications were found to be necessary.

As an alternative to X-rays, 3D medical imaging, such as CT or MRI, could be adopted to obtain more precise geometrical information of subjects' anatomies, whilst minimising alignment and calibration requirements. Although MRI scans would not incur the same radiation risk, CT is far more accessible (Ginde et al., 2008). It also incurs less imaging time, is less expensive, and can usually achieve a clearer contrast between bone and flesh compared to MRI. Due to these advantages, CT is more commonly used for orthopaedic applications, including knee replacement (Rathnayaka et al., 2012).

As outlined in Chapter 2.3, all CT based knee replacement implant shape customisation solutions identified in the literature required some level of manual work to facilitate. This generally involved segmenting CT scans to generate 3D bone models, refining mesh files, and/or completing design work in CAD programmes. Such tasks require highly skilled user inputs, and consequentially, the time and (up front) cost constraints required to produce customised implants currently make the solutions commercially unattractive. This chapter therefore sought to explore how AI/ML and statistical models could be used to enable a fully automated, CT based knee replacement implant shape customisation pipeline and investigate the potential benefits compared to the X-ray based alternative.

8.2. Pipeline Development and Test Method

In the following sub-sections, the various stages of the CT based implant shape customisation pipeline (summarised in Figure 73) are outlined. Details of the data used to train and test the pipeline are also provided.

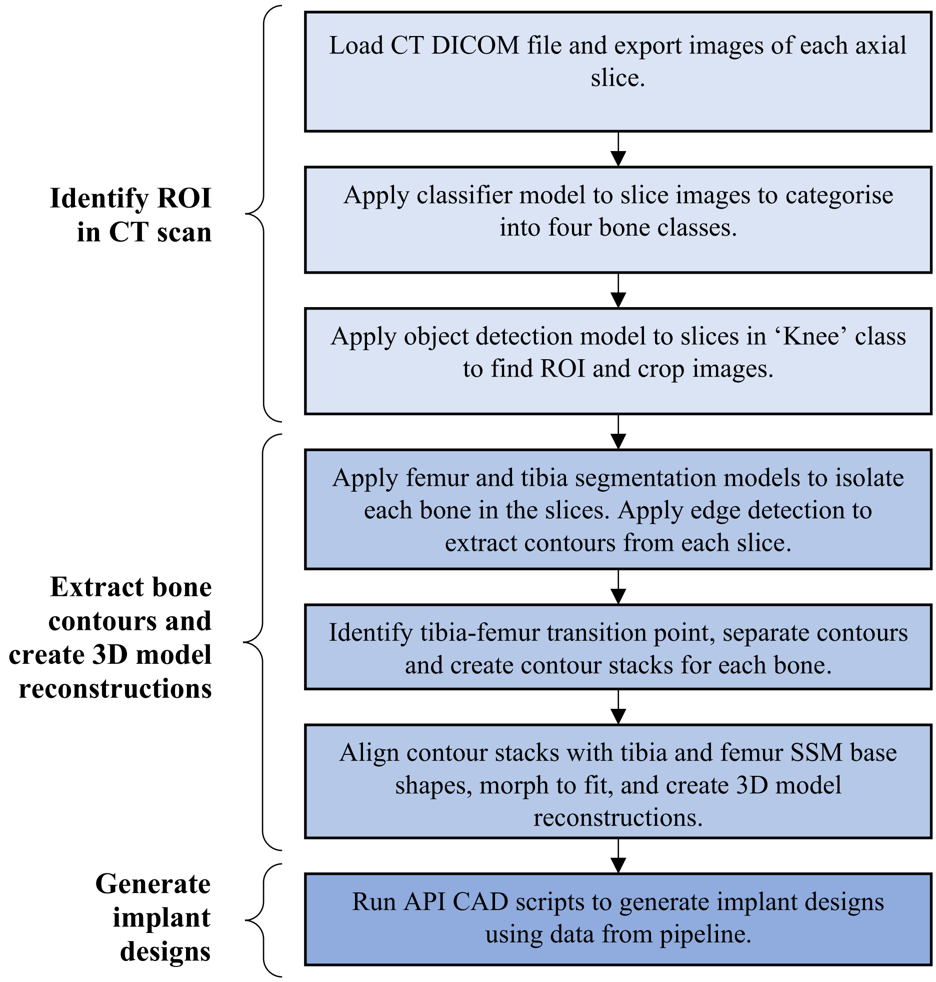

Figure 73: Key stages and workflow of the CT based implant shape customisation pipeline

8.2.1. Pipeline Training Data and Test Subjects

As the OAI dataset did not contain CT data and 3D bone models were not supplied with the CT scans retrieved from Charing Cross Hospital, the KISTI dataset was used exclusively for training and testing the CT based pipeline. Subjects were split into two approximately equal sized groups for training and testing. Where possible, data for both knees for each subject was used. 3D models and CT scans found to be of poor quality were excluded. In total, data from 51 different subjects (33 female and 28 male) was used for training the pipeline. This consisted of slice images from 43 CT scans, as well as 90 femur and 96 tibia 3D models (including both left and right bones).

Test subjects were only selected if both patients' CT scans and 3D bone models were available. 45 subjects (20 female and 25 male) were used for testing the performance of the pipeline for the femur. 43 subjects (22 female and 21 male) were used for the tibia. No CT data or 3D bone models used for training were also included in the test set.

8.2.2. Identify Region of Interest in CT Stack

Firstly, the inputted CT DICOM files were loaded into the pipeline and information such as pixel resolution, slice spacing, and the number of slices in the stack was recorded. Each slice from the CT scan was exported and saved as individual .PNG files (Figure 74A). A classifier model was then applied to the slice images to categorise them into four classes: 'Fibula/Tibia', 'Knee', 'Femur', and 'Other'. The 'Knee' class comprised of images of the condylar region of the distal femur, proximal tibia, and patella bones (Figure 74B).

A CNN architecture, similar to that outlined by Hou & Gao (2021), was utilised for the classifier model. The number of filter channels used in each layer were set to those detailed in Figure 75 to sufficiently learn the nuances between the four classes and achieve f1 classification results > 98% on allocated validation data. 8,000 slice images (2,000 for each class) from the training set were categorised and utilised with the method detailed in Chapter 3.4.1 and hyperparameters detailed in Chapter 3.4 to train the model. 800 (200 for each class) were reserved for validation. After classifying the CT slices in the pipeline, the bone order was determined as 'tibia-knee-femur' or 'femur-knee-tibia'.

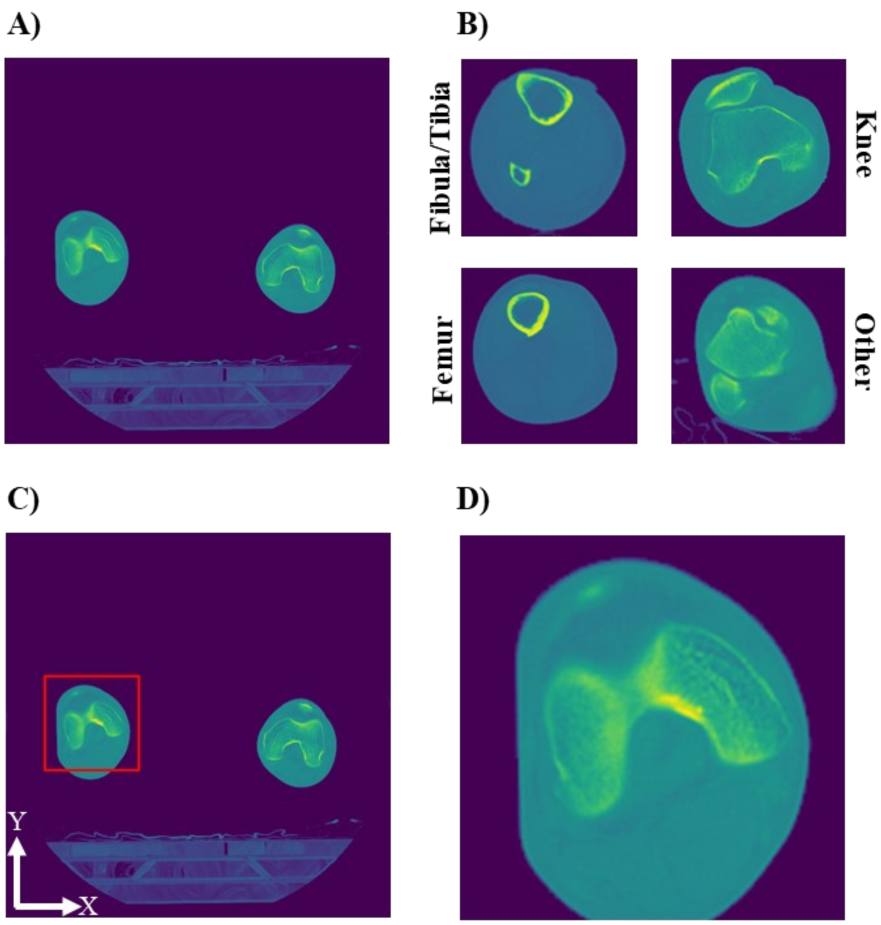

Figure 74: A) CT slice image, B) Four bone classes, C) Bounding box created around ROI, D) Slice image cropped to ROI © (Burge et al., 2023b)

An object detection model was applied to each slice determined to be within the 'Knee' section of the CT scan to locate the ROI around the left knee (Figure 74C). This was because, like for the X-ray based pipeline, the algorithm was also trained to work with left sided geometry to take advantage of the anatomical symmetry of the knee joint. A 'bounding box regression' object detection model was utilised due to their high accuracy, simplicity and because there was no need to detect multiple types of bone within each slice (Lee et al., 2019). A CNN architecture, similar to that outlined by Galvez et al. (2018), was utilised as illustrated in Figure 76. Due to the relatively small area that the left leg occupied in the full CT slice (Figure 74C), it was found that the input layer required a high resolution (512 x 512 pixels) to adequately capture sufficient detail and reliably identify the ROI. However, since the model only needed to be able to identify bone shapes within the 'Knee' section, the number of filters used in each layer could be reduced compared to those used in Figure 75. A 5th layer was also added to the architecture (like shown in Figure 47 for the X-ray segmentation model) as this was found to further improve the accuracy of the bounding box placement.

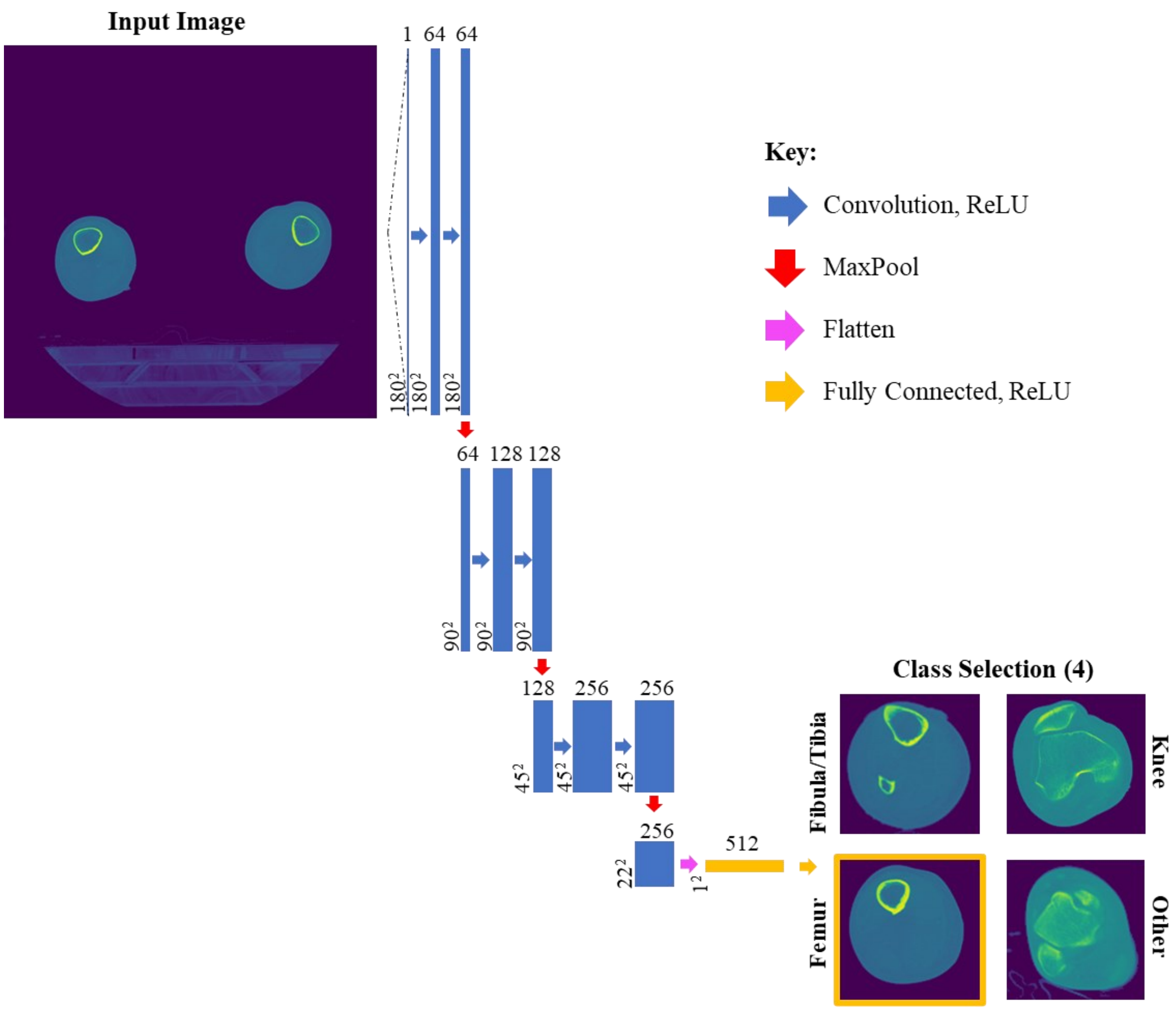

Figure 75: Architecture of classification model used to split CT slices into four classes

To train the object detection model, 1,000 images of the 'Knee' region, labelled with bounding box coordinates around the left knee (defined via the process detailed in Chapter 3.4.2), were used with 100 reserved for validation. The same hyperparameters and optimiser as employed for the classifier model (listed in Chapter 3.4) were used to facilitate the model training.

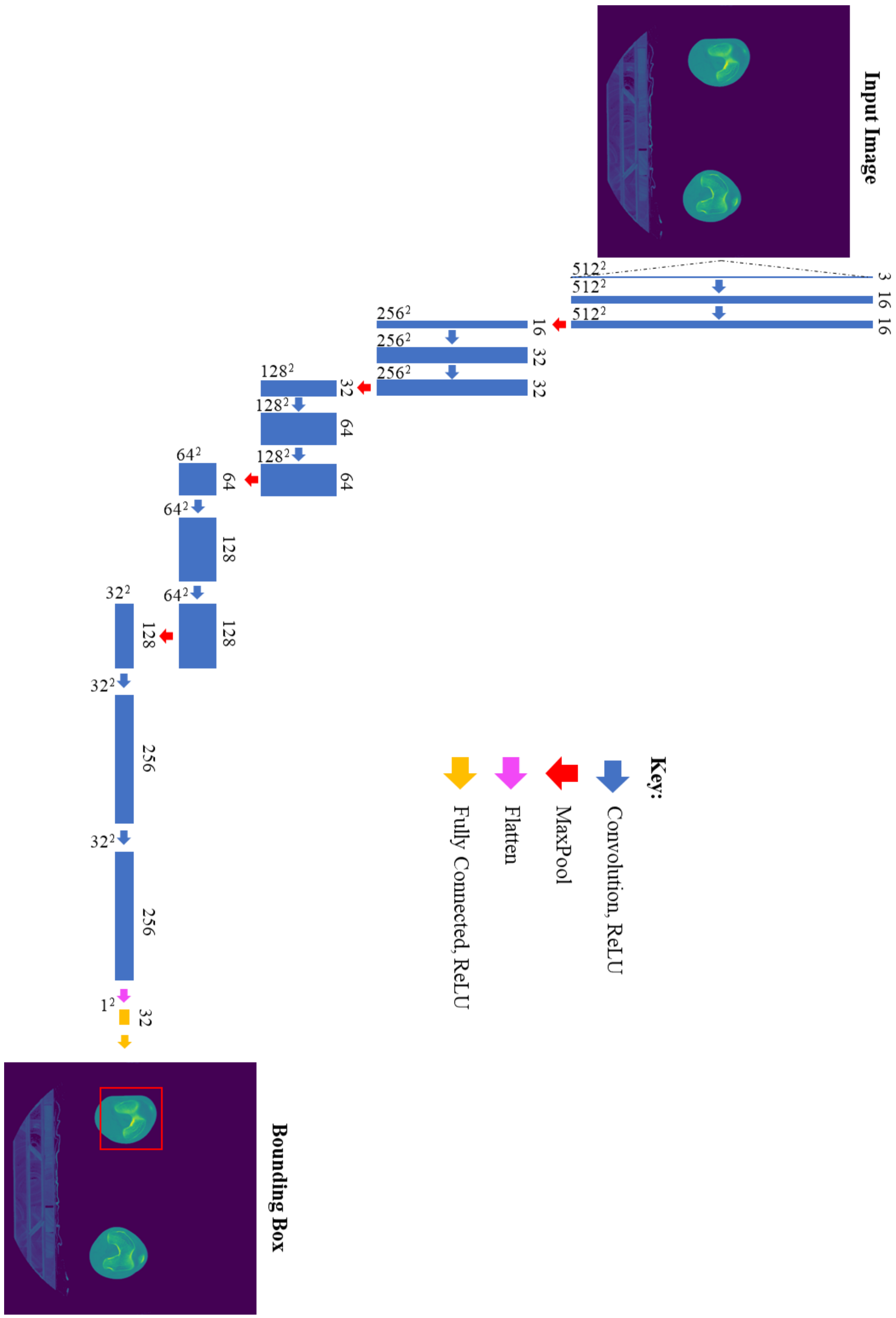

Figure 76: Architecture of object detection model used to identify the ROI in CT slices

After the pipeline had determined the centre of the ROI for each slice, a consistent 160 x 160 pixel square box, positioned at the median X and Y coordinates, was defined as the average ROI across all slices in the ‘Knee’ portion of inputted CT scans. Each slice was then cropped to the ROI and outputted as a new .PNG file (Figure 74D). If the pipeline was to be used for a subject’s right knee, (un-cropped) slice images were automatically flipped horizontally by the pipeline before the object detection step was completed.

8.2.3. Extract Bone Contours and Create 3D Model Reconstructions

To isolate the femur and tibia bones from the surrounding tissue in the cropped ROI CT slice images, segmentation models for both bones (utilising the same U-net CNN architecture as adopted for the X-ray based pipelines (Figure 47)), were applied. To train the segmentation models, the hyperparameters and optimiser detailed in Chapter 3.4 were again utilised. 1,832 and 1,623 training image/mask pairs were generated for the femur and tibia respectively following the process detailed in Chapter 3.4.3. These featured CT slices cropped to the ROI around the left knee, as well as the right after a horizontal transformation had been applied. This helped to increase the volume of training data available. 200 image/mask pairs were reserved for validation for each model.

Both segmentation models were applied to the cropped images before a Canny edge detector and filter were employed (as detailed in Chapter 3.5) to extract the bone contours from all ‘Knee’ slices (illustrated in Figure 77A). To identify the tibia-femur transition point and separate the contours into the respective bones, firstly, the area of each slice’s segmented bone (for both femur and tibia segmentation model results) was calculated and a univariate spline curve fitted to reduce slice-slice noise (illustrated in Figure 78). The transition point was then determined by first locating the positions of the largest area for both the femur and tibia bones according to the corresponding segmentation models. The slice number at which the tibia and femur curves intersected between these reference points, i.e., where the condyles of the femur ended and the tibia plateau began, was then identified as the transition point (highlighted in Figure 78). It should be noted that the slight negative segmentation area shown for the tibia at the tibia-femur transition point in Figure 78 was an artifact of the univariate spline curve and did not affect the pipeline accuracy.

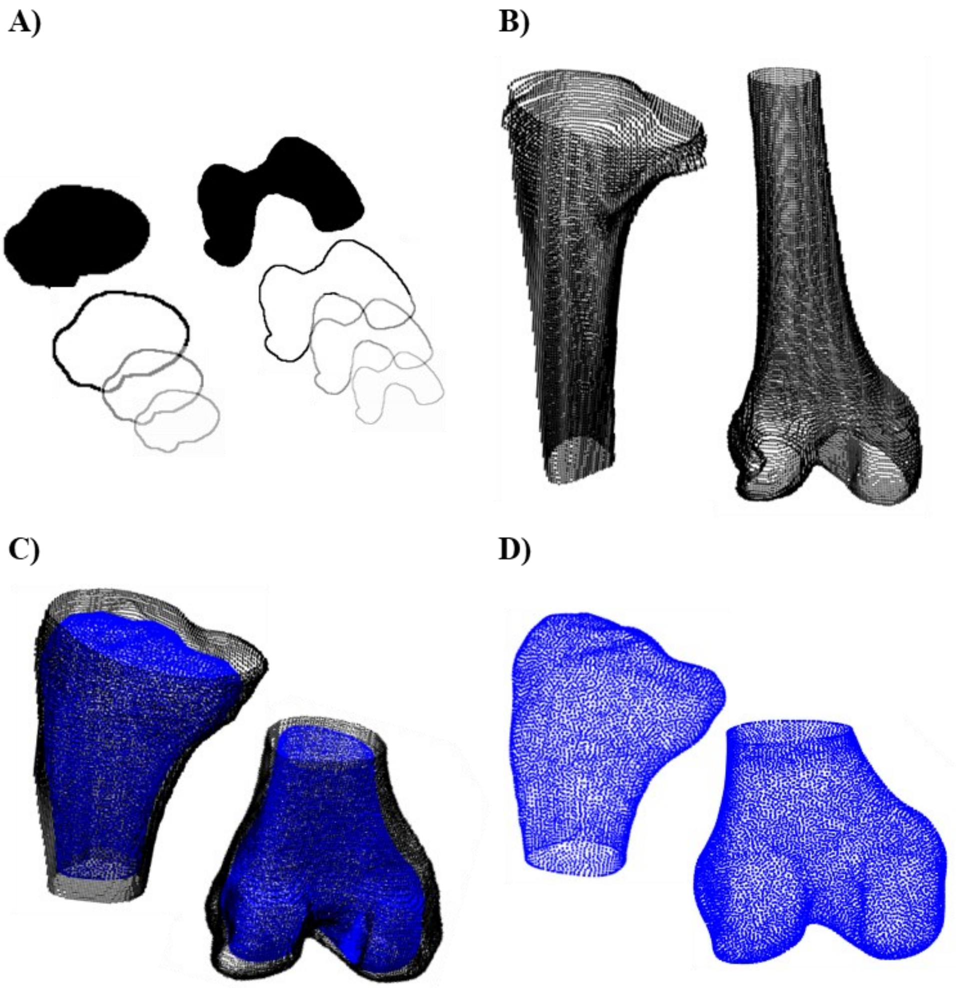

Figure 77: A) Isolated bone areas and extracted contours for the tibia and femur, B) Contour stacks, C) Contour stacks positioned on SSM base shapes, D) 3D model reconstructions © (Burge et al., 2023b)

To form 'contour stacks' for the tibia, the 2D contours produced using the tibia segmentation model, up to the defined tibia-femur transition point, were positioned on top of each other in 3D space. The contours were separated in the Z direction (normal to the slices) according to slice spacing information retrieved from inputted CT DICOM files. The same was completed to form femur contour stacks using contours generated by the femur segmentation model after the tibia-femur transition point. The contour stacks were trimmed by five slices at the proximal end of the tibia and the distal end of the femur as excessive segmentation noise was found to occur in these regions. Example contour stacks for both bones are illustrated in Figure 77B.

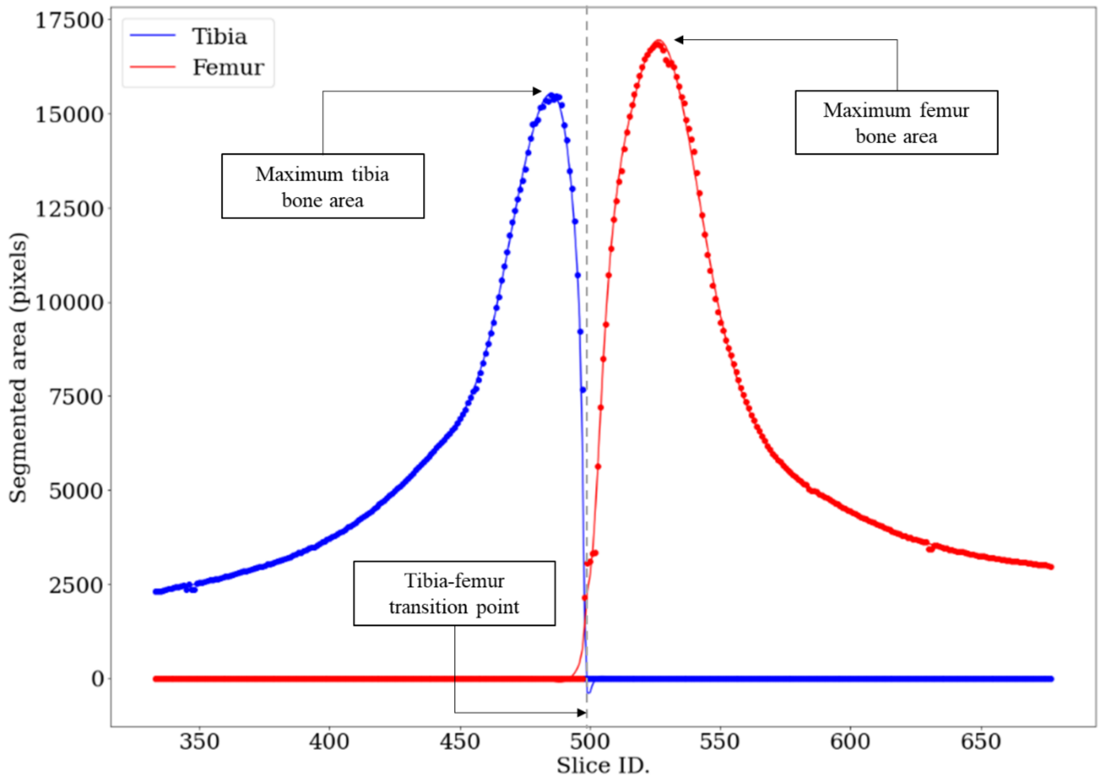

Figure 78: Segmented tibia and femur bone cross-sectional areas plotted for each slice within the 'Knee' region of a CT stack © (Burge et al., 2023b)

Two SSMs, one for the femur and another for the tibia, were developed following the process detailed in Chapter 3.8 using the 90 and 96 3D bone models from the KISTI dataset respectively. New SSMs were built instead of using those created previously for the X-ray based pipeline to optimise the amount of data available for both train and test whilst ensuring independence between the groups. The models comprised of left bones, as well as right bones after horizontal transformations had been applied. To create 3D reconstructions of subjects' bones, the contour stacks generated were aligned to the base shapes of each SSM model using a ridged ICP method as detailed in Chapter 3.7 and illustrated in Figure 77C. The process detailed in Chapter 3.8 was then used to morph the SSM base shapes to the contour stacks and enable 3D model reconstructions of the femur and tibia bones to be generated (Figure 77D).

In line with the X-ray based pipeline developed in Chapter 5, the base shapes of the SSMs built for the CT based pipeline were 'idealised' and smoothed to ensure outputs were well-suited for designing custom implants. Unlike in the X-ray based pipeline, only one tibia SSM size was found to be needed. This was because the contour stacks contained more complete geometrical detail compared to the sparse 3D point clouds created from the biplanar X-rays, which facilitated simpler alignment with the SSM base shapes.

It is noted that authors have typically used tools included within segmentation software packages (such as 3D Slicer) to generate the 3D bone models required directly from CT scans (Jun, 2011) (Li et al., 2017) (Balwan & Shinde, 2020). The resulting triangulated meshes then needed refinement, such as smoothing processes, and the quality of the models produced was highly dependent on the resolution of the inputted scans. In addition, the number and indexing of the resulting mesh faces and vertices, as well as the alignment of outputted models, would have differed between scans. This would lead to problems if attempting to automate the process. By adopting the contour stack driven SSM approach outlined in this section, these issues were mitigated, enabling a reliable fully automated method.

8.2.4. Generate Custom Implant Designs

Once 3D model reconstructions were created, the same process used in Chapter 5.2.4.1 was adopted to generate custom shape TKR implant components. Like in the X-ray based pipeline, the outputs from the CT based pipeline could also be used to produce uni-condylar designs, as well as other varieties of TKR styles if desired, as described in Chapter 5.2.4.2.

8.3. Pipeline Test Results and Discussion

In this section, how the parameters of the CT based implant shape customisation pipeline were optimised is described, an analysis of performance results obtained for the pipeline is outlined, and the necessary computational requirements to run the workflow are detailed.

8.3.1. Pipeline Parameter Optimisation

Like for the X-ray based pipeline, the impact of adjusting important parameters associated with the CT based pipeline was evaluated before running the full analysis. As increasing the number of training models used to build SSMs was previously demonstrated to continuously improve results in Chapter 5.3.1, an equivalent analysis was not repeated here. As PDMs were not used in the CT based pipeline, this was also not considered. The analysis therefore concentrated solely on the number of principal components utilised in the femur and tibia SSMs.

Like before, a subset of 20 was randomly selected from the test subjects detailed in Section 8.2.1 to facilitate the parameter optimisation analysis. The number of principal components were adjusted from one to five and the mean reconstruction to ground truth RMSE (detailed in Chapter 3.11.1) across the 20 test subjects was used to assess performance. The results of the analysis are shown in Figure 79. Like with the results presented for the X-ray pipeline in Chapter 5.3.1 and illustrated in Figure 60, employing two principal components was found to afford the most accurate 3D model reconstructions on average. This was unexpected since more geometrical information was available from the 3D CT scans, thus the hypothesis was this would better inform the SSM morphing. Yet perhaps the subtleties of the higher order principal components learned by the SSMs could not be captured adequately due to the reasonably coarse KISTI CT resolution (1 mm axial slice thickness). Nonetheless, to optimise anatomical reconstruction and avoid capturing damaged patient anatomy too closely, the number of SSM principal components used for the full results analysis was limited to two.

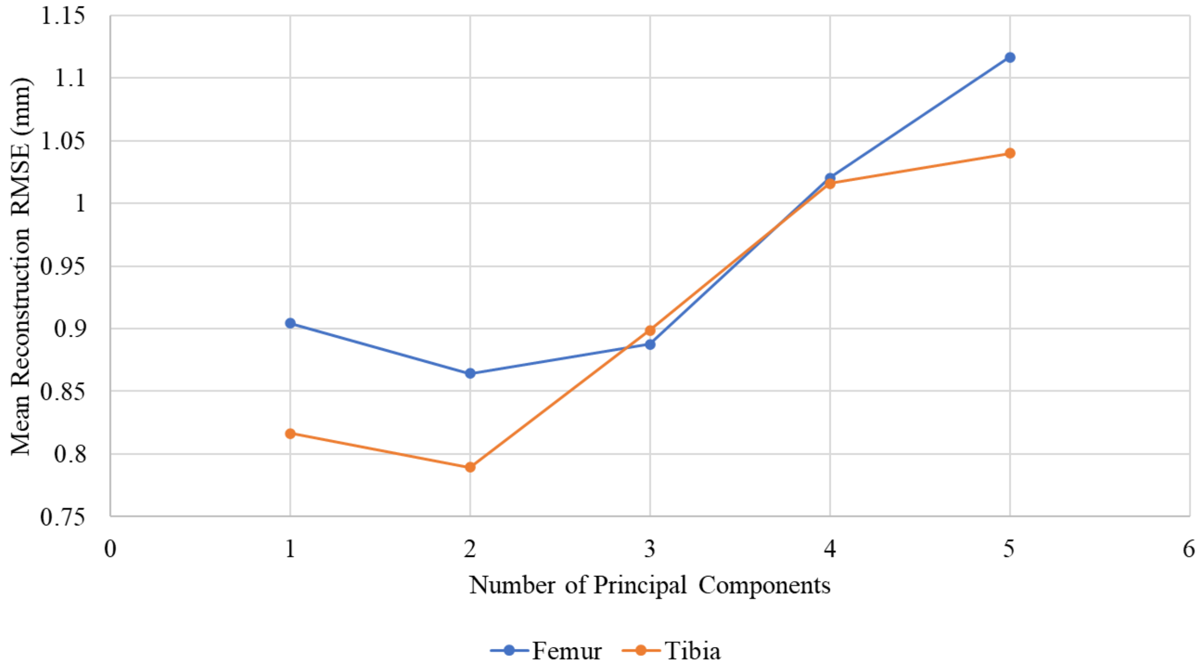

Figure 79: Impact of varying the number of SSM principal components in the CT pipeline

8.3.2. Pipeline Performance Results Analysis

When evaluated on the test subjects detailed in Section 8.2.1, the CT based pipeline successfully generated 3D reconstructions of almost all subjects' anatomies and created highly accurate custom implant designs (like shown in Figure 80). Nevertheless, in the case of one subject's tibia bones, the pipeline failed to segment the CT slices and produce contour stacks due to erroneous results obtained from the tibia segmentation model. Consequently, the subject's left and right knees were removed from the tibia analysis, leaving 42 subjects (81 bones). Summaries of the pipeline performance for both the femur and tibia are provided in Table 16 and Table 17 respectively.

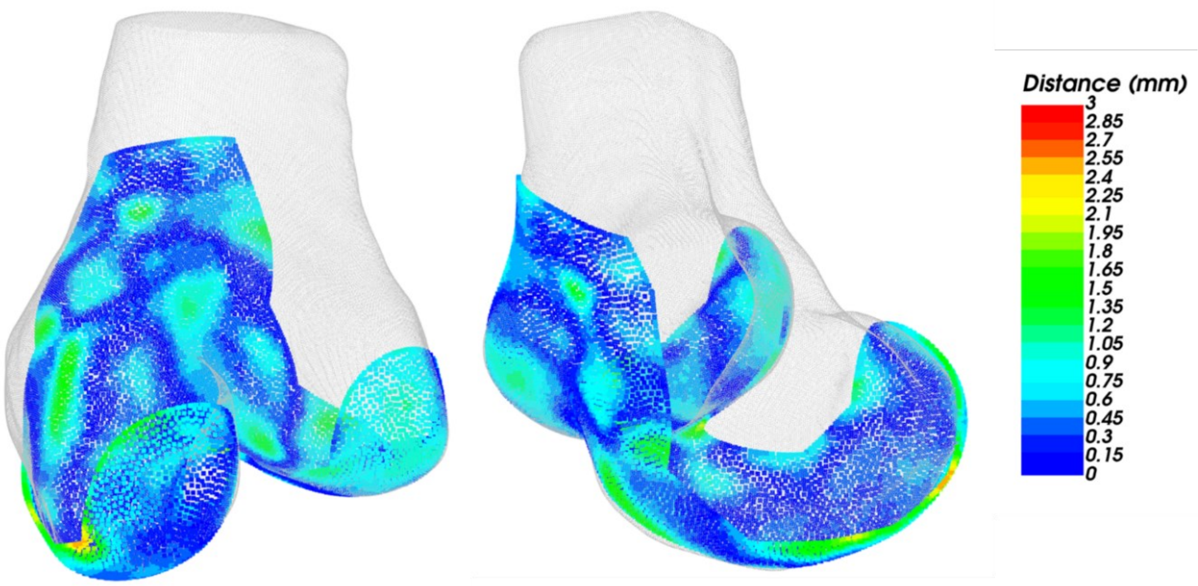

Figure 80: Distance heat map of a custom femur component produced by the CT based implant shape customisation pipeline in relation to the ground truth model

The results show that the CT based pipeline produced more accurate results for both bones across all three fit metrics compared to that reported for the X-ray based pipeline in Chapter 5.3.2, as well as when the DRR method was adopted in Chapter 6.3.1. In particular, the proportion of subjects with maximum OUH breaching the clinical threshold of 3 mm was substantially improved. The differences between the CT based pipeline and the X-ray and DRR results were all found to be strongly statistically different for all fit metrics for both bones (utilising the method detailed in Chapter 3.12). A comparison of the performance results across the three shape customisation pipelines is provided in Figure 81 and Figure 82 for the femur and tibia respectively. It should be noted that, due to the data available, different test subjects were used between the three analyses which could have contributed to some of the discrepancy.

Table 16: Summary of CT based implant shape customisation pipeline femur results

	Total knees, (%)	*Mean reconstruction RMSE (mm), (SD)*	*Mean component RMSE (mm), (SD)*	*Component maximum OUH ≥ 3 mm, (%)*
Overall	**84**	**0.87 (0.20)**	**0.85 (0.21)**	**6 (7.1)**
Sex				
Female	37 (44.0)	0.87 (0.19)	0.84 (0.21)	2 (5.4)
Male	47 (56.0)	0.87 (0.21)	0.85 (0.22)	4 (8.5)
Knee				
Left	42 (50.0)	0.86 (0.19)	0.83 (0.21)	3 (7.1)
Right	42 (50.0)	0.88 (0.21)	0.86 (0.22)	3 (7.1)

Table 17: Summary of CT based implant shape customisation pipeline tibia results

	Total knees, (%)	*Mean reconstruction RMSE (mm), (SD)*	*Mean component RMSE (mm), (SD)*	*Component maximum OUH ≥ 3 mm, (%)*
Overall	**81**	**0.80 (0.15)**	**0.82 (0.27)**	**1 (1.2)**
Sex				
Female	37 (45.7)	0.76 (0.14)	0.79 (0.26)	1 (2.7)
Male	44 (54.3)	0.83 (0.16)	0.84 (0.28)	0 (0.0)
Knee				
Left	41 (50.6)	0.82 (0.15)	0.83 (0.29)	1 (2.4)
Right	40 (49.4)	0.78 (0.15)	0.81 (0.25)	0 (0.0)

Like for the X-ray based pipeline, the results for the CT shape customisation pipeline showed lower errors across the three performance metrics for the tibia compared to the femur. The differences were again calculated to be significant for 3D model reconstruction RMSE and maximum component OUH, but not component RMSE. This therefore reinforced the previous observation that, even with the additional 3D geometrical information available from using CT scans, capturing the more complex femur morphology via the use of SSMs was more challenging than for the tibia.

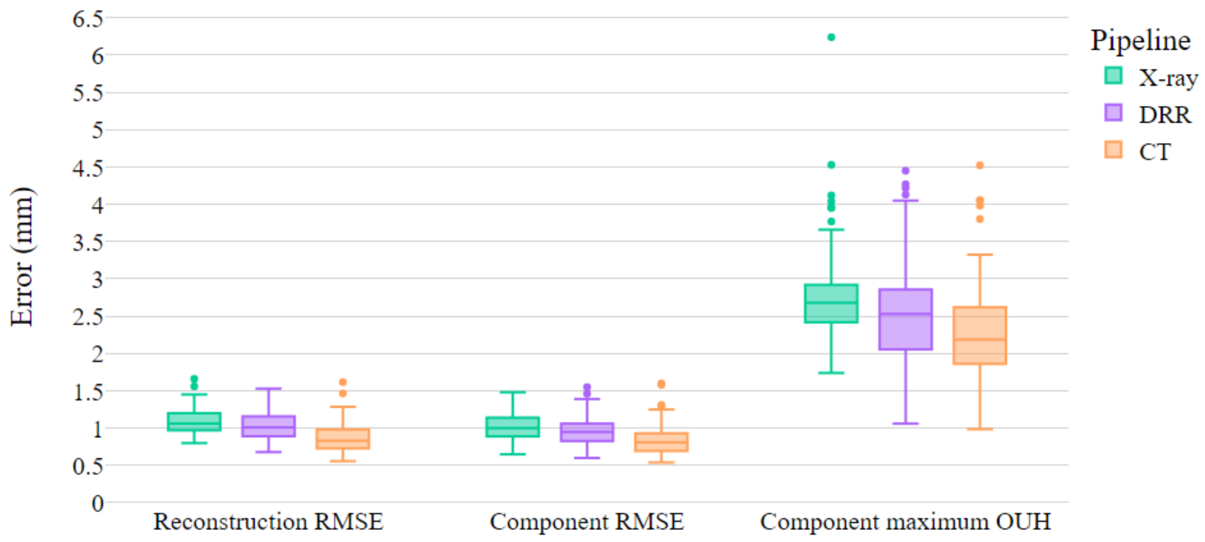

Figure 81: Box plot comparison of X-ray, DRR and CT implant shape customisation pipelines results for the femur

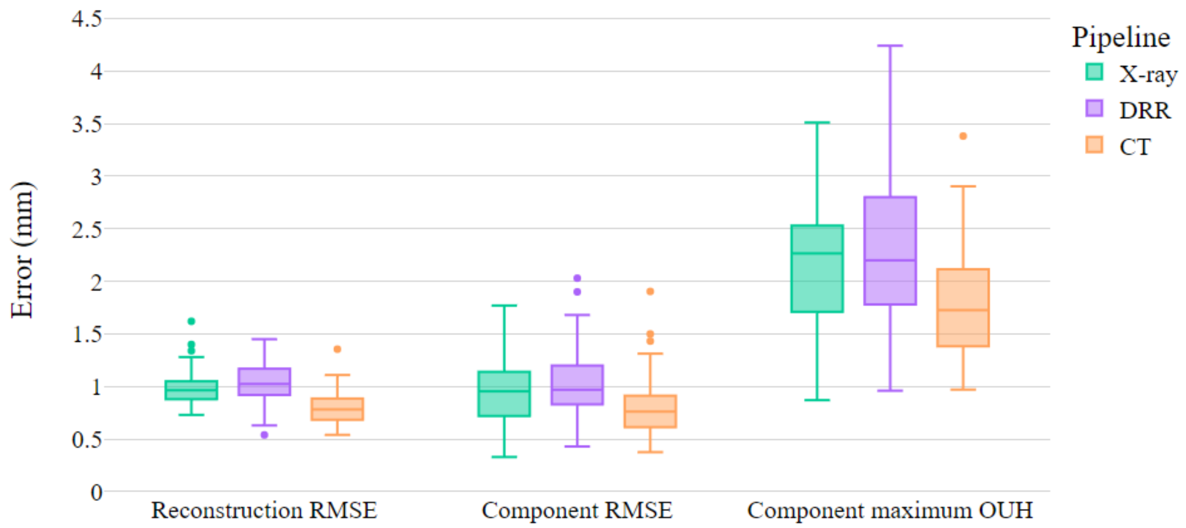

Figure 82: Box plot comparison of X-ray, DRR and CT implant shape customisation pipelines results for the tibia

Within the results for each bone, the difference in the CT based pipeline's performance due to sex and knee side was not found to be statistically significant for any of the performance metrics. Additionally, neither subject age nor height were found to significantly impact performance as all Spearman's coefficients calculated (r) were $-0.1 < r < 0.3$. These findings were all consistent with the X-ray based pipeline when the DRR approach was used.

A limited number of outliers (data points located outside the box plot whiskers) for both bones were recorded for the CT based pipeline which can be seen in Figure 81 and Figure 82. It was found that, like in the case of the tibia subject that failed, typically these isolated cases of poor fit were due to low quality segmentation results. This issue was likely due to overfitting in the machine learning and statistical models, caused by the limited data available for training. Although a reasonably large number of images were used to train the segmentation models, these were sourced from just 43 CT scans, captured via the same equipment, and were purely of Asian Korean subjects. Since the accuracy of the pipeline was dependent on quality segmentations being acquired for multiple CT slices through the thickness of subjects' knee joints, significantly increasing the volume and diversity of the model's training data would likely be required to completely avoid such failures.

In comparison to results reported for other (not fully automated) CT based custom shape TKR solutions, Chapter 2.3 detailed that Ogura et al. (2019) and Arnholdt et al. (2020) reported no instances of OUH ≥ 3 mm. Schroeder & Martin (2019) however concluded 18% of subjects in their study had tibia plates that did not meet this threshold. This discrepancy may be because, in the first two studies, OUH was measured post-operatively via 2D X-rays and defined as the distance between the outermost edges of the tibia/femur condyles and the outermost edges of the component. Whereas this differed to the method utilised in this research (detailed in Chapter 3.11.2) which considered the entire bone-implant interface and likely resulted in higher levels of OUH being recorded. The results published by Schroeder & Martin (2019) who also measured OUH along the entire bone-implant interface are therefore probably a more relevant comparison. Hence, it can be reasoned that the performance of the pipeline could be comparable to manual or semi-automated customisation alternatives.

8.3.3. Pipeline Computational Requirements

In terms of solve time, the pipeline was found to consistently process inputted CT DICOM files and generate both custom femur and tibia plate components in less than 10 minutes when run on a personal laptop computer (2.38 GHz AMD Ryzen 5 4500U CPU with 6 cores/8 Gb memory). The longer duration required compared to the X-ray based pipeline was mostly due to the requirement of processing thousands of slices in the CT DICOM files to extract the contour stacks used to drive the SSMs. This was necessary regardless of the desired pipeline output, meaning minimal time savings were realised for subjects requiring just one component type (femur component or tibia plate). This was unlike the X-ray pipeline where just the femur or tibia bones could be segmented separately from inputted X-rays if purely one type was desired. Despite this, the required computation time was still extremely low compared to what would be incurred via a manual process.

8.4. Summary

In this chapter, it was demonstrated that the CT based implant shape customisation pipeline was capable of repeatably producing significantly more accurate 3D model reconstructions and custom implant designs for both bones compared to the X-ray alternative outlined in Chapter 5, as well as when the DRR method was adopted in Chapter 6. The CT based pipeline produced virtually no cases of custom tibia plates with maximum OUH $\geq$ 3 mm, and only 7.1% of femur components breached this threshold (when tested on over 80 subject bones). Such results were also considerably better than the theoretical best possible calculated for OTS implants (based on the analysis in Chapter 4), as well as potentially better than those reported for non-automated, CT based customisation solutions. In addition, the automated process was demonstrated to consistently take less than 10 minutes which would help save a significant amount of the current 6 – 8 week lead times currently associated with customisation solutions (Seekingalpha.com, 2019). In summary, using CT data as an input to an automated knee replacement implant shape customisation pipeline was therefore shown to offer a robust solution which could afford high quality outcomes for most patients, with reduced time and resource requirements compared to currently available workflows.

Chapter 9

CT Based Implant Stiffness Customisation Pipeline

The following chapter presents a method for, and results of, an automatic knee replacement implant stiffness customisation pipeline, using CT scans as an input medium.

Most of the contents of this chapter have been published in the following paper:

- Burge, T.A., Munford M.J., Kechagias S., Jeffers, J.R.T. & Myant, C.W. (2023) Automating the customization of stiffness matched knee implants using machine learning techniques. *The International Journal of Advanced Manufacturing Technology.*

9.1. Introduction

Thus far, the focus of the customisation pipelines developed has been on optimising the shape and fit of TKR implants. However, as previously detailed in Chapter 2.4, the stiffness of these products can also be customised to further optimise performance. Implants incorporating lattice structures matched to the stiffness of subjects' bones have been shown to form a mechanical environment closer to natural trabecular bone than traditional solid components, enabling stresses and strains to be better distributed (Munford et al., 2022). These porous structures with localised strain gradients can promote positive bone remodelling and reduce resorption, thereby reducing the probability of early revisions being required (Elliott et al., 2016).

As highlighted previously, authors have outlined methodologies for how the design of lattice structures can be matched to the stiffness of trabecular bones via the use of imaging mediums containing spatial density information, predominantly CT scans (Ghouse et al., 2019) (Munford et al., 2020). Munford et al. (2022) also demonstrated that implant stiffness could be matched at differing levels, such as uniformly to a calculated average across the resected bone interface, as well as being graded to replicate differences in native condyles and subchondral depth. Nonetheless, no studies were found that detailed how the design of such lattice structures could be automated to address the significant amount of time necessary to manually process CT scans, calibrate, and extract the density information needed to design custom stiffness implants. This chapter therefore sought to explore how automated implant stiffness customisation could be facilitated by adopting the AI/ML techniques outlined throughout the previous chapters. It should be noted that the focus and novelty of the work was not on the design of the implant lattice structures themselves, but on how the required density information can be extracted from volumetric medical images, calibrated, and converted to stiffness data in a fully automated manner. The stochastic lattice design method developed by Kechagias et al. (2022) was then adopted to facilitate an automated end-to-end workflow for generating stiffness matched implant designs.

Although both X-ray and CT images contain density information, the latter does so with a high degree of 3D spatial accuracy. It also allows for axial cross sections to be taken at precise locations on the anatomy so trabecular and cortical bone can be differentiated (Whitmarsh et al., 2011). The implant stiffness customisation pipeline was thus developed solely for CT scans. Furthermore, the proof-of-concept framework was developed purely for TKR tibia plates due to their lower geometrical complexity and 2D interaction with the bone.

9.2. Pipeline Development and Test Method

In the following sub-sections, the various stages of the CT based knee replacement implant stiffness customisation pipeline (summarised in Figure 83) are outlined. Details of the data used to train, and subjects used to test the pipeline are also provided.

9.2.1. Pipeline Training Data and Test Subjects

Of the datasets available, only the four CT scans retrieved from the Charing Cross Hospital contained material density phantoms (further detailed in Chapter 3.2.3). Three of these scans were used to train various modules within the pipeline, whilst the fourth was kept separate to be used as a test subject. Additional CT scans were taken from the KISTI dataset to train aspects of the pipeline that did not require a density phantom to be visible within the image.

9.2.2. Identify Slice of Interest in CT Stack

To enable the pipeline to extract density information at the point a tibia plate would interface with a resected tibia bone, the relevant CT slice from the DICOM image stack first needed to be identified. This was completed in much the same way as the process outlined in Chapter 8.2.2 for the CT based implant shape customisation pipeline in which the tibia-femur transition point was found. The steps equivalent to those in Figure 73 are highlighted in green in Figure 83. The updated models and workflow implemented for this pipeline are described as follows.

To better work with CT slices containing a density phantom, a new image classifier model was built using the same architecture outlined in Figure 75. The model was trained in line with the process described in Chapter 3.4.1 with 4,374 CT slice images obtained from the three Charing Cross CT DICOM files designated for training. The images were categorised into the same four classes (‘Fibula/Tibia’, ‘Knee’, ‘Femur’, and ‘Other’) as before (Figure 74B). Due to the limited diversity in the training data (three CT scans), model validation was completed using 1,463 slice images from the scan reserved for testing the full pipeline. This is not best practice for training AI/ML models as it can lead to overfitting and misleading results. However, for the proof-of-concept, it was deemed acceptable in lieu of more data being available.

An updated boundary box regression object detection model was created (using the same architecture shown in Figure 76) to identify the (160 x 160 pixel square) ROI around the left knee (as detailed in Figure 74C). 138 CT slice images (containing density phantoms) from the ‘Knee’ regions in the three Charing Cross CT scans were labelled using the method detailed in Chapter 3.4.2 and used for training. Like for the updated classifier model, validation was performed using 45 labelled images taken from the one test scan. As before, the pipeline was developed solely for the left knee to take advantage of the symmetry between the two sides of the human body. Therefore, if the right knee was required, a horizontal transform was applied to the slice images in the pipeline before the object detection model was used.

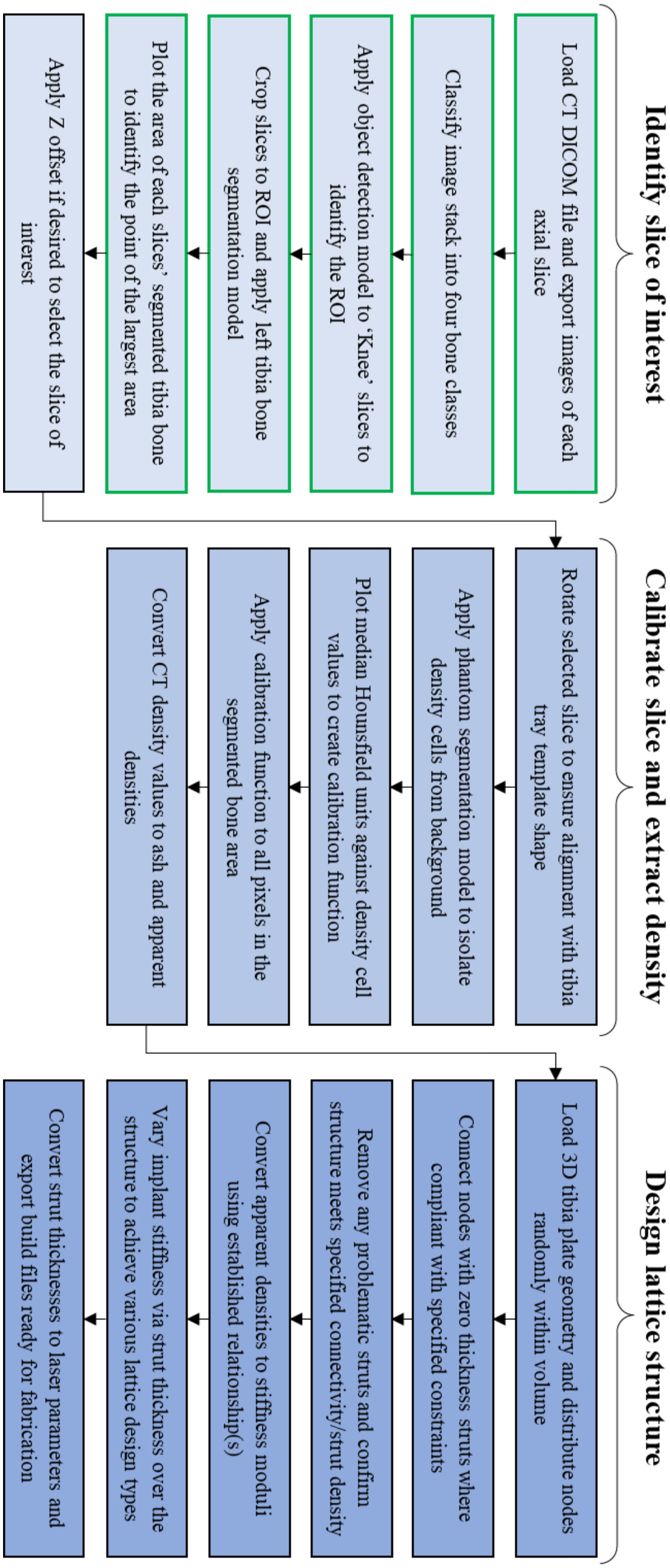

Figure 83: Key stages of the CT based implant stiffness customisation pipeline

After the average ROI across all slices in the 'Knee' section was identified in the same way as described in Chapter 8.2.2, the slice images were cropped to size. A segmentation model was then used to isolate the bone area from the background in each of the slices (like illustrated previously in Figure 77A). Since the cropped images no longer contained phantoms, the same left tibia bone segmentation model outlined in Chapter 8.2.3 (trained using data obtained from the KISTI dataset) was used. The femur segmentation model was not used in this pipeline since accurate segmentations of the femur were not needed. After segmentation, the tibia bone cross-sectional areas (in terms of pixel count) were plotted through the stack as shown in Figure 84. As in Figure 78, a univariate spline curve is shown fitted to the results to reduce slice-slice noise and enable the position of the maximum bone area to be identified more reliably. If an offset was specified by the user to position the implant more distally or proximally on the tibia, the pipeline accounted for this before the slice of interest was selected.

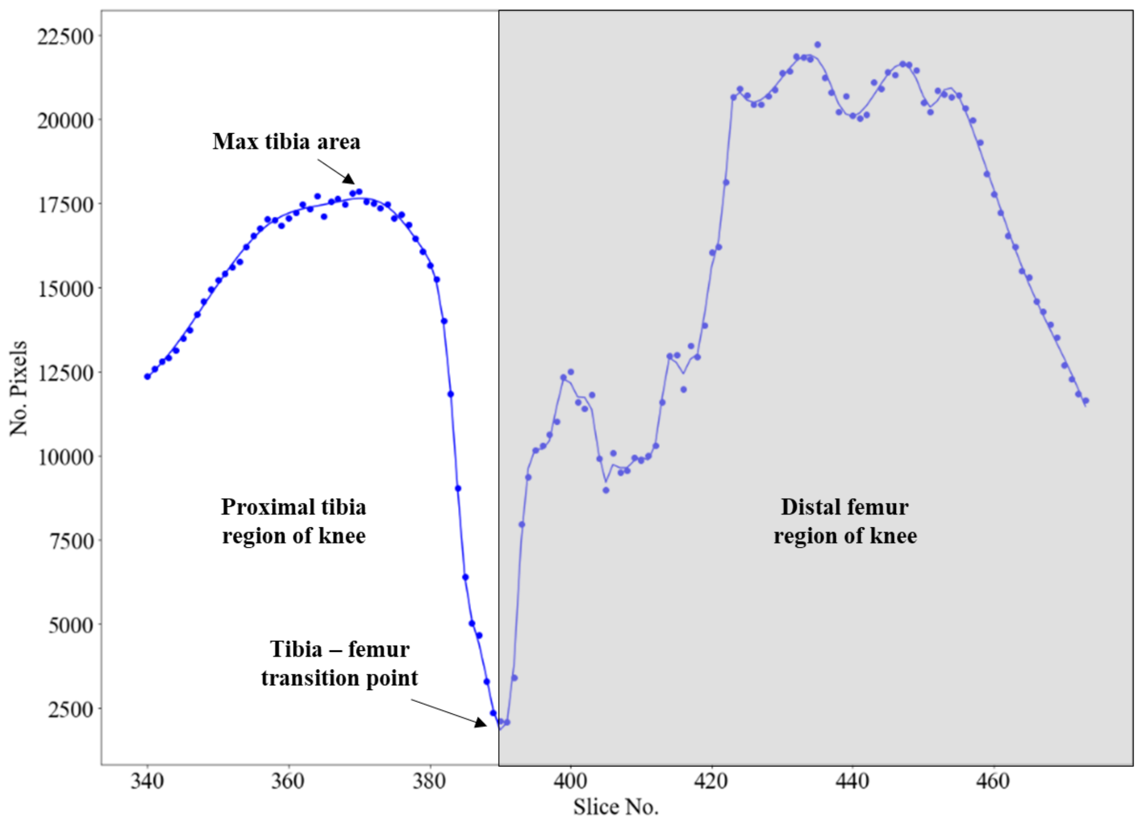

Figure 84: Number of pixels within segmented tibia bone area for each slice within the 'Knee' region of a CT scan © (Burge et al., 2023c)

9.2.3. Calibrate Selected CT Slice and Extract Density Information

Before selected slices could be calibrated and density information obtained, their orientation was adjusted in the pipeline to account for variability in patients' positioning during imaging and ensure the bone was aligned in a consistent way. To achieve this, the segmented 2D bone area from the selected slice (Figure 85A) was rotated (Figure 85B) and fitted via a rigid ICP method (detailed in Chapter 3.7) to a template tibia plate shape of known alignment (Figure 85C). The calculated rotation was then applied to the selected slice image (Figure 85D).

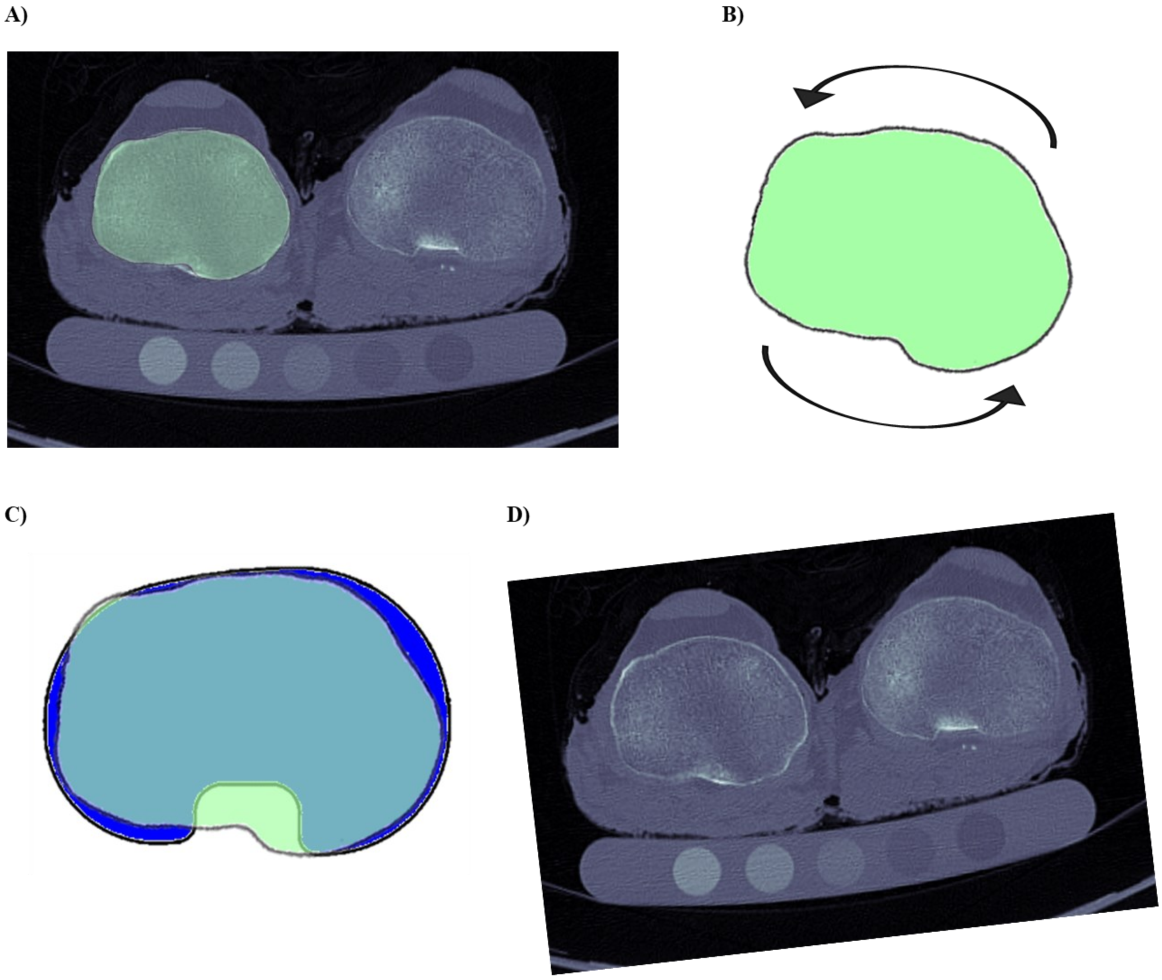

Figure 85: A) Segmented 2D bone area from selected CT slice, B) Rotation of segmented bone, C) Segmented bone rotated to fit a template tibia plate, D) Rotated selected slice

Next, a further segmentation model was created using the same CNN architecture as used in Figure 47. This was applied to the aligned selected slice image to isolate the five phantom material cells from the background detail (illustrated in Figure 86). To train the density cell segmentation model, 384 slice image/mask pairings were created (following the process detailed in Chapter 3.4.3), utilising images from the 'Knee' region in the three Charing Cross CT scans, along with 133 pairs from the test scan for validation.

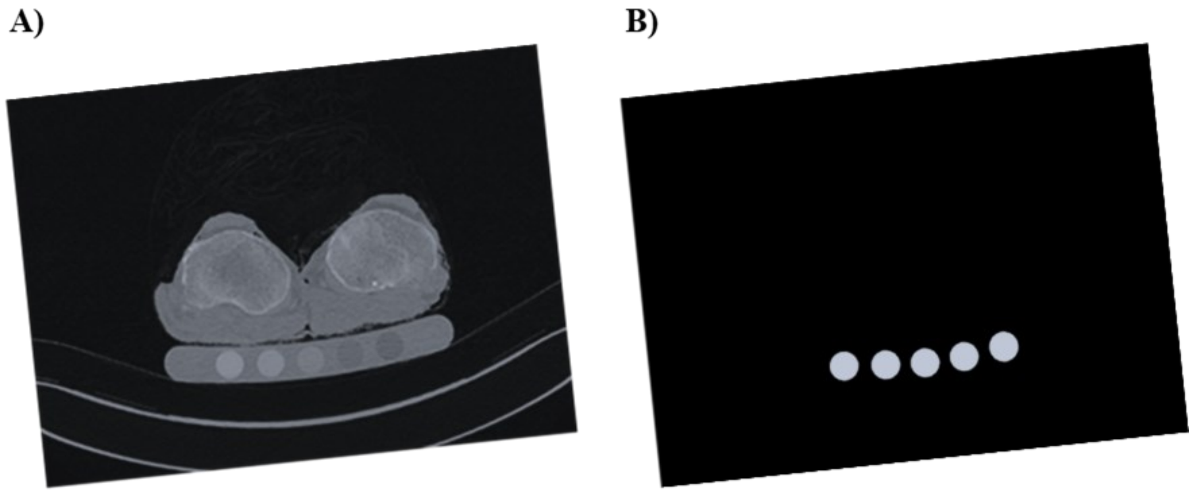

Figure 86: A) CT scan image, B) Density phantom cells segmented from background

Once isolated, the median pixel intensity values within each segmented circle, in terms of Hounsfield units, were calculated. A linear function relating the known densities of the phantom's five K_2HPO_4 cells, adjusted for water content, against the calculated Hounsfield unit values could then be plotted as demonstrated in Figure 87. Using the function of the plot, the pixels in the segmented cross-sectional bone area of the selected CT slice (Figure 85A) could then be calibrated in line with the approaches detailed in (Ng et al., 2019), as illustrated in Figure 18, and (Munford et al., 2020).

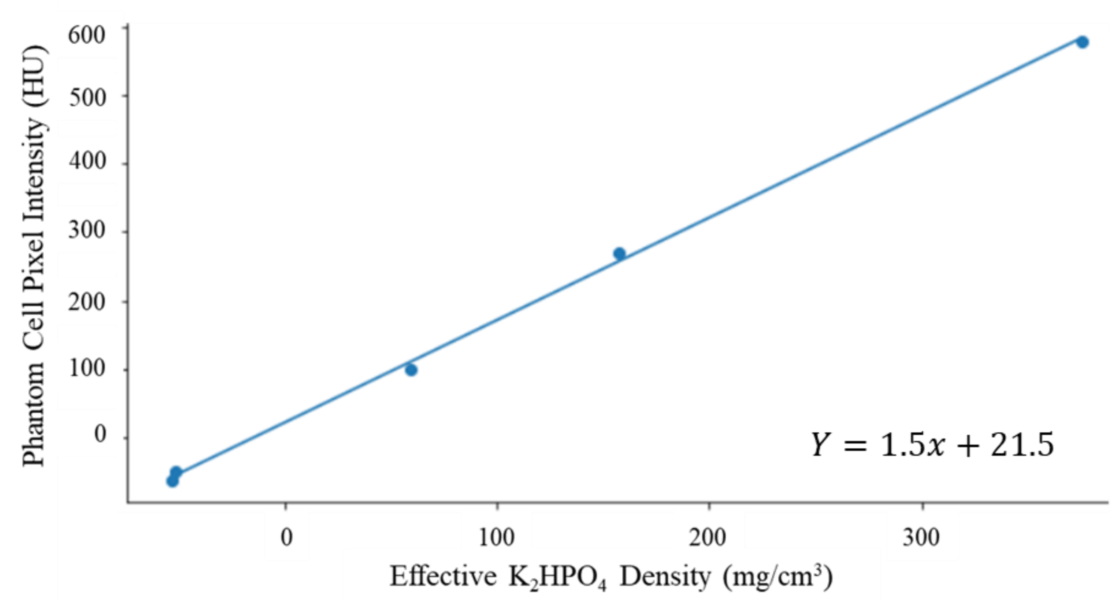

Figure 87: Plot of density phantom cell pixel intensities (adjusted for water) vs. effective K_2HPO_4 density © (Burge et al., 2023c)

To correspond better with the density of porous trabecular bone structures, the pipeline adjusted the calibrated density values of each pixel from the CT scan image (ρ_{CT}) to ash (ρ_{Ash}), and then apparent (ρ_{App}) densities using Equation 8 and Equation 9 shown below from (Munford et al., 2020).

Equation 8: Calculation of ash density

$$\rho_{Ash} = 1.22\rho_{CT} + 52.6$$

Equation 9: Calculation of apparent density

$$\rho_{App} = 1.64\rho_{Ash} + 10$$

Multiple lattice infill design styles were explored which are illustrated in Figure 91 and Figure 92. To facilitate these designs, first a global average apparent density, taken over the full cross sectional bone area, was calculated. The bone area was then split into the left and right condyles (using a midline created using global Min and Max functions) and mean apparent densities for each were recorded. Lastly, the bone area was split into an array of a specified number of columns and rows (25 x 20) and mean apparent density values for each cell within the array were calculated. This was investigated in 2D on the selected slice only as well as through the thickness of the tibia to form a 3D density array by repeating the process for each slice distally from the selected slice down axially through the length of the tibia bone for the height of the tibia plate component.

9.2.4. Design Implant Lattice Structures

The method used for creating the lattice designs was adopted from the approach outlined by Kechagias et al. (2022), shown in Figure 19. A stochastic lattice with randomly distributed nodes was utilised over a more regulated (periodic) structure to better mimic the biological randomness of bone and to enable a greater degree of control over the stiffness distribution.

To characterise the 3D volume of the tibia plate, a simplified version of the generic design shown in Figure 57 was utilised for the proof-of-concept. However, the pipeline could be adopted for any tibia plate geometry. The 3D model was first loaded by the pipeline as a mesh (.stl file), as shown in Figure 88A. Then, using a series of reference points calculated using Min and Max functions, including the maximum left, right, top, and bottom component points, the mesh points were separated into those comprising of the plate (blue points), the pin (red points), and cut-out section (green points), illustrated in Figure 88B.

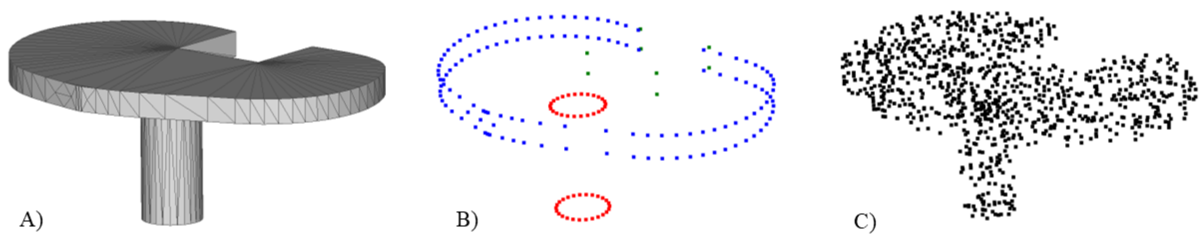

Figure 88: A) Generic tibia plate mesh model, B) Mesh points split into sections, C) Nodes randomly distributed within tibia plate volume © (Burge et al., 2023c)

To distribute nodes within the tibia plate model, the plate and pin volumes were first separated and enclosed in cuboids as defined by the reference points stated previously. Sufficient nodes were then distributed within the two cuboid volumes by setting random X, Y and Z coordinates within the constraints of the cuboids so that the required overall nodal density (d_{Nodes}) was achieved. This was calculated using Equation 10 with the target nodal connectivity (Z) and strut density (d_{Struts}) as struts/mm^3 specified as pipeline input parameters.

Equation 10: Calculation of nodal density

$$d_{Nodes} = \frac{2d_{Struts}}{Z}$$

A specified proportion of the nodes were forced to be allocated to the outer faces of the structure during the random distribution process to help ensure adequate structural integrity. Nodes found to be outside of the plate volume (minus the cut out), or pin, or that did not satisfy a Nearest Neighbour (Yianilos, 1993) criterion of $0.5 \leq x \leq 3$ mm, were eliminated. This distance criterion was used to help ensure a reasonable degree of homogeneity of nodes across the volume. The node distribution process was repeated iteratively until sufficient nodes had been inserted within the total tibia plate volume to satisfy the target nodal density (illustrated with a low density in Figure 88C).

After distributing the nodes, the pipeline then worked through each one systematically and assigned zero thickness struts between pairs that satisfied specified user constraints. The constraints consisted of minimum and maximum strut lengths (typically 0.5 and 3 mm respectively), the minimum angle between struts and the print bed (typically > 25° to ensure manufacturability via powder bed fusion), and maximum node connectivity (varied from between 4 – 8). The pipeline also checked to confirm that no struts were intersecting and removed any duplicates created between the same nodes. Once complete, a check was made for and removed any outstanding nodes that fell below a specified minimum connectivity to avoid floating struts which would not contribute to the lattice's mechanical response (typically 2). These steps were also repeated iteratively until all nodes present within the structure had at least the minimum specified connectivity.

As detailed in (Kechagias et al., 2022), the stiffness of a stochastic lattice structure can be controlled by adjusting the strut density, nodal connectivity, and/or the strut thickness. For simplicity, the pipeline was designed to keep the first two variables constant over the total tibia plate volume with solely strut thickness altered to achieve stiffness variation. Equation 11, taken from (Munford et al., 2020), was used to estimate the apparent stiffness modulus (*E*) from the apparent density (ρ_{App}) data extracted from the earlier stages of the pipeline.

Equation 11: Calculation of apparent stiffness modulus

$$E = 0.9{\rho_{App}}^{0.55}$$

For the lattice structure to have the same stiffness (*E*) as a patient's trabecular bone, its relative density ($\tilde{\rho}$), which is the ratio of its apparent density to solid material's density, first needed to be estimated. Relative density was calculated using power-law regression models in the form of Equation 12 where the values of a (71598.2) and b (2.22) depended on the lattice's localised connectivity (Kechagias et al., 2022).

Equation 12: Form of relative density

$$\tilde{\rho} = \sqrt[b]{\frac{E}{a}}$$

Equation 13 then allowed for the required strut thicknesses (*t*) for the various lattice designs to be calculated for given E values, with node connectivity (*Z*) and strut density (d_{Struts}) kept constant (Kechagias et al., 2022).

Equation 13: Calculation of strut thickness

$$t = \frac{\sqrt[b]{\frac{E}{a}} - 0.0110Z - 0.0252d_{Struts} + 0.344}{1.29}$$

9.3. Pipeline Test Results and Discussion

To test the performance of the implant stiffness customisation pipeline, its accuracy when selecting the CT slice of interest and ability to generate various lattice designs were evaluated.

9.3.1. Accuracy of Identifying CT Slice of Interest

To verify the accuracy of the implant stiffness customisation pipeline in terms of identifying the correct CT slice where the tibia plate would interface with the bone (Section 9.2.2), segmentation results for both knee sides from the test CT scan were compared with those obtained manually. The analysis is shown in Figure 89 and is limited to the results for the tibia condylar regions for clarity. It is demonstrated that (for the one test CT scan) the pipeline was able to closely replicate the manual segmentation and slice selection to within one slice (0.6 mm in terms of Z positioning) for both knees.

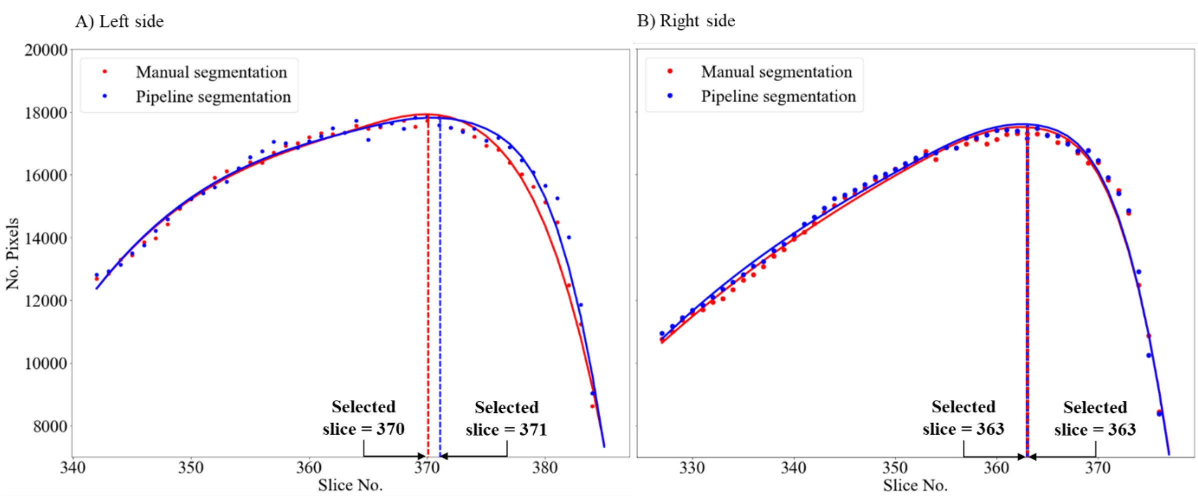

Figure 89: Number of pixels in segmented bone area by slice number for manual and automatic methods. A) Left knee side and B) Right knee side © (Burge et al., 2023c)

Figure 90 shows the outputs from the manual (A) and automated (B) processes to demonstrate the negligible difference in the selected slice of interest a discrepancy of one slice (0.6mm axial distance in this case) would have. To further quantify the difference, the global mean apparent densities for the two slices were calculated using the method detailed earlier in this chapter. The manual approach resulted in a density of 233 mg/cm^3, whilst the automated approach predicted 240 mg/cm^3 – a 3% difference. It should be noted that if a CT scan with a larger axial spacing between slices was used then a discrepancy of one slice may be more impactful. That being said, the greater difference between neighbouring slices likely associated with lower resolution scans would also make identifying the correct slice more reliable.

A) B)

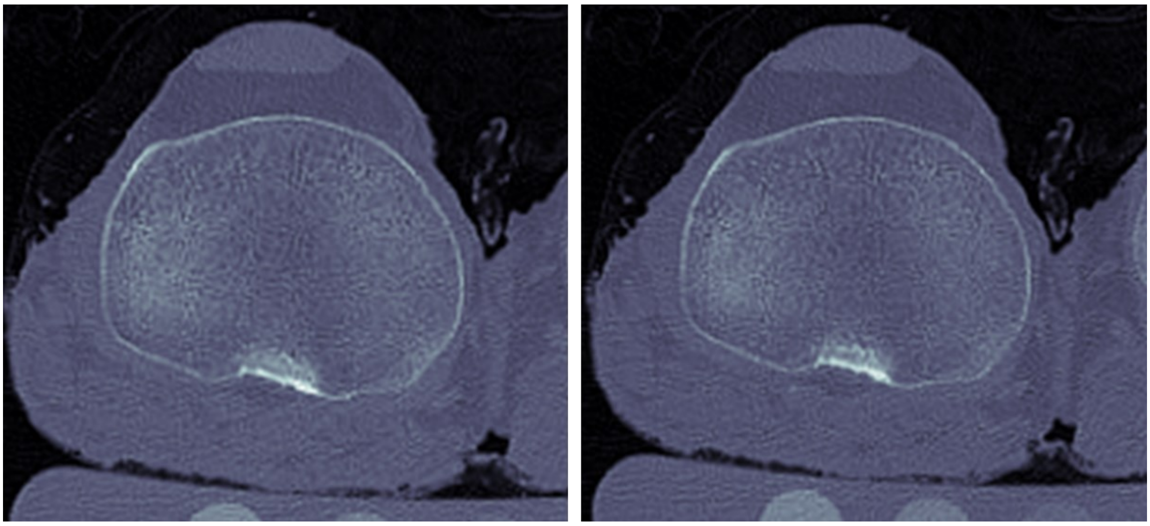

Figure 90: A) Left knee slice selected via manual approach (slice 370), B) Left knee slice selected via automated approach (slice 371)

A limitation of the pipeline that should be noted is that a consistent density phantom was needed in the inputted scans to ensure compatibility with the segmentation models. This could however be addressed by training the pipeline with slice images containing a range of commonly used phantoms.

9.3.2. Generation of Implant Lattice Designs and Prototypes

Using the methods outlined above, different lattice design styles were produced for each knee side reflecting the density distribution in the selected CT slices (an example for the left side is shown in Figure 91A). Figure 91B demonstrates a structure with a consistent global mean strut thickness. Figure 91C demonstrates a structure with left and right condyle mean strut thicknesses. Lastly, Figure 91D demonstrates a structure with strut thicknesses mapped over the slice as a 25 x 20 cell array. It is clear in Figure 91C that the struts on the left (lateral) side are considerably thicker than on the right (medial). Moreover, in Figure 91D the strut thicknesses over the area correspond well with the denser (brighter) regions of the bone visible in Figure 91A, particularly around the contact point with the lateral femur condyle.

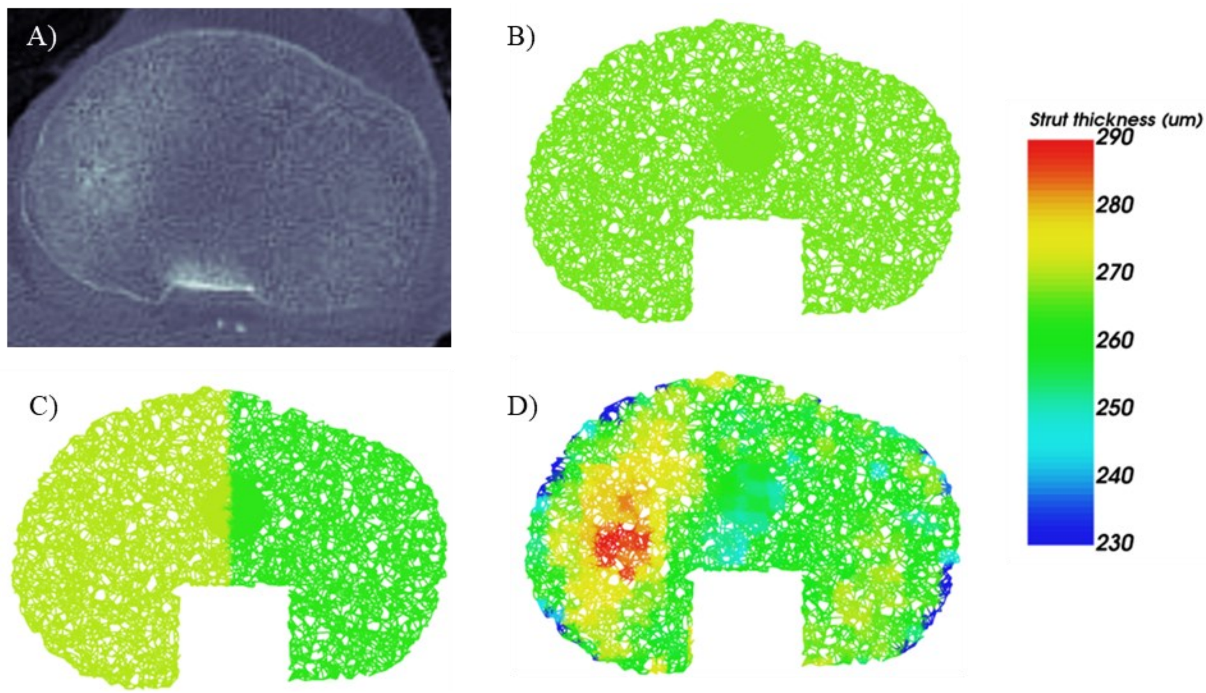

Figure 91: A) Selected CT slice cropped to ROI, B) Global mean strut thickness, C) Left and right condyle mean strut thicknesses, D) Strut thicknesses mapped over the slice area © (Burge et al., 2023c)

Figure 92 demonstrates a lattice design created using a 3D density array. In this example, the struts in the pin can be seen to be thinner compared to the proximal (top) surface of the plate as the density of the tibia trabecular bone reduces distally from the condylar plateau.

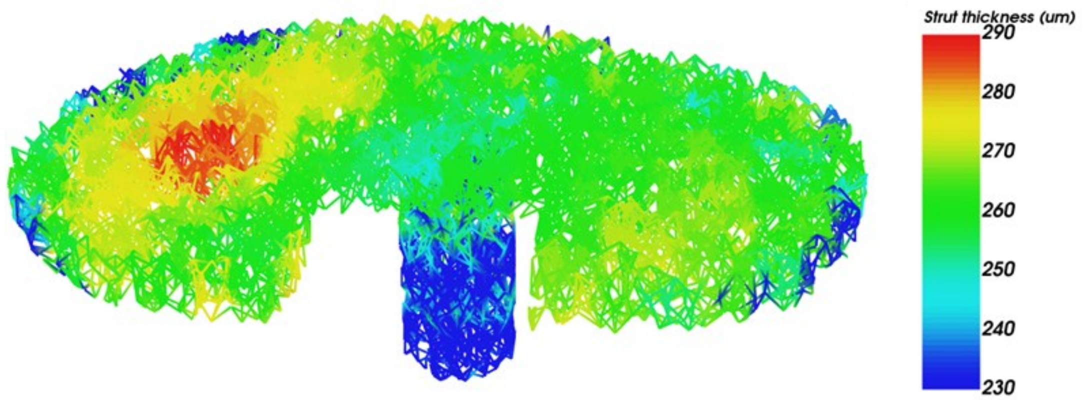

Figure 92: Strut thicknesses mapped in 3D through the tibia bone © (Burge et al., 2023c)

Prototype designs to trial the full implant stiffness customisation pipeline were fabricated using the process detailed in Chapter 3.13. The resulting structures, employing a constant target connectivity of 6, minimum connectivity of 2, strut density of 3 struts/mm^3, minimum strut angle 30°, but varied strut thickness, are shown in Figure 93. The structures in Figure 93A correspond to the left and right condyle mean strut thicknesses design shown in Figure 91C, while the structure in Figure 93B was designed with strut thicknesses mapped across the bone cross section like in Figure 91D. Figure 93C shows the full lattice structure of a prototype tibia plate.

It was identified that, as the angle of the CT slice images (and therefore the density information extracted) was determined by the positioning of subjects' anatomies during the imaging process, errors in stiffness matching could potentially occur if the intended bone resection angle was substantially different. An imaging protocol to control anatomical alignment, like proposed for the X-ray based pipelines, may therefore be required to ensure optimal results.

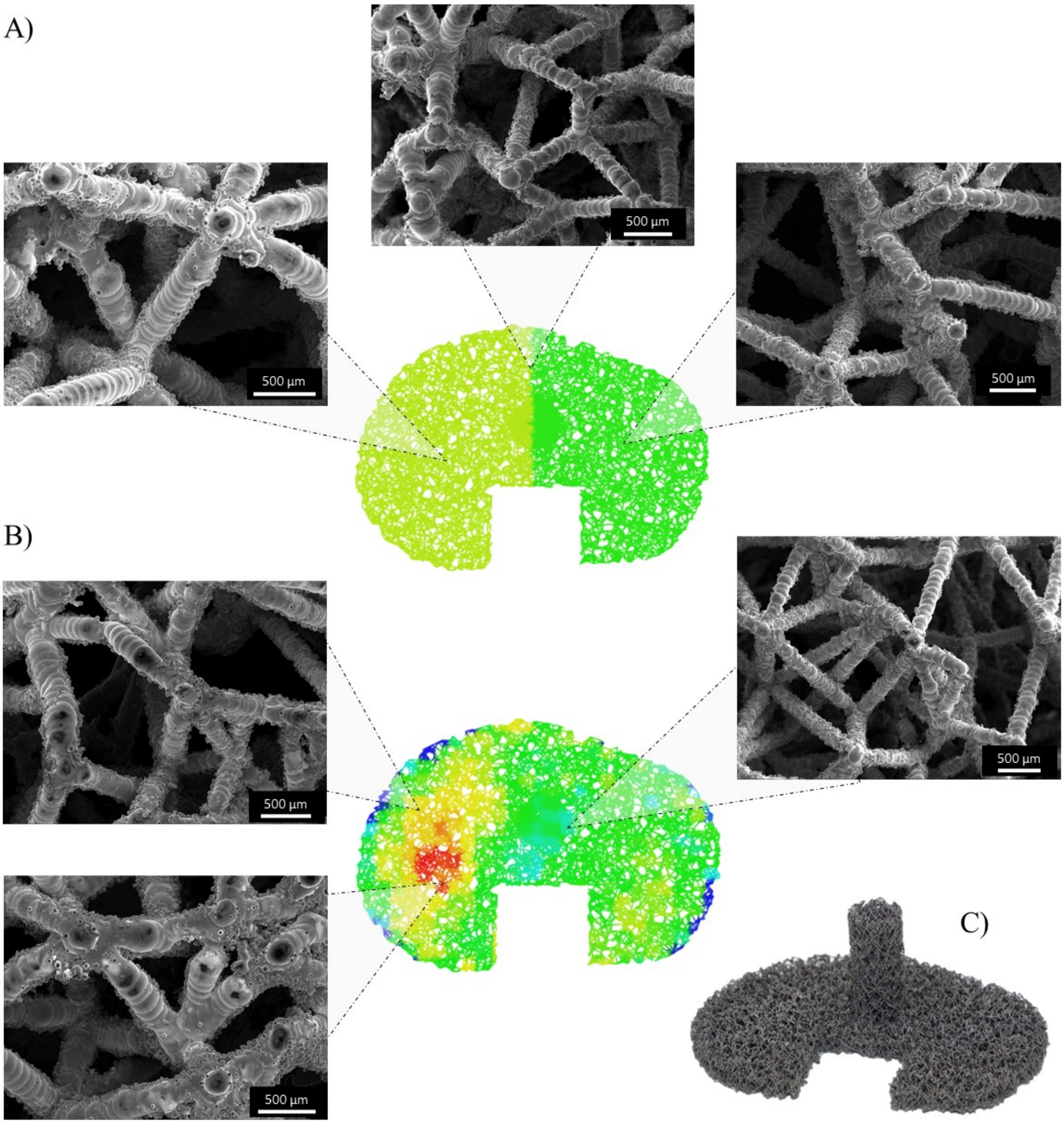

Figure 93: A) & B) show regions of the two prototyped customised lattice designs, imaged via scanning electron microscopy. C) Shows a full prototype lattice structure © (Burge et al., 2023c)

9.3.3. Pipeline Computational Requirements

The computational requirements of the implant stiffness customisation pipeline were evaluated by running the process on a personal laptop computer (2.38 GHz AMD Ryzen 5 4500U CPU with 6 cores/8 GB memory). For the first stage (processing the inputted CT scan and selecting the appropriate slice), the pipeline was found to take between 7 – 8 minutes. Following this, between 1 – 2 minutes were required to align the selected slice, calibrate the image, and export the density information. The time taken to generate the lattice structure designs constituted the greatest proportion of the total computation time and depended on specified connectivity and strut density targets. Figure 94 shows the relationship observed between computation time to generate the lattice designs and both these lattice design parameters. Consistent minimum and maximum strut lengths (0.5 and 3 mm), minimum strut angle (30°), and minimum connectivity (Z = 2) were used for the analysis. For reference, Figure 93C shows a lattice structure built with these parameters.

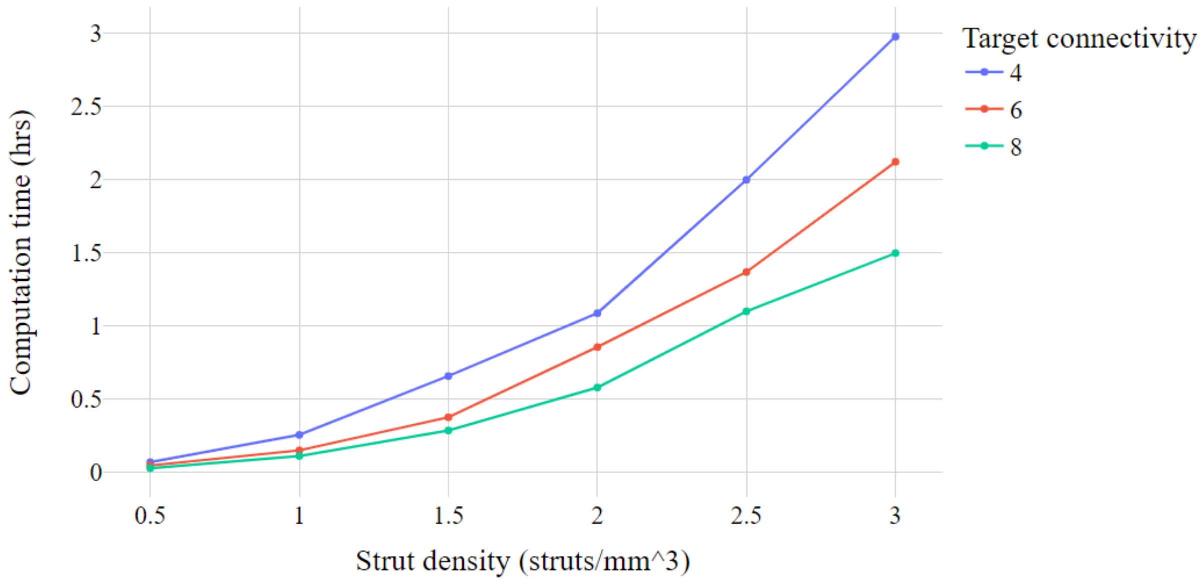

Figure 94: Relationship of computation time to generate lattice structures with differing strut densities and connectivity © (Burge et al., 2023c)

Due to the intricacy of the stochastic lattice structures, conventional CAD packages run on computers with standard graphics cards would struggle to render the enormous number of resulting faces if such structures were modelled as solids (Munford et al., 2022). Furthermore, achieving lattice designs like shown in Figure 93 via a manual approach would take an immense amount of time and would be practically unworkable. These issues were overcome, enabling a time efficient process, by adopting the automated, script based approach to design lattices with zero thickness struts, adopted from (Kechagias et al., 2022).

9.4. Summary

In this chapter, the ability to customise the mechanical properties of implant components to match the stiffness distribution in subjects' bones to a range of fidelities, via the use of CT scans, was demonstrated. The pipeline was shown to be able to accurately identify the CT slice of interest from a DICOM file and obtain the density information necessary to generate various lattice designs with differing levels of stiffness matching, all without any user input required. Although a range of customisation levels were shown possible via the workflow, it should be noted that Munford et al. (2022) indicated lower levels, such as lattices matched to uniform mean stiffnesses, may be sufficient to achieve adequate stress/strain distribution and promote bone remodelling effects. Further mechanical and clinical testing would therefore be required to fully understand the benefit of the different customisation options exemplified. Computation time was shown to take, at maximum, three hours when run on a personal laptop computer when a dense lattice infill was specified. This time, although already significantly lower than that required to complete the customisation process manually, would be significantly less if the pipeline was run on a high-performance computer. It is therefore believed that the potential elimination of manual work, high design flexibility, and low computational time requirements facilitated through the proposed pipeline, could offer significant cost and resource savings over previously published manual methods.

Chapter 10

Conclusion

In this chapter, the various knee replacement customisation pipelines developed are compared and the main findings of the research are concluded. The feasibility of a true, mass-customisation solution for knee replacement is discussed and suggestions for future work are given.

10.1. Review of Customisation Pipelines Developed

In this research, various knee replacement customisation pipelines were developed to work with two commonly used medical imaging mediums: X-rays and CT scans. Using the former as input would offer the significant benefit of not requiring any additional imaging than what is currently adopted for most knee replacement pre-operative assessments. Fully automated implant shape customisation and OTS size prediction pipelines were shown to be feasible using the 2D medium as input, as detailed through Chapters 5 – 7. Although initial results for shape customisation were not found to afford meaningful improvements on the theoretically best possible performance for standard OTS products (based on the analysis in Chapter 4), superior performance was recorded when X-ray alignment and calibration were artificially controlled utilising the DRR method in Chapter 6. Furthermore, the performance of the pipeline was shown to likely not be significantly impacted by demographical attributes including subject sex, knee side, age, and height. Nevertheless, the sensitivity analysis conducted in Chapter 6 highlighted accuracy was highly dependent on the quality of inputted X-rays, meaning consistent anatomical alignment and accurate X-ray dimensional calibration with tight specifications would be needed to ensure quality results. Nguyen et al. (2022) demonstrated such requirements could be achieved via the adoption of an imaging protocol, however, the additional admin incurred may limit the viability of this for implant shape customisation in practice. In terms of OTS implant size prediction, the X-ray based pipeline was shown to substantially improve upon selection accuracies reported for current manual based approaches, even when real X-rays were used as input. Better implant size prediction accuracies were also obtained compared to other semi and fully automated software based solutions.

Chapter 8 explored the benefits of using CT imaging as an alternative input to biplanar X-rays. Although CT would expose patients to significantly higher doses of radiation, increase imaging costs and lead times, and access to the imaging equipment is not as widely available as X-ray, the enhanced geometrical information available was demonstrated to afford significantly more accurate 3D bone model reconstructions. Mean reconstructions of 1.09 mm (femur) and 0.98 mm (tibia) RMSE were recorded for the X-ray based pipeline. Whereas 0.87 mm (femur) and 0.80 mm (tibia) RMSE were recorded for the CT based pipeline. This subsequently enabled customised implants to be produced with on average 7.1% of cases of maximum OUH ≥ 3 mm for the femur and just 1.2% for the tibia, compared with 18.0% and 9.0% respectively when X-rays were used. Furthermore, the results for the CT based pipeline were found to be comparable, or potentially better than, those reported for currently available (non-automated) solutions. However, due to the data available for testing, it was not possible to complete a demographical results analysis as thorough as was done for the X-ray based pipeline. As such, the pipeline's sensitivity to different ethnicities and arthritis severities could not be quantified. More accurate OTS implant size predictions would most likely be achievable using the CT based pipeline. This was however not evaluated in depth since the analysis in Chapter 7 demonstrated that size prediction accuracy was directly correlated with reconstruction accuracy. In addition to the benefits afforded by increased geometrical information, using CT over X-rays would also reduce the need for tightly controlled anatomical alignment and no dimensional calibration would be required. This could afford benefits in terms of resourcing and would minimise the possibility of human error being introduced into the process.

By using CT data, the ability to automatically customise the mechanical properties of implants with lattice structures closely mapped to the stiffness gradients in subjects' trabecular bones was demonstrated. Despite this, whether such a high level of stiffness customisation would really be needed to achieve the outcomes argued possible by Elliott et al. (2016) is unconfirmed. An alternative form of imaging for this application could be 'Dual-Energy X-Ray Absorptiometry' which, due to the datasets available, was not possible to explore in this research. Such imaging would not offer the same degree of density and geometry accuracy, but would avoid the inherently high radiation exposure and costs associated with CT (Whitmarsh et al., 2011) (Grassi et al., 2017). Additionally, depending on the level of accurateness needed to achieve successful patient outcomes, another option could be to use a statistical or AI/ML based model trained using density/stiffness data from a range of subjects with differing ages, sexes, and ethnicities.

Using CT data as input was found to incur slightly higher computation times compared to the X-ray based pipelines. Nevertheless, both the X-ray and CT based implant size prediction and shape customisation pipelines were found to take under ten minutes from image files being inputted to producing the desired outputs. This was negligible compared to the hours needed to complete the process manually. Significantly more computation time was necessitated for the stiffness customisation pipeline due to the complexity of generating stochastic lattice designs, especially when high strut densities were specified. The time requirements associated with this could however be greatly reduced if additional compute power was available.

In conclusion, both the X-ray and CT based automated customisation pipelines developed in this research presented various opportunities to save costs, lead times, resource, and afford improved outcomes for patients compared to currently available manual or semi-automated solutions. Instead of picking one over the other, the X-ray and CT based customisation solutions could be offered in tandem, allowing users to choose their input preference (given the highlighted advantages and disadvantages of each), or to simply use what is available to them. The implant size prediction and shape customisation pipelines could also be used in partnership. For instance, the former could be used initially to estimate whether satisfactory results could be obtained using the best size available from a particular manufacturer's OTS model, before deciding whether an alternative product or full customisation would be needed.

10.2. Towards a Mass-Customisation Solution

The main objective of this research was to develop both X-ray and CT based, fully automated mass-customisation pipelines for knee replacement. The various pipelines outlined were built in a consistent way which did not require users to segment inputted images, select reference points, guide live wire programmes to extract bone contours, or assist in the design of customised implants. Users simply need to input X-rays or CT scans, and the algorithms operate autonomously. Moreover, various degrees of customisation were exhibited including implant size prediction, as well as shape and stiffness customisation. It is believed that these reflect the 'patient-matched' and 'custom-made' levels described by Paxton et al. (2022) and satisfy the 'holy grail' of medical implant customisation (Figure 13).

In addition to automating the customisation of products, it was argued by Da Silveira et al. (2001) that efficiency in information transfer from customers to manufacturers can determine the success of mass-customisation programmes. Since the various pipelines developed in this research required an understanding of Python coding to operate, a software application with a simple GUI was developed and is outlined in Appendix 1. The software brings together the X-ray and CT based pipelines into one easy to use interface which requires no knowledge of programming and is intended to demonstrate how the solution could be integrated into hospitals and/or healthcare practises. Users (clinicians) could easily upload their choice of patient image data and then use the software GUI to determine the most appropriate OTS implant sizes, customise the shape of implant components, and/or customise stiffness. Thereby facilitating the way of working suggested at the end of the previous section. Outputted implant build files could be sent directly by the software to a contract manufacturer for production and finished components delivered back to hospitals. Due to the high level of autonomy, flexibility in the level of customisation possible, ease of use, and potential for simple integration into the healthcare environment, it is believed that this constitutes a true mass-customisation solution for knee replacement in line with the definitions outlined by Davis (1989) and Da Silveira et al. (2001). Additionally, it is believed that the software GUI also exemplifies the three fundamental capabilities argued by Salvador et al. (2009) as necessary for a successful mass-customisation solution (ease of use, robust process design and choice navigation).

10.3. Significance of this Project

It was argued at the beginning of this thesis that prior works were all found to require some level of manual input to process images, and/or guide the implant customisation process. Consequentially, they fell short of meeting the definition of true mass-customisation solutions and this was likely a key reason for their relatively low market adoption. However, by adopting AI/ML and statistical techniques, it is believed that the first mass-customisation solution for knee replacement surgery has been developed through this research. The proof-of-concept software developed (outlined in Appendix 1) would not require extensive training or highly skilled users to operate and could be integrated easily into hospitals for clinicians to use. The accuracy of the underlying customisation pipelines was thoroughly evaluated across a broad patient population to validate the respective processes. Furthermore, by conducting a sensitivity analysis, the limits of the (X-ray based) solution were quantified and necessary imaging specifications defined. It is therefore believed that the proposed solution is robust and has the potential to save healthcare providers significant costs, resource, and lead times. It is hoped these benefits will enable knee replacement customisation to become more commercially viable so the numerous benefits can be realised by a larger proportion of patients.

To help illustrate the significance of this project and justify why it is believed to be the first true mass-customisation solution, Figure 95 provides an updated version of Figure 20 with the various customisation pipelines developed through the research project incorporated. The illustration shows the only comparable solution found to be fully automatic was the Traumacad Auto-Knee OTS size prediction tool, detailed previously in Chapter 2.2. As highlighted earlier however, this was shown to be highly inaccurate and unreliable (Seaver et al., 2020). The area shaded in red to the top right shows the customisation options of the software outlined in Appendix 1 are unmatched in terms of the level of automation and the choice of imaging input mediums (distinguished by dot colour). In addition to the cost savings likely enabled by being fully automatic, the imaging input choice afforded by the solution could be particularly important for developing countries where accessibility and the higher cost of CT imaging may be prohibitive. Having the option of implant customisation via X-rays as an alternative, with only a marginally lower performance, could therefore be a real game changer for these markets.

Lastly, although the focus of the research was on knee replacement implants, the automated customisation frameworks developed could provide significant opportunities for other medical products. For example, the pipelines could be modified and applied to many other therapy areas such as hip replacements, prosthetics (both orthopaedic and dental), surgical tools and guides, face masks, wrist splints and spine disks.

Based on the conclusions outlined above, it is believed that the objectives of the research project, outlined in detail in Chapter 1.7, were met.

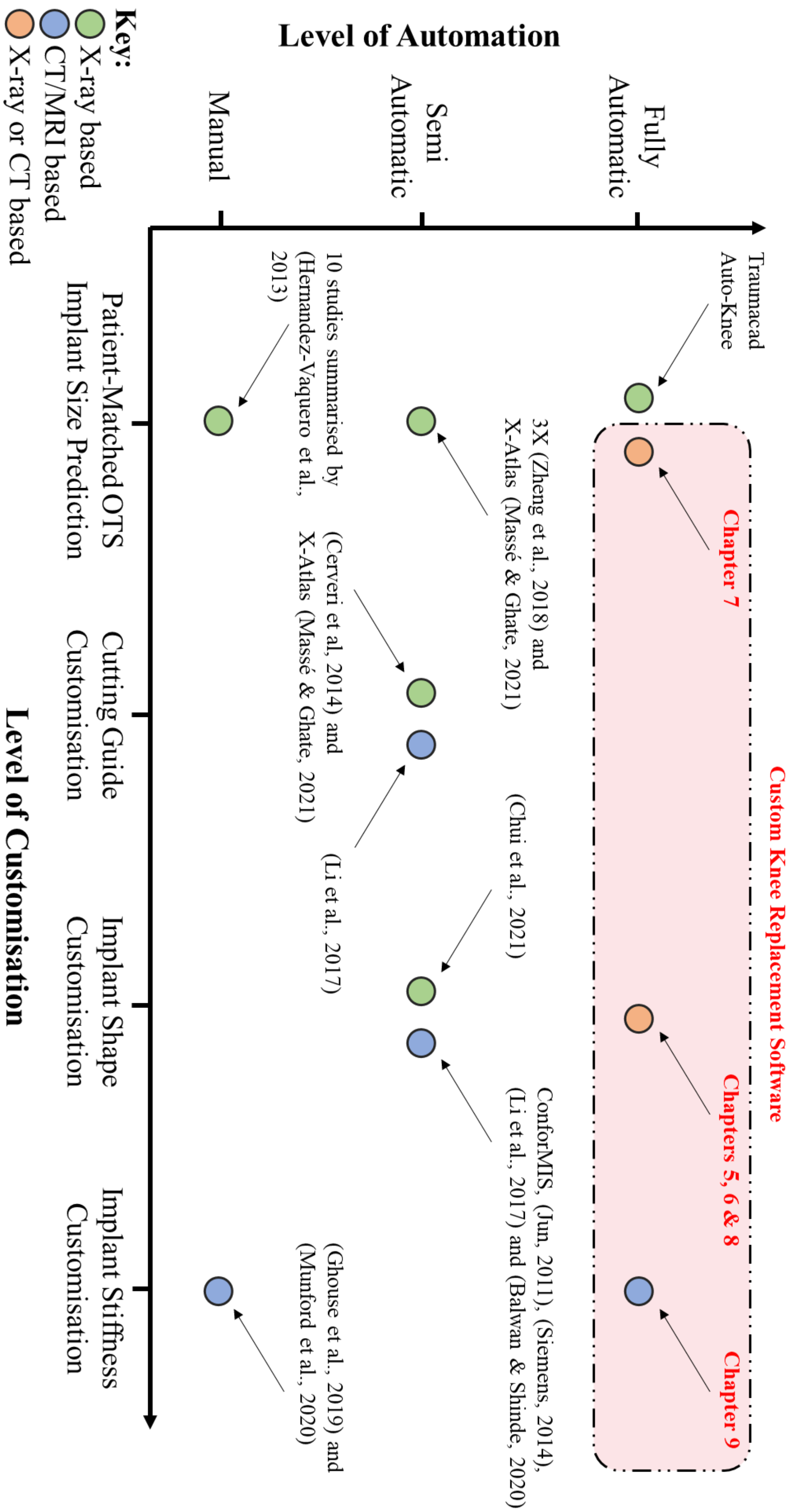

Figure 95: Comparison of thesis outputs with commercial products and research articles

10.4. Future Work

To enable the customisation pipelines to be better generalised and work more robustly across a wide range of patient demographics, a more diverse dataset including subjects from multiple backgrounds and imaged using numerous X-ray and CT machines could be established. This would be particularly useful for training the stiffness customisation pipeline where only four CT scans containing density phantoms could be sourced in this thesis. Collecting primary data, as opposed to solely using retrospective secondary data, would allow for properties such as anatomical alignment to be better controlled and for calibration objects to be included. A larger, more controlled dataset would also facilitate a more comprehensive evaluation of the pipelines to supplement and further validate the analysis performed in Chapter 6. In addition, future work could look to use methods for obtaining ground truth data with higher accuracies than the typical 0.5 mm RMSE possible from CT or MRI scans (Van den Broeck et al., 2014). For example, using hand scanning equipment with dissected cadaver bones to obtain 3D models with resolutions < 0.1 mm could be investigated (Cazon et al., 2014).

In this research, the performance of the various customisation pipelines was assessed purely via computational methods and no clinical work was completed. Factors such as poor surgical implementation were not considered and real patient outcomes, especially for subjects with moderate to severe arthritis damage, were not possible to evaluate. Physical prototypes of stiffness matched implant designs were fabricated. However, prototypes were not made using designs produced by the implant shape customisation pipelines and no mechanical strength testing was performed. Future work could therefore look to build on the computational approach by further validating performance via laboratory based and clinical means. Moreover, limited data for the performance of other customisation solutions was found to be available. To further quantify the benefit of the solutions developed in this work, partnering with the likes of ConforMIS to acquire further comparator data would be advantageous.

In terms of the customisation pipelines, future development could look to integrate finite element modelling to predict performance ahead of fabrication (Jun, 2011) (Peto et al., 2019). This could facilitate an iterative design optimisation cycle in which implant lattice structures and shapes are incrementally adjusted based on results obtained by simulating each iteration and calculating sensitivities. Additionally, the possibility of feeding patient and surgeon specific data not obtained from image/volume data, such as subject demographical details, information about subjects' lifestyles, and surgeon preferences over implant type/style etc., into the customisation pipelines, could also be explored to further improve performance.

In the literature, mass-customisation is described as broader than just customised design and manufacturing methodologies. Ferguson et al. (2014) argued that marketing and distribution should also be considered. Further work could therefore look at how the technology could be effectively promoted to healthcare providers, how the business model behind the implant customisation service should be structured, and how the designs produced could be supplied rapidly for surgery. Da Silveira et al. (2001) highlighted that mass-customisation solutions must be compatible with high volume production. Work could therefore further explore the proposal to use AM as a fabrication process and/or investigate the possibility of using other production methods. Further study into compatible build materials, post-processing required, sterilisation routes etc. could also be important areas to explore. Additionally, authors have studied the economics of mass-customisation (Laureijs et al., 2019). This was not investigated in depth in this research but would be valuable to further consider to ensure such a solution could be commercially viable.

Finally, the practical implications of certifying and commercialising a fully automatic knee replacement customisation solution should be further studied. The most significant challenge of bringing such a product/service to market would likely be the regulatory requirements associated with fully autonomous processes. For example, regulators may require each patient's custom implant designs to be evaluated by trained medical professionals and/or engineers before surgery. This could potentially diminish the cost, resource and lead time advantages gained from the automatic workflows and adjustments may need to be made to the pipelines to negate this. To progress the technology further, the proof-of-concept software and individual customisation pipelines outlined could be adapted for specific manufacturer models. Partnering with an implant manufacturer to trial this, as well as leveraging their regulatory and clinical trial expertise, could hence afford the most streamlined route forwards.

References

Abadi, M., Barham, P., Chen, J., Chen, Z., Davis, A., et al. (2016) TensorFlow: A System for Large-Scale Machine Learning. In: *Proceedings of the 12th USENIX Symposium on Operating Systems*. 2016 pp. 265–283. doi:10.1016/0076-6879(83)01039-3.

Abulhasan, J.F. & Grey, M.J. (2017) Anatomy and physiology of knee stability. *Journal of Functional Morphology and Kinesiology*. 2 (4). doi:10.3390/jfmk2040034.

Ahmed, S.M. & Mstafa, R.J. (2022) A Comprehensive Survey on Bone Segmentation Techniques in Knee Osteoarthritis Research: From Conventional Methods to Deep Learning. *Diagnostics*. 12 (3). doi:10.3390/diagnostics12030611.

Ambellan, F., Lamecker, H., von Tycowicz, C. & Zachow, S. (2019) Statistical Shape Models: Understanding and Mastering Variation in Anatomy. In: *Advances in Experimental Medicine and Biology*. pp. 67–84. doi:10.1007/978-3-030-19385-0_5.

Arnholdt, J., Kamawal, Y., Horas, K., Holzapfel, B.M., Gilbert, F., Ripp, A., Rudert, M. & Steinert, A.F. (2020) Accurate implant fit and leg alignment after cruciate-retaining patient-specific total knee arthroplasty. *BMC Musculoskeletal Disorders*. 21 (699), 1–8. doi:10.1186/s12891-020-03707-2.

Aspert, N., Santa-Cruz, D. & Ebrahimi, T. (2002) MESH: Measuring errors between surfaces using the Hausdorff distance. *Proceedings - 2002 IEEE International Conference on Multimedia and Expo, ICME 2002*. 1, 705–708. doi:10.1109/ICME.2002.1035879.

Baka, N., Kapteina, B.L., Giphartb, J.E., Staringc, M., de Bruijned, M., Lelieveldtc, B.P.F. & Valstar, E. (2014) Evaluation of automated statistical shape model based knee kinematics from biplane fluoroscopy. *J Biomech*. 47 (1), 122–129. doi:10.1016/j.jbiomech.2013.09.022.

Barratt, D.C., Chan, C.S.K., Edwards, P.J., Penney, G.P., Slomczykowski, M., Carter, T.J. & Hawkes, D.J. (2008) Instantiation and registration of statistical shape models of the femur and pelvis using 3D ultrasound imaging. *Medical Image Analysis*. 12 (3), 358–374. doi:10.1016/J.MEDIA.2007.12.006.

Basavaprasad, B. & Ravi, M. (2014) A Study on the Importance of Image Processing and Its Apllications. *International Journal of Research in Engineering and Technology*. 3 (3), 2321–7308. doi:10.15623/ijret.2014.0315029.

Beaman, J.J., Bourell, D.L., Seepersad, C.C. & Kovar, D. (2020) Additive Manufacturing Review: Early Past to Current Practice. *Journal of Manufacturing Science and Engineering, Transactions of the ASME*.142 (11) pp.1–20. doi:10.1115/1.4048193.

Berghe, P., Demol, J., Gelaude, F. & Sloten, J. (2017) Virtual anatomical reconstruction of large acetabular bone defects using a statistical shape model. *Computer Methods in Biomechanics and Biomedical Engineering*. 20 (6), 577–586. doi:10.1080/10255842.2016.1265110.

Beswick, A.D., Wylde, V., Gooberman-Hill, R., Blom, A. & Dieppe, P. (2012) What proportion of patients report long-term pain after total hip or knee replacement for osteoarthritis? A systematic review of Prospective studies in unselected patients. *BMJ Open*. 2 (1), 1–12. doi:10.1136/bmjopen-2011-000435.

Blatov, I.A., Kitaeva, E. V., Shevchenko, A.P. & Blatov, V.A. (2019) A universal algorithm for finding the shortest distance between systems of points. *Acta Crystallographica Section A: Foundations and Advances*. 75, 827–832. doi:10.1107/S2053273319011628.

BoneSmart (2022) *Types of Total Knee Implants*. 2022. http://bonesmart.org/knee/types-of-total-knee-implants/ [Accessed: 31 October 2022].

Bonnin, M.P., Schmidt, A., Basiglini, L., Bossard, N. & Dantony, E. (2013) Mediolateral oversizing influences pain, function, and flexion after TKA. *Knee Surgery, Sports Traumatology, Arthroscopy*. 21 (10), 2314–2324. doi:10.1007/s00167-013-2443-x.

Van den Broeck, J., Vereecke, E., Wirix-Speetjens, R. & Sloten, J. (2014) Segmentation accuracy of long bones. *Medical Engineering and Physics*. 36 (7), 949–953. doi:10.1016/j.medengphy.2014.03.016.

Budhiparama, N.C., Lumban-Gaol, I., Ifran, N.N., de Groot, P.C.J., Utomo, D.N. & Nelissen, R.G.H.H. (2021) Mismatched knee implants in Indonesian and Dutch patients: a need for increasing the size. *Knee Surgery, Sports Traumatology, Arthroscopy*. 29 (2), 358–369. doi:10.1007/s00167-020-05914-9.

Buller, L.T., Menken, L. & Rodriguez, J.A. (2018) The custom total knee replacement: A bespoke solution. *Seminars in Arthroplasty*. 29 (3), 209–213. doi:10.1053/j.sart.2019.01.006.

Burge, T.A., Jeffers, J.R.T. & Myant, C.W. (2023a) A computational design of experiments based method for evaluation of off-the-shelf total knee replacement implants. *Computer Methods in Biomechanics and Biomedical Engineering*. 26 (6), 629–638. doi:10.1080/10255842.2022.2075224.

Burge, T.A., Jeffers, J.R.T. & Myant, C.W. (2023b) Applying machine learning methods to enable automatic customisation of knee replacement implants from CT data. *Scientific Reports*. 13, 1–9. doi:10.1038/s41598-023-30483-5.

Burge, T.A., Jeffers, J.R.T. & Myant, C.W. (2022a) Development of an Automated Mass-Customization Pipeline for Knee Replacement Surgery Using Biplanar X-Rays. *Journal of Mechanical Design*. 144 (2), 1–11. doi:10.1115/1.4052192.

Burge, T.A., Jeffers, J.R.T. & Myant, C.W. (2022b) Performance and Sensitivity Analysis of an Automated X-Ray Based Total Knee Replacement Mass-Customization Pipeline. *Journal of Medical Devices*. 16 (4), 1–12. doi:10.1115/1.4055000.

Burge, T.A., Jones, G.G., Jordan, C.M., Jeffers, J.R.T. & Myant, C.W. (2022c) A computational tool for automatic selection of total knee replacement implant size using X-ray images. *Frontiers in Bioengineering and Biotechnology*. 10, 1–11. doi:10.3389/fbioe.2022.971096.

Burge, T.A., Munford, M.J., Kechagias, S., Jeffers, J.R.T. & Myant, C.W. (2023c) Automating the customization of stiffness - matched knee implants using machine learning techniques. *The International Journal of Advanced Manufacturing Technology*. doi:10.1007/s00170-023-

11357-6.

Burger, H., van Daele, P.L.A., Algra, D., van den Ouweland, F.A., Grobbee, D.E., Hofman, A., van Kuijk, C., Schütte, H.E., Birkenhäger, J.C. & Pols, H.A.P. (1994) The association between age and bone mineral density in men and women aged 55 years and over: The Rotterdam Study. *Bone and Mineral*. 25 (1), 1–13. doi:10.1016/S0169-6009(08)80203-6.

Canny, J. (1986) A Computational Approach to Edge Detection. *IEEE Transactions on Pattern Analysis and Machine Intelligence*. PAMI-8 (6), 679–698. doi:10.1109/TPAMI.1986.4767851.

Carr, A.J., Robertsson, O., Graves, S., Price, A.J., Arden, N.K., Judge, A. & Beard, D.J. (2012) Knee replacement. *The Lancet*. 379 (9823), 1331–1340. doi:10.1016/S0140-6736(11)60752-6.

Cazon, A., Aizpurua, J., Paterson, A., Bibb, R. & Campbell, R.I. (2014) Customised design and manufacture of protective face masks combining a practitioner-friendly modelling approach and low-cost devices for digitising and additive manufacturing. *Virtual and Physical Prototyping*. 9 (4), 251–261. doi:10.1080/17452759.2014.958648.

Cernazanu-Glavan, C. & Holban, S. (2013) Segmentation of bone structure in X-ray images using convolutional neural network. *Advances in Electrical and Computer Engineering*. 13 (1), 87–94. doi:10.4316/AECE.2013.01015.

Cerveri, P., Manzotti, A., Confalonieri, N. & Baroni, G. (2014) Automating the design of resection guides specific to patient anatomy in knee replacement surgery by enhanced 3D curvature and surface modeling of distal femur shape models. *Computerized Medical Imaging and Graphics*. 38 (8), 664–674. doi:10.1016/j.compmedimag.2014.09.001.

Cerveri, P., Sacco, C., Olgiati, G., Manzotti, A. & Baroni, G. (2017) 2D/3D reconstruction of the distal femur using statistical shape models addressing personalized surgical instruments in knee arthroplasty: A feasibility analysis. *International Journal of Medical Robotics and Computer Assisted Surgery*. 13 (4), 1–13. doi:10.1002/rcs.1823.

Chen, F., Xie, Y., Xu, P., Zhao, Z., Zhang, D. & Liao, H. (2022) Efficient lower-limb segmentation for large-scale volumetric CT by using projection view and voxel group attention. *Medical and Biological Engineering and Computing*. 60 (8), 2201–2216. doi:10.1007/s11517-022-02598-w.

Chen, R.K., an Jin, Y., Wensman, J. & Shih, A. (2016) Additive manufacturing of custom orthoses and prostheses - A review. *Additive Manufacturing*. 12, 77–89. doi:10.1016/j.addma.2016.04.002.

Chui, C.S., Leung, K.S., Qin, J., Shi, D., Augat, P., Wong, R.M.Y., Chow, S.K.H., Huang, X.Y., Chen, C.Y., Lai, Y.X., Yung, P.S.H., Qin, L. & Cheung, W.H. (2021) Population-Based and Personalized Design of Total Knee Replacement Prosthesis for Additive Manufacturing Based on Chinese Anthropometric Data. *Engineering*. 7 (3), 386–394. doi:10.1016/j.eng.2020.02.017.

Cignoni, P., Callieri, M., Corsini, M., Dellepiane, M., Ganovelli, F. & Ranzuglia, G. (2008) MeshLab: An open-source mesh processing tool. *6th Eurographics Italian Chapter Conference 2008 - Proceedings*. 129–136.

Clary, C., Aram, L., Deffenbaugh, D. & Heldreth, M. (2014) Tibial base design and patient morphology affecting tibial coverage and rotational alignment after total knee arthroplasty. *Knee Surgery, Sports Traumatology, Arthroscopy*. 22 (12), 3012–3018. doi:10.1007/s00167-014-3402-x.

ConforMIS (2022) *Customized Knee & Hip Replacements | Conformis*. 2022. https://www.conformis.com/ [Accessed: 31 October 2022].

ConforMIS (2018) *Implant Summary Report for the iTotal G2 XE and iTotal G2*. (2018).

Cronskär, M., Rännar, L.E., Bäckström, M., Nilsson, K.G. & Samuelsson, B. (2015) Patient-Specific Clavicle Reconstruction Using Digital Design and Additive Manufacturing. *Journal of Mechanical Design, Transactions of the ASME*. 137 (11), 1–4. doi:10.1115/1.4030992.

Culler, S.D., Martin, G.M. & Swearingen, A. (2017) Comparison of adverse events rates and hospital cost between customized individually made implants and standard off-the-shelf implants for total knee arthroplasty. *Arthroplasty Today*. 3 (4), 257–263. doi:10.1016/j.artd.2017.05.001.

Dai, Y., Scuderi, G.R., Bischoff, J.E., Bertin, K., Tarabichi, S. & Rajgopal, A. (2014a) Anatomic tibial component design can increase tibial coverage and rotational alignment accuracy: a comparison of six contemporary designs. *Knee Surgery, Sports Traumatology, Arthroscopy*. 22 (12), 2911–2923. doi:10.1007/s00167-014-3282-0.

Dai, Y., Scuderi, G.R., Penninger, C., Bischoff, J.E. & Rosenberg, A. (2014b) Increased shape and size offerings of femoral components improve fit during total knee arthroplasty. *Knee Surgery, Sports Traumatology, Arthroscopy*. 22 (12), 2931–2940. doi:10.1007/s00167-014-3163-6.

Davies, R., Twining, C. & Taylor, C. (2008) *Statistical Models of Shape*. Springer London. doi:10.1017/CBO9781107415324.004.

Davis, S.M. (1989) From "future perfect": Mass customizing. *Planning Review*. 17 (2), 16–21.

Deen, J.T., Clay, T.B., Iams, D.A., Horodyski, M.B. & Parvataneni, H.K. (2018) Proximal tibial resorption in a modern total knee prosthesis. *Arthroplasty Today*. 4 (2), 244–248. doi:10.1016/j.artd.2017.10.005.

Deradjat, D. & Minshall, T. (2017) Implementation of rapid manufacturing for mass customisation. *Journal of Manufacturing Technology Management*. 28 (1), 95–121. doi:10.1108/JMTM-01-2016-0007.

Dutt, A. (2021) *A Step By Step Implementation of Principal Component Analysis*. 2021. Towards Data Science. https://towardsdatascience.com/a-step-by-step-implementation-of-principal-component-analysis-5520cc6cd598 [Accessed: 3 July 2023].

El-Sayed, M.A. & Sennari, H.A.M. (2014) Convolutional Neural Network for Edge Detection in SAR Grayscale Images. *IOSR journal of VLSI and Signal Processing*. 4 (2), 75–83. doi:10.9790/4200-04217583.

Elliott, D.S., Newman, K.J.H., Forward, D.P., Hahn, D.M., Ollivere, B., Kojima, K., Handley, R., Rossiter, N.D., Wixted, J.J., Smith, R.M. & Moran, C.G. (2016) A unified theory of bone healing and nonunion. *Bone and Joint Journal*. 98B (7), 884–891. doi:10.1302/0301-620X.98B7.36061.

Evers, M. (2019) *Robotics, ASCs Will Continue to Drive Knee Replacement Market Trends | ORTHOWORLD*. 2019. orthoworld.com. https://www.orthoworld.com/robotics-ascs-will-continue-to-drive-knee-market-trends/ [Accessed: 25 June 2021].

Fawzy, E., Pandit, H., Jenkins, C., Dodd, C.A.F. & Murray, D.W. (2008) Determination of femoral component size in unicompartmental knee replacement. *Knee*. 15 (5), 403–406. doi:10.1016/j.knee.2008.05.011.

Fedorov, A., Beichel, R., Kalpathy-Cramer, J., Finet, J., Fillion-Robin, J.C., Pujol, S., Bauer, C., Jennings, D., Fennessy, F., Sonka, M., Buatti, J., Aylward, S., Miller, J. V., Pieper, S. & Kikinis, R. (2012) 3D Slicer as an image computing platform for the Quantitative Imaging Network. *Magnetic Resonance Imaging*. 30 (9), 1323–1341. doi:10.1016/j.mri.2012.05.001.

Ferguson, S.M., Olewnik, A.T. & Cormier, P. (2014) A review of mass customization across marketing, engineering and distribution domains toward development of a process framework. *Research in Engineering Design*. 25 (1), 11–30. doi:10.1007/s00163-013-0162-4.

Foran, J.R.H. & Manner, P.W. (2021) *Knee Replacement Implants - OrthoInfo - AAOS*. 2021. OrthoInfo. https://orthoinfo.aaos.org/en/treatment/knee-replacement-implants/ [Accessed: 30 January 2022].

Galvez, R.L., Bandala, A.A., Dadios, E.P., Vicerra, R.R.P. & Maningo, J.M.Z. (2018) Object Detection Using Convolutional Neural Networks. In: *TENCON 2018 - 2018 IEEE Region 10 Conference*. 2018 Jeju, South Korea, IEEE. pp. 2023–2027. doi:10.1109/TENCON.2018.8650517.

Gandhi, A., Magar, C. & Roberts, R. (2013) How technology can drive the next wave of mass customization. *McKinsey & Company's Business Technology Journal*. 32, 1–8. doi:10.1016/j.techfore.2015.02.015.

Ghouse, S., Babu, S., Van Arkel, R.J., Nai, K., Hooper, P.A. & Jeffers, J.R.T. (2017) The influence of laser parameters and scanning strategies on the mechanical properties of a stochastic porous material. *Materials and Design*. 131, 498–508. doi:10.1016/j.matdes.2017.06.041.

Ghouse, S., Reznikov, N., Boughton, O.R., Babu, S., Ng, K.C.G., Blunn, G., Cobb, J.P., Stevens, M.M. & Jeffers, J.R.T. (2019) The design and in vivo testing of a locally stiffness-matched porous scaffold. *Applied Materials Today*. 15, 377–388. doi:10.1016/j.apmt.2019.02.017.

Giannatsis, J. & Dedoussis, V. (2009) Additive fabrication technologies applied to medicine and health care: A review. *International Journal of Advanced Manufacturing Technology*. 40 (1–2), 116–127. doi:10.1007/s00170-007-1308-1.

Ginde, A.A., Foianini, A., Renner, D.M., Valley, M. & Camargo, C.A. (2008) Availability and quality of computed tomography and magnetic resonance imaging equipment in U.S. emergency departments. *Academic Emergency Medicine*. 15 (8), 780–783. doi:10.1111/j.1553-2712.2008.00192.x.

Grassi, L., Väänänen, S.P., Ristinmaa, M., Jurvelin, J.S. & Isaksson, H. (2017) Prediction of femoral strength using 3D finite element models reconstructed from DXA images: validation against experiments. *Biomechanics and Modeling in Mechanobiology*. 16 (3), 989–1000. doi:10.1007/s10237-016-0866-2.

Grothues, S., Hohlmann, B., Zingde, S.M. & Radermacher, K. (2022) Potential for femoral size optimization for Off-the-Shelf implants: A CT derived implant database analysis. *Journal of Orthopaedic Research*. doi:10.1002/jor.25464.

Guha, R., Stanton, D.T. & Jurs, P.C. (2005) Interpreting computational neural network quantitative structure-activity relationship models: A detailed interpretation of the weights and biases. *Journal of Chemical Information and Modeling*. 45 (4), 1109–1121. doi:10.1021/ci050110v.

Hamet, P. & Tremblay, J. (2017) Artificial intelligence in medicine. *Metabolism: Clinical and Experimental*. 69, S36–S40. doi:10.1016/j.metabol.2017.01.011.

Hamilton, K.C., Fisher, G., Roy, J.L., Gower, B.A. & Hunter, G.R. (2013) The effects of weight loss on relative bone mineral density in premenopausal women. *Obesity*. 21 (3), 441–448. doi:10.1002/oby.20052.

Hansen, G.A., Douglass, R.W. & Zardecki, A. (2005) *Mesh enhancement*. London, UK, Imperial College Press.

Hernandez-Vaquero, D., Abat, F., Sarasquete, J. & Monllau, J.C. (2013) Reliability of preoperative measurement with standardized templating in Total Knee Arthroplasty. *World Journal of Orthopaedics*. 4 (4), 287–290. doi:10.5312/wjo.v4.i4.287.

Hernández-Vaquero, D., Noriega-Fernandez, A., Roncero-Gonzalez, S., Perez-Coto, I., Sierra-Pereira, A.A. & Sandoval-Garcia, M.A. (2019) Agreement in component size between preoperative measurement, navigation and final implant in total knee replacement. *Journal of Orthopaedic Translation*. 18, 84–91. doi:10.1016/j.jot.2018.10.006.

Herrmann, L.R. (1976) Laplacian-Isoparametric Grid Generation Scheme. *Journal of the Engineering Mechanics Division*. 102 (5), 749–756. doi:10.1061/JMCEA3.0002158.

Hitt, K., Shurman, J.R., Greene, K., McCarthy, J., Moskal, J., Hoeman, T. & Mont, M.A. (2003) Anthropometric measurements of the human knee: Correlation to the sizing of current knee arthroplasty systems. In: *Journal of Bone and Joint Surgery*. 2003 pp. 115–122. doi:10.2106/00004623-200300004-00015.

Hou, J. & Gao, T. (2021) Explainable DCNN based chest X-ray image analysis and classification for COVID-19 pneumonia detection. *Scientific Reports*. 11 (1), 1–15. doi:10.1038/s41598-021-95680-6.

Huiskes, R., Weinans, H. & Van Rietbergen, B. (1992) The relationship between stress shielding and bone resorption around total hip stems and the effects of flexible materials. *Clinical Orthopaedics and Related Research*. 274, 124–134. doi:10.1097/00003086-199201000-00014.

Javaid, M. & Haleem, A. (2018) Additive manufacturing applications in medical cases: A literature based review. *Alexandria Journal of Medicine*. 54 (4), 411–422.

doi:10.1016/J.AJME.2017.09.003.

Jun, Y. (2011) Morphological analysis of the human knee joint for creating custom-made implant models. *International Journal of Advanced Manufacturing Technology*. 52 (9–12), 841–853. doi:10.1007/s00170-010-2785-1.

Kechagias, S., Oosterbeek, R.N., Munford, M.J., Ghouse, S. & Jeffers, J.R.T. (2022) Controlling the mechanical behaviour of stochastic lattice structures: The key role of nodal connectivity. *Additive Manufacturing*. 54, 1–12. doi:10.1016/j.addma.2022.102730.

Kellgren, J.H. & Lawrence, J.S. (1956) Radiological Assessment of Osteo-Arthritis. *Annals of the Rheumatic Diseases*. 16 (4), 494–502. doi:doi: 10.1136/ard.16.4.494.

Kent, B.R. (2014) *Meshes, models and textures*. doi:10.1088/978-1-6270-5612-0ch3.

Khodadadyan-Klostermann, C., Von Seebach, M., Taylor, W.R., Duda, G.N. & Haas, N.P. (2004) Distribution of bone mineral density with age and gender in the proximal tibia. *Clinical Biomechanics*. 19 (4), 370–376. doi:10.1016/j.clinbiomech.2003.12.013.

Kingma, D.P. & Ba, J.L. (2015) Adam: A method for stochastic optimization. In: *3rd International Conference on Learning Representations*. 2015 San Diego, US. pp. 1–15.

Koller, O., Ney, H. & Bowden, R. (2016) Deep Hand: How to Train a CNN on 1 Million Hand Images When Your Data is Continuous and Weakly Labelled. In: *Proceedings of the IEEE Computer Society Conference on Computer Vision and Pattern Recognition*. 2016 Las Vegas, NV, USA. pp. 3793–3802. doi:10.1109/CVPR.2016.412.

Konovalov, D.A., Domingos, J.A., Bajema, C., White, R.D. & Jerry, D.R. (2017) Ruler detection for automatic scaling of fish images. *ACM International Conference Proceeding Series*. Part F1312 (August), 90–95. doi:DOI: http://dx.doi.org/10.1145/12345.67890.

Kumar, G. & Narayan, B. (1984) Regulation of bone formation by applied dynamic loads. *Classic Papers in Orthopaedics*. 66 (3), 397–402. doi:10.1007/978-1-4471-5451-8_134.

Laporte, S., Skalli, W., de Guise, J.A., Lavaste, F. & Mitton, D. (2003) A biplanar reconstruction method based on 2D and 3D contours: Application to the distal femur. *Computer Methods in Biomechanics and Biomedical Engineering*. 6 (1), 1–6. doi:10.1080/1025584031000065956.

Laureijs, R.E., Fuchs, E.R.H. & Whitefoot, K.S. (2019) Is more less? Benefits and costs of high-variety production in nonassembled manufacturing. *Journal of Mechanical Design, Transactions of the ASME*. 141 (6), 1–11. doi:10.1115/1.4041943.

Lecun, Y., Bengio, Y. & Hinton, G. (2015) Deep learning. *Nature*. 521 (7553), 436–444. doi:10.1038/nature14539.

Lee, J.-A., Koh, Y.-G. & Kang, K.-T. (2020) Biomechanical and Clinical Effect of Patient-Specific or Customized Knee Implants: A Review. *Journal of Clinical Medicine*. 9 (5), 1559. doi:10.3390/jcm9051559.

Lee, S.-H. & Lee, S.-B. (2010) Production and Usage of Korean Human Information in KISTI. *The Journal of the Korea Contents Association*. 10 (5), 416–421.

doi:10.5392/jkca.2010.10.5.416.

Lee, S., Kwak, S. & Cho, M. (2019) Universal Bounding Box Regression and Its Applications. *Lecture Notes in Computer Science (including subseries Lecture Notes in Artificial Intelligence and Lecture Notes in Bioinformatics)*. 11366 LNCS, 373–387. doi:10.1007/978-3-030-20876-9_24.

Lessmann, N., van Ginneken, B., de Jong, P.A. & Išgum, I. (2019) Iterative fully convolutional neural networks for automatic vertebra segmentation and identification. *Medical Image Analysis*. 53, 142–155. doi:10.1016/j.media.2019.02.005.

Levine, B.R., Sporer, S., Poggie, R.A., Della Valle, C.J. & Jacobs, J.J. (2006) Experimental and clinical performance of porous tantalum in orthopedic surgery. *Biomaterials*. 27 (27), 4671–4681. doi:10.1016/j.biomaterials.2006.04.041.

Li, K., Saffarini, M., Valluy, J., Desseroit, M.C., Morvan, Y., Telmon, N. & Cavaignac, E. (2019) Sexual and ethnic polymorphism render prosthetic overhang and under-coverage inevitable using off-the shelf TKA implants. *Knee Surgery, Sports Traumatology, Arthroscopy*. 27 (7), 2130–2139. doi:10.1007/s00167-019-05410-9.

Li, X., Wang, C., Guo, Y. & Chen, W. (2017) An Approach to Developing Customized Total Knee Replacement Implants. *Journal of Healthcare Engineering*. 2017, 1–8. doi:10.1155/2017/9298061.

Liaw, C.Y. & Guvendiren, M. (2017) Current and emerging applications of 3D printing in medicine. *Biofabrication*. 9 (2). doi:10.1088/1758-5090/aa7279.

Lim, H.C., Bae, J.H., Yoon, J.Y., Kim, S.J., Kim, J.G. & Lee, J.M. (2013) Gender differences of the morphology of the distal femur and proximal tibia in a Korean population. *Knee*. 20 (1), 26–30. doi:10.1016/j.knee.2012.05.010.

Liu, C., Cao, Y., Alcantara, M., Liu, B., Brunette, M., Peinado, J. & Curioso, W. (2017) TX-CNN: Detecting tuberculosis in chest X-ray images using convolutional neural network. In: *International Conference on Image Processing (ICIP)*. 2017 Beijing, China. pp. 2314–2318. doi:10.1109/ICIP.2017.8296695.

Machado, F., Malpica, N. & Borromeo, S. (2019) Parametric CAD modeling for open source scientific hardware: Comparing OpenSCAD and FreeCAD Python scripts. *PLoS ONE*. 14 (12), 1–30. doi:10.1371/journal.pone.0225795.

Mahfouz, M., Fatah, E.E.A., Bowers, L.S. & Scuderi, G. (2012) Three-dimensional morphology of the knee reveals ethnic differences. *Clinical Orthopaedics and Related Research*. 470 (1), 172–185. doi:10.1007/s11999-011-2089-2.

Mahoney, O.M. & Kinsey, T. (2010) Overhang of the femoral component in total knee arthroplasty: Risk factors and clinical consequences. *Journal of Bone and Joint Surgery - Series A*. 92 (5), 1115–1121. doi:10.2106/JBJS.H.00434.

Massé, V. & Ghate, R.S. (2021) Using standard X-ray images to create 3D digital bone models and patient-matched guides for aiding implant positioning and sizing in total knee arthroplasty. *Computer Assisted Surgery*. 26 (1), 31–40. doi:10.1080/24699322.2021.1894239.

Matsugu, M., Mori, K., Mitari, Y. & Kaneda, Y. (2003) Subject independent facial expression recognition with robust face detection using a convolutional neural network. *Neural Networks*. 16, 555–559. doi:10.1016/S0893-6080(03)00115-1.

Mihajlovic, I. (2019) *Everything You Ever Wanted To Know About Computer Vision*. 2019. Towards Data Science. https://towardsdatascience.com/everything-you-ever-wanted-to-know-about-computer-vision-heres-a-look-why-it-s-so-awesome-e8a58dfb641e [Accessed: 3 November 2022].

Minnema, J., van Eijnatten, M., Kouw, W., Diblen, F., Mendrik, A. & Wolff, J. (2018) CT image segmentation of bone for medical additive manufacturing using a convolutional neural network. *Computers in Biology and Medicine*. 103 (October), 130–139. doi:10.1016/j.compbiomed.2018.10.012.

Mitra, N.J., Gelfand, N., Pottmann, H. & Guibas, L. (2004) Registration of point cloud data from a geometric optimization perspective. *ACM International Conference Proceeding Series*. 71, 22–31. doi:10.1145/1057432.1057435.

Moore, C., Avery, G., Balcam, S., Needler, L., Swift, A., Beavis, A.W. & Saunderson, J.R. (2012) Use of a digitally reconstructed radiograph-based computer simulation for the optimisation of chest radiographic techniques for computed radiography imaging systems. *British Journal of Radiology*. 85 (1017), 630–639. doi:10.1259/bjr/47377285.

Moore, C.S., Liney, G.P., Beavis, A.W. & Saunderson, J.R. (2011) A method to produce and validate a digitally reconstructed radiograph-based computer simulation for optimisation of chest radiographs acquired with a computed radiography imaging system. *British Journal of Radiology*. 84 (1006), 890–902. doi:10.1259/bjr/30125639.

Munford, M.J., Ng, K.C.G. & Jeffers, J.R.T. (2020) Mapping the Multi-Directional Mechanical Properties of Bone in the Proximal Tibia. *Advanced Functional Materials*. 30 (46), 1–9. doi:10.1002/adfm.202004323.

Munford, M.J., Stoddart, J.C., Liddle, A.D., Cobb, J.P. & Jeffers, J.R.T. (2022) Total and partial knee arthroplasty implants that maintain native load transfer in the tibia. *Bone & Joint Research*. 11 (2), 91–101. doi:10.1302/2046-3758.112.bjr-2021-0304.r1.

Munford, M.J., Xiao, D. & Jeffers, J.R.T. (2021) Lattice implants that generate homeostatic and remodeling strains in bone. *Journal of Orthopaedic Research*. (February), 1–7. doi:10.1002/jor.25114.

Murphy, K.P. (2012) *Machine Learning: A Probabilistic Perspective*. Cambridge, Massachusetts, US, MIT Press.

Mustra, M., Delac, K. & Grgic, M. (2008) Overview of the DICOM standard. *Proceedings Elmar - International Symposium Electronics in Marine*. 1 (September), 39–44.

Namin, A.T., Jalali, M.S., Vahdat, V., Bedair, H.S., O'Connor, M.I., Kamarthi, S. & Isaacs, J.A. (2019) Adoption of New Medical Technologies: The Case of Customized Individually Made Knee Implants. *Value in Health*. 22 (4), 423–430. doi:10.1016/j.jval.2019.01.008.

Narin, A., Kaya, C. & Pamuk, Z. (2021) Automatic detection of coronavirus disease (COVID-19) using X-ray images and deep convolutional neural networks. *Pattern Analysis and*

Applications. 24 (3), 1207–1220. doi:10.1007/s10044-021-00984-y.

Nevitt, M., Felson, D. & Lester, G. (2006) The osteoarthritis initiative: protocol for the cohort study. *The Osteoarthritis Initiative*. 1–74. doi:10.1055/s-0038-1653966.

Ng, K.C.G., Mantovani, G., Lamontagne, M., Labrosse, M.R. & Beaulé, P.E. (2019) Cam FAI and Smaller Neck Angles Increase Subchondral Bone Stresses during Squatting: A Finite Element Analysis. *Clinical Orthopaedics and Related Research*. 477 (5), 1053–1063. doi:10.1097/CORR.0000000000000528.

Nguyen, H.C., van Egmond, N., Hevesi, M., Weinans, H., Gielis, W.P. & Custers, R.J.H. (2022) A new protocol for obtaining whole leg radiographs with excellent reproducibility. *Journal of Cartilage and Joint Preservation*. 2 (1), 1–9. doi:10.1016/j.jcjp.2022.100042.

Nikita, E. (2017) The Human Skeleton. In: *Osteoarchaeology*. Academic Press. pp. 1–75. doi:10.1016/b978-0-12-804021-8.00001-2.

Nolte, D., Ko, S.-T., Bull, A.M.J. & Kedgley, A.E. (2020) Reconstruction of the lower limb bones from digitised anatomical landmarks using statistical shape modelling. *Gait & Posture*. 77, 269–275. doi:10.1016/J.GAITPOST.2020.02.010.

Ogura, T., Le, K., Merkely, G., Bryant, T. & Minas, T. (2019) A high level of satisfaction after bicompartmental individualized knee arthroplasty with patient-specific implants and instruments. *Knee Surgery, Sports Traumatology, Arthroscopy*. 27 (5), 1487–1496. doi:10.1007/s00167-018-5155-4.

Oomori, S., Nishida, T. & Kurogi, S. (2016) Point cloud matching using singular value decomposition. *Artificial Life and Robotics*. 21 (2), 149–154. doi:10.1007/s10015-016-0265-x.

Ortho Baltic Implants (2020) *Mass Customization of Implants : The Business Model*.

Parmar, R. (2018) *Common Loss functions in machine learning*. 2018. Towards Data Science. https://towardsdatascience.com/common-loss-functions-in-machine-learning-46af0ffc4d23 [Accessed: 3 July 2023].

Parratte, S., Argenson, J.N.A., Pearce, O., Pauly, V., Auquier, P. & Aubaniac, J.M. (2009) Medial unicompartmental knee replacement in the under-50s. *Journal of Bone and Joint Surgery - Series B*. 91 (3), 351–356. doi:10.1302/0301-620X.91B3.21588.

Paterson, A.M., Donnison, E., Bibb, R.J. & Ian Campbell, R. (2014) Computer-aided design to support fabrication of wrist splints using 3D printing: A feasibility study. *Hand Therapy*. 19 (4), 102–113. doi:10.1177/1758998314544802.

Paxton, N.C., Nightingale, R.C. & Woodruff, M.A. (2022) Capturing patient anatomy for designing and manufacturing personalized prostheses. *Current Opinion in Biotechnology*. 73, 282–289. doi:10.1016/j.copbio.2021.09.004.

Peto, M., Ramírez-Cedillo, E., Hernández, A. & Siller, H.R. (2019) Structural design optimization of knee replacement implants for Additive Manufacturing. *Procedia Manufacturing*. 34, 574–583. doi:10.1016/j.promfg.2019.06.222.

Postler, A., Lützner, C., Beyer, F., Tille, E. & Lützner, J. (2018) Analysis of Total Knee Arthroplasty revision causes. *BMC Musculoskeletal Disorders*. 19 (1). doi:10.1186/s12891-018-1977-y.

Price, A.J., Alvand, A., Troelsen, A., Katz, J.N., Hooper, G., Gray, A., Carr, A. & Beard, D. (2018) Knee replacement. *The Lancet*. 392 (10158), 1672–1682. doi:10.1016/S0140-6736(18)32344-4.

Rathnayaka, K., Momot, K.I., Noser, H., Volp, A., Schuetz, M.A., Sahama, T. & Schmutz, B. (2012) Quantification of the accuracy of MRI generated 3D models of long bones compared to CT generated 3D models. *Medical Engineering and Physics*. 34 (3), 357–363. doi:10.1016/j.medengphy.2011.07.027.

Reddy, M. (2011) *API Design for C plus plus*. 1st edition. Morgan Kaufmann. http://store.elsevier.com/product.jsp?isbn=9780123850034.

Ribeiro, N.S., Fernandes, P.C., Lopes, D.S., Folgado, J.O. & Fernandes, P.R. (2009) 3-D Solid and Finite Element Modeling of Biomechanical Structures - A Software Pipeline. In: *7th EUROMECH Solid Mechanics Conference*. 2009 Lisbon, Portugal. pp. 1–18.

Ringnér, M. (2008) What is principal component analysis? *Nature Biotechnology*. 26 (3), 303–304. doi:10.1038/nbt0308-303.

Ronneberger, O., Fischer, P. & Brox, T. (2015) U-Net: Convolutional Networks for Biomedical Image Segmentation. *Medical Image Computing and Computer-Assisted Intervention – MICCAI 2015. Lecture Notes in Computer Science*. 9351, 234–241. doi:10.1007/978-3-319-24574-4.

Salvador, F., de Holan, P.M. & Piller, F. (2009) Cracking the Code of Mass Customization | MIT Sloan Management Review. *MIT Sloan Management Review*. 50 (July), 71–78.

Schneider, C.A., Rasband, W.S. & Eliceiri, K.W. (2012) NIH Image to ImageJ: 25 years of image analysis. *Nature Methods*. 9 (7), 671–675. doi:10.1038/nmeth.2089.

Schnurr, C., Csécsei, G., Nessler, J., Eysel, P. & König, D.P. (2011) How much tibial resection is required in total knee arthroplasty? *International Orthopaedics*. 35 (7), 989–994. doi:10.1007/s00264-010-1025-5.

Schroeder, L. & Martin, G. (2019) In Vivo Tibial Fit and Rotational Analysis of a Customized, Patient-Specific TKA versus Off-the-Shelf TKA. *Journal of Knee Surgery*. 32 (6), 499–505. doi:10.1055/s-0038-1653966.

Schumann, S., Thelen, B., Ballestra, S., Nolte, L.P., Büchler, P. & Zheng, G. (2014) X-ray image calibration and its application to clinical orthopedics. *Medical Engineering and Physics*. 36 (7), 968–974. doi:10.1016/j.medengphy.2014.04.001.

Scott, D. & Kowalczyk, A. (2006) Osteoarthritis of the knee. *The New England Journal of Medicine*. 354 (8), 841–848.

Seaver, T., McAlpine, K., Garcia, E., Niu, R. & Smith, E.L. (2020) Algorithm based automatic templating is less accurate than manual digital templating in total knee arthroplasty. *Journal of Orthopaedic Research*. 38 (7), 1472–1476. doi:10.1002/jor.24696.

Seber, G. (2009) *Multivariate observations*. New York, New York, US, Wiley.

Seekingalpha.com (2019) *Conformis Is A Failed Market Experiment, No Justification For Its 400%+ Rally - $0.50 Price Target (NASDAQ:CFMS) | Seeking Alpha*. 2019. https://seekingalpha.com/article/4253620-conformis-is-failed-market-experiment-no-justification-for-400-rally-0_50-price-target [Accessed: 6 February 2022].

Shah, Y., Shah, P., Patel, M., Khamkar, C. & Kanani, P. (2020) Deep learning model-based multimedia forgery detection. In: *Fourth International Conference on I-SMAC (IoT in Social, Mobile, Analytics and Cloud) (I-SMAC)*. 2020 Palladam, India. pp. 564–572. doi:10.1109/I-SMAC49090.2020.9243530.

Shao, L., Wu, X.D., Wang, T., Liu, X.K., Xu, W., Huang, W. & Zeng, Z.M. (2020) Approximating the maximum tibial coverage in total knee arthroplasty does not necessarily result in implant malrotation. *Scientific Reports*. 10 (10529), 1–9. doi:10.1038/s41598-020-67613-2.

Shapiro, L. & Stockman, G. (2001) *Computer Vision*. Prentice Hall.

Sharma, G., Liu, D., Malhotra, R., Zhou, Y.X., Akagi, M. & Kim, T.K. (2017) Availability of additional mediolateral implant option during total knee arthroplasty improves femoral component fit across ethnicities results of a multicenter study. *JBJS Open Access*. 2 (2), 1–10.

Sheth, N.P., Husain, A. & Nelson, C.L. (2017) Surgical Techniques for Total Knee Arthroplasty: Measured Resection, Gap Balancing, and Hybrid. *Journal of the American Academy of Orthopaedic Surgeons*.25 (7) pp.499–508. doi:10.5435/JAAOS-D-14-00320.

Shubhangi, D.C., Chinchansoor, R.S. & Hiremath, P.S. (2012) Edge Detection of Femur Bones in X-ray images - A comparative study of Edge Detectors. *International Journal of Computer Applications*. 42 (2), 13–16. doi:10.5120/5663-7696.

Siemens (2014) Image-to-Implant solution for personalized medical devices. *White Paper*.

Da Silveira, G., Borenstein, D. & Fogliatto, F.S. (2001) Mass customization: Literature review and research directions. *International Journal of Production Economics*. 72 (1), 1–13. doi:10.1016/S0925-5273(00)00079-7.

Singh, S. (2018) *Cousins of Artificial Intelligence*. 2018. Towards Data Science. https://towardsdatascience.com/cousins-of-artificial-intelligence-dda4edc27b55 [Accessed: 26 October 2022].

Skou, S.T., Roos, E.M., Laursen, M.B., Rathleff, M.S., Arendt-Nielsen, L., Rasmussen, S. & Simonsen, O. (2018) Total knee replacement and non-surgical treatment of knee osteoarthritis: 2-year outcome from two parallel randomized controlled trials. *Osteoarthritis and Cartilage*. 26 (9), 1170–1180. doi:10.1016/j.joca.2018.04.014.

Smith-Bindman, R., Lipson, J., Marcus, R., Kim, K.P., Mahesh, M., Gould, R., Berrington De González, A. & Miglioretti, D.L. (2009) Radiation dose associated with common computed tomography examinations and the associated lifetime attributable risk of cancer. *Archives of Internal Medicine*. 169 (22), 2078–2086. doi:10.1001/archinternmed.2009.427.

Smith & Nephew (2015) *Legion Total System Specification Guide and Product Catalog*.

https://www.smith-nephew.com/global/assets/pdf/products/surgical/legion_tks_primary_through_hinge_specifications_guide_02861v1.pdf.

Smoger, L.M., Fitzpatrick, C.K., Clary, C.W., Cyr, A.J., Maletsky, L.P., Rullkoetter, P.J. & Laz, P.J. (2015) Statistical modeling to characterize relationships between knee anatomy and kinematics. *Journal of Orthopaedic Research*. 33 (11), 1620–1630. doi:10.1002/jor.22948.

Smoger, L.M., Shelburne, K.B., Cyr, A.J., Rullkoetter, P.J. & Laz, P.J. (2017) Statistical Shape Modeling Predicts Patellar Bone Geometry to Enable Stereo-Radiographic Kinematic Tracking. *Journal of Biomechanics*. 58, 187–194. doi:10.1016/j.physbeh.2017.03.040.

Song, P.P., Qi, Y.M. & Cai, D.C. (2018) Research and Application of Autodesk Fusion360 in Industrial Design. In: *IOP Conference Series: Materials Science and Engineering*. 2018 p. doi:10.1088/1757-899X/359/1/012037.

Sorkine, O. (2005) Laplacian Mesh Processing. In: *26th Annual Conference of the European Association for Computer Graphics - EUROGRAPHICS*. 2005 Dublin, Ireland. pp. 53–70. doi:10.2312/egst.20051044.

Stulberg, S.D. & Goyal, N. (2015) Which Tibial Tray Design Achieves Maximum Coverage and Ideal Rotation: Anatomic, Symmetric, or Asymmetric? An MRI-based study. *Journal of Arthroplasty*. 30 (10), 1839–1841. doi:10.1016/j.arth.2015.04.033.

Surazhsky, V. & Gotsman, C. (2003) Explicit Surface Remeshing. In: *Eurographics Symposium on Geometry Processing*. 2003 Aachen, Germany. pp. 1–11.

Tack, A., Preim, B. & Zachow, S. (2021) Fully automated Assessment of Knee Alignment from Full-Leg X-Rays employing a ”YOLOv4 And Resnet Landmark regression Algorithm” (YARLA): Data from the Osteoarthritis Initiative. *Computer Methods and Programs in Biomedicine*. 205 (April), 1–10. doi:10.1016/j.cmpb.2021.106080.

Tang, T.S.Y. & Ellis, R.E. (2005) 2D/3D deformable registration using a hybrid atlas. *Lecture Notes in Computer Science (including subseries Lecture Notes in Artificial Intelligence and Lecture Notes in Bioinformatics)*. 3750 LNCS, 223–230. doi:10.1007/11566489_28.

Tanzer, M. & Makhdom, A.M. (2016) Preoperative Planning in Primary Total Knee Arthroplasty. *Journal of the American Academy of Orthopaedic Surgeons*. 24 (4), 220–230. doi:10.5435/JAAOS-D-14-00332.

Tsai, T.Y., Li, J.S., Wang, S., Li, P., Kwon, Y.M. & Li, G. (2015) Principal component analysis in construction of 3D human knee joint models using a statistical shape model method. *Computer Methods in Biomechanics and Biomedical Engineering*. 18 (7), 721–729. doi:10.1080/10255842.2013.843676.

Tuck, C.J., Hague, R.J.M., Ruffo, M., Ransley, M. & Adams, P. (2008) Rapid manufacturing facilitated customization. *International Journal of Computer Integrated Manufacturing*. 21 (3), 245–258. doi:10.1080/09511920701216238.

Velásquez-García, L.F. & Kornbluth, Y. (2021) Biomedical Applications of Metal 3D Printing. *Annual Review of Biomedical Engineering*.23 pp.307–338. doi:10.1146/annurev-bioeng-082020-032402.

Veloso, F., Gomes-Fonseca, J., Morais, P., Correia-Pinto, J., Pinho, A.C.M. & Vilaça, J.L. (2022) Overview of Methods and Software for the Design of Functionally Graded Lattice Structures. *Advanced Engineering Materials*.24 (11) pp.1–23. doi:10.1002/adem.202200483.

Venugopal, V., Ghalsasi, O., McConaha, M., Xu, A., Forbes, J. & Anand, S. (2021) Image processing-based method for automatic design of patient-specific cranial implant for additive manufacturing. *Procedia Manufacturing*. 53 (2020), 375–386. doi:10.1016/j.promfg.2021.06.090.

Voulodimos, A., Doulamis, N., Doulamis, A. & Protopapadakis, E. (2018) Deep Learning for Computer Vision: A Brief Review. *Computational Intelligence and Neuroscience*. 2018, 1–13. doi:10.1155/2018/7068349.

Wang, F. & Zhao, Z. (2017) A survey of iterative closest point algorithm. In: *Chinese Automation Congress (CAC)*. 2017 Jinan, China. pp. 4395–4399. doi:10.1109/CAC.2017.8243553.

Wernecke, G.C., Harris, I.A., Houang, M.T.W., Seeto, B.G., Chen, D.B. & MacDessi, S.J. (2012) Comparison of tibial bone coverage of 6 knee prostheses: a magnetic resonance imaging study with controlled rotation. *Journal of orthopaedic surgery (Hong Kong)*. 20 (2), 143–147. doi:10.1177/230949901202000201.

Whitmarsh, T., Humbert, L., De Craene, M., Del Rio Barquero, L.M. & Frangi, A.F. (2011) Reconstructing the 3D shape and bone mineral density distribution of the proximal femur from dual-energy x-ray absorptiometry. *IEEE Transactions on Medical Imaging*. 30 (12), 2101–2114. doi:10.1109/TMI.2011.2163074.

Wimsey, S., Pickard, R. & Shaw, G. (2006) Accurate scaling of digital radiographs of the pelvis. A prospective trial of two methods. *Journal of Bone and Joint Surgery - Series B*. 88 (11), 1508–1512. doi:10.1302/0301-620X.88B11.18017.

Wong, K. V & Hernandez, A. (2012) A Review of Additive Manufacturing. *ISRN Mechanical Engineering*. 2012, 1–10. doi:10.5402/2012/208760.

Wu, X., Sahoo, D. & Hoi, S.C.H. (2020) Recent advances in deep learning for object detection. *Neurocomputing*. 396, 39–64. doi:10.1016/j.neucom.2020.01.085.

Xu, Z., Baojie, X. & Guoxin, W. (2017) Canny edge detection based on Open CV. In: *ICEMI 2017 - Proceedings of IEEE 13th International Conference on Electronic Measurement and Instruments*. 2017 pp. 53–56. doi:10.1109/ICEMI.2017.8265710.

Ye, X., Wang, S., Zhu, Y., Shao, H., Lou, L., Qian, D. & Ye, J. (2018) Automatic Design and Fabrication of a Custom Ocular Prosthesis Using 3D Volume Difference Reconstruction (VDR). *IEEE Access*. 6, 14339–14346. doi:10.1109/ACCESS.2018.2802700.

Yianilos, P.N. (1993) Data structures and algorithms for nearest neighbor search in general metric spaces. In: *Proceedings of the Fourth Annual ACM-SIAM Symposium on Discrete Algorithms*. 1993 pp. 311–321.

Yu, Z., Shea, K. & Stankovic, T. (2019) A Computational Method for the Design of an Additively Manufactured Personalized Artificial Spinal Disc With Physiological Stiffness Under Multiple Loading Conditions. *Journal of Mechanical Design*. (June).

doi:10.1115/1.4043931.

Zeller, I.M., Sharma, A., Kurtz, W.B., Anderle, M.R. & Komistek, R.D. (2017) Customized versus Patient-Sized Cruciate-Retaining Total Knee Arthroplasty: An In Vivo Kinematics Study Using Mobile Fluoroscopy. *Journal of Arthroplasty*. 32 (4), 1344–1350. doi:10.1016/j.arth.2016.09.034.

Zhao, Z.Q., Zheng, P., Xu, S.T. & Wu, X. (2019) Object Detection with Deep Learning: A Review. *IEEE Transactions on Neural Networks and Learning Systems*. 30 (11), 3212–3232. doi:10.1109/TNNLS.2018.2876865.

Zheng, G., Hommel, H., Akcoltekin, A., Thelen, B., Stifter, J. & Peersman, G. (2018) A novel technology for 3D knee prosthesis planning and treatment evaluation using 2D X-ray radiographs: a clinical evaluation. *International Journal of Computer Assisted Radiology and Surgery*. 13 (8), 1151–1158. doi:10.1007/s11548-018-1789-4.

Zhu, Z. & Li, G. (2011) Construction of 3D human distal femoral surface models using a 3D statistical deformable model. *Journal of Biomechanics*. 44 (13), 2362–2368. doi:10.1016/J.JBIOMECH.2011.07.006.

Zimmer Biomet (2023) *Persona® The Personalized Knee®*. 2023. https://www.zimmerbiomet.com/en/products-and-solutions/specialties/knee/persona-knee-system.html#:~:text=E polyethylene options.-,Femur,%2C 12 A%2FP sizes.

Appendix 1

Custom Knee Replacement Software Graphical User Interface

In this appendix an overview of the software GUI developed to serve as a mass-customisation solution for knee replacement implants is detailed.

Settings & Input Files Tab

The GUI is divided into multiple tabs which facilitate the various forms of implant customisation. The first tab (shown below) allows users to turn pop-out visuals on/off to present results of 3D model reconstructions, component predictions, customised implants, and ground truth comparisons. The desired knee side (left or right) can be selected which informs the software what information should be extracted from the inputted imaging data and sets the geometrical form of any outputted implant designs. The imaging medium (X-ray or CT) can be selected and then the relevant file/folder paths for these files can be specified. If ground truth 3D models are available for results analysis, the location of these files can also be specified.

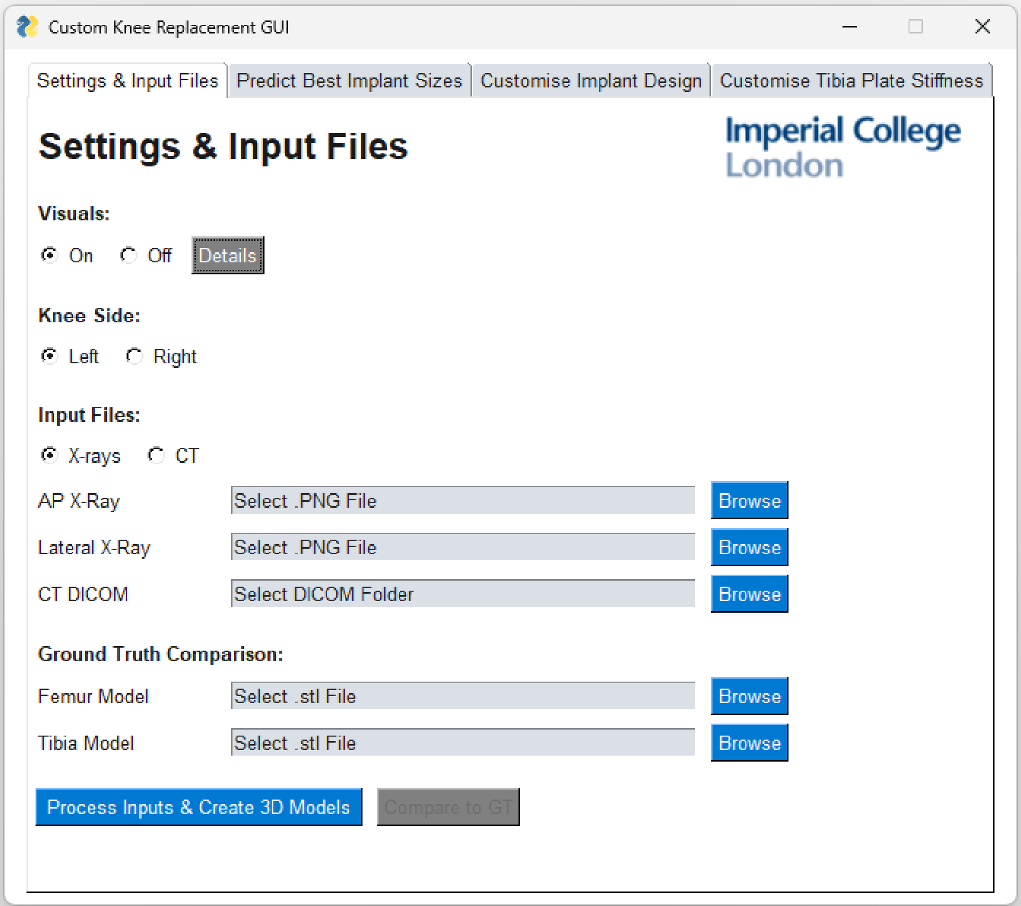

Selecting the ‘Details’ button next to the visuals radio buttons results in the pop out window below becoming visible. The window contains supplementary information on the colouring used in the result visuals.

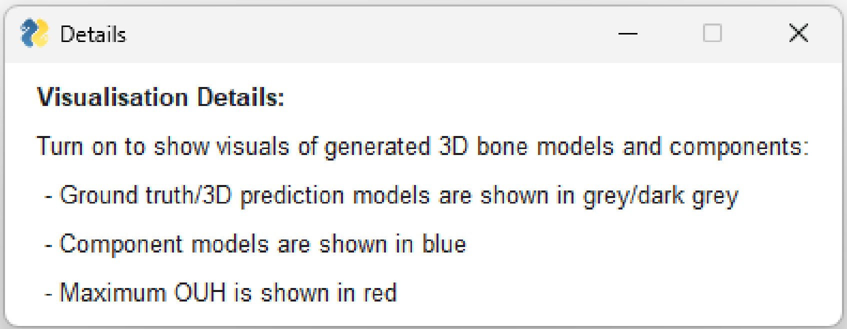

Before the user has inputted the necessary input files and selected the ‘Process Inputs & Create 3D Models’ button, the other pipeline tabs are locked since these require the anatomy to be reconstructed as a prerequisite. Once the button is pressed, the relevant pipelines (described in Chapters 5.2 and 8.2) will run to produce 3D model reconstructions. If visuals are set to ‘On’, windows will pop up after completion with resulting 3D models like those shown below.

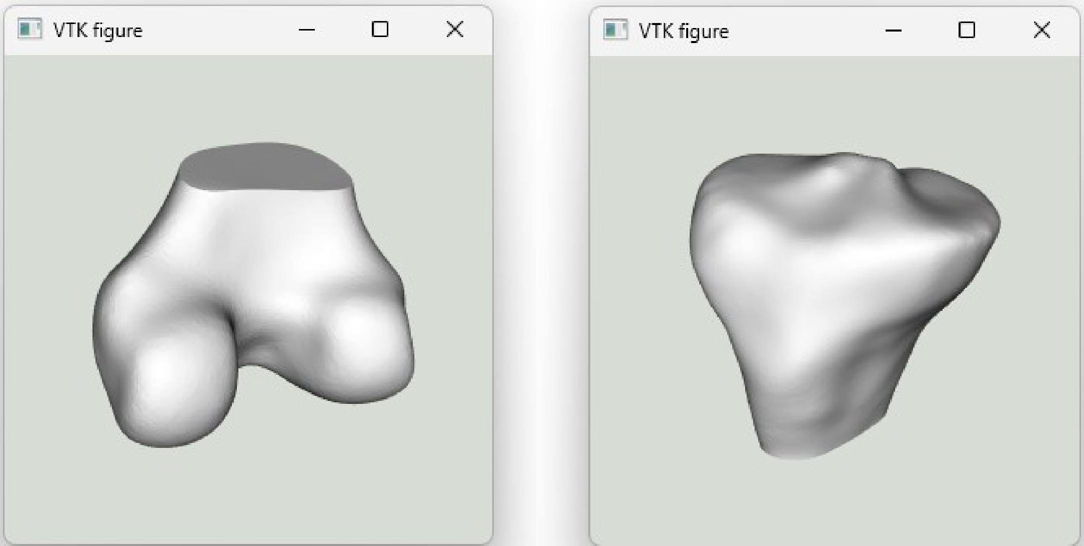

Once finished, the additional GUI tabs will no longer be greyed out and will be free to select. Moreover, if ground truth models were specified, the dark grey 'Compare to GT' button to the right of 'Process Inputs', will also be unlocked. Selecting this button will then position the 3D reconstruction models on the ground truth models for visual comparison as shown below.

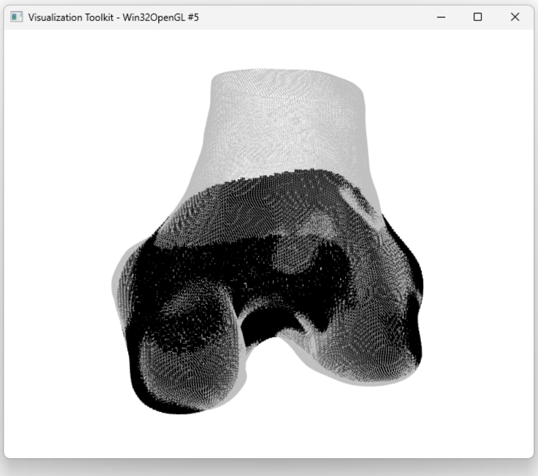

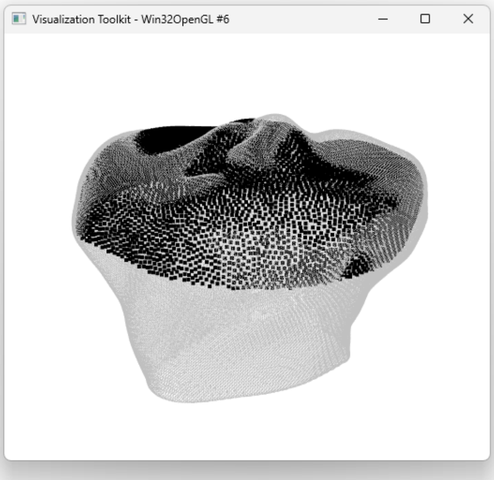

A further window will also appear with reconstruction to ground truth RMSE fit results as shown below.

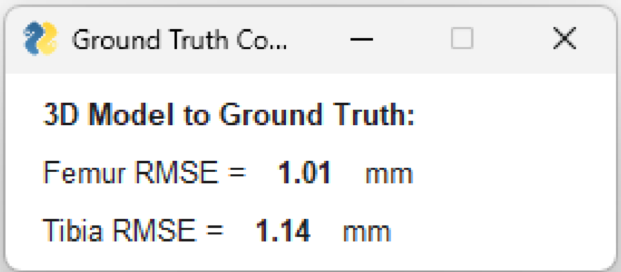

Predict Best OTS Implant Sizes Tab

The next tab allows for users to identify the best possible OTS implant sizes for the anatomy in the inputted X-ray or CT image data. Firstly, the user can select whether femur components, tibia plates, or both should be evaluated. The specific manufacturer model to be studied can be selected from five different options, each with a different number of sizes, as shown below. The 'Find Best Implant Sizes' button can then be pressed which runs the size prediction pipeline (outlined in Chapter 7.2).

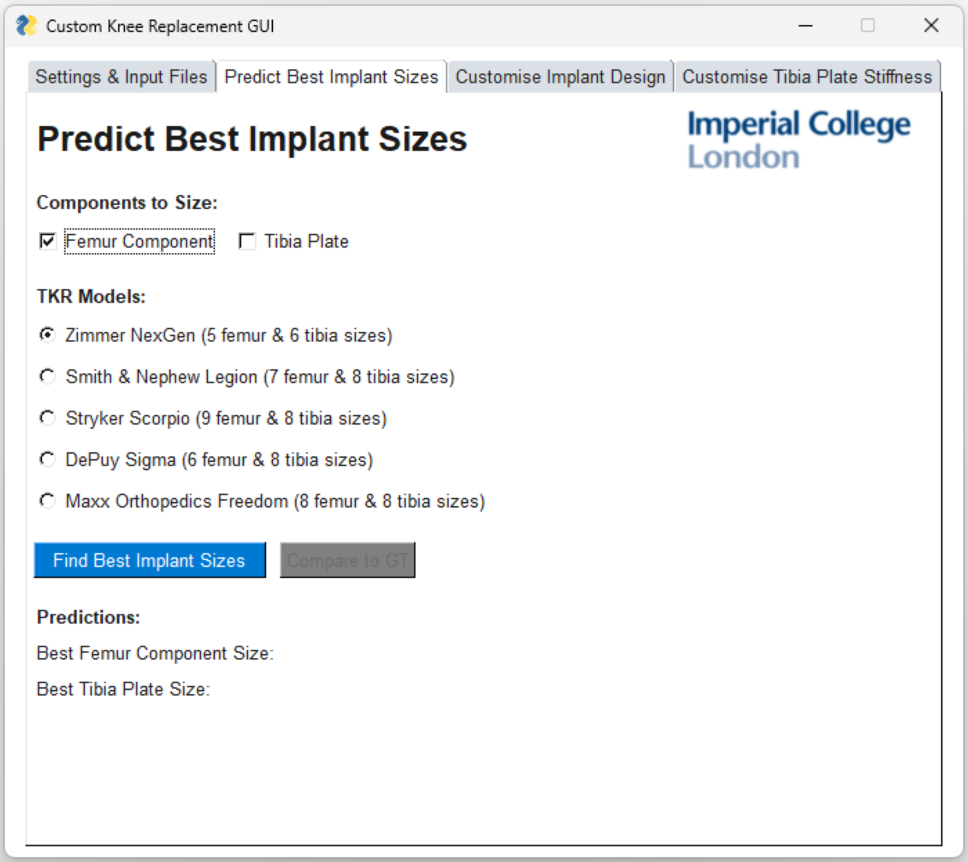

If visuals are set to 'On' on the first tab, once the software has identified the best implant size(s), these will then be displayed fitted to the 3D model reconstructions for the patient in pop out windows as demonstrated below. The location of where the component maximum OUH between the component edges and 3D model reconstructions is predicted to occur (red dots), will also be shown in another window.

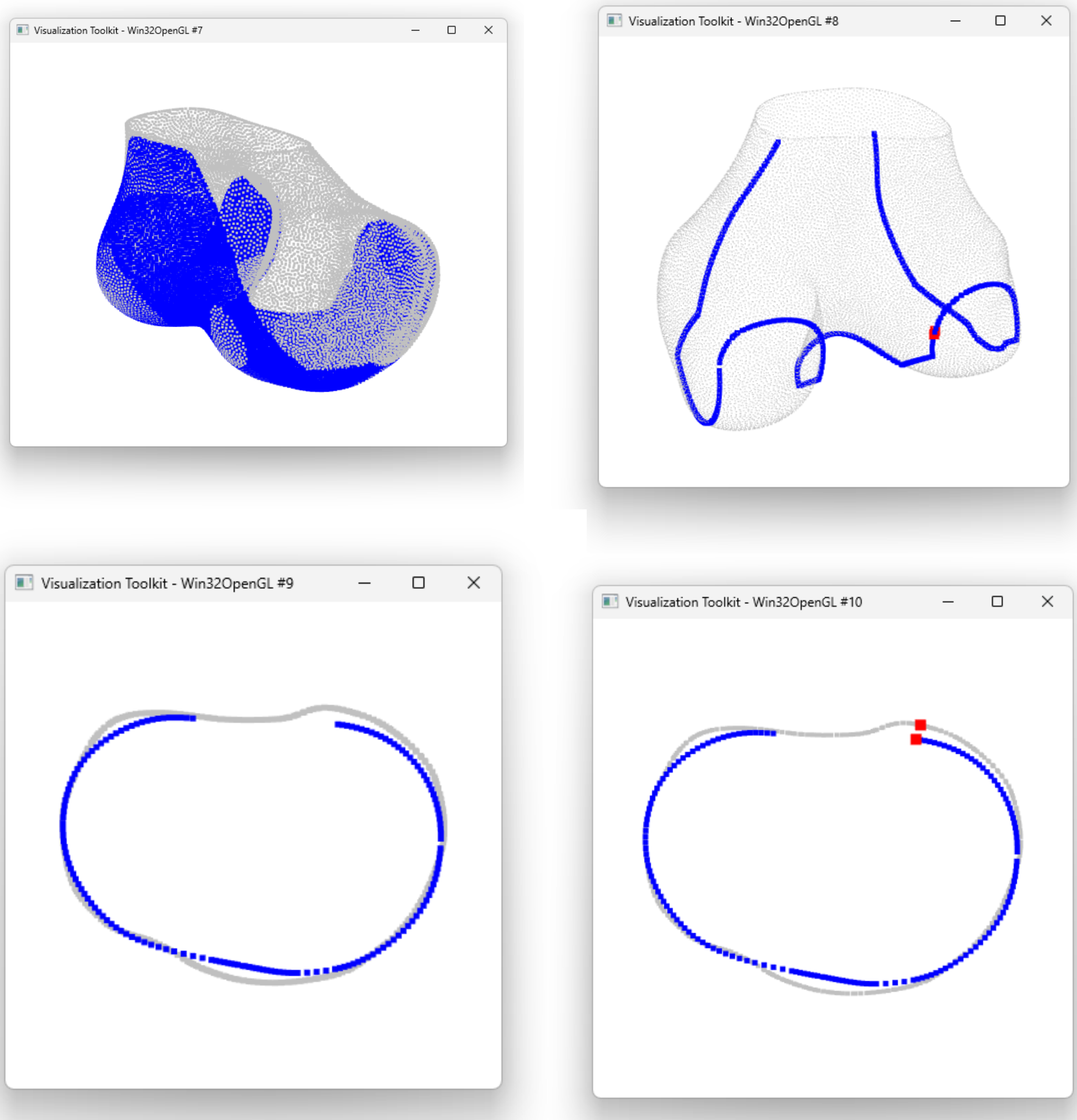

Once the process has completed, the predicted best sizes for the individual for the selected manufacturer model are shown at the bottom of the tab (exemplified below). Note, the 'Find Best Implant Sizes' has turned green to indicate that the process has been completed.

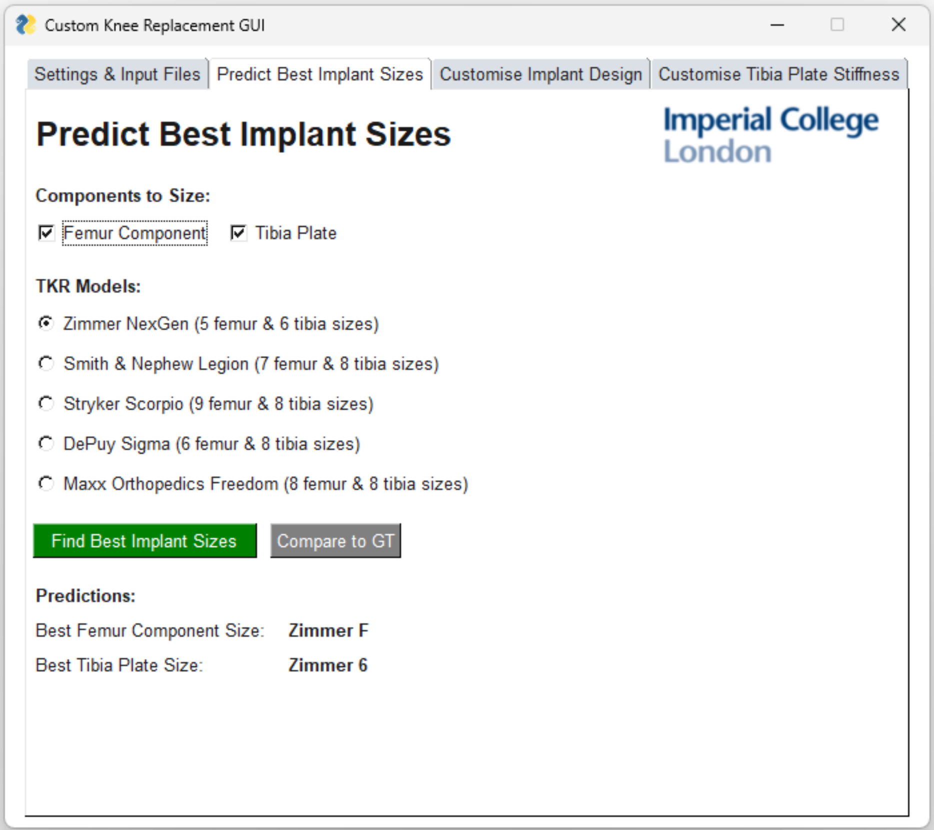

Like before, the 'Compare to GT' button will then be unlocked if ground truth files have been specified in the first tab. This will position 3D models of the best OTS components predicted by the software on the ground truth models for comparison and highlight the maximum OUH as illustrated before. A further window will then appear which will detail the ground truth best possible implant sizes as shown below.

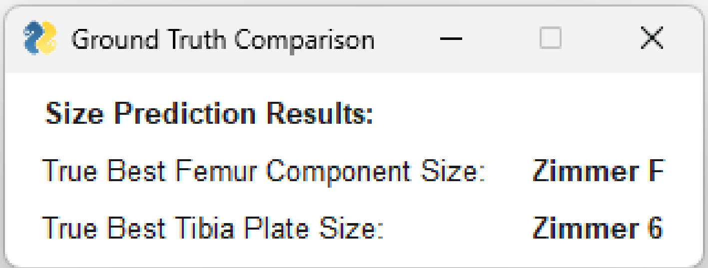

Customise Implant Design Tab

The next tab allows for implant components with customised shapes to be generated. Here either TKR or uni-condylar implants can be selected. Various design options can be chosen such as polyethylene insert (spacer) edge designs and how the implant components are aligned (centred or by using patients' natural alignments). The custom implant components desired (femur component, tibia plate, and/or insert (spacer)) can then be selected, along with the directory that resulting designs should be saved to.

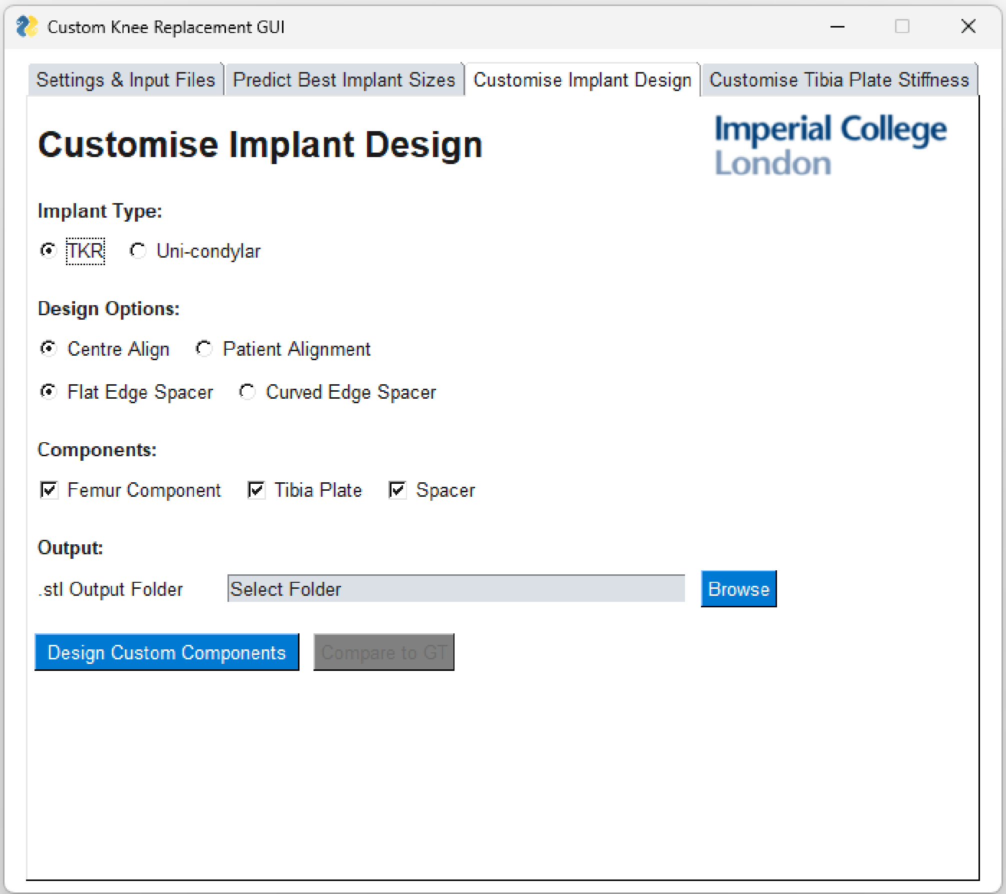

When the 'Design custom components' button is selected, the software runs the pipeline detailed in Chapter 5.2.4 and produces the specified custom implant components. If visuals are set to 'On' on the first tab, the produced custom component models will be displayed in pop out windows. Exemplary TKR components (top row) with two different insert designs (middle row), as well as custom unicondylar implant designs (bottom row) are shown below.

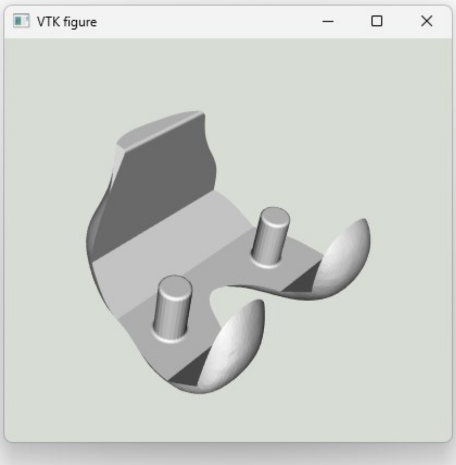

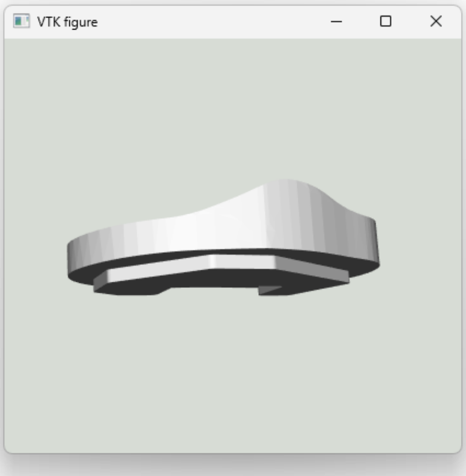

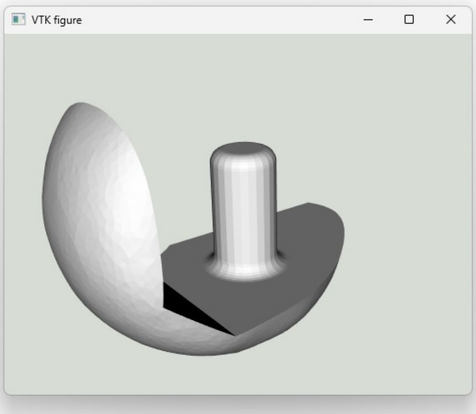

As before, when the custom implant design process is completed, the ‘Compare to GT’ button will then be unlocked. If this button is pressed, models of the custom components will be fitted to the ground truth 3D models and the location of the maximum OUH highlighted – like shown before for implant size prediction. A further window will also appear with component to ground truth RMSE and maximum OUH fit results as demonstrated below.

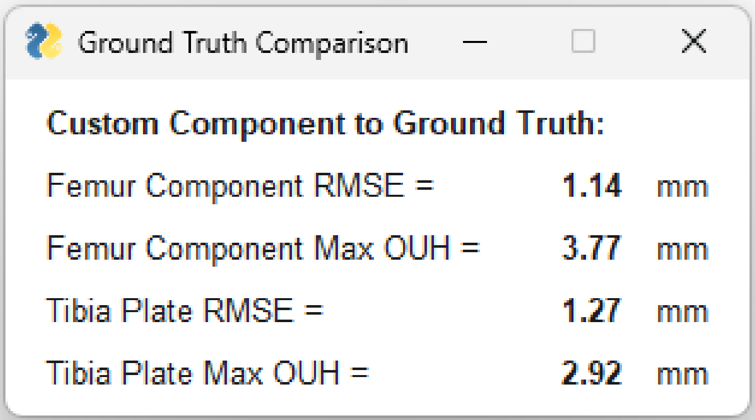

Customise Tibia Plate Stiffness Tab

The final tab allows for users to run the implant stiffness customisation pipeline. An additional CT file selection option is provided for users to specify a DICOM file where a density phantom has been included. The tibia plate geometry that the lattice structure will be designed for can then be specified – this could be a custom implant model created by the software, or a specified OTS model. An option is provided for users to specify which style of lattice structure they would like from the designs detailed in Figure 91, including a uniform mean stiffness, left/right condyle mean stiffness, as well as a full stiffness matched array. A desired Z offset can be inputted to control where the density information is taken from subjects’ bones. Various lattice design parameters can also be specified in the following text boxes including target connectivity, strut density and strut length. Lastly, the directory that the outputted build files are to be saved to can be specified.

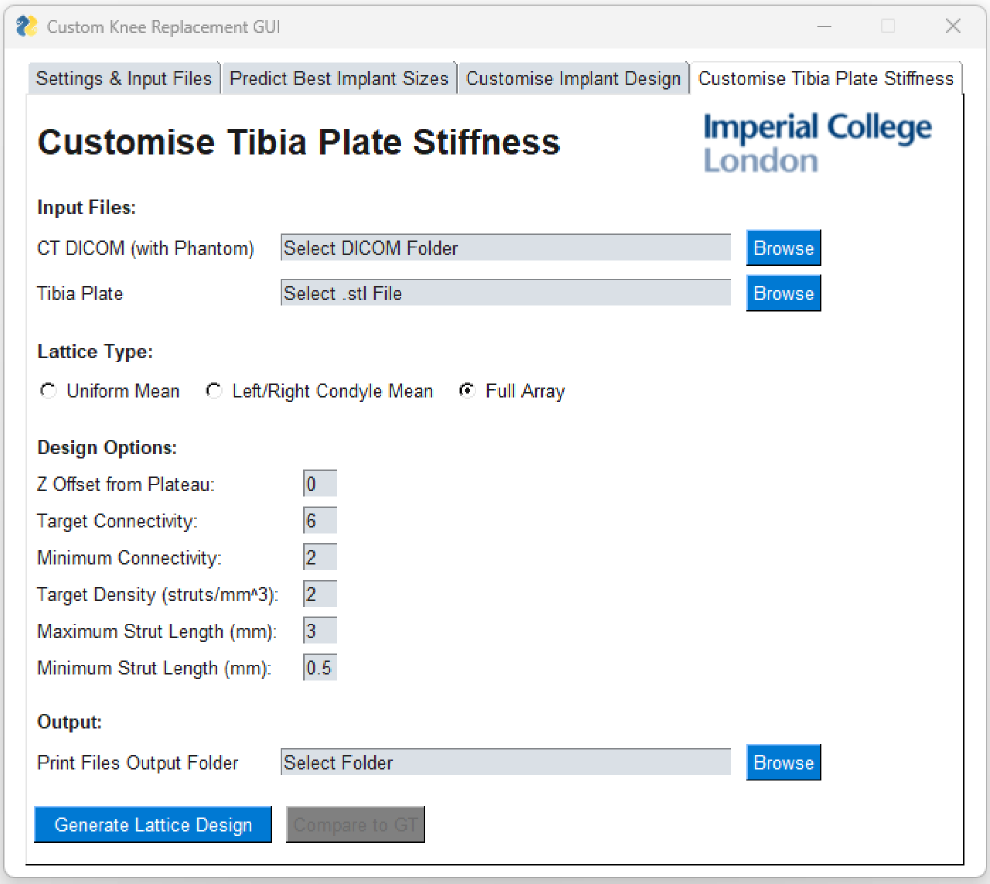

When the 'Generate lattice design' button is pressed, the software will run the pipeline outlined in Chapter 9.2 and produce a lattice design and corresponding printing files for additive manufacture. If visuals are set to 'On' on the first tab, a pop out window will demonstrate the lattice structure created as illustrated below.

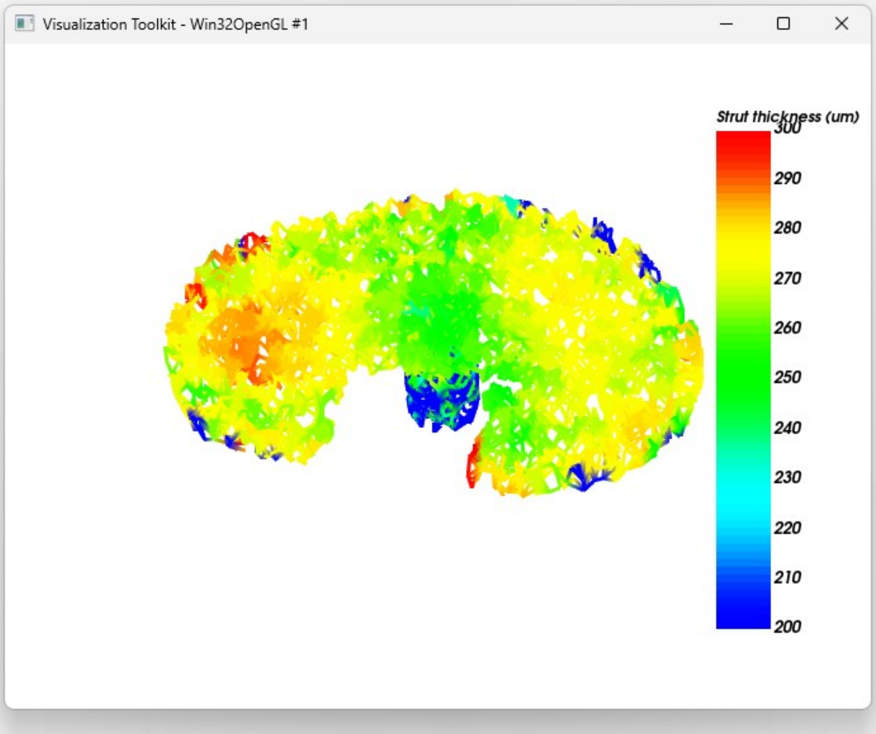

Once the stiffness customisation process is complete, the user will be able to press the 'Compare to GT' button. Here, unlike in the previous tabs, the created lattice design will be displayed again in a pop out window alongside the CT slice selected by the software as shown below. This allows the user to compare resulting lattice designs against the density distribution visible at the relevant point in the bone.

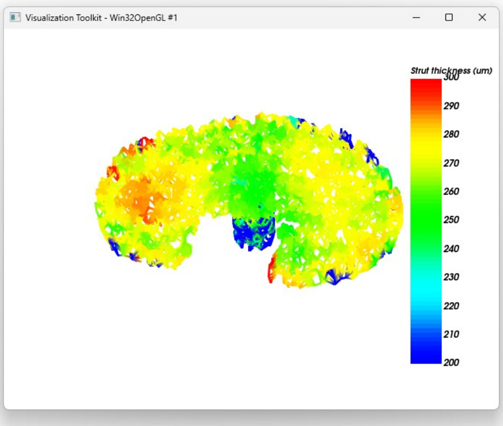

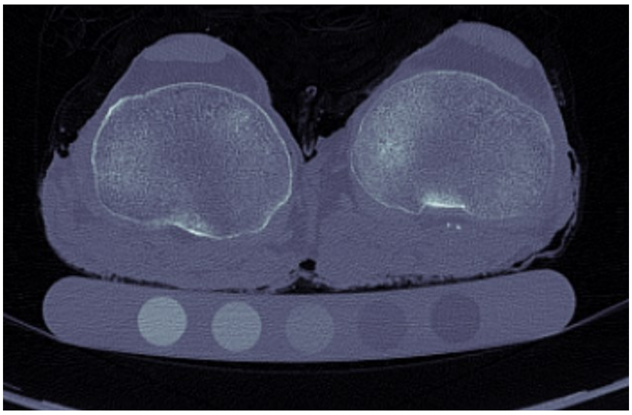

Appendix 2

Permissions Summary Table

In this appendix a table is provided which summarises permissions gained to reproduce third party copyrighted works in this thesis.

Figure number	Name and source	Copyright holder	Permission granted on	Permission note
1	Figure 1 from (Tandeter et al., 1999)	Christy Krames	18th February 2023	Written permission obtaimned via email - ckrames@swbell.net © 1999.
2	Figure 1.6.1 from (Nikita, 2017)	Elsevier	17th February 2023	Reprinted from Nikita, E. (2017) The Human Skeleton. In: Osteoarchaeology. Academic Press. pp. 1–75. Copyright (2017), with permission from Elsevier. License no. 5491380811218.
3	Figure 2 from (Jun, 2011)	Springer Nature	12th January 2023	Reprinted from Jun, Y. (2011) Morphological analysis of the human knee joint for creating custom-made implant models. International Journal of Advanced Manufacturing Technology. 52 (9–12). Copyright (2010), with permission from Springer Nature. License no. 5466490281924.
5 (A&B)	Two figures from website: https://orthoinfo.aaos.org/en/treatment/knee-replacement-implants/	OrthoInfo	12th January 2023	Reproduced with permission from OrthoInfo. © American Academy of Orthopaedic Surgeons. https://orthoinfo.org/
6	Figure 1a from (Lee et al., 2020)	The authors	N/A	Open access article distributed under a Creative Commons Attribution 4.0 International (CC BY 4.0) license. © 2020.

7	Figure 5 from (Shah et al., 2020)	Institute of Electrical and Electronics Engineers (IEEE)	N/A	Reprinted from Shah, Y., Shah, P., Patel, M., Khamkar, C. & Kanani, P. (2020) Deep learning model-based multimedia forgery detection. In: Proceedings of the 4th International Conference on IoT in Social, Mobile, Analytics and Cloud, ISMAC 2020. 2020 pp. 564–572. Copyright IEEE (2020) with permission.
8	Figure 1 from (Wu et al., 2020)	Elsevier	17th February 2023	Reprinted from Wu, X., Sahoo, D. & Hoi, S.C.H. (2020) Recent advances in deep learning for object detection. Neurocomputing. 396, 39–64. Copyright (2020), with permission from Elsevier. License no. 5491450632246.
9	Figure 1 from (Ronneberger et al., 2015)	Springer Nature	12th January 2023	Reprinted from Ronneberger, O., Fischer, P. & Brox, T. (2015) U-Net: Convolutional Networks for Biomedical Image Segmentation. Medical Image Computing and Computer-Assisted Intervention – MICCAI 2015. Lecture Notes in Computer Science. 9351, 234–241. Copyright (2015), with permission from Springer Nature. License no. 5466500408494.
10	Figure 3 from (Smoger et al., 2015)	John Wiley & Sons	22nd February 2023	Used with permission of John Wiley & Sons, from Smoger, L.M., Fitzpatrick, C.K., Clary, C.W., Cyr, A.J., Maletsky, L.P.,

				Rullkoetter, P.J. & Laz, P.J. (2015) Statistical modeling to characterize relationships between knee anatomy and kinematics. Journal of Orthopaedic Research. 33 (11), 1620–1630. Copyright (2015).
11	Figure 1 (A & D) from (Velásquez-García & Kornbluth, 2021)	Annual Reviews	N/A	Open access article distributed under a Creative Commons Attribution 4.0 International (CC BY 4.0) license. © 2021.
13	Figure 1 from (Paxton et al., 2022)	Elsevier	13th January 2023	Reprinted from Paxton, N.C., Nightingale, R.C. & Woodruff, M.A. (2022) Capturing patient anatomy for designing and manufacturing personalized prostheses. Current Opinion in Biotechnology. 73, 282–289. Copyright (2021), with permission from Elsevier. Permissions to use all sub-figures from within main figure were also obtained from the respective copyright holders.
14	Figure 1 from (Zheng et al., 2018)	Springer Nature	19th February 2023	Reprinted from Zheng, G., Hommel, H., Akcoltekin, A., Thelen, B., Stifter, J. & Peersman, G. (2018) A novel technology for 3D knee prosthesis planning and treatment evaluation using 2D X-

				ray radiographs: a clinical evaluation. International Journal of Computer Assisted Radiology and Surgery. 13 (8), 1151–1158. Copyright (2018), with permission from Springer Nature. License no. 5492570304397.
15	Figure 2 from (Tsai et al., 2015)	Informa UK Limited, (Taylor & Francis Group)	12th January 2023	Reprinted from Tsai, T.Y., Li, J.S., Wang, S., Li, P., Kwon, Y.M. & Li, G. (2015) Principal component analysis in construction of 3D human knee joint models using a statistical shape model method. Computer Methods in Biomechanics and Biomedical Engineering. 18 (7), 721–729. Copyright (2015), with permission from Informa UK Limited, trading as Taylor & Francis Group, http://www.tandfonline.com
16	Figure 3 from (Jun, 2011)	Springer Nature	20th February 2023	Reprinted from Jun, Y. (2011) Morphological analysis of the human knee joint for creating custom-made implant models. International Journal of Advanced Manufacturing Technology. 52 (9–12). Copyright (2010), with permission from Springer Nature. License no. 5492950194598.
17A	Figure 3 from (Levine et al., 2006)	Elsevier	20th February 2023	Reprinted from Levine, B.R., Sporer, S., Poggie, R.A., Della Valle, C.J. & Jacobs, J.J. (2006)

				Experimental and clinical performance of porous tantalum in orthopedic surgery. Biomaterials. 27 (27), 4671–4681. Copyright (2006), with permission from Elsevier. License no. 5493270927826.
17B and 19	Figure 1 from (Kechagias et al., 2022)	The Authors	N/A	Open access article distributed under a Creative Commons Attribution 4.0 International (CC BY 4.0) license. © 2022.
18	Figure 1 from (Ghouse et al., 2019)	The Authors	N/A	Open access article distributed under a Creative Commons Attribution 4.0 International (CC BY 4.0) license. © 2019.
21 (A&B)	Figure 3 (A & C) from (Chen et al., 2022)	Springer Nature	14th February 2023	Reprinted from Chen, F., Xie, Y., Xu, P., Zhao, Z., Zhang, D. & Liao, H. (2022) Efficient lower-limb segmentation for large-scale volumetric CT by using projection view and voxel group attention. Medical and Biological Engineering and Computing. 60 (8), 2201–2216. Copyright (2022), with permission from Springer Nature. License no. 5487820077416.
25, 26, 84, 87 – 89, 91 – 94	Multiple figures from (Burge et al., 2023c)	Springer Nature	11th April 2023	Reprinted from Burge, T.A., Munford, M.J., Kechagias, S., Jeffers, J.R.T. & Myant, C.W. (2023) Automating the customization of stiffness-matched knee implants

				using machine learning techniques. The International Journal of Advanced Manufacturing Technology. Copyright (2023), with permission from Springer Nature. License no. 5526000935314.
28, 48, 55, 63, 65 – 69	Multiple figures from (Burge et al., 2022b)	American Society of Mechanical Engineers (ASME)	25th January 2023	Reprinted from Burge, T.A., Jeffers, J.R.T. & Myant, C.W. (2022) Performance and Sensitivity Analysis of an Automated X-Ray Based Total Knee Replacement Mass-Customization Pipeline. Journal of Medical Devices. 16 (4), 1–12. Copyright (2022), with permission from ASME.
31, 51 – 54, 59	Multiple figures from (Burge et al., 2022a)	American Society of Mechanical Engineers (ASME)	25th January 2023	Reprinted from Burge, T.A., Jeffers, J.R.T. & Myant, C.W. (2022) Development of an Automated Mass-Customization Pipeline for Knee Replacement Surgery Using Biplanar X-Rays. Journal of Mechanical Design. 144 (2), 1–11. Copyright (2021), with permission from ASME.
32, 33, 56, 57, 74, 77, 78	Multiple figures from (Burge et al., 2023b)	The Authors	N/A	Open access article distributed under a Creative Commons Attribution 4.0 International (CC BY 4.0) license. © 2023.
35 – 40, 44, 45	Multiple figures from	The Authors	N/A	Open access article distributed under a Creative Commons

	(Burge et al., 2023a)			Attribution 4.0 International (CC BY 4.0) license. © 2022.
43	Figure 1 from (Stulberg & Goyal, 2015)	Elsevier	15th February 2023	Reprinted from Stulberg, S.D. & Goyal, N. (2015) Which Tibial Tray Design Achieves Maximum Coverage and Ideal Rotation: Anatomic, Symmetric, or Asymmetric? An MRI-based study. Journal of Arthroplasty. 30 (10), 1839–1841. Copyright (2015), with permission from Elsevier License no. 5490081200868.
47, 71, 72	Multiple figures from (Burge et al., 2022c)	The Authors	N/A	Open access article distributed under a Creative Commons Attribution 4.0 International (CC BY 4.0) license. © 2022.

gcmb20:Principal component analysis in construction of 3D human knee joint models using a statistical shape model method

Taylor & Francis Journal Permissions Support <taylorandfrancissupport@tandf.co.uk>

Thu 1/12/2023 2:24 PM

To:Burge, Thomas <t.burge20@imperial.ac.uk>

This email from taylorandfrancissupport@tandf.co.uk originates from outside Imperial. Do not click on links and attachments unless you recognise the sender. If you trust the sender, add them to your safe senders list to disable email stamping for this address.

journal_permissions_header_logo - Dec 22

Our Ref: gcmb/02878116

1/12/2023

Dear Requester,

Thank you for your correspondence requesting permission to reproduce content from a Taylor & Francis Group journal content in your thesis to be posted on your university's repository.

We will be pleased to grant free permission on the condition that your acknowledgement must be included showing article title, author, full Journal title, and **© copyright # [year]**, reprinted by permission of Informa UK Limited, trading as Taylor & Taylor & Francis Group, http://www.tandfonline.com

This permission does not cover any third party copyrighted work which may appear in the article by permission. Please ensure you have checked all original source details for the rights holder and if need apply for permission from the original rightsholder.

Please note that this license **does not allow you to post our content on any other third-party websites.**

Please note permission does not provide access to our article, if you are affiliated to an institution and your institution holds a subscription to the content you are requesting you will be able to view the article free of charge, if your institution does not hold a subscription or you are not affiliated to an institution that has a subscription then you will need to purchase this for your own personal use as we do not provide our articles free of charge for research.

Thank you for your interest in our Journal.

With best wishes,

Taylor & Francis Journal Permissions
Web: www.tandfonline.com
4 Park Square, Milton Park, Abingdon, OX14 4RN
(+44 (0)20 8052 0600

Disclaimer: T&F publish Open Access articles in our subscription priced journals, please check if the article you are interested in is an OA article and if so, which license was it published under.

Before printing, think about the environment.

ref:_00D0Y35Iji._5007TGdY2V:ref

Permissions Request

Type of use: Academic
Article title: Principal component analysis in construction of 3D human knee joint models using a statistical shape model method
Article DOI: 10.1080/10255842.2013.843676
Author name: Tsung-Yuan Tsai, Jing-Sheng Li, Shaobai Wang, Pingyue Li, Young-Min Kwon & Guoan Li
Journal title: Computer Methods in Biomechanics and Biomedical Engineering
Volume number: 18
Issue number: 7
Year of publication: 2015
Name: Thomas Burge
Street address: Imperial College Rd, Kensington
Town: London
Postcode/ZIP code: SW7 1AL
Country: United Kingdom
Email: t.burge20@imperial.ac.uk
Telephone: [redacted]
Intended use: To be used in your Thesis?
Are you requesting the full article?: No
Extract and number of words: N/A - just looking to use Figure 2
Details of figure/table: Figure 2
Which University?: Imperial College
Title of your Thesis?: Applied AI/ML for Automatic Customisation of Medical Implants
University repository URL: https://spiral.imperial.ac.uk/
Is this a “Closed” or “Open” deposit?: open
Additional comments: Please could I use Figure 2 in my PhD thesis? <img src="https://taylorandfrancis.my.salesforce.com/servlet/servlet.ImageServer?oid=00D0Y0000035Iji&esid=0187T000009MzgB&from=ext"

FW: Permission request to use images in PhD thesis

Decker, Monica <mdecker@aaos.org>
Thu 1/12/2023 7:18 PM
To:Burge, Thomas <t.burge20@imperial.ac.uk>

Dear Thomas,

Your request for permission was forwarded to my attention, thank you. You have permission to use the images referenced below from AAOS's *OrthoInfo* in your thesis provided that you use the following credit line:

Reproduced with permission from OrthoInfo. © American Academy of Orthopaedic Surgeons. https://orthoinfo.org/.

Thank you.

Sincerely,
Monica Decker

AAOS
American Academy of Orthopaedic Surgeons
American Association of Orthopaedic Surgeons

Monica Decker
Compliance Specialist
Office of General Counsel
9400 West Higgins Road, Rosemont, IL 60018
847.384.4047
mdecker@aaos.org

From: Burge, Thomas <t.burge20@imperial.ac.uk>
Sent: Thursday, January 12, 2023 10:44 AM
To: orthoinfo <orthoinfo@aaos.org>
Subject: Permission request to use images in PhD thesis

Caution - External

Dear Sir/Madam

I am completing my PhD thesis at Imperial College London entitled Applied AI/ML for 'Automatic Customisation of Medical Implants'.

I seek your permission to reprint, in my thesis three images from an OrthoInfo article. Accessibly at the following address: https://orthoinfo.aaos.org/en/treatment/knee-replacement-implants/

I specifically wish to reprint the following figures:

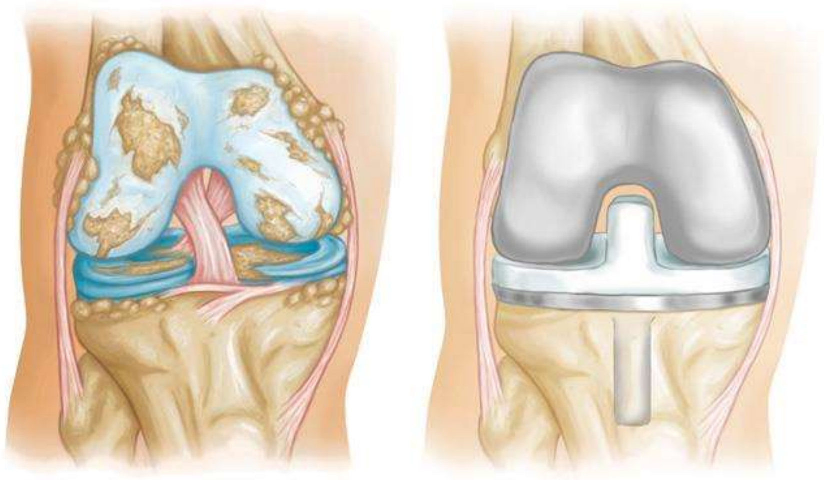

After acceptance, my thesis will be added to Spiral, Imperial's institutional repository http://spiral.imperial.ac.uk/ and made available to the public.

If this is acceptable please could you confirm via email?

Regards
Thomas Burge

Re: Using Figure in PhD thesis [230112-022626]

Permissions Helpdesk <permissionshelpdesk@elsevier.com>
Fri 1/13/2023 6:56 AM
To:Burge, Thomas <t.burge20@imperial.ac.uk>

Dear Thomas Burge,

Hope you are well.

We hereby grant you permission to reprint the material below at no charge in your thesis subject to the following conditions:

RE: Capturing patient anatomy for designing and manufacturing personalized prostheses, Current Opinion in Biotechnology, Volume 73, February 2022, Pages 282-289, 1 Figure only.

1. If any part of the material to be used (for example, figures) has appeared in our publication with credit or acknowledgement to another source, permission must also be sought from that source. If such permission is not obtained then that material may not be included in your publication/copies.

2. Suitable acknowledgment to the source must be made, either as a footnote or in a reference list at the end of your publication, as follows:
"This article was published in Publication title, Vol number, Author(s), Title of article, Page Nos, Copyright Elsevier (or appropriate Society name) (Year)."

3. Your thesis may be submitted to your institution in either print or electronic form.

4. Reproduction of this material is confined to the purpose for which permission is hereby given

5. This permission is granted for non-exclusive world English rights only. For other languages please reapply separately for each one required. Permission excludes use in an electronic form other than submission. Should you have a

specific electronic project in mind please reapply for permission.

6. Should your thesis be published commercially, please reapply for permission.

This includes permission for the Library and Archives of Canada to supply single copies, on demand, of the complete thesis. Should your thesis be published commercially, please reapply for permission-Canada
This includes permission for UMI to supply single copies, on demand, of the complete thesis. Should your thesis be published commercially, please reapply for permission-ROW

7. Posting of the full article online is not permitted. You may post an abstract with a link to the Elsevier website www.elsevier.com, or to the article on ScienceDirect if it is available on that platform.

8. Article can used be in the University library if it is embedded in the thesis and not used commercially.

Kind regards,

Thomas Rexson Yesudoss
Copyrights Coordinator
ELSEVIER | HCM - Health Content Management

Visit Elsevier Permissions

From: Administrator
Date: Thursday, January 12, 2023 01:55 PM GMT

Dear Customer

Thank you for contacting Elsevier's Permissions Helpdesk.

This is an automated acknowledgement to confirm we have received your query. Ticket number 230112-022626 has been opened on your behalf and we aim to respond within two business days.

Regards,

Permissions Helpdesk

From: Thomas Burge
Date: Thursday, January 12, 2023 01:55 PM GMT

Please could I use Figure 1 from "Capturing patient anatomy for designing and manufacturing personalized prostheses" - 10.1016/j.copbio.2021.09.004 in my PhD thesis? Figure attached below for reference

---

FW: New website enquiry "Contact us"

Cooper, Sean <Sean.Cooper@ottobock.com>
Mon 1/16/2023 11:36 AM

To:Burge, Thomas <t.burge20@imperial.ac.uk>

Good morning Tom.

Further to your enquiry, it is permissible to use the image in question.

Kind Regards

Sean R.J Cooper
Customer Support Advisor

Otto Bock Healthcare PLC
32 Parsonage Road Egham TW20 0LD

Tel +44 (0)1784 744 911

www.ottobock.co.uk

From: t.burge20@imperial.ac.uk <t.burge20@imperial.ac.uk>
Sent: 13 January 2023 16:13
To: bockuk <bockuk@ottobock.com>
Subject: New website enquiry "Contact us"

A new request from your B2C Contact us form is pending:

[redacted]
ZIP:
City: London
Country: bockuk@ottobock.com

Phone: 07805770594
eMail: t.burge20@imperial.ac.uk

Topic: Other
Question: Hi I would like to use the photo of a hand, included on your website at the following address: https://www.ottobock.com/en-gb/custom-silicone, in my PhD thesis. Please could you confirm by email if this is permittable? Thanks Tom

Contact method: email
Newsletter:

RE: Inclusion of Paper Content in PhD Thesis

Permissions <Permissions@asme.org>
Wed 1/25/2023 7:40 PM
To:Burge, Thomas <t.burge20@imperial.ac.uk>

Dear Mr. Burge,
It is our pleasure to grant you permission to use **all or any part of** the following ASME papers:

- Development of an Automated Mass-Customization Pipeline for Knee Replacement Surgery Using Biplanar X-Rays , by Thomas A. Burge, Jonathan R. T. Jeffers, Connor W. Myant, J. Mech. Des. February 2022, 144(2)
- Performance and Sensitivity Analysis of an Automated X-Ray Based Total Knee Replacement Mass-Customization Pipeline, by Thomas A. Burge, Jonathan R. T. Jeffers, Connor W. Myant, J. Med. Devices. December 2022, 16(4)

cited in your letter for inclusion in a publication entitled Applied AI/ML for Automatic Customisation of Medical Implants to be published by Imperial College London.

Permission is granted for the specific use as stated herein and does not permit further use of the materials without proper authorization. Proper attribution must be made to the author(s) of the materials. **Please note**: if any or all of the figures and/or Tables are of another source, permission should be granted from that outside source or include the reference of the original source. ASME does not grant permission for outside source material that may be referenced in the ASME works.

As is customary, we request that you ensure full acknowledgment of this material, the author(s), source and ASME as original publisher.

Many thanks for your interest in ASME publications.

Sincerely,

Beth Darchi
Publishing Administrator
ASME
2 Park Avenue, 6th Floor
New York, NY 10016-5990
darchib@asme.org

From: Burge, Thomas <t.burge20@imperial.ac.uk>
Sent: Saturday, January 21, 2023 6:09 AM
To: Permissions <Permissions@asme.org>
Subject: Re: Inclusion of Paper Content in PhD Thesis

WARNING: This Message Came From Outside of ASME. Do not click on links or attachments unless you know the content to be safe.
Dear Sir/Madam

I have completed the form below as requested. Please let me know if you need any further detail.

Regards
Thomas Burge

From: Permissions <Permissions@asme.org>
Sent: Friday, January 20, 2023 12:49 PM
To: Burge, Thomas <t.burge20@imperial.ac.uk>
Subject: RE: Inclusion of Paper Content in PhD Thesis

In order for us to address permission requests to use ASME material, please be sure to fill out all required fields (*) to complete the form. Please send the form to permissions@asme.org.

Upon receipt of this form, I will be happy to give this matter my immediate attention and consideration, applying royalties if applicable.

ASME CONFERENCE/JOURNAL /BOOKS PUBLICATIONS PERMISSION REQUEST FORM:
*Please **TYPE** in all required fields. Please do not write in.

ASME Publication Title

(Conference/Journal/Book)*:

- Development of an Automated Mass-Customization Pipeline for Knee Replacement Surgery Using Biplanar X-Rays (Journal of Mechanical Design)
- Performance and Sensitivity Analysis of an Automated X-Ray Based Total Knee Replacement Mass-Customization Pipeline (Journal of Medical Devices)

Complete List of ASME Authors*:

- Burge, Thomas A
- Jeffers, Jonathan R T
- Myant, Connor W

(Same for both papers)

ASME Paper Title (Conference or Journal) *:

- Development of an Automated Mass-Customization Pipeline for Knee Replacement Surgery Using Biplanar X-Rays (Journal of Mechanical Design)
- Performance and Sensitivity Analysis of an Automated X-Ray Based Total Knee Replacement Mass-Customization Pipeline (Journal of Medical Devices)

Conference Paper Number (if conference)*: N/A

(Journal) paper number *:

Papers 021702-1 and 041007-9 respectively

Volume Number

DOI Number: 10.1115/1

.4052192
and 10.1115/1.4055
000

Indicate Page(s) in the ASME publication: All pages

Year of Publication*: 2022 and
2022

List ASME Figure Numbers:
All

List ASME Table Numbers:
All
Number of Copies:

Usage (Please check box): ☐ **Print** ☒ **Academic** ☐ **Online** ☐ **Intranet**

Title of outside publication / Thesis*:

Applied AI/ML for Automatic Customisation of Medical Implants

Name of Outside Publisher or University*:

Imperial College London

Explanation of Usage:

I am writing my PhD thesis. I would like to rework and use the two papers that I published with the detailed ASME journals as chapters in the thesis. I would like to use the majority of the figures and the results included in the tables. I am the first author on both the papers and my coauthors have given me permission to include the work in my thesis. Please confirm this is acceptable.

First Name*:
Thomas

Last Name*:
Burge

Address Line 1*:
[redacted]

Address Line 2:

City*: [redacted]

State*: UK

Zip [redacted]

Phone:

Fax: [redacted]

Email*: t.burge20@imperial.ac.uk

Regards,

Permissions
ASME
2 Park Avenue, 6th Floor

New York, NY 10016-5990
permissions@asme.org

From: Burge, Thomas <t.burge20@imperial.ac.uk>
Sent: Thursday, January 12, 2023 7:00 AM
To: Permissions <Permissions@asme.org>
Subject: Inclusion of Paper Content in PhD Thesis

WARNING: This Message Came From Outside of ASME. Do not click on links or attachments unless you know the content to be safe.

Dear Sir/Madam

Please could you confirm the correct course of action for me to include figures and results from articles I have published in ASME journals in my PhD thesis?

On your website the following is stated in the permissions section:

"Authors may reproduce and distribute the Paper for non-commercial purposes only. Non-commercial applies only to the sale of the paper per se. For all copies of the Paper made by Authors, Authors must acknowledge ASME as original publisher and include the names of all author(s), the publication title, and an appropriate copyright notice that identifies ASME as the copyright holder."

Does the above cover the inclusion of results in theses, or will I need to submit a separate request?

Regards
Thomas Burge

Re: Permission to use figure in PhD thesis

Christy LANGENBERG <ckrames@swbell.net>

Fri 2/17/2023 9:51 PM

To:Burge, Thomas <t.burge20@imperial.ac.uk>

Dear Thomas,

You have my permission to reproduce my knee illustration in your thesis. Good luck with everything.

Kind regards,

Christy Krames
Sent from my iPhone

> On Feb 17, 2023, at 11:50 AM, Burge, Thomas <t.burge20@imperial.ac.uk> wrote:
>
> Dear Christy Krames
>
> I am completing my PhD thesis at Imperial College London, entitled 'Applied AI/ML for Automatic Customisation of Medical Implants'.
>
> I seek your permission to reprint in my thesis the image below which I believe you own the copywrite of and is included as Figure 1 in the paper titled "Acute Knee Injuries: Use of Decision Rules for Selective Radiograph Ordering" by HOWARD B. TANDETER, M.D., PESACH SHVARTZMAN, M.D., AND MAX A. STEVENS, M.D. Am Fam Physician. 1999;60(9):2599-2608
>
> <image.png>
>
> After acceptance, my thesis will be added to Spiral, Imperial's institutional repository http://spiral.imperial.ac.uk/ and made available to the public.
>
> If this is acceptable, please could you confirm via email?
>
> Regards
> Thomas Burge

Re.: Request for permission to use image from website

Jette Brandt <dkjbt@coloplast.com>
Tue 2/14/2023 10:12 AM
To:Burge, Thomas <t.burge20@imperial.ac.uk>

Dear Thomas Burge,

Thank you for your request.
Please see the consent below.

Permission for usage of Coloplast Assets

Dear Thomas Burge,

In response to your request of February 7th 2023, for usage of Coloplast Product Photo of **Torosa ®Intestinal Prostesis**

in your PhD thesis at Imperial College London, entitled "Applied AI/ML for Automatic Customisation of Medical

Implants", we hereby grant the consent requested.

We accept the thesis being added to the institutional repository.

Please credit "Coloplast A/S, Denmark" as the source and grantor of the consent.

Kind regards

Knowledge Center
Jette Brandt

Venlig hilsen/Best regards,

Jette Brandt

Information Specialist
Group IP
Group Legal, IP & Business Ethics
M: +45 4911 1979
T: +45 4911 1979

Coloplast

Coloplast A/S
Holtedam 1, 3050 Humlebæk
Denmark
www.coloplast.com
+45 49111111

From: Burge, Thomas <t.burge20@imperial.ac.uk>
Sent: Tuesday, February 7, 2023 10:50 PM
To: CP_Group_Legal_IP_&_Business_Ethics_Legal_Aspects
<CP_Group_Legal_IP_&_Business_Ethics_Legal_Aspects@coloplast.com>
Subject: Re: Request for permission to use image from website

Dear Sir/Madam

I am completing my PhD thesis at Imperial College London, entitled 'Applied AI/ML for Automatic Customisation of Medical Implants'.

I seek your permission to reprint in my thesis the image below from your website: https://www.coloplast.us/torosa-en-us.aspx

I specifically want to use Figure 1 from the article "Capturing patient anatomy for designing and manufacturing personalized prostheses" which can be found here
- https://reader.elsevier.com/reader/sd/pii/S0958166921001695?token=7252290DD04269C433F69DAD1D2E263F5D29024743413D916E03ED9CA29C438E5695B71F08C198507131070EB08BAF3B&originRegion=eu-west-1&originCreation=20230113160141

This contains your image above, but notes I need to contact the original copyright holder if I want to use the Figure.

After acceptance, my thesis will be added to Spiral, Imperial's institutional repository http://spiral.imperial.ac.uk/ and made available to the public.

If this is acceptable, please could you confirm via email?

Regards
Thomas Burge

SPRINGER NATURE LICENSE
TERMS AND CONDITIONS

Sep 11, 2023

This Agreement between Mr. Thomas Burge ("You") and Springer Nature ("Springer Nature") consists of your license details and the terms and conditions provided by Springer Nature and Copyright Clearance Center.

License Number	5466490281924
License date	Jan 12, 2023
Licensed Content Publisher	Springer Nature
Licensed Content Publication	The International Journal of Advanced Manufacturing Technology
Licensed Content Title	Morphological analysis of the human knee joint for creating custom-made implant models
Licensed Content Author	Yongtae Jun
Licensed Content Date	Jun 27, 2010
Type of Use	Thesis/Dissertation
Requestor type	academic/university or research institute
Format	print and electronic
Portion	figures/tables/illustrations
Number of figures/tables/illustrations	1
Will you be translating?	no
Circulation/distribution	1 - 29

Author of this Springer Nature content	no
Title	Applying machine learning to automate the customisation of medical implants (PhD thesis)
Institution name	Imperial College
Expected presentation date	Apr 2023
Portions	I would like to use figure 2 in a PhD thesis
Requestor Location	Mr. Thomas Burge Imperial College Rd, Kensington London, SW7 1AL United Kingdom Attn: Imperial College
Total	0.00 GBP

Terms and Conditions

Springer Nature Customer Service Centre GmbH Terms and Conditions

The following terms and conditions ("Terms and Conditions") together with the terms specified in your [RightsLink] constitute the License ("License") between you as Licensee and Springer Nature Customer Service Centre GmbH as Licensor. By clicking 'accept' and completing the transaction for your use of the material ("Licensed Material"), you confirm your acceptance of and obligation to be bound by these Terms and Conditions.

1. Grant and Scope of License

1. 1. The Licensor grants you a personal, non-exclusive, non-transferable, non-sublicensable, revocable, world-wide License to reproduce, distribute, communicate to the public, make available, broadcast, electronically transmit or create derivative works using the Licensed Material for the purpose(s) specified in your RightsLink Licence Details only. Licenses are granted for the specific use requested in the order and for no other use, subject to these Terms and Conditions. You acknowledge and agree that the rights granted to you under this License do not include the right to modify, edit, translate, include in collective works, or create derivative works of the Licensed Material in whole or in part unless expressly stated in your RightsLink Licence Details. You may use the Licensed Material only as permitted under this Agreement and will not reproduce, distribute, display, perform, or otherwise use or exploit any Licensed Material in any way, in whole or in part, except as expressly permitted by this License.

1. 2. You may only use the Licensed Content in the manner and to the extent permitted by these Terms and Conditions, by your RightsLink Licence Details and by any applicable laws.

1. 3. A separate license may be required for any additional use of the Licensed Material, e.g. where a license has been purchased for print use only, separate permission must be obtained for electronic re-use. Similarly, a License is only valid in the language selected and does not apply for editions in other languages unless additional translation rights have been granted separately in the License.

1. 4. Any content within the Licensed Material that is owned by third parties is expressly excluded from the License.

1. 5. Rights for additional reuses such as custom editions, computer/mobile applications, film or TV reuses and/or any other derivative rights requests require additional permission and may be subject to an additional fee. Please apply to journalpermissions@springernature.com or bookpermissions@springernature.com for these rights.

2. Reservation of Rights

Licensor reserves all rights not expressly granted to you under this License. You acknowledge and agree that nothing in this License limits or restricts Licensor's rights in or use of the Licensed Material in any way. Neither this License, nor any act, omission, or statement by Licensor or you, conveys any ownership right to you in any Licensed Material, or to any element or portion thereof. As between Licensor and you, Licensor owns and retains all right, title, and interest in and to the Licensed Material subject to the license granted in Section 1.1. Your permission to use the Licensed Material is expressly conditioned on you not impairing Licensor's or the applicable copyright owner's rights in the Licensed Material in any way.

3. Restrictions on use

3. 1. Minor editing privileges are allowed for adaptations for stylistic purposes or formatting purposes provided such alterations do not alter the original meaning or intention of the Licensed Material and the new figure(s) are still accurate and representative of the Licensed Material. Any other changes including but not limited to, cropping, adapting, and/or omitting material that affect the meaning, intention or moral rights of the author(s) are strictly prohibited.

3. 2. You must not use any Licensed Material as part of any design or trademark.

3. 3. Licensed Material may be used in Open Access Publications (OAP), but any such reuse must include a clear acknowledgment of this permission visible at the same time as the figures/tables/illustration or abstract and which must indicate that the Licensed Material is not part of the governing OA license but has been reproduced with permission. This may be indicated according to any standard referencing system but must include at a minimum 'Book/Journal title, Author, Journal Name (if applicable), Volume (if applicable), Publisher, Year, reproduced with permission from SNCSC'.

4. STM Permission Guidelines

4. 1. An alternative scope of license may apply to signatories of the STM Permissions Guidelines ("STM PG") as amended from time to time and made available at https://www.stm-assoc.org/intellectual-property/permissions/permissions-guidelines/.

4. 2. For content reuse requests that qualify for permission under the STM PG, and which may be updated from time to time, the STM PG supersede the terms and

conditions contained in this License.

4. 3. If a License has been granted under the STM PG, but the STM PG no longer apply at the time of publication, further permission must be sought from the Rightsholder. Contact journalpermissions@springernature.com or bookpermissions@springernature.com for these rights.

5. Duration of License

5. 1. Unless otherwise indicated on your License, a License is valid from the date of purchase ("License Date") until the end of the relevant period in the below table:

Reuse in a medical communications project	Reuse up to distribution or time period indicated in License
Reuse in a dissertation/thesis	Lifetime of thesis
Reuse in a journal/magazine	Lifetime of journal/magazine
Reuse in a book/textbook	Lifetime of edition
Reuse on a website	1 year unless otherwise specified in the License
Reuse in a presentation/slide kit/poster	Lifetime of presentation/slide kit/poster. Note: publication whether electronic or in print of presentation/slide kit/poster may require further permission.
Reuse in conference proceedings	Lifetime of conference proceedings
Reuse in an annual report	Lifetime of annual report
Reuse in training/CME materials	Reuse up to distribution or time period indicated in License
Reuse in newsmedia	Lifetime of newsmedia
Reuse in coursepack/classroom materials	Reuse up to distribution and/or time period indicated in license

6. Acknowledgement

6. 1. The Licensor's permission must be acknowledged next to the Licensed Material in print. In electronic form, this acknowledgement must be visible at the same time as the figures/tables/illustrations or abstract and must be hyperlinked to the journal/book's homepage.

6. 2. Acknowledgement may be provided according to any standard referencing system and at a minimum should include "Author, Article/Book Title, Journal name/Book imprint, volume, page number, year, Springer Nature".

7. Reuse in a dissertation or thesis

7. 1. Where 'reuse in a dissertation/thesis' has been selected, the following terms apply: Print rights of the Version of Record are provided for; electronic rights for use only on institutional repository as defined by the Sherpa guideline (www.sherpa.ac.uk/romeo/) and only up to what is required by the awarding institution.

7. 2. For theses published under an ISBN or ISSN, separate permission is required. Please contact journalpermissions@springernature.com or bookpermissions@springernature.com for these rights.

7. 3. Authors must properly cite the published manuscript in their thesis according to current citation standards and include the following acknowledgement: '*Reproduced with permission from Springer Nature'*.

8. License Fee

You must pay the fee set forth in the License Agreement (the "License Fees"). All amounts payable by you under this License are exclusive of any sales, use, withholding, value added or similar taxes, government fees or levies or other assessments. Collection and/or remittance of such taxes to the relevant tax authority shall be the responsibility of the party who has the legal obligation to do so.

9. Warranty

9. 1. The Licensor warrants that it has, to the best of its knowledge, the rights to license reuse of the Licensed Material. **You are solely responsible for ensuring that the material you wish to license is original to the Licensor and does not carry the copyright of another entity or third party (as credited in the published version).** If the credit line on any part of the Licensed Material indicates that it was reprinted or adapted with permission from another source, then you should seek additional permission from that source to reuse the material.

9. 2. EXCEPT FOR THE EXPRESS WARRANTY STATED HEREIN AND TO THE EXTENT PERMITTED BY APPLICABLE LAW, LICENSOR PROVIDES THE LICENSED MATERIAL "AS IS" AND MAKES NO OTHER REPRESENTATION OR WARRANTY. LICENSOR EXPRESSLY DISCLAIMS ANY LIABILITY FOR ANY CLAIM ARISING FROM OR OUT OF THE CONTENT, INCLUDING BUT NOT LIMITED TO ANY ERRORS, INACCURACIES, OMISSIONS, OR DEFECTS CONTAINED THEREIN, AND ANY IMPLIED OR EXPRESS WARRANTY AS TO MERCHANTABILITY OR FITNESS FOR A PARTICULAR PURPOSE. IN NO EVENT SHALL LICENSOR BE LIABLE TO YOU OR ANY OTHER PARTY OR ANY OTHER PERSON OR FOR ANY SPECIAL, CONSEQUENTIAL, INCIDENTAL, INDIRECT, PUNITIVE, OR EXEMPLARY DAMAGES, HOWEVER CAUSED, ARISING OUT OF OR IN CONNECTION WITH THE DOWNLOADING, VIEWING OR USE OF THE LICENSED MATERIAL REGARDLESS OF THE FORM OF ACTION, WHETHER FOR BREACH OF CONTRACT, BREACH OF WARRANTY, TORT, NEGLIGENCE, INFRINGEMENT OR OTHERWISE (INCLUDING, WITHOUT LIMITATION, DAMAGES BASED ON LOSS OF PROFITS, DATA, FILES, USE, BUSINESS OPPORTUNITY OR CLAIMS OF THIRD PARTIES), AND WHETHER OR NOT THE PARTY HAS BEEN ADVISED OF THE POSSIBILITY OF SUCH DAMAGES. THIS LIMITATION APPLIES NOTWITHSTANDING ANY FAILURE OF ESSENTIAL PURPOSE OF ANY LIMITED REMEDY PROVIDED HEREIN.

10. Termination and Cancellation

10. 1. The License and all rights granted hereunder will continue until the end of the applicable period shown in Clause 5.1 above. Thereafter, this license will be terminated and all rights granted hereunder will cease.

10. 2. Licensor reserves the right to terminate the License in the event that payment is not received in full or if you breach the terms of this License.

11. General

11. 1. The License and the rights and obligations of the parties hereto shall be construed, interpreted and determined in accordance with the laws of the Federal

Republic of Germany without reference to the stipulations of the CISG (United Nations Convention on Contracts for the International Sale of Goods) or to Germany´s choice-of-law principle.

11. 2. The parties acknowledge and agree that any controversies and disputes arising out of this License shall be decided exclusively by the courts of or having jurisdiction for Heidelberg, Germany, as far as legally permissible.

11. 3. This License is solely for Licensor's and Licensee's benefit. It is not for the benefit of any other person or entity.

Questions? For questions on Copyright Clearance Center accounts or website issues please contact springernaturesupport@copyright.com or +1-855-239-3415 (toll free in the US) or +1-978-646-2777. For questions on Springer Nature licensing please visit https://www.springernature.com/gp/partners/rights-permissions-third-party-distribution

Other Conditions:

Version 1.4 - Dec 2022

Questions? customercare@copyright.com.

SPRINGER NATURE LICENSE
TERMS AND CONDITIONS

Sep 11, 2023

This Agreement between Mr. Thomas Burge ("You") and Springer Nature ("Springer Nature") consists of your license details and the terms and conditions provided by Springer Nature and Copyright Clearance Center.

License Number	5466500408494
License date	Jan 12, 2023
Licensed Content Publisher	Springer Nature
Licensed Content Publication	Springer eBook
Licensed Content Title	U-Net: Convolutional Networks for Biomedical Image Segmentation
Licensed Content Author	Olaf Ronneberger, Philipp Fischer, Thomas Brox
Licensed Content Date	Jan 1, 2015
Type of Use	Thesis/Dissertation
Requestor type	academic/university or research institute
Format	print and electronic
Portion	figures/tables/illustrations
Number of figures/tables/illustrations	1
Will you be translating?	no
Circulation/distribution	1 - 29

Author of this Springer Nature content	no
Title	Applied AI/ML for Automatic Customisation of Medical Implants
Institution name	Imperial College
Expected presentation date	Apr 2023
Portions	Figure 1
Requestor Location	Mr. Thomas Burge Imperial College Rd, Kensington London, SW7 1AL United Kingdom Attn: Imperial College
Total	0.00 GBP

Terms and Conditions

Springer Nature Customer Service Centre GmbH Terms and Conditions

The following terms and conditions ("Terms and Conditions") together with the terms specified in your [RightsLink] constitute the License ("License") between you as Licensee and Springer Nature Customer Service Centre GmbH as Licensor. By clicking 'accept' and completing the transaction for your use of the material ("Licensed Material"), you confirm your acceptance of and obligation to be bound by these Terms and Conditions.

1. Grant and Scope of License

1. 1. The Licensor grants you a personal, non-exclusive, non-transferable, non-sublicensable, revocable, world-wide License to reproduce, distribute, communicate to the public, make available, broadcast, electronically transmit or create derivative works using the Licensed Material for the purpose(s) specified in your RightsLink Licence Details only. Licenses are granted for the specific use requested in the order and for no other use, subject to these Terms and Conditions. You acknowledge and agree that the rights granted to you under this License do not include the right to modify, edit, translate, include in collective works, or create derivative works of the Licensed Material in whole or in part unless expressly stated in your RightsLink Licence Details. You may use the Licensed Material only as permitted under this Agreement and will not reproduce, distribute, display, perform, or otherwise use or exploit any Licensed Material in any way, in whole or in part, except as expressly permitted by this License.

1. 2. You may only use the Licensed Content in the manner and to the extent permitted by these Terms and Conditions, by your RightsLink Licence Details and by any applicable laws.

1. 3. A separate license may be required for any additional use of the Licensed Material, e.g. where a license has been purchased for print use only, separate permission must be obtained for electronic re-use. Similarly, a License is only valid in the language selected and does not apply for editions in other languages unless additional translation rights have been granted separately in the License.

1. 4. Any content within the Licensed Material that is owned by third parties is expressly excluded from the License.

1. 5. Rights for additional reuses such as custom editions, computer/mobile applications, film or TV reuses and/or any other derivative rights requests require additional permission and may be subject to an additional fee. Please apply to journalpermissions@springernature.com or bookpermissions@springernature.com for these rights.

2. Reservation of Rights

Licensor reserves all rights not expressly granted to you under this License. You acknowledge and agree that nothing in this License limits or restricts Licensor's rights in or use of the Licensed Material in any way. Neither this License, nor any act, omission, or statement by Licensor or you, conveys any ownership right to you in any Licensed Material, or to any element or portion thereof. As between Licensor and you, Licensor owns and retains all right, title, and interest in and to the Licensed Material subject to the license granted in Section 1.1. Your permission to use the Licensed Material is expressly conditioned on you not impairing Licensor's or the applicable copyright owner's rights in the Licensed Material in any way.

3. Restrictions on use

3. 1. Minor editing privileges are allowed for adaptations for stylistic purposes or formatting purposes provided such alterations do not alter the original meaning or intention of the Licensed Material and the new figure(s) are still accurate and representative of the Licensed Material. Any other changes including but not limited to, cropping, adapting, and/or omitting material that affect the meaning, intention or moral rights of the author(s) are strictly prohibited.

3. 2. You must not use any Licensed Material as part of any design or trademark.

3. 3. Licensed Material may be used in Open Access Publications (OAP), but any such reuse must include a clear acknowledgment of this permission visible at the same time as the figures/tables/illustration or abstract and which must indicate that the Licensed Material is not part of the governing OA license but has been reproduced with permission. This may be indicated according to any standard referencing system but must include at a minimum 'Book/Journal title, Author, Journal Name (if applicable), Volume (if applicable), Publisher, Year, reproduced with permission from SNCSC'.

4. STM Permission Guidelines

4. 1. An alternative scope of license may apply to signatories of the STM Permissions Guidelines ("STM PG") as amended from time to time and made available at https://www.stm-assoc.org/intellectual-property/permissions/permissions-guidelines/.

4. 2. For content reuse requests that qualify for permission under the STM PG, and which may be updated from time to time, the STM PG supersede the terms and

conditions contained in this License.

4. 3. If a License has been granted under the STM PG, but the STM PG no longer apply at the time of publication, further permission must be sought from the Rightsholder. Contact journalpermissions@springernature.com or bookpermissions@springernature.com for these rights.

5. Duration of License

5. 1. Unless otherwise indicated on your License, a License is valid from the date of purchase ("License Date") until the end of the relevant period in the below table:

Reuse in a medical communications project	Reuse up to distribution or time period indicated in License
Reuse in a dissertation/thesis	Lifetime of thesis
Reuse in a journal/magazine	Lifetime of journal/magazine
Reuse in a book/textbook	Lifetime of edition
Reuse on a website	1 year unless otherwise specified in the License
Reuse in a presentation/slide kit/poster	Lifetime of presentation/slide kit/poster. Note: publication whether electronic or in print of presentation/slide kit/poster may require further permission.
Reuse in conference proceedings	Lifetime of conference proceedings
Reuse in an annual report	Lifetime of annual report
Reuse in training/CME materials	Reuse up to distribution or time period indicated in License
Reuse in newsmedia	Lifetime of newsmedia
Reuse in coursepack/classroom materials	Reuse up to distribution and/or time period indicated in license

6. Acknowledgement

6. 1. The Licensor's permission must be acknowledged next to the Licensed Material in print. In electronic form, this acknowledgement must be visible at the same time as the figures/tables/illustrations or abstract and must be hyperlinked to the journal/book's homepage.

6. 2. Acknowledgement may be provided according to any standard referencing system and at a minimum should include "Author, Article/Book Title, Journal name/Book imprint, volume, page number, year, Springer Nature".

7. Reuse in a dissertation or thesis

7. 1. Where 'reuse in a dissertation/thesis' has been selected, the following terms apply: Print rights of the Version of Record are provided for; electronic rights for use only on institutional repository as defined by the Sherpa guideline (www.sherpa.ac.uk/romeo/) and only up to what is required by the awarding institution.

7. 2. For theses published under an ISBN or ISSN, separate permission is required. Please contact journalpermissions@springernature.com or bookpermissions@springernature.com for these rights.

7. 3. Authors must properly cite the published manuscript in their thesis according to current citation standards and include the following acknowledgement: '*Reproduced with permission from Springer Nature'*.

8. License Fee

You must pay the fee set forth in the License Agreement (the "License Fees"). All amounts payable by you under this License are exclusive of any sales, use, withholding, value added or similar taxes, government fees or levies or other assessments. Collection and/or remittance of such taxes to the relevant tax authority shall be the responsibility of the party who has the legal obligation to do so.

9. Warranty

9. 1. The Licensor warrants that it has, to the best of its knowledge, the rights to license reuse of the Licensed Material. **You are solely responsible for ensuring that the material you wish to license is original to the Licensor and does not carry the copyright of another entity or third party (as credited in the published version).** If the credit line on any part of the Licensed Material indicates that it was reprinted or adapted with permission from another source, then you should seek additional permission from that source to reuse the material.

9. 2. EXCEPT FOR THE EXPRESS WARRANTY STATED HEREIN AND TO THE EXTENT PERMITTED BY APPLICABLE LAW, LICENSOR PROVIDES THE LICENSED MATERIAL "AS IS" AND MAKES NO OTHER REPRESENTATION OR WARRANTY. LICENSOR EXPRESSLY DISCLAIMS ANY LIABILITY FOR ANY CLAIM ARISING FROM OR OUT OF THE CONTENT, INCLUDING BUT NOT LIMITED TO ANY ERRORS, INACCURACIES, OMISSIONS, OR DEFECTS CONTAINED THEREIN, AND ANY IMPLIED OR EXPRESS WARRANTY AS TO MERCHANTABILITY OR FITNESS FOR A PARTICULAR PURPOSE. IN NO EVENT SHALL LICENSOR BE LIABLE TO YOU OR ANY OTHER PARTY OR ANY OTHER PERSON OR FOR ANY SPECIAL, CONSEQUENTIAL, INCIDENTAL, INDIRECT, PUNITIVE, OR EXEMPLARY DAMAGES, HOWEVER CAUSED, ARISING OUT OF OR IN CONNECTION WITH THE DOWNLOADING, VIEWING OR USE OF THE LICENSED MATERIAL REGARDLESS OF THE FORM OF ACTION, WHETHER FOR BREACH OF CONTRACT, BREACH OF WARRANTY, TORT, NEGLIGENCE, INFRINGEMENT OR OTHERWISE (INCLUDING, WITHOUT LIMITATION, DAMAGES BASED ON LOSS OF PROFITS, DATA, FILES, USE, BUSINESS OPPORTUNITY OR CLAIMS OF THIRD PARTIES), AND WHETHER OR NOT THE PARTY HAS BEEN ADVISED OF THE POSSIBILITY OF SUCH DAMAGES. THIS LIMITATION APPLIES NOTWITHSTANDING ANY FAILURE OF ESSENTIAL PURPOSE OF ANY LIMITED REMEDY PROVIDED HEREIN.

10. Termination and Cancellation

10. 1. The License and all rights granted hereunder will continue until the end of the applicable period shown in Clause 5.1 above. Thereafter, this license will be terminated and all rights granted hereunder will cease.

10. 2. Licensor reserves the right to terminate the License in the event that payment is not received in full or if you breach the terms of this License.

11. General

11. 1. The License and the rights and obligations of the parties hereto shall be construed, interpreted and determined in accordance with the laws of the Federal

Republic of Germany without reference to the stipulations of the CISG (United Nations Convention on Contracts for the International Sale of Goods) or to Germany´s choice-of-law principle.

11. 2. The parties acknowledge and agree that any controversies and disputes arising out of this License shall be decided exclusively by the courts of or having jurisdiction for Heidelberg, Germany, as far as legally permissible.

11. 3. This License is solely for Licensor's and Licensee's benefit. It is not for the benefit of any other person or entity.

Questions? For questions on Copyright Clearance Center accounts or website issues please contact springernaturesupport@copyright.com or +1-855-239-3415 (toll free in the US) or +1-978-646-2777. For questions on Springer Nature licensing please visit https://www.springernature.com/gp/partners/rights-permissions-third-party-distribution

Other Conditions:

Version 1.4 - Dec 2022

Questions? customercare@copyright.com.

SPRINGER NATURE LICENSE
TERMS AND CONDITIONS

Sep 11, 2023

This Agreement between Mr. Thomas Burge ("You") and Springer Nature ("Springer Nature") consists of your license details and the terms and conditions provided by Springer Nature and Copyright Clearance Center.

License Number	5487820077416
License date	Feb 14, 2023
Licensed Content Publisher	Springer Nature
Licensed Content Publication	Medical & Biological Engineering & Computing
Licensed Content Title	Efficient lower-limb segmentation for large-scale volumetric CT by using projection view and voxel group attention
Licensed Content Author	Fang Chen et al
Licensed Content Date	Jun 6, 2022
Type of Use	Thesis/Dissertation
Requestor type	academic/university or research institute
Format	print and electronic
Portion	figures/tables/illustrations
Number of figures/tables/illustrations	2
Will you be translating?	no

Circulation/distribution	1 - 29
Author of this Springer Nature content	no
Title	Applied AI/ML for Automatic Customisation of Medical Implants
Institution name	Imperial College
Expected presentation date	Apr 2023
Portions	Figure 3 (A & C)
Requestor Location	Mr. Thomas Burge Imperial College Rd, Kensington London, SW7 1AL United Kingdom Attn: Imperial College
Total	0.00 GBP

Terms and Conditions

Springer Nature Customer Service Centre GmbH Terms and Conditions

The following terms and conditions ("Terms and Conditions") together with the terms specified in your [RightsLink] constitute the License ("License") between you as Licensee and Springer Nature Customer Service Centre GmbH as Licensor. By clicking 'accept' and completing the transaction for your use of the material ("Licensed Material"), you confirm your acceptance of and obligation to be bound by these Terms and Conditions.

1. Grant and Scope of License

1. 1. The Licensor grants you a personal, non-exclusive, non-transferable, non-sublicensable, revocable, world-wide License to reproduce, distribute, communicate to the public, make available, broadcast, electronically transmit or create derivative works using the Licensed Material for the purpose(s) specified in your RightsLink Licence Details only. Licenses are granted for the specific use requested in the order and for no other use, subject to these Terms and Conditions. You acknowledge and agree that the rights granted to you under this License do not include the right to modify, edit, translate, include in collective works, or create derivative works of the Licensed Material in whole or in part unless expressly stated in your RightsLink Licence Details. You may use the Licensed Material only as permitted under this Agreement and will not reproduce, distribute, display, perform, or otherwise use or

exploit any Licensed Material in any way, in whole or in part, except as expressly permitted by this License.

1. 2. You may only use the Licensed Content in the manner and to the extent permitted by these Terms and Conditions, by your RightsLink Licence Details and by any applicable laws.

1. 3. A separate license may be required for any additional use of the Licensed Material, e.g. where a license has been purchased for print use only, separate permission must be obtained for electronic re-use. Similarly, a License is only valid in the language selected and does not apply for editions in other languages unless additional translation rights have been granted separately in the License.

1. 4. Any content within the Licensed Material that is owned by third parties is expressly excluded from the License.

1. 5. Rights for additional reuses such as custom editions, computer/mobile applications, film or TV reuses and/or any other derivative rights requests require additional permission and may be subject to an additional fee. Please apply to journalpermissions@springernature.com or bookpermissions@springernature.com for these rights.

2. Reservation of Rights

Licensor reserves all rights not expressly granted to you under this License. You acknowledge and agree that nothing in this License limits or restricts Licensor's rights in or use of the Licensed Material in any way. Neither this License, nor any act, omission, or statement by Licensor or you, conveys any ownership right to you in any Licensed Material, or to any element or portion thereof. As between Licensor and you, Licensor owns and retains all right, title, and interest in and to the Licensed Material subject to the license granted in Section 1.1. Your permission to use the Licensed Material is expressly conditioned on you not impairing Licensor's or the applicable copyright owner's rights in the Licensed Material in any way.

3. Restrictions on use

3. 1. Minor editing privileges are allowed for adaptations for stylistic purposes or formatting purposes provided such alterations do not alter the original meaning or intention of the Licensed Material and the new figure(s) are still accurate and representative of the Licensed Material. Any other changes including but not limited to, cropping, adapting, and/or omitting material that affect the meaning, intention or moral rights of the author(s) are strictly prohibited.

3. 2. You must not use any Licensed Material as part of any design or trademark.

3. 3. Licensed Material may be used in Open Access Publications (OAP), but any such reuse must include a clear acknowledgment of this permission visible at the same time as the figures/tables/illustration or abstract and which must indicate that the Licensed Material is not part of the governing OA license but has been reproduced with permission. This may be indicated according to any standard referencing system but must include at a minimum 'Book/Journal title, Author, Journal Name (if applicable), Volume (if applicable), Publisher, Year, reproduced with permission from SNCSC'.

4. STM Permission Guidelines

4. 1. An alternative scope of license may apply to signatories of the STM Permissions Guidelines ("STM PG") as amended from time to time and made available at

https://www.stm-assoc.org/intellectual-property/permissions/permissions-guidelines/.

4. 2. For content reuse requests that qualify for permission under the STM PG, and which may be updated from time to time, the STM PG supersede the terms and conditions contained in this License.

4. 3. If a License has been granted under the STM PG, but the STM PG no longer apply at the time of publication, further permission must be sought from the Rightsholder. Contact journalpermissions@springernature.com or bookpermissions@springernature.com for these rights.

5. Duration of License

5. 1. Unless otherwise indicated on your License, a License is valid from the date of purchase ("License Date") until the end of the relevant period in the below table:

Reuse in a medical communications project	Reuse up to distribution or time period indicated in License
Reuse in a dissertation/thesis	Lifetime of thesis
Reuse in a journal/magazine	Lifetime of journal/magazine
Reuse in a book/textbook	Lifetime of edition
Reuse on a website	1 year unless otherwise specified in the License
Reuse in a presentation/slide kit/poster	Lifetime of presentation/slide kit/poster. Note: publication whether electronic or in print of presentation/slide kit/poster may require further permission.
Reuse in conference proceedings	Lifetime of conference proceedings
Reuse in an annual report	Lifetime of annual report
Reuse in training/CME materials	Reuse up to distribution or time period indicated in License
Reuse in newsmedia	Lifetime of newsmedia
Reuse in coursepack/classroom materials	Reuse up to distribution and/or time period indicated in license

6. Acknowledgement

6. 1. The Licensor's permission must be acknowledged next to the Licensed Material in print. In electronic form, this acknowledgement must be visible at the same time as the figures/tables/illustrations or abstract and must be hyperlinked to the journal/book's homepage.

6. 2. Acknowledgement may be provided according to any standard referencing system and at a minimum should include "Author, Article/Book Title, Journal name/Book imprint, volume, page number, year, Springer Nature".

7. Reuse in a dissertation or thesis

7. 1. Where 'reuse in a dissertation/thesis' has been selected, the following terms apply: Print rights of the Version of Record are provided for; electronic rights for use only on institutional repository as defined by the Sherpa guideline (www.sherpa.ac.uk/romeo/) and only up to what is required by the awarding institution.

7. 2. For theses published under an ISBN or ISSN, separate permission is required. Please contact journalpermissions@springernature.com or bookpermissions@springernature.com for these rights.

7. 3. Authors must properly cite the published manuscript in their thesis according to current citation standards and include the following acknowledgement: '*Reproduced with permission from Springer Nature*'.

8. License Fee

You must pay the fee set forth in the License Agreement (the "License Fees"). All amounts payable by you under this License are exclusive of any sales, use, withholding, value added or similar taxes, government fees or levies or other assessments. Collection and/or remittance of such taxes to the relevant tax authority shall be the responsibility of the party who has the legal obligation to do so.

9. Warranty

9. 1. The Licensor warrants that it has, to the best of its knowledge, the rights to license reuse of the Licensed Material. **You are solely responsible for ensuring that the material you wish to license is original to the Licensor and does not carry the copyright of another entity or third party (as credited in the published version).** If the credit line on any part of the Licensed Material indicates that it was reprinted or adapted with permission from another source, then you should seek additional permission from that source to reuse the material.

9. 2. EXCEPT FOR THE EXPRESS WARRANTY STATED HEREIN AND TO THE EXTENT PERMITTED BY APPLICABLE LAW, LICENSOR PROVIDES THE LICENSED MATERIAL "AS IS" AND MAKES NO OTHER REPRESENTATION OR WARRANTY. LICENSOR EXPRESSLY DISCLAIMS ANY LIABILITY FOR ANY CLAIM ARISING FROM OR OUT OF THE CONTENT, INCLUDING BUT NOT LIMITED TO ANY ERRORS, INACCURACIES, OMISSIONS, OR DEFECTS CONTAINED THEREIN, AND ANY IMPLIED OR EXPRESS WARRANTY AS TO MERCHANTABILITY OR FITNESS FOR A PARTICULAR PURPOSE. IN NO EVENT SHALL LICENSOR BE LIABLE TO YOU OR ANY OTHER PARTY OR ANY OTHER PERSON OR FOR ANY SPECIAL, CONSEQUENTIAL, INCIDENTAL, INDIRECT, PUNITIVE, OR EXEMPLARY DAMAGES, HOWEVER CAUSED, ARISING OUT OF OR IN CONNECTION WITH THE DOWNLOADING, VIEWING OR USE OF THE LICENSED MATERIAL REGARDLESS OF THE FORM OF ACTION, WHETHER FOR BREACH OF CONTRACT, BREACH OF WARRANTY, TORT, NEGLIGENCE, INFRINGEMENT OR OTHERWISE (INCLUDING, WITHOUT LIMITATION, DAMAGES BASED ON LOSS OF PROFITS, DATA, FILES, USE, BUSINESS OPPORTUNITY OR CLAIMS OF THIRD PARTIES), AND WHETHER OR NOT THE PARTY HAS BEEN ADVISED OF THE POSSIBILITY OF SUCH DAMAGES. THIS LIMITATION APPLIES NOTWITHSTANDING ANY FAILURE OF ESSENTIAL PURPOSE OF ANY LIMITED REMEDY PROVIDED HEREIN.

10. Termination and Cancellation

10. 1. The License and all rights granted hereunder will continue until the end of the applicable period shown in Clause 5.1 above. Thereafter, this license will be terminated and all rights granted hereunder will cease.

10. 2. Licensor reserves the right to terminate the License in the event that payment is not received in full or if you breach the terms of this License.

11. General

11. 1. The License and the rights and obligations of the parties hereto shall be construed, interpreted and determined in accordance with the laws of the Federal Republic of Germany without reference to the stipulations of the CISG (United Nations Convention on Contracts for the International Sale of Goods) or to Germany´s choice-of-law principle.

11. 2. The parties acknowledge and agree that any controversies and disputes arising out of this License shall be decided exclusively by the courts of or having jurisdiction for Heidelberg, Germany, as far as legally permissible.

11. 3. This License is solely for Licensor's and Licensee's benefit. It is not for the benefit of any other person or entity.

Questions? For questions on Copyright Clearance Center accounts or website issues please contact springernaturesupport@copyright.com or +1-855-239-3415 (toll free in the US) or +1-978-646-2777. For questions on Springer Nature licensing please visit https://www.springernature.com/gp/partners/rights-permissions-third-party-distribution

Other Conditions:

Version 1.4 - Dec 2022

Questions? customercare@copyright.com.

ELSEVIER LICENSE
TERMS AND CONDITIONS

Sep 11, 2023

This Agreement between Mr. Thomas Burge ("You") and Elsevier ("Elsevier") consists of your license details and the terms and conditions provided by Elsevier and Copyright Clearance Center.

License Number	5490081200868
License date	Feb 15, 2023
Licensed Content Publisher	Elsevier
Licensed Content Publication	The Journal of Arthroplasty
Licensed Content Title	Which Tibial Tray Design Achieves Maximum Coverage and Ideal Rotation: Anatomic, Symmetric, or Asymmetric? An MRI-based study
Licensed Content Author	S. David Stulberg,Nitin Goyal
Licensed Content Date	Oct 1, 2015
Licensed Content Volume	30
Licensed Content Issue	10
Licensed Content Pages	3
Start Page	1839
End Page	1841
Type of Use	reuse in a thesis/dissertation
Portion	figures/tables/illustrations

Number of figures/tables/illustrations	1
Format	both print and electronic
Are you the author of this Elsevier article?	No
Will you be translating?	No
Title	Applied AI/ML for Automatic Customisation of Medical Implants
Institution name	Imperial College
Expected presentation date	Apr 2023
Portions	Figure 1
Requestor Location	Mr. Thomas Burge Imperial College Rd, Kensington London, SW7 1AL United Kingdom Attn: Imperial College
Publisher Tax ID	GB 494 6272 12
Total	0.00 GBP

Terms and Conditions

INTRODUCTION

1. The publisher for this copyrighted material is Elsevier. By clicking "accept" in connection with completing this licensing transaction, you agree that the following terms and conditions apply to this transaction (along with the Billing and Payment terms and conditions established by Copyright Clearance Center, Inc. ("CCC"), at the time that you opened your RightsLink account and that are available at any time at https://myaccount.copyright.com).

GENERAL TERMS

2. Elsevier hereby grants you permission to reproduce the aforementioned material subject to the terms and conditions indicated.

3. Acknowledgement: If any part of the material to be used (for example, figures) has appeared in our publication with credit or acknowledgement to another source, permission must also be sought from that source. If such permission is not obtained then that material may not be included in your publication/copies. Suitable acknowledgement to the source must be made, either as a footnote or in a reference list at the end of your publication, as follows:

"Reprinted from Publication title, Vol /edition number, Author(s), Title of article / title of chapter, Pages No., Copyright (Year), with permission from Elsevier [OR APPLICABLE SOCIETY COPYRIGHT OWNER]." Also Lancet special credit - "Reprinted from The Lancet, Vol. number, Author(s), Title of article, Pages No., Copyright (Year), with permission from Elsevier."

4. Reproduction of this material is confined to the purpose and/or media for which permission is hereby given. The material may not be reproduced or used in any other way, including use in combination with an artificial intelligence tool (including to train an algorithm, test, process, analyse, generate output and/or develop any form of artificial intelligence tool), or to create any derivative work and/or service (including resulting from the use of artificial intelligence tools).

5. Altering/Modifying Material: Not Permitted. However figures and illustrations may be altered/adapted minimally to serve your work. Any other abbreviations, additions, deletions and/or any other alterations shall be made only with prior written authorization of Elsevier Ltd. (Please contact Elsevier's permissions helpdesk here). No modifications can be made to any Lancet figures/tables and they must be reproduced in full.

6. If the permission fee for the requested use of our material is waived in this instance, please be advised that your future requests for Elsevier materials may attract a fee.

7. Reservation of Rights: Publisher reserves all rights not specifically granted in the combination of (i) the license details provided by you and accepted in the course of this licensing transaction, (ii) these terms and conditions and (iii) CCC's Billing and Payment terms and conditions.

8. License Contingent Upon Payment: While you may exercise the rights licensed immediately upon issuance of the license at the end of the licensing process for the transaction, provided that you have disclosed complete and accurate details of your proposed use, no license is finally effective unless and until full payment is received from you (either by publisher or by CCC) as provided in CCC's Billing and Payment terms and conditions. If full payment is not received on a timely basis, then any license preliminarily granted shall be deemed automatically revoked and shall be void as if never granted. Further, in the event that you breach any of these terms and conditions or any of CCC's Billing and Payment terms and conditions, the license is automatically revoked and shall be void as if never granted. Use of materials as described in a revoked license, as well as any use of the materials beyond the scope of an unrevoked license, may constitute copyright infringement and publisher reserves the right to take any and all action to protect its copyright in the materials.

9. Warranties: Publisher makes no representations or warranties with respect to the licensed material.

10. Indemnity: You hereby indemnify and agree to hold harmless publisher and CCC, and their respective officers, directors, employees and agents, from and against any and all claims arising out of your use of the licensed material other than as specifically authorized pursuant to this license.

11. No Transfer of License: This license is personal to you and may not be sublicensed, assigned, or transferred by you to any other person without publisher's written permission.

12. No Amendment Except in Writing: This license may not be amended except in a writing signed by both parties (or, in the case of publisher, by CCC on publisher's behalf).

13. Objection to Contrary Terms: Publisher hereby objects to any terms contained in any purchase order, acknowledgment, check endorsement or other writing prepared by you, which terms are inconsistent with these terms and conditions or CCC's Billing and Payment terms and conditions. These terms and conditions, together with CCC's Billing and Payment terms and conditions (which are incorporated herein), comprise the entire agreement between you and publisher (and CCC) concerning this licensing transaction. In the event of any conflict between your obligations established by these terms and conditions and those established by CCC's Billing and Payment terms and conditions, these terms and conditions shall control.

14. Revocation: Elsevier or Copyright Clearance Center may deny the permissions described in this License at their sole discretion, for any reason or no reason, with a full refund payable to you. Notice of such denial will be made using the contact information provided by you. Failure to receive such notice will not alter or invalidate the denial. In no event will Elsevier or Copyright Clearance Center be responsible or liable for any costs, expenses or damage incurred by you as a result of a denial of your permission request, other than a refund of the amount(s) paid by you to Elsevier and/or Copyright Clearance Center for denied permissions.

LIMITED LICENSE

The following terms and conditions apply only to specific license types:

15. **Translation**: This permission is granted for non-exclusive world **English** rights only unless your license was granted for translation rights. If you licensed translation rights you may only translate this content into the languages you requested. A professional translator must perform all translations and reproduce the content word for word preserving the integrity of the article.

16. **Posting licensed content on any Website**: The following terms and conditions apply as follows: Licensing material from an Elsevier journal: All content posted to the web site must maintain the copyright information line on the bottom of each image; A hyper-text must be included to the Homepage of the journal from which you are licensing at http://www.sciencedirect.com/science/journal/xxxxx or the Elsevier homepage for books at http://www.elsevier.com; Central Storage: This license does not include permission for a scanned version of the material to be stored in a central repository such as that provided by Heron/XanEdu.

Licensing material from an Elsevier book: A hyper-text link must be included to the Elsevier homepage at http://www.elsevier.com . All content posted to the web site must maintain the copyright information line on the bottom of each image.

Posting licensed content on Electronic reserve: In addition to the above the following clauses are applicable: The web site must be password-protected and made available only to bona fide students registered on a relevant course. This permission is granted for 1 year only. You may obtain a new license for future website posting.

17. **For journal authors:** the following clauses are applicable in addition to the above:

Preprints:

A preprint is an author's own write-up of research results and analysis, it has not been peer-reviewed, nor has it had any other value added to it by a publisher (such as formatting, copyright, technical enhancement etc.).

Authors can share their preprints anywhere at any time. Preprints should not be added to or enhanced in any way in order to appear more like, or to substitute for, the final versions of articles however authors can update their preprints on arXiv or RePEc with their Accepted Author Manuscript (see below).

If accepted for publication, we encourage authors to link from the preprint to their formal publication via its DOI. Millions of researchers have access to the formal publications on ScienceDirect, and so links will help users to find, access, cite and use the best available version. Please note that Cell Press, The Lancet and some society-owned have different preprint policies. Information on these policies is available on the journal homepage.

Accepted Author Manuscripts: An accepted author manuscript is the manuscript of an article that has been accepted for publication and which typically includes author-incorporated changes suggested during submission, peer review and editor-author communications.

Authors can share their accepted author manuscript:

- immediately
  - via their non-commercial person homepage or blog
  - by updating a preprint in arXiv or RePEc with the accepted manuscript
  - via their research institute or institutional repository for internal institutional uses or as part of an invitation-only research collaboration work-group
  - directly by providing copies to their students or to research collaborators for their personal use
  - for private scholarly sharing as part of an invitation-only work group on commercial sites with which Elsevier has an agreement
- After the embargo period
  - via non-commercial hosting platforms such as their institutional repository
  - via commercial sites with which Elsevier has an agreement

In all cases accepted manuscripts should:

- link to the formal publication via its DOI
- bear a CC-BY-NC-ND license - this is easy to do
- if aggregated with other manuscripts, for example in a repository or other site, be shared in alignment with our hosting policy not be added to or enhanced in any way to appear more like, or to substitute for, the published journal article.

Published journal article (JPA): A published journal article (PJA) is the definitive final record of published research that appears or will appear in the journal and embodies all value-adding publishing activities including peer review co-ordination, copy-editing, formatting, (if relevant) pagination and online enrichment.

Policies for sharing publishing journal articles differ for subscription and gold open access articles:

Subscription Articles: If you are an author, please share a link to your article rather than the full-text. Millions of researchers have access to the formal publications on ScienceDirect, and so links will help your users to find, access, cite, and use the best available version.

Theses and dissertations which contain embedded PJAs as part of the formal submission can be posted publicly by the awarding institution with DOI links back to the formal publications on ScienceDirect.

If you are affiliated with a library that subscribes to ScienceDirect you have additional private sharing rights for others' research accessed under that agreement. This includes use for classroom teaching and internal training at the institution (including use in course packs and courseware programs), and inclusion of the article for grant funding purposes.

ELSEVIER LICENSE
TERMS AND CONDITIONS

Sep 11, 2023

This Agreement between Mr. Thomas Burge ("You") and Elsevier ("Elsevier") consists of your license details and the terms and conditions provided by Elsevier and Copyright Clearance Center.

License Number	5491380811218
License date	Feb 17, 2023
Licensed Content Publisher	Elsevier
Licensed Content Publication	Elsevier Books
Licensed Content Title	Osteoarchaeology
Licensed Content Author	Efthymia Nikita
Licensed Content Date	Jan 1, 2017
Licensed Content Pages	75
Start Page	1
End Page	75
Type of Use	reuse in a thesis/dissertation
Portion	figures/tables/illustrations
Number of figures/tables/illustrations	1
Format	both print and electronic

Are you the author of this Elsevier chapter?	No
Will you be translating?	No
Title	Applied AI/ML for Automatic Customisation of Medical Implants
Institution name	Imperial College
Expected presentation date	Apr 2023
Portions	Figure 1.6.1
Requestor Location	Mr. Thomas Burge Imperial College Rd, Kensington London, SW7 1AL United Kingdom Attn: Imperial College
Publisher Tax ID	GB 494 6272 12
Total	0.00 GBP

Terms and Conditions

INTRODUCTION

1. The publisher for this copyrighted material is Elsevier. By clicking "accept" in connection with completing this licensing transaction, you agree that the following terms and conditions apply to this transaction (along with the Billing and Payment terms and conditions established by Copyright Clearance Center, Inc. ("CCC"), at the time that you opened your RightsLink account and that are available at any time at https://myaccount.copyright.com).

GENERAL TERMS

2. Elsevier hereby grants you permission to reproduce the aforementioned material subject to the terms and conditions indicated.

3. Acknowledgement: If any part of the material to be used (for example, figures) has appeared in our publication with credit or acknowledgement to another source, permission must also be sought from that source. If such permission is not obtained then that material may not be included in your publication/copies. Suitable acknowledgement to the source must be made, either as a footnote or in a reference list at the end of your publication, as follows:

"Reprinted from Publication title, Vol /edition number, Author(s), Title of article / title of chapter, Pages No., Copyright (Year), with permission from Elsevier [OR APPLICABLE SOCIETY COPYRIGHT OWNER]." Also Lancet special credit - "Reprinted from The Lancet, Vol. number, Author(s), Title of article, Pages No., Copyright (Year), with permission from Elsevier."

4. Reproduction of this material is confined to the purpose and/or media for which permission is hereby given. The material may not be reproduced or used in any other way, including use in combination with an artificial intelligence tool (including to train an algorithm, test, process, analyse, generate output and/or develop any form of artificial intelligence tool), or to create any derivative work and/or service (including resulting from the use of artificial intelligence tools).

5. Altering/Modifying Material: Not Permitted. However figures and illustrations may be altered/adapted minimally to serve your work. Any other abbreviations, additions, deletions and/or any other alterations shall be made only with prior written authorization of Elsevier Ltd. (Please contact Elsevier's permissions helpdesk here). No modifications can be made to any Lancet figures/tables and they must be reproduced in full.

6. If the permission fee for the requested use of our material is waived in this instance, please be advised that your future requests for Elsevier materials may attract a fee.

7. Reservation of Rights: Publisher reserves all rights not specifically granted in the combination of (i) the license details provided by you and accepted in the course of this licensing transaction, (ii) these terms and conditions and (iii) CCC's Billing and Payment terms and conditions.

8. License Contingent Upon Payment: While you may exercise the rights licensed immediately upon issuance of the license at the end of the licensing process for the transaction, provided that you have disclosed complete and accurate details of your proposed use, no license is finally effective unless and until full payment is received from you (either by publisher or by CCC) as provided in CCC's Billing and Payment terms and conditions. If full payment is not received on a timely basis, then any license preliminarily granted shall be deemed automatically revoked and shall be void as if never granted. Further, in the event that you breach any of these terms and conditions or any of CCC's Billing and Payment terms and conditions, the license is automatically revoked and shall be void as if never granted. Use of materials as described in a revoked license, as well as any use of the materials beyond the scope of an unrevoked license, may constitute copyright infringement and publisher reserves the right to take any and all action to protect its copyright in the materials.

9. Warranties: Publisher makes no representations or warranties with respect to the licensed material.

10. Indemnity: You hereby indemnify and agree to hold harmless publisher and CCC, and their respective officers, directors, employees and agents, from and against any and all claims arising out of your use of the licensed material other than as specifically authorized pursuant to this license.

11. No Transfer of License: This license is personal to you and may not be sublicensed, assigned, or transferred by you to any other person without publisher's written permission.

12. No Amendment Except in Writing: This license may not be amended except in a writing signed by both parties (or, in the case of publisher, by CCC on publisher's behalf).

13. Objection to Contrary Terms: Publisher hereby objects to any terms contained in any purchase order, acknowledgment, check endorsement or other writing prepared by you, which terms are inconsistent with these terms and conditions or CCC's Billing and Payment terms and conditions. These terms and conditions, together with CCC's Billing and Payment

terms and conditions (which are incorporated herein), comprise the entire agreement between you and publisher (and CCC) concerning this licensing transaction. In the event of any conflict between your obligations established by these terms and conditions and those established by CCC's Billing and Payment terms and conditions, these terms and conditions shall control.

14. Revocation: Elsevier or Copyright Clearance Center may deny the permissions described in this License at their sole discretion, for any reason or no reason, with a full refund payable to you. Notice of such denial will be made using the contact information provided by you. Failure to receive such notice will not alter or invalidate the denial. In no event will Elsevier or Copyright Clearance Center be responsible or liable for any costs, expenses or damage incurred by you as a result of a denial of your permission request, other than a refund of the amount(s) paid by you to Elsevier and/or Copyright Clearance Center for denied permissions.

LIMITED LICENSE

The following terms and conditions apply only to specific license types:

15. **Translation**: This permission is granted for non-exclusive world **English** rights only unless your license was granted for translation rights. If you licensed translation rights you may only translate this content into the languages you requested. A professional translator must perform all translations and reproduce the content word for word preserving the integrity of the article.

16. **Posting licensed content on any Website**: The following terms and conditions apply as follows: Licensing material from an Elsevier journal: All content posted to the web site must maintain the copyright information line on the bottom of each image; A hyper-text must be included to the Homepage of the journal from which you are licensing at http://www.sciencedirect.com/science/journal/xxxxx or the Elsevier homepage for books at http://www.elsevier.com; Central Storage: This license does not include permission for a scanned version of the material to be stored in a central repository such as that provided by Heron/XanEdu.

Licensing material from an Elsevier book: A hyper-text link must be included to the Elsevier homepage at http://www.elsevier.com . All content posted to the web site must maintain the copyright information line on the bottom of each image.

Posting licensed content on Electronic reserve: In addition to the above the following clauses are applicable: The web site must be password-protected and made available only to bona fide students registered on a relevant course. This permission is granted for 1 year only. You may obtain a new license for future website posting.

17. **For journal authors:** the following clauses are applicable in addition to the above:

Preprints:

A preprint is an author's own write-up of research results and analysis, it has not been peer-reviewed, nor has it had any other value added to it by a publisher (such as formatting, copyright, technical enhancement etc.).

Authors can share their preprints anywhere at any time. Preprints should not be added to or enhanced in any way in order to appear more like, or to substitute for, the final versions of articles however authors can update their preprints on arXiv or RePEc with their Accepted Author Manuscript (see below).

If accepted for publication, we encourage authors to link from the preprint to their formal publication via its DOI. Millions of researchers have access to the formal publications on

ScienceDirect, and so links will help users to find, access, cite and use the best available version. Please note that Cell Press, The Lancet and some society-owned have different preprint policies. Information on these policies is available on the journal homepage.

Accepted Author Manuscripts: An accepted author manuscript is the manuscript of an article that has been accepted for publication and which typically includes author-incorporated changes suggested during submission, peer review and editor-author communications.

Authors can share their accepted author manuscript:

- immediately
  - via their non-commercial person homepage or blog
  - by updating a preprint in arXiv or RePEc with the accepted manuscript
  - via their research institute or institutional repository for internal institutional uses or as part of an invitation-only research collaboration work-group
  - directly by providing copies to their students or to research collaborators for their personal use
  - for private scholarly sharing as part of an invitation-only work group on commercial sites with which Elsevier has an agreement
- After the embargo period
  - via non-commercial hosting platforms such as their institutional repository
  - via commercial sites with which Elsevier has an agreement

In all cases accepted manuscripts should:

- link to the formal publication via its DOI
- bear a CC-BY-NC-ND license - this is easy to do
- if aggregated with other manuscripts, for example in a repository or other site, be shared in alignment with our hosting policy not be added to or enhanced in any way to appear more like, or to substitute for, the published journal article.

Published journal article (JPA): A published journal article (PJA) is the definitive final record of published research that appears or will appear in the journal and embodies all value-adding publishing activities including peer review co-ordination, copy-editing, formatting, (if relevant) pagination and online enrichment.

Policies for sharing publishing journal articles differ for subscription and gold open access articles:

Subscription Articles: If you are an author, please share a link to your article rather than the full-text. Millions of researchers have access to the formal publications on ScienceDirect, and so links will help your users to find, access, cite, and use the best available version.

Theses and dissertations which contain embedded PJAs as part of the formal submission can be posted publicly by the awarding institution with DOI links back to the formal publications on ScienceDirect.

If you are affiliated with a library that subscribes to ScienceDirect you have additional private sharing rights for others' research accessed under that agreement. This includes use for classroom teaching and internal training at the institution (including use in course packs and courseware programs), and inclusion of the article for grant funding purposes.

Gold Open Access Articles: May be shared according to the author-selected end-user license and should contain a CrossMark logo, the end user license, and a DOI link to the formal publication on ScienceDirect.

Please refer to Elsevier's posting policy for further information.

18. **For book authors** the following clauses are applicable in addition to the above: Authors are permitted to place a brief summary of their work online only. You are not allowed to download and post the published electronic version of your chapter, nor may you scan the printed edition to create an electronic version. **Posting to a repository:** Authors are permitted to post a summary of their chapter only in their institution's repository.

19. **Thesis/Dissertation**: If your license is for use in a thesis/dissertation your thesis may be submitted to your institution in either print or electronic form. Should your thesis be published commercially, please reapply for permission. These requirements include permission for the Library and Archives of Canada to supply single copies, on demand, of the complete thesis and include permission for Proquest/UMI to supply single copies, on demand, of the complete thesis. Should your thesis be published commercially, please reapply for permission. Theses and dissertations which contain embedded PJAs as part of the formal submission can be posted publicly by the awarding institution with DOI links back to the formal publications on ScienceDirect.

Elsevier Open Access Terms and Conditions

You can publish open access with Elsevier in hundreds of open access journals or in nearly 2000 established subscription journals that support open access publishing. Permitted third party re-use of these open access articles is defined by the author's choice of Creative Commons user license. See our open access license policy for more information.

Terms & Conditions applicable to all Open Access articles published with Elsevier:

Any reuse of the article must not represent the author as endorsing the adaptation of the article nor should the article be modified in such a way as to damage the author's honour or reputation. If any changes have been made, such changes must be clearly indicated.

The author(s) must be appropriately credited and we ask that you include the end user license and a DOI link to the formal publication on ScienceDirect.

If any part of the material to be used (for example, figures) has appeared in our publication with credit or acknowledgement to another source it is the responsibility of the user to ensure their reuse complies with the terms and conditions determined by the rights holder.

Additional Terms & Conditions applicable to each Creative Commons user license:

CC BY: The CC-BY license allows users to copy, to create extracts, abstracts and new works from the Article, to alter and revise the Article and to make commercial use of the Article (including reuse and/or resale of the Article by commercial entities), provided the user gives appropriate credit (with a link to the formal publication through the relevant DOI), provides a link to the license, indicates if changes were made and the licensor is not represented as endorsing the use made of the work. The full details of the license are available at http://creativecommons.org/licenses/by/4.0.

CC BY NC SA: The CC BY-NC-SA license allows users to copy, to create extracts, abstracts and new works from the Article, to alter and revise the Article, provided this is not done for commercial purposes, and that the user gives appropriate credit (with a link to the formal publication through the relevant DOI), provides a link to the license, indicates if changes were made and the licensor is not represented as endorsing the use made of the work. Further, any new works must be made available on the same conditions. The full details of the license are available at http://creativecommons.org/licenses/by-nc-sa/4.0.

CC BY NC ND: The CC BY-NC-ND license allows users to copy and distribute the Article, provided this is not done for commercial purposes and further does not permit distribution of the Article if it is changed or edited in any way, and provided the user gives appropriate

ELSEVIER LICENSE
TERMS AND CONDITIONS

Sep 11, 2023

This Agreement between Mr. Thomas Burge ("You") and Elsevier ("Elsevier") consists of your license details and the terms and conditions provided by Elsevier and Copyright Clearance Center.

License Number	5491450632246
License date	Feb 17, 2023
Licensed Content Publisher	Elsevier
Licensed Content Publication	Neurocomputing
Licensed Content Title	Recent advances in deep learning for object detection
Licensed Content Author	Xiongwei Wu,Doyen Sahoo,Steven C.H. Hoi
Licensed Content Date	Jul 5, 2020
Licensed Content Volume	396
Licensed Content Issue	n/a
Licensed Content Pages	26
Start Page	39
End Page	64
Type of Use	reuse in a thesis/dissertation
Portion	figures/tables/illustrations

Number of figures/tables/illustrations	1
Format	both print and electronic
Are you the author of this Elsevier article?	No
Will you be translating?	No
Title	Applied AI/ML for Automatic Customisation of Medical Implants
Institution name	Imperial College
Expected presentation date	Apr 2023
Portions	Figure 1
Requestor Location	Mr. Thomas Burge Imperial College Rd, Kensington London, SW7 1AL United Kingdom Attn: Imperial College
Publisher Tax ID	GB 494 6272 12
Total	0.00 GBP

Terms and Conditions

INTRODUCTION

1. The publisher for this copyrighted material is Elsevier. By clicking "accept" in connection with completing this licensing transaction, you agree that the following terms and conditions apply to this transaction (along with the Billing and Payment terms and conditions established by Copyright Clearance Center, Inc. ("CCC"), at the time that you opened your RightsLink account and that are available at any time at https://myaccount.copyright.com).

GENERAL TERMS

2. Elsevier hereby grants you permission to reproduce the aforementioned material subject to the terms and conditions indicated.

3. Acknowledgement: If any part of the material to be used (for example, figures) has appeared in our publication with credit or acknowledgement to another source, permission must also be sought from that source. If such permission is not obtained then that material may not be included in your publication/copies. Suitable acknowledgement to the source must be made, either as a footnote or in a reference list at the end of your publication, as follows:

"Reprinted from Publication title, Vol /edition number, Author(s), Title of article / title of chapter, Pages No., Copyright (Year), with permission from Elsevier [OR APPLICABLE SOCIETY COPYRIGHT OWNER]." Also Lancet special credit - "Reprinted from The Lancet, Vol. number, Author(s), Title of article, Pages No., Copyright (Year), with permission from Elsevier."

4. Reproduction of this material is confined to the purpose and/or media for which permission is hereby given. The material may not be reproduced or used in any other way, including use in combination with an artificial intelligence tool (including to train an algorithm, test, process, analyse, generate output and/or develop any form of artificial intelligence tool), or to create any derivative work and/or service (including resulting from the use of artificial intelligence tools).

5. Altering/Modifying Material: Not Permitted. However figures and illustrations may be altered/adapted minimally to serve your work. Any other abbreviations, additions, deletions and/or any other alterations shall be made only with prior written authorization of Elsevier Ltd. (Please contact Elsevier's permissions helpdesk here). No modifications can be made to any Lancet figures/tables and they must be reproduced in full.

6. If the permission fee for the requested use of our material is waived in this instance, please be advised that your future requests for Elsevier materials may attract a fee.

7. Reservation of Rights: Publisher reserves all rights not specifically granted in the combination of (i) the license details provided by you and accepted in the course of this licensing transaction, (ii) these terms and conditions and (iii) CCC's Billing and Payment terms and conditions.

8. License Contingent Upon Payment: While you may exercise the rights licensed immediately upon issuance of the license at the end of the licensing process for the transaction, provided that you have disclosed complete and accurate details of your proposed use, no license is finally effective unless and until full payment is received from you (either by publisher or by CCC) as provided in CCC's Billing and Payment terms and conditions. If full payment is not received on a timely basis, then any license preliminarily granted shall be deemed automatically revoked and shall be void as if never granted. Further, in the event that you breach any of these terms and conditions or any of CCC's Billing and Payment terms and conditions, the license is automatically revoked and shall be void as if never granted. Use of materials as described in a revoked license, as well as any use of the materials beyond the scope of an unrevoked license, may constitute copyright infringement and publisher reserves the right to take any and all action to protect its copyright in the materials.

9. Warranties: Publisher makes no representations or warranties with respect to the licensed material.

10. Indemnity: You hereby indemnify and agree to hold harmless publisher and CCC, and their respective officers, directors, employees and agents, from and against any and all claims arising out of your use of the licensed material other than as specifically authorized pursuant to this license.

11. No Transfer of License: This license is personal to you and may not be sublicensed, assigned, or transferred by you to any other person without publisher's written permission.

12. No Amendment Except in Writing: This license may not be amended except in a writing signed by both parties (or, in the case of publisher, by CCC on publisher's behalf).

13. Objection to Contrary Terms: Publisher hereby objects to any terms contained in any purchase order, acknowledgment, check endorsement or other writing prepared by you, which terms are inconsistent with these terms and conditions or CCC's Billing and Payment terms and conditions. These terms and conditions, together with CCC's Billing and Payment terms and conditions (which are incorporated herein), comprise the entire agreement between you and publisher (and CCC) concerning this licensing transaction. In the event of any conflict between your obligations established by these terms and conditions and those established by CCC's Billing and Payment terms and conditions, these terms and conditions shall control.

14. Revocation: Elsevier or Copyright Clearance Center may deny the permissions described in this License at their sole discretion, for any reason or no reason, with a full refund payable to you. Notice of such denial will be made using the contact information provided by you. Failure to receive such notice will not alter or invalidate the denial. In no event will Elsevier or Copyright Clearance Center be responsible or liable for any costs, expenses or damage incurred by you as a result of a denial of your permission request, other than a refund of the amount(s) paid by you to Elsevier and/or Copyright Clearance Center for denied permissions.

LIMITED LICENSE

The following terms and conditions apply only to specific license types:

15. **Translation**: This permission is granted for non-exclusive world **English** rights only unless your license was granted for translation rights. If you licensed translation rights you may only translate this content into the languages you requested. A professional translator must perform all translations and reproduce the content word for word preserving the integrity of the article.

16. **Posting licensed content on any Website**: The following terms and conditions apply as follows: Licensing material from an Elsevier journal: All content posted to the web site must maintain the copyright information line on the bottom of each image; A hyper-text must be included to the Homepage of the journal from which you are licensing at http://www.sciencedirect.com/science/journal/xxxxx or the Elsevier homepage for books at http://www.elsevier.com; Central Storage: This license does not include permission for a scanned version of the material to be stored in a central repository such as that provided by Heron/XanEdu.

Licensing material from an Elsevier book: A hyper-text link must be included to the Elsevier homepage at http://www.elsevier.com . All content posted to the web site must maintain the copyright information line on the bottom of each image.

Posting licensed content on Electronic reserve: In addition to the above the following clauses are applicable: The web site must be password-protected and made available only to bona fide students registered on a relevant course. This permission is granted for 1 year only. You may obtain a new license for future website posting.

17. **For journal authors:** the following clauses are applicable in addition to the above:

Preprints:

A preprint is an author's own write-up of research results and analysis, it has not been peer-reviewed, nor has it had any other value added to it by a publisher (such as formatting, copyright, technical enhancement etc.).

Authors can share their preprints anywhere at any time. Preprints should not be added to or enhanced in any way in order to appear more like, or to substitute for, the final versions of articles however authors can update their preprints on arXiv or RePEc with their Accepted Author Manuscript (see below).

If accepted for publication, we encourage authors to link from the preprint to their formal publication via its DOI. Millions of researchers have access to the formal publications on ScienceDirect, and so links will help users to find, access, cite and use the best available version. Please note that Cell Press, The Lancet and some society-owned have different preprint policies. Information on these policies is available on the journal homepage.

Accepted Author Manuscripts: An accepted author manuscript is the manuscript of an article that has been accepted for publication and which typically includes author-incorporated changes suggested during submission, peer review and editor-author communications.

Authors can share their accepted author manuscript:

- immediately
  - via their non-commercial person homepage or blog
  - by updating a preprint in arXiv or RePEc with the accepted manuscript
  - via their research institute or institutional repository for internal institutional uses or as part of an invitation-only research collaboration work-group
  - directly by providing copies to their students or to research collaborators for their personal use
  - for private scholarly sharing as part of an invitation-only work group on commercial sites with which Elsevier has an agreement
- After the embargo period
  - via non-commercial hosting platforms such as their institutional repository
  - via commercial sites with which Elsevier has an agreement

In all cases accepted manuscripts should:

- link to the formal publication via its DOI
- bear a CC-BY-NC-ND license - this is easy to do
- if aggregated with other manuscripts, for example in a repository or other site, be shared in alignment with our hosting policy not be added to or enhanced in any way to appear more like, or to substitute for, the published journal article.

Published journal article (JPA): A published journal article (PJA) is the definitive final record of published research that appears or will appear in the journal and embodies all value-adding publishing activities including peer review co-ordination, copy-editing, formatting, (if relevant) pagination and online enrichment.

Policies for sharing publishing journal articles differ for subscription and gold open access articles:

Subscription Articles: If you are an author, please share a link to your article rather than the full-text. Millions of researchers have access to the formal publications on ScienceDirect, and so links will help your users to find, access, cite, and use the best available version.

Theses and dissertations which contain embedded PJAs as part of the formal submission can be posted publicly by the awarding institution with DOI links back to the formal publications on ScienceDirect.

If you are affiliated with a library that subscribes to ScienceDirect you have additional private sharing rights for others' research accessed under that agreement. This includes use for classroom teaching and internal training at the institution (including use in course packs and courseware programs), and inclusion of the article for grant funding purposes.

Gold Open Access Articles: May be shared according to the author-selected end-user license and should contain a CrossMark logo, the end user license, and a DOI link to the formal publication on ScienceDirect.

Please refer to Elsevier's posting policy for further information.

18. **For book authors** the following clauses are applicable in addition to the above: Authors are permitted to place a brief summary of their work online only. You are not allowed to download and post the published electronic version of your chapter, nor may you scan the printed edition to create an electronic version. **Posting to a repository:** Authors are permitted to post a summary of their chapter only in their institution's repository.

19. **Thesis/Dissertation**: If your license is for use in a thesis/dissertation your thesis may be submitted to your institution in either print or electronic form. Should your thesis be published commercially, please reapply for permission. These requirements include permission for the Library and Archives of Canada to supply single copies, on demand, of the complete thesis and include permission for Proquest/UMI to supply single copies, on demand, of the complete thesis. Should your thesis be published commercially, please reapply for permission. Theses and dissertations which contain embedded PJAs as part of the formal submission can be posted publicly by the awarding institution with DOI links back to the formal publications on ScienceDirect.

Elsevier Open Access Terms and Conditions

You can publish open access with Elsevier in hundreds of open access journals or in nearly 2000 established subscription journals that support open access publishing. Permitted third party re-use of these open access articles is defined by the author's choice of Creative Commons user license. See our open access license policy for more information.

Terms & Conditions applicable to all Open Access articles published with Elsevier:

Any reuse of the article must not represent the author as endorsing the adaptation of the article nor should the article be modified in such a way as to damage the author's honour or reputation. If any changes have been made, such changes must be clearly indicated.

The author(s) must be appropriately credited and we ask that you include the end user license and a DOI link to the formal publication on ScienceDirect.

If any part of the material to be used (for example, figures) has appeared in our publication with credit or acknowledgement to another source it is the responsibility of the user to ensure their reuse complies with the terms and conditions determined by the rights holder.

Additional Terms & Conditions applicable to each Creative Commons user license:

CC BY: The CC-BY license allows users to copy, to create extracts, abstracts and new works from the Article, to alter and revise the Article and to make commercial use of the Article (including reuse and/or resale of the Article by commercial entities), provided the user gives appropriate credit (with a link to the formal publication through the relevant DOI), provides a link to the license, indicates if changes were made and the licensor is not represented as endorsing the use made of the work. The full details of the license are available at http://creativecommons.org/licenses/by/4.0.

CC BY NC SA: The CC BY-NC-SA license allows users to copy, to create extracts, abstracts and new works from the Article, to alter and revise the Article, provided this is not done for commercial purposes, and that the user gives appropriate credit (with a link to the formal publication through the relevant DOI), provides a link to the license, indicates if changes were made and the licensor is not represented as endorsing the use made of the

SPRINGER NATURE LICENSE
TERMS AND CONDITIONS

Sep 11, 2023

This Agreement between Mr. Thomas Burge ("You") and Springer Nature ("Springer Nature") consists of your license details and the terms and conditions provided by Springer Nature and Copyright Clearance Center.

License Number	5492570304397
License date	Feb 19, 2023
Licensed Content Publisher	Springer Nature
Licensed Content Publication	International Journal of Computer Assisted Radiology and Surgery
Licensed Content Title	A novel technology for 3D knee prosthesis planning and treatment evaluation using 2D X-ray radiographs: a clinical evaluation
Licensed Content Author	Guoyan Zheng et al
Licensed Content Date	May 21, 2018
Type of Use	Thesis/Dissertation
Requestor type	academic/university or research institute
Format	print and electronic
Portion	figures/tables/illustrations
Number of figures/tables/illustrations	1
Will you be translating?	no

Circulation/distribution	1 - 29
Author of this Springer Nature content	no
Title	Applied AI/ML for Automatic Customisation of Medical Implants
Institution name	Imperial College
Expected presentation date	Apr 2023
Portions	Figure 1
Requestor Location	Mr. Thomas Burge Imperial College Rd, Kensington London, SW7 1AL United Kingdom Attn: Imperial College
Total	0.00 GBP

Terms and Conditions

Springer Nature Customer Service Centre GmbH Terms and Conditions

The following terms and conditions ("Terms and Conditions") together with the terms specified in your [RightsLink] constitute the License ("License") between you as Licensee and Springer Nature Customer Service Centre GmbH as Licensor. By clicking 'accept' and completing the transaction for your use of the material ("Licensed Material"), you confirm your acceptance of and obligation to be bound by these Terms and Conditions.

1. Grant and Scope of License

1. 1. The Licensor grants you a personal, non-exclusive, non-transferable, non-sublicensable, revocable, world-wide License to reproduce, distribute, communicate to the public, make available, broadcast, electronically transmit or create derivative works using the Licensed Material for the purpose(s) specified in your RightsLink Licence Details only. Licenses are granted for the specific use requested in the order and for no other use, subject to these Terms and Conditions. You acknowledge and agree that the rights granted to you under this License do not include the right to modify, edit, translate, include in collective works, or create derivative works of the Licensed Material in whole or in part unless expressly stated in your RightsLink Licence Details. You may use the Licensed Material only as permitted under this Agreement and will not reproduce, distribute, display, perform, or otherwise use or

exploit any Licensed Material in any way, in whole or in part, except as expressly permitted by this License.

1. 2. You may only use the Licensed Content in the manner and to the extent permitted by these Terms and Conditions, by your RightsLink Licence Details and by any applicable laws.

1. 3. A separate license may be required for any additional use of the Licensed Material, e.g. where a license has been purchased for print use only, separate permission must be obtained for electronic re-use. Similarly, a License is only valid in the language selected and does not apply for editions in other languages unless additional translation rights have been granted separately in the License.

1. 4. Any content within the Licensed Material that is owned by third parties is expressly excluded from the License.

1. 5. Rights for additional reuses such as custom editions, computer/mobile applications, film or TV reuses and/or any other derivative rights requests require additional permission and may be subject to an additional fee. Please apply to journalpermissions@springernature.com or bookpermissions@springernature.com for these rights.

2. Reservation of Rights

Licensor reserves all rights not expressly granted to you under this License. You acknowledge and agree that nothing in this License limits or restricts Licensor's rights in or use of the Licensed Material in any way. Neither this License, nor any act, omission, or statement by Licensor or you, conveys any ownership right to you in any Licensed Material, or to any element or portion thereof. As between Licensor and you, Licensor owns and retains all right, title, and interest in and to the Licensed Material subject to the license granted in Section 1.1. Your permission to use the Licensed Material is expressly conditioned on you not impairing Licensor's or the applicable copyright owner's rights in the Licensed Material in any way.

3. Restrictions on use

3. 1. Minor editing privileges are allowed for adaptations for stylistic purposes or formatting purposes provided such alterations do not alter the original meaning or intention of the Licensed Material and the new figure(s) are still accurate and representative of the Licensed Material. Any other changes including but not limited to, cropping, adapting, and/or omitting material that affect the meaning, intention or moral rights of the author(s) are strictly prohibited.

3. 2. You must not use any Licensed Material as part of any design or trademark.

3. 3. Licensed Material may be used in Open Access Publications (OAP), but any such reuse must include a clear acknowledgment of this permission visible at the same time as the figures/tables/illustration or abstract and which must indicate that the Licensed Material is not part of the governing OA license but has been reproduced with permission. This may be indicated according to any standard referencing system but must include at a minimum 'Book/Journal title, Author, Journal Name (if applicable), Volume (if applicable), Publisher, Year, reproduced with permission from SNCSC'.

4. STM Permission Guidelines

4. 1. An alternative scope of license may apply to signatories of the STM Permissions Guidelines ("STM PG") as amended from time to time and made available at

https://www.stm-assoc.org/intellectual-property/permissions/permissions-guidelines/.

4. 2. For content reuse requests that qualify for permission under the STM PG, and which may be updated from time to time, the STM PG supersede the terms and conditions contained in this License.

4. 3. If a License has been granted under the STM PG, but the STM PG no longer apply at the time of publication, further permission must be sought from the Rightsholder. Contact journalpermissions@springernature.com or bookpermissions@springernature.com for these rights.

5. Duration of License

5. 1. Unless otherwise indicated on your License, a License is valid from the date of purchase ("License Date") until the end of the relevant period in the below table:

Reuse in a medical communications project	Reuse up to distribution or time period indicated in License
Reuse in a dissertation/thesis	Lifetime of thesis
Reuse in a journal/magazine	Lifetime of journal/magazine
Reuse in a book/textbook	Lifetime of edition
Reuse on a website	1 year unless otherwise specified in the License
Reuse in a presentation/slide kit/poster	Lifetime of presentation/slide kit/poster. Note: publication whether electronic or in print of presentation/slide kit/poster may require further permission.
Reuse in conference proceedings	Lifetime of conference proceedings
Reuse in an annual report	Lifetime of annual report
Reuse in training/CME materials	Reuse up to distribution or time period indicated in License
Reuse in newsmedia	Lifetime of newsmedia
Reuse in coursepack/classroom materials	Reuse up to distribution and/or time period indicated in license

6. Acknowledgement

6. 1. The Licensor's permission must be acknowledged next to the Licensed Material in print. In electronic form, this acknowledgement must be visible at the same time as the figures/tables/illustrations or abstract and must be hyperlinked to the journal/book's homepage.

6. 2. Acknowledgement may be provided according to any standard referencing system and at a minimum should include "Author, Article/Book Title, Journal name/Book imprint, volume, page number, year, Springer Nature".

7. Reuse in a dissertation or thesis

7. 1. Where 'reuse in a dissertation/thesis' has been selected, the following terms apply: Print rights of the Version of Record are provided for; electronic rights for use only on institutional repository as defined by the Sherpa guideline (www.sherpa.ac.uk/romeo/) and only up to what is required by the awarding institution.

7. 2. For theses published under an ISBN or ISSN, separate permission is required. Please contact journalpermissions@springernature.com or bookpermissions@springernature.com for these rights.

7. 3. Authors must properly cite the published manuscript in their thesis according to current citation standards and include the following acknowledgement: '*Reproduced with permission from Springer Nature*'.

8. License Fee

You must pay the fee set forth in the License Agreement (the "License Fees"). All amounts payable by you under this License are exclusive of any sales, use, withholding, value added or similar taxes, government fees or levies or other assessments. Collection and/or remittance of such taxes to the relevant tax authority shall be the responsibility of the party who has the legal obligation to do so.

9. Warranty

9. 1. The Licensor warrants that it has, to the best of its knowledge, the rights to license reuse of the Licensed Material. **You are solely responsible for ensuring that the material you wish to license is original to the Licensor and does not carry the copyright of another entity or third party (as credited in the published version).** If the credit line on any part of the Licensed Material indicates that it was reprinted or adapted with permission from another source, then you should seek additional permission from that source to reuse the material.

9. 2. EXCEPT FOR THE EXPRESS WARRANTY STATED HEREIN AND TO THE EXTENT PERMITTED BY APPLICABLE LAW, LICENSOR PROVIDES THE LICENSED MATERIAL "AS IS" AND MAKES NO OTHER REPRESENTATION OR WARRANTY. LICENSOR EXPRESSLY DISCLAIMS ANY LIABILITY FOR ANY CLAIM ARISING FROM OR OUT OF THE CONTENT, INCLUDING BUT NOT LIMITED TO ANY ERRORS, INACCURACIES, OMISSIONS, OR DEFECTS CONTAINED THEREIN, AND ANY IMPLIED OR EXPRESS WARRANTY AS TO MERCHANTABILITY OR FITNESS FOR A PARTICULAR PURPOSE. IN NO EVENT SHALL LICENSOR BE LIABLE TO YOU OR ANY OTHER PARTY OR ANY OTHER PERSON OR FOR ANY SPECIAL, CONSEQUENTIAL, INCIDENTAL, INDIRECT, PUNITIVE, OR EXEMPLARY DAMAGES, HOWEVER CAUSED, ARISING OUT OF OR IN CONNECTION WITH THE DOWNLOADING, VIEWING OR USE OF THE LICENSED MATERIAL REGARDLESS OF THE FORM OF ACTION, WHETHER FOR BREACH OF CONTRACT, BREACH OF WARRANTY, TORT, NEGLIGENCE, INFRINGEMENT OR OTHERWISE (INCLUDING, WITHOUT LIMITATION, DAMAGES BASED ON LOSS OF PROFITS, DATA, FILES, USE, BUSINESS OPPORTUNITY OR CLAIMS OF THIRD PARTIES), AND WHETHER OR NOT THE PARTY HAS BEEN ADVISED OF THE POSSIBILITY OF SUCH DAMAGES. THIS LIMITATION APPLIES NOTWITHSTANDING ANY FAILURE OF ESSENTIAL PURPOSE OF ANY LIMITED REMEDY PROVIDED HEREIN.

10. Termination and Cancellation

10. 1. The License and all rights granted hereunder will continue until the end of the applicable period shown in Clause 5.1 above. Thereafter, this license will be terminated and all rights granted hereunder will cease.

10. 2. Licensor reserves the right to terminate the License in the event that payment is not received in full or if you breach the terms of this License.

11. General

11. 1. The License and the rights and obligations of the parties hereto shall be construed, interpreted and determined in accordance with the laws of the Federal Republic of Germany without reference to the stipulations of the CISG (United Nations Convention on Contracts for the International Sale of Goods) or to Germany´s choice-of-law principle.

11. 2. The parties acknowledge and agree that any controversies and disputes arising out of this License shall be decided exclusively by the courts of or having jurisdiction for Heidelberg, Germany, as far as legally permissible.

11. 3. This License is solely for Licensor's and Licensee's benefit. It is not for the benefit of any other person or entity.

Questions? For questions on Copyright Clearance Center accounts or website issues please contact springernaturesupport@copyright.com or +1-855-239-3415 (toll free in the US) or +1-978-646-2777. For questions on Springer Nature licensing please visit https://www.springernature.com/gp/partners/rights-permissions-third-party-distribution

Other Conditions:

Version 1.4 - Dec 2022

Questions? customercare@copyright.com.

SPRINGER NATURE LICENSE
TERMS AND CONDITIONS

Sep 11, 2023

This Agreement between Mr. Thomas Burge ("You") and Springer Nature ("Springer Nature") consists of your license details and the terms and conditions provided by Springer Nature and Copyright Clearance Center.

License Number	5492950194598
License date	Feb 20, 2023
Licensed Content Publisher	Springer Nature
Licensed Content Publication	The International Journal of Advanced Manufacturing Technology
Licensed Content Title	Morphological analysis of the human knee joint for creating custom-made implant models
Licensed Content Author	Yongtae Jun
Licensed Content Date	Jun 27, 2010
Type of Use	Thesis/Dissertation
Requestor type	academic/university or research institute
Format	print and electronic
Portion	figures/tables/illustrations
Number of figures/tables/illustrations	1
Will you be translating?	no
Circulation/distribution	1 - 29

Author of this Springer Nature content	no
Title	Applied AI/ML for Automatic Customisation of Medical Implants
Institution name	Imperial College
Expected presentation date	Apr 2023
Portions	Figure 3
Requestor Location	Mr. Thomas Burge Imperial College Rd, Kensington London, SW7 1AL United Kingdom Attn: Imperial College
Total	0.00 GBP

Terms and Conditions

Springer Nature Customer Service Centre GmbH Terms and Conditions

The following terms and conditions ("Terms and Conditions") together with the terms specified in your [RightsLink] constitute the License ("License") between you as Licensee and Springer Nature Customer Service Centre GmbH as Licensor. By clicking 'accept' and completing the transaction for your use of the material ("Licensed Material"), you confirm your acceptance of and obligation to be bound by these Terms and Conditions.

1. Grant and Scope of License

1. 1. The Licensor grants you a personal, non-exclusive, non-transferable, non-sublicensable, revocable, world-wide License to reproduce, distribute, communicate to the public, make available, broadcast, electronically transmit or create derivative works using the Licensed Material for the purpose(s) specified in your RightsLink Licence Details only. Licenses are granted for the specific use requested in the order and for no other use, subject to these Terms and Conditions. You acknowledge and agree that the rights granted to you under this License do not include the right to modify, edit, translate, include in collective works, or create derivative works of the Licensed Material in whole or in part unless expressly stated in your RightsLink Licence Details. You may use the Licensed Material only as permitted under this Agreement and will not reproduce, distribute, display, perform, or otherwise use or exploit any Licensed Material in any way, in whole or in part, except as expressly permitted by this License.

1. 2. You may only use the Licensed Content in the manner and to the extent permitted by these Terms and Conditions, by your RightsLink Licence Details and by any applicable laws.

1. 3. A separate license may be required for any additional use of the Licensed Material, e.g. where a license has been purchased for print use only, separate permission must be obtained for electronic re-use. Similarly, a License is only valid in the language selected and does not apply for editions in other languages unless additional translation rights have been granted separately in the License.

1. 4. Any content within the Licensed Material that is owned by third parties is expressly excluded from the License.

1. 5. Rights for additional reuses such as custom editions, computer/mobile applications, film or TV reuses and/or any other derivative rights requests require additional permission and may be subject to an additional fee. Please apply to journalpermissions@springernature.com or bookpermissions@springernature.com for these rights.

2. Reservation of Rights

Licensor reserves all rights not expressly granted to you under this License. You acknowledge and agree that nothing in this License limits or restricts Licensor's rights in or use of the Licensed Material in any way. Neither this License, nor any act, omission, or statement by Licensor or you, conveys any ownership right to you in any Licensed Material, or to any element or portion thereof. As between Licensor and you, Licensor owns and retains all right, title, and interest in and to the Licensed Material subject to the license granted in Section 1.1. Your permission to use the Licensed Material is expressly conditioned on you not impairing Licensor's or the applicable copyright owner's rights in the Licensed Material in any way.

3. Restrictions on use

3. 1. Minor editing privileges are allowed for adaptations for stylistic purposes or formatting purposes provided such alterations do not alter the original meaning or intention of the Licensed Material and the new figure(s) are still accurate and representative of the Licensed Material. Any other changes including but not limited to, cropping, adapting, and/or omitting material that affect the meaning, intention or moral rights of the author(s) are strictly prohibited.

3. 2. You must not use any Licensed Material as part of any design or trademark.

3. 3. Licensed Material may be used in Open Access Publications (OAP), but any such reuse must include a clear acknowledgment of this permission visible at the same time as the figures/tables/illustration or abstract and which must indicate that the Licensed Material is not part of the governing OA license but has been reproduced with permission. This may be indicated according to any standard referencing system but must include at a minimum 'Book/Journal title, Author, Journal Name (if applicable), Volume (if applicable), Publisher, Year, reproduced with permission from SNCSC'.

4. STM Permission Guidelines

4. 1. An alternative scope of license may apply to signatories of the STM Permissions Guidelines ("STM PG") as amended from time to time and made available at https://www.stm-assoc.org/intellectual-property/permissions/permissions-guidelines/.

4. 2. For content reuse requests that qualify for permission under the STM PG, and which may be updated from time to time, the STM PG supersede the terms and

conditions contained in this License.

4. 3. If a License has been granted under the STM PG, but the STM PG no longer apply at the time of publication, further permission must be sought from the Rightsholder. Contact journalpermissions@springernature.com or bookpermissions@springernature.com for these rights.

5. Duration of License

5. 1. Unless otherwise indicated on your License, a License is valid from the date of purchase ("License Date") until the end of the relevant period in the below table:

Reuse in a medical communications project	Reuse up to distribution or time period indicated in License
Reuse in a dissertation/thesis	Lifetime of thesis
Reuse in a journal/magazine	Lifetime of journal/magazine
Reuse in a book/textbook	Lifetime of edition
Reuse on a website	1 year unless otherwise specified in the License
Reuse in a presentation/slide kit/poster	Lifetime of presentation/slide kit/poster. Note: publication whether electronic or in print of presentation/slide kit/poster may require further permission.
Reuse in conference proceedings	Lifetime of conference proceedings
Reuse in an annual report	Lifetime of annual report
Reuse in training/CME materials	Reuse up to distribution or time period indicated in License
Reuse in newsmedia	Lifetime of newsmedia
Reuse in coursepack/classroom materials	Reuse up to distribution and/or time period indicated in license

6. Acknowledgement

6. 1. The Licensor's permission must be acknowledged next to the Licensed Material in print. In electronic form, this acknowledgement must be visible at the same time as the figures/tables/illustrations or abstract and must be hyperlinked to the journal/book's homepage.

6. 2. Acknowledgement may be provided according to any standard referencing system and at a minimum should include "Author, Article/Book Title, Journal name/Book imprint, volume, page number, year, Springer Nature".

7. Reuse in a dissertation or thesis

7. 1. Where 'reuse in a dissertation/thesis' has been selected, the following terms apply: Print rights of the Version of Record are provided for; electronic rights for use only on institutional repository as defined by the Sherpa guideline (www.sherpa.ac.uk/romeo/) and only up to what is required by the awarding institution.

7. 2. For theses published under an ISBN or ISSN, separate permission is required. Please contact journalpermissions@springernature.com or bookpermissions@springernature.com for these rights.

7. 3. Authors must properly cite the published manuscript in their thesis according to current citation standards and include the following acknowledgement: '*Reproduced with permission from Springer Nature'*.

8. License Fee

You must pay the fee set forth in the License Agreement (the "License Fees"). All amounts payable by you under this License are exclusive of any sales, use, withholding, value added or similar taxes, government fees or levies or other assessments. Collection and/or remittance of such taxes to the relevant tax authority shall be the responsibility of the party who has the legal obligation to do so.

9. Warranty

9. 1. The Licensor warrants that it has, to the best of its knowledge, the rights to license reuse of the Licensed Material. **You are solely responsible for ensuring that the material you wish to license is original to the Licensor and does not carry the copyright of another entity or third party (as credited in the published version).** If the credit line on any part of the Licensed Material indicates that it was reprinted or adapted with permission from another source, then you should seek additional permission from that source to reuse the material.

9. 2. EXCEPT FOR THE EXPRESS WARRANTY STATED HEREIN AND TO THE EXTENT PERMITTED BY APPLICABLE LAW, LICENSOR PROVIDES THE LICENSED MATERIAL "AS IS" AND MAKES NO OTHER REPRESENTATION OR WARRANTY. LICENSOR EXPRESSLY DISCLAIMS ANY LIABILITY FOR ANY CLAIM ARISING FROM OR OUT OF THE CONTENT, INCLUDING BUT NOT LIMITED TO ANY ERRORS, INACCURACIES, OMISSIONS, OR DEFECTS CONTAINED THEREIN, AND ANY IMPLIED OR EXPRESS WARRANTY AS TO MERCHANTABILITY OR FITNESS FOR A PARTICULAR PURPOSE. IN NO EVENT SHALL LICENSOR BE LIABLE TO YOU OR ANY OTHER PARTY OR ANY OTHER PERSON OR FOR ANY SPECIAL, CONSEQUENTIAL, INCIDENTAL, INDIRECT, PUNITIVE, OR EXEMPLARY DAMAGES, HOWEVER CAUSED, ARISING OUT OF OR IN CONNECTION WITH THE DOWNLOADING, VIEWING OR USE OF THE LICENSED MATERIAL REGARDLESS OF THE FORM OF ACTION, WHETHER FOR BREACH OF CONTRACT, BREACH OF WARRANTY, TORT, NEGLIGENCE, INFRINGEMENT OR OTHERWISE (INCLUDING, WITHOUT LIMITATION, DAMAGES BASED ON LOSS OF PROFITS, DATA, FILES, USE, BUSINESS OPPORTUNITY OR CLAIMS OF THIRD PARTIES), AND WHETHER OR NOT THE PARTY HAS BEEN ADVISED OF THE POSSIBILITY OF SUCH DAMAGES. THIS LIMITATION APPLIES NOTWITHSTANDING ANY FAILURE OF ESSENTIAL PURPOSE OF ANY LIMITED REMEDY PROVIDED HEREIN.

10. Termination and Cancellation

10. 1. The License and all rights granted hereunder will continue until the end of the applicable period shown in Clause 5.1 above. Thereafter, this license will be terminated and all rights granted hereunder will cease.

10. 2. Licensor reserves the right to terminate the License in the event that payment is not received in full or if you breach the terms of this License.

11. General

11. 1. The License and the rights and obligations of the parties hereto shall be construed, interpreted and determined in accordance with the laws of the Federal

Republic of Germany without reference to the stipulations of the CISG (United Nations Convention on Contracts for the International Sale of Goods) or to Germany´s choice-of-law principle.

11. 2. The parties acknowledge and agree that any controversies and disputes arising out of this License shall be decided exclusively by the courts of or having jurisdiction for Heidelberg, Germany, as far as legally permissible.

11. 3. This License is solely for Licensor's and Licensee's benefit. It is not for the benefit of any other person or entity.

Questions? For questions on Copyright Clearance Center accounts or website issues please contact springernaturesupport@copyright.com or +1-855-239-3415 (toll free in the US) or +1-978-646-2777. For questions on Springer Nature licensing please visit https://www.springernature.com/gp/partners/rights-permissions-third-party-distribution

Other Conditions:

Version 1.4 - Dec 2022

Questions? customercare@copyright.com.

ELSEVIER LICENSE
TERMS AND CONDITIONS

Sep 11, 2023

This Agreement between Mr. Thomas Burge ("You") and Elsevier ("Elsevier") consists of your license details and the terms and conditions provided by Elsevier and Copyright Clearance Center.

License Number	5493270927826
License date	Feb 20, 2023
Licensed Content Publisher	Elsevier
Licensed Content Publication	Biomaterials
Licensed Content Title	Experimental and clinical performance of porous tantalum in orthopedic surgery
Licensed Content Author	Brett Russell Levine,Scott Sporer,Robert A. Poggie,Craig J. Della Valle,Joshua J. Jacobs
Licensed Content Date	Sep 1, 2006
Licensed Content Volume	27
Licensed Content Issue	27
Licensed Content Pages	11
Start Page	4671
End Page	4681
Type of Use	reuse in a thesis/dissertation
Portion	figures/tables/illustrations

Number of figures/tables/illustrations	1
Format	both print and electronic
Are you the author of this Elsevier article?	No
Will you be translating?	No
Title	Applied AI/ML for Automatic Customisation of Medical Implants
Institution name	Imperial College
Expected presentation date	Apr 2023
Portions	Figure 3
Requestor Location	Mr. Thomas Burge Imperial College Rd, Kensington London, SW7 1AL United Kingdom Attn: Imperial College
Publisher Tax ID	GB 494 6272 12
Total	0.00 GBP
Terms and Conditions	

INTRODUCTION

1. The publisher for this copyrighted material is Elsevier. By clicking "accept" in connection with completing this licensing transaction, you agree that the following terms and conditions apply to this transaction (along with the Billing and Payment terms and conditions established by Copyright Clearance Center, Inc. ("CCC"), at the time that you opened your RightsLink account and that are available at any time at https://myaccount.copyright.com).

GENERAL TERMS

2. Elsevier hereby grants you permission to reproduce the aforementioned material subject to the terms and conditions indicated.

3. Acknowledgement: If any part of the material to be used (for example, figures) has appeared in our publication with credit or acknowledgement to another source, permission must also be sought from that source. If such permission is not obtained then that material may not be included in your publication/copies. Suitable acknowledgement to the source must be made, either as a footnote or in a reference list at the end of your publication, as follows:

"Reprinted from Publication title, Vol /edition number, Author(s), Title of article / title of chapter, Pages No., Copyright (Year), with permission from Elsevier [OR APPLICABLE SOCIETY COPYRIGHT OWNER]." Also Lancet special credit - "Reprinted from The Lancet, Vol. number, Author(s), Title of article, Pages No., Copyright (Year), with permission from Elsevier."

4. Reproduction of this material is confined to the purpose and/or media for which permission is hereby given. The material may not be reproduced or used in any other way, including use in combination with an artificial intelligence tool (including to train an algorithm, test, process, analyse, generate output and/or develop any form of artificial intelligence tool), or to create any derivative work and/or service (including resulting from the use of artificial intelligence tools).

5. Altering/Modifying Material: Not Permitted. However figures and illustrations may be altered/adapted minimally to serve your work. Any other abbreviations, additions, deletions and/or any other alterations shall be made only with prior written authorization of Elsevier Ltd. (Please contact Elsevier's permissions helpdesk here). No modifications can be made to any Lancet figures/tables and they must be reproduced in full.

6. If the permission fee for the requested use of our material is waived in this instance, please be advised that your future requests for Elsevier materials may attract a fee.

7. Reservation of Rights: Publisher reserves all rights not specifically granted in the combination of (i) the license details provided by you and accepted in the course of this licensing transaction, (ii) these terms and conditions and (iii) CCC's Billing and Payment terms and conditions.

8. License Contingent Upon Payment: While you may exercise the rights licensed immediately upon issuance of the license at the end of the licensing process for the transaction, provided that you have disclosed complete and accurate details of your proposed use, no license is finally effective unless and until full payment is received from you (either by publisher or by CCC) as provided in CCC's Billing and Payment terms and conditions. If full payment is not received on a timely basis, then any license preliminarily granted shall be deemed automatically revoked and shall be void as if never granted. Further, in the event that you breach any of these terms and conditions or any of CCC's Billing and Payment terms and conditions, the license is automatically revoked and shall be void as if never granted. Use of materials as described in a revoked license, as well as any use of the materials beyond the scope of an unrevoked license, may constitute copyright infringement and publisher reserves the right to take any and all action to protect its copyright in the materials.

9. Warranties: Publisher makes no representations or warranties with respect to the licensed material.

10. Indemnity: You hereby indemnify and agree to hold harmless publisher and CCC, and their respective officers, directors, employees and agents, from and against any and all claims arising out of your use of the licensed material other than as specifically authorized pursuant to this license.

11. No Transfer of License: This license is personal to you and may not be sublicensed, assigned, or transferred by you to any other person without publisher's written permission.

12. No Amendment Except in Writing: This license may not be amended except in a writing signed by both parties (or, in the case of publisher, by CCC on publisher's behalf).

13. Objection to Contrary Terms: Publisher hereby objects to any terms contained in any purchase order, acknowledgment, check endorsement or other writing prepared by you, which terms are inconsistent with these terms and conditions or CCC's Billing and Payment terms and conditions. These terms and conditions, together with CCC's Billing and Payment terms and conditions (which are incorporated herein), comprise the entire agreement between you and publisher (and CCC) concerning this licensing transaction. In the event of any conflict between your obligations established by these terms and conditions and those established by CCC's Billing and Payment terms and conditions, these terms and conditions shall control.

14. Revocation: Elsevier or Copyright Clearance Center may deny the permissions described in this License at their sole discretion, for any reason or no reason, with a full refund payable to you. Notice of such denial will be made using the contact information provided by you. Failure to receive such notice will not alter or invalidate the denial. In no event will Elsevier or Copyright Clearance Center be responsible or liable for any costs, expenses or damage incurred by you as a result of a denial of your permission request, other than a refund of the amount(s) paid by you to Elsevier and/or Copyright Clearance Center for denied permissions.

LIMITED LICENSE

The following terms and conditions apply only to specific license types:

15. **Translation**: This permission is granted for non-exclusive world **English** rights only unless your license was granted for translation rights. If you licensed translation rights you may only translate this content into the languages you requested. A professional translator must perform all translations and reproduce the content word for word preserving the integrity of the article.

16. **Posting licensed content on any Website**: The following terms and conditions apply as follows: Licensing material from an Elsevier journal: All content posted to the web site must maintain the copyright information line on the bottom of each image; A hyper-text must be included to the Homepage of the journal from which you are licensing at http://www.sciencedirect.com/science/journal/xxxxx or the Elsevier homepage for books at http://www.elsevier.com; Central Storage: This license does not include permission for a scanned version of the material to be stored in a central repository such as that provided by Heron/XanEdu.

Licensing material from an Elsevier book: A hyper-text link must be included to the Elsevier homepage at http://www.elsevier.com . All content posted to the web site must maintain the copyright information line on the bottom of each image.

Posting licensed content on Electronic reserve: In addition to the above the following clauses are applicable: The web site must be password-protected and made available only to bona fide students registered on a relevant course. This permission is granted for 1 year only. You may obtain a new license for future website posting.

17. **For journal authors:** the following clauses are applicable in addition to the above:

Preprints:

A preprint is an author's own write-up of research results and analysis, it has not been peer-reviewed, nor has it had any other value added to it by a publisher (such as formatting, copyright, technical enhancement etc.).

Authors can share their preprints anywhere at any time. Preprints should not be added to or enhanced in any way in order to appear more like, or to substitute for, the final versions of articles however authors can update their preprints on arXiv or RePEc with their Accepted Author Manuscript (see below).

If accepted for publication, we encourage authors to link from the preprint to their formal publication via its DOI. Millions of researchers have access to the formal publications on ScienceDirect, and so links will help users to find, access, cite and use the best available version. Please note that Cell Press, The Lancet and some society-owned have different preprint policies. Information on these policies is available on the journal homepage.

Accepted Author Manuscripts: An accepted author manuscript is the manuscript of an article that has been accepted for publication and which typically includes author-incorporated changes suggested during submission, peer review and editor-author communications.

Authors can share their accepted author manuscript:

- immediately
  - via their non-commercial person homepage or blog
  - by updating a preprint in arXiv or RePEc with the accepted manuscript
  - via their research institute or institutional repository for internal institutional uses or as part of an invitation-only research collaboration work-group
  - directly by providing copies to their students or to research collaborators for their personal use
  - for private scholarly sharing as part of an invitation-only work group on commercial sites with which Elsevier has an agreement
- After the embargo period
  - via non-commercial hosting platforms such as their institutional repository
  - via commercial sites with which Elsevier has an agreement

In all cases accepted manuscripts should:

- link to the formal publication via its DOI
- bear a CC-BY-NC-ND license - this is easy to do
- if aggregated with other manuscripts, for example in a repository or other site, be shared in alignment with our hosting policy not be added to or enhanced in any way to appear more like, or to substitute for, the published journal article.

Published journal article (JPA): A published journal article (PJA) is the definitive final record of published research that appears or will appear in the journal and embodies all value-adding publishing activities including peer review co-ordination, copy-editing, formatting, (if relevant) pagination and online enrichment.

Policies for sharing publishing journal articles differ for subscription and gold open access articles:

Subscription Articles: If you are an author, please share a link to your article rather than the full-text. Millions of researchers have access to the formal publications on ScienceDirect, and so links will help your users to find, access, cite, and use the best available version.

Theses and dissertations which contain embedded PJAs as part of the formal submission can be posted publicly by the awarding institution with DOI links back to the formal publications on ScienceDirect.

If you are affiliated with a library that subscribes to ScienceDirect you have additional private sharing rights for others' research accessed under that agreement. This includes use for classroom teaching and internal training at the institution (including use in course packs and courseware programs), and inclusion of the article for grant funding purposes.

Gold Open Access Articles: May be shared according to the author-selected end-user license and should contain a CrossMark logo, the end user license, and a DOI link to the formal publication on ScienceDirect.

Please refer to Elsevier's posting policy for further information.

18. **For book authors** the following clauses are applicable in addition to the above: Authors are permitted to place a brief summary of their work online only. You are not allowed to download and post the published electronic version of your chapter, nor may you scan the printed edition to create an electronic version. **Posting to a repository:** Authors are permitted to post a summary of their chapter only in their institution's repository.

19. **Thesis/Dissertation**: If your license is for use in a thesis/dissertation your thesis may be submitted to your institution in either print or electronic form. Should your thesis be published commercially, please reapply for permission. These requirements include permission for the Library and Archives of Canada to supply single copies, on demand, of the complete thesis and include permission for Proquest/UMI to supply single copies, on demand, of the complete thesis. Should your thesis be published commercially, please reapply for permission. Theses and dissertations which contain embedded PJAs as part of the formal submission can be posted publicly by the awarding institution with DOI links back to the formal publications on ScienceDirect.

Elsevier Open Access Terms and Conditions

You can publish open access with Elsevier in hundreds of open access journals or in nearly 2000 established subscription journals that support open access publishing. Permitted third party re-use of these open access articles is defined by the author's choice of Creative Commons user license. See our open access license policy for more information.

Terms & Conditions applicable to all Open Access articles published with Elsevier:

Any reuse of the article must not represent the author as endorsing the adaptation of the article nor should the article be modified in such a way as to damage the author's honour or reputation. If any changes have been made, such changes must be clearly indicated.

The author(s) must be appropriately credited and we ask that you include the end user license and a DOI link to the formal publication on ScienceDirect.

If any part of the material to be used (for example, figures) has appeared in our publication with credit or acknowledgement to another source it is the responsibility of the user to ensure their reuse complies with the terms and conditions determined by the rights holder.

Additional Terms & Conditions applicable to each Creative Commons user license:

CC BY: The CC-BY license allows users to copy, to create extracts, abstracts and new works from the Article, to alter and revise the Article and to make commercial use of the Article (including reuse and/or resale of the Article by commercial entities), provided the user gives appropriate credit (with a link to the formal publication through the relevant DOI), provides a link to the license, indicates if changes were made and the licensor is not represented as endorsing the use made of the work. The full details of the license are available at http://creativecommons.org/licenses/by/4.0.

CC BY NC SA: The CC BY-NC-SA license allows users to copy, to create extracts, abstracts and new works from the Article, to alter and revise the Article, provided this is not done for commercial purposes, and that the user gives appropriate credit (with a link to the formal publication through the relevant DOI), provides a link to the license, indicates if changes were made and the licensor is not represented as endorsing the use made of the

SPRINGER NATURE LICENSE
TERMS AND CONDITIONS

Sep 11, 2023

This Agreement between Mr. Thomas Burge ("You") and Springer Nature ("Springer Nature") consists of your license details and the terms and conditions provided by Springer Nature and Copyright Clearance Center.

License Number	5526000935314
License date	Apr 11, 2023
Licensed Content Publisher	Springer Nature
Licensed Content Publication	The International Journal of Advanced Manufacturing Technology
Licensed Content Title	Automating the customization of stiffness-matched knee implants using machine learning techniques
Licensed Content Author	Thomas A. Burge et al
Licensed Content Date	Apr 10, 2023
Type of Use	Thesis/Dissertation
Requestor type	academic/university or research institute
Format	print and electronic
Portion	figures/tables/illustrations
Number of figures/tables/illustrations	9
Will you be translating?	no
Circulation/distribution	1 - 29

Author of this Springer Nature content	yes
Title	Applied AI/ML for Automatic Customisation of Medical Implants
Institution name	Imperial College
Expected presentation date	Apr 2023
Portions	Figure 1 (A&B). Figs 4 - 11
Requestor Location	Mr. Thomas Burge Imperial College Rd, Kensington London, SW7 1AL United Kingdom Attn: Imperial College
Total	0.00 EUR

Terms and Conditions

Springer Nature Customer Service Centre GmbH Terms and Conditions

The following terms and conditions ("Terms and Conditions") together with the terms specified in your [RightsLink] constitute the License ("License") between you as Licensee and Springer Nature Customer Service Centre GmbH as Licensor. By clicking 'accept' and completing the transaction for your use of the material ("Licensed Material"), you confirm your acceptance of and obligation to be bound by these Terms and Conditions.

1. Grant and Scope of License

1. 1. The Licensor grants you a personal, non-exclusive, non-transferable, non-sublicensable, revocable, world-wide License to reproduce, distribute, communicate to the public, make available, broadcast, electronically transmit or create derivative works using the Licensed Material for the purpose(s) specified in your RightsLink Licence Details only. Licenses are granted for the specific use requested in the order and for no other use, subject to these Terms and Conditions. You acknowledge and agree that the rights granted to you under this License do not include the right to modify, edit, translate, include in collective works, or create derivative works of the Licensed Material in whole or in part unless expressly stated in your RightsLink Licence Details. You may use the Licensed Material only as permitted under this Agreement and will not reproduce, distribute, display, perform, or otherwise use or exploit any Licensed Material in any way, in whole or in part, except as expressly

permitted by this License.

1. 2. You may only use the Licensed Content in the manner and to the extent permitted by these Terms and Conditions, by your RightsLink Licence Details and by any applicable laws.

1. 3. A separate license may be required for any additional use of the Licensed Material, e.g. where a license has been purchased for print use only, separate permission must be obtained for electronic re-use. Similarly, a License is only valid in the language selected and does not apply for editions in other languages unless additional translation rights have been granted separately in the License.

1. 4. Any content within the Licensed Material that is owned by third parties is expressly excluded from the License.

1. 5. Rights for additional reuses such as custom editions, computer/mobile applications, film or TV reuses and/or any other derivative rights requests require additional permission and may be subject to an additional fee. Please apply to journalpermissions@springernature.com or bookpermissions@springernature.com for these rights.

2. Reservation of Rights

Licensor reserves all rights not expressly granted to you under this License. You acknowledge and agree that nothing in this License limits or restricts Licensor's rights in or use of the Licensed Material in any way. Neither this License, nor any act, omission, or statement by Licensor or you, conveys any ownership right to you in any Licensed Material, or to any element or portion thereof. As between Licensor and you, Licensor owns and retains all right, title, and interest in and to the Licensed Material subject to the license granted in Section 1.1. Your permission to use the Licensed Material is expressly conditioned on you not impairing Licensor's or the applicable copyright owner's rights in the Licensed Material in any way.

3. Restrictions on use

3. 1. Minor editing privileges are allowed for adaptations for stylistic purposes or formatting purposes provided such alterations do not alter the original meaning or intention of the Licensed Material and the new figure(s) are still accurate and representative of the Licensed Material. Any other changes including but not limited to, cropping, adapting, and/or omitting material that affect the meaning, intention or moral rights of the author(s) are strictly prohibited.

3. 2. You must not use any Licensed Material as part of any design or trademark.

3. 3. Licensed Material may be used in Open Access Publications (OAP), but any such reuse must include a clear acknowledgment of this permission visible at the same time as the figures/tables/illustration or abstract and which must indicate that the Licensed Material is not part of the governing OA license but has been reproduced with permission. This may be indicated according to any standard referencing system but must include at a minimum 'Book/Journal title, Author, Journal Name (if applicable), Volume (if applicable), Publisher, Year, reproduced with permission from SNCSC'.

4. STM Permission Guidelines

4. 1. An alternative scope of license may apply to signatories of the STM Permissions Guidelines ("STM PG") as amended from time to time and made available at https://www.stm-assoc.org/intellectual-property/permissions/permissions-guidelines/.

4. 2. For content reuse requests that qualify for permission under the STM PG, and which may be updated from time to time, the STM PG supersede the terms and conditions contained in this License.

4. 3. If a License has been granted under the STM PG, but the STM PG no longer apply at the time of publication, further permission must be sought from the Rightsholder. Contact journalpermissions@springernature.com or bookpermissions@springernature.com for these rights.

5. Duration of License

5. 1. Unless otherwise indicated on your License, a License is valid from the date of purchase ("License Date") until the end of the relevant period in the below table:

Reuse in a medical communications project	Reuse up to distribution or time period indicated in License
Reuse in a dissertation/thesis	Lifetime of thesis
Reuse in a journal/magazine	Lifetime of journal/magazine
Reuse in a book/textbook	Lifetime of edition
Reuse on a website	1 year unless otherwise specified in the License
Reuse in a presentation/slide kit/poster	Lifetime of presentation/slide kit/poster. Note: publication whether electronic or in print of presentation/slide kit/poster may require further permission.
Reuse in conference proceedings	Lifetime of conference proceedings
Reuse in an annual report	Lifetime of annual report
Reuse in training/CME materials	Reuse up to distribution or time period indicated in License
Reuse in newsmedia	Lifetime of newsmedia
Reuse in coursepack/classroom materials	Reuse up to distribution and/or time period indicated in license

6. Acknowledgement

6. 1. The Licensor's permission must be acknowledged next to the Licensed Material in print. In electronic form, this acknowledgement must be visible at the same time as the figures/tables/illustrations or abstract and must be hyperlinked to the journal/book's homepage.

6. 2. Acknowledgement may be provided according to any standard referencing system and at a minimum should include "Author, Article/Book Title, Journal name/Book imprint, volume, page number, year, Springer Nature".

7. Reuse in a dissertation or thesis

7. 1. Where 'reuse in a dissertation/thesis' has been selected, the following terms apply: Print rights of the Version of Record are provided for; electronic rights for use only on institutional repository as defined by the Sherpa guideline (www.sherpa.ac.uk/romeo/) and only up to what is required by the awarding institution.

7. 2. For theses published under an ISBN or ISSN, separate permission is required. Please contact journalpermissions@springernature.com or bookpermissions@springernature.com for these rights.

7. 3. Authors must properly cite the published manuscript in their thesis according to current citation standards and include the following acknowledgement: '*Reproduced with permission from Springer Nature*'.

8. License Fee

You must pay the fee set forth in the License Agreement (the "License Fees"). All amounts payable by you under this License are exclusive of any sales, use, withholding, value added or similar taxes, government fees or levies or other assessments. Collection and/or remittance of such taxes to the relevant tax authority shall be the responsibility of the party who has the legal obligation to do so.

9. Warranty

9. 1. The Licensor warrants that it has, to the best of its knowledge, the rights to license reuse of the Licensed Material. **You are solely responsible for ensuring that the material you wish to license is original to the Licensor and does not carry the copyright of another entity or third party (as credited in the published version).** If the credit line on any part of the Licensed Material indicates that it was reprinted or adapted with permission from another source, then you should seek additional permission from that source to reuse the material.

9. 2. EXCEPT FOR THE EXPRESS WARRANTY STATED HEREIN AND TO THE EXTENT PERMITTED BY APPLICABLE LAW, LICENSOR PROVIDES THE LICENSED MATERIAL "AS IS" AND MAKES NO OTHER REPRESENTATION OR WARRANTY. LICENSOR EXPRESSLY DISCLAIMS ANY LIABILITY FOR ANY CLAIM ARISING FROM OR OUT OF THE CONTENT, INCLUDING BUT NOT LIMITED TO ANY ERRORS, INACCURACIES, OMISSIONS, OR DEFECTS CONTAINED THEREIN, AND ANY IMPLIED OR EXPRESS WARRANTY AS TO MERCHANTABILITY OR FITNESS FOR A PARTICULAR PURPOSE. IN NO EVENT SHALL LICENSOR BE LIABLE TO YOU OR ANY OTHER PARTY OR ANY OTHER PERSON OR FOR ANY SPECIAL, CONSEQUENTIAL, INCIDENTAL, INDIRECT, PUNITIVE, OR EXEMPLARY DAMAGES, HOWEVER CAUSED, ARISING OUT OF OR IN CONNECTION WITH THE DOWNLOADING, VIEWING OR USE OF THE LICENSED MATERIAL REGARDLESS OF THE FORM OF ACTION, WHETHER FOR BREACH OF CONTRACT, BREACH OF WARRANTY, TORT, NEGLIGENCE, INFRINGEMENT OR OTHERWISE (INCLUDING, WITHOUT LIMITATION, DAMAGES BASED ON LOSS OF PROFITS, DATA, FILES, USE, BUSINESS OPPORTUNITY OR CLAIMS OF THIRD PARTIES), AND WHETHER OR NOT THE PARTY HAS BEEN ADVISED OF THE POSSIBILITY OF SUCH DAMAGES. THIS LIMITATION APPLIES NOTWITHSTANDING ANY FAILURE OF ESSENTIAL PURPOSE OF ANY LIMITED REMEDY PROVIDED HEREIN.

10. Termination and Cancellation

10. 1. The License and all rights granted hereunder will continue until the end of the applicable period shown in Clause 5.1 above. Thereafter, this license will be terminated and all rights granted hereunder will cease.

10. 2. Licensor reserves the right to terminate the License in the event that payment is not received in full or if you breach the terms of this License.

11. General

11. 1. The License and the rights and obligations of the parties hereto shall be construed, interpreted and determined in accordance with the laws of the Federal Republic of Germany without reference to the stipulations of the CISG (United Nations Convention on Contracts for the International Sale of Goods) or to Germany´s choice-of-law principle.

11. 2. The parties acknowledge and agree that any controversies and disputes arising out of this License shall be decided exclusively by the courts of or having jurisdiction for Heidelberg, Germany, as far as legally permissible.

11. 3. This License is solely for Licensor's and Licensee's benefit. It is not for the benefit of any other person or entity.

Questions? For questions on Copyright Clearance Center accounts or website issues please contact springernaturesupport@copyright.com or +1-855-239-3415 (toll free in the US) or +1-978-646-2777. For questions on Springer Nature licensing please visit https://www.springernature.com/gp/partners/rights-permissions-third-party-distribution

Other Conditions:

Version 1.4 - Dec 2022

Questions? customercare@copyright.com.